

2013

Advancements in resonant column testing of soils using random vibration techniques

Bing Yu

Iowa State University

Follow this and additional works at: <https://lib.dr.iastate.edu/etd>



Part of the [Civil Engineering Commons](#)

Recommended Citation

Yu, Bing, "Advancements in resonant column testing of soils using random vibration techniques" (2013). *Graduate Theses and Dissertations*. 13218.

<https://lib.dr.iastate.edu/etd/13218>

This Thesis is brought to you for free and open access by the Iowa State University Capstones, Theses and Dissertations at Iowa State University Digital Repository. It has been accepted for inclusion in Graduate Theses and Dissertations by an authorized administrator of Iowa State University Digital Repository. For more information, please contact digirep@iastate.edu.

**Advancements in resonant column testing of soils using random
vibration techniques**

by

Bing Yu

A thesis submitted to the graduate faculty
in partial fulfillment of the requirements for the degree of
MASTER OF SCIENCE

Major: Civil Engineering (Geotechnical Engineering)

Program of Study Committee:
Jeramy C. Ashlock, Major Professor
Vernon R. Schaefer
Mervyn G. Marasinghe

Iowa State University
Ames, Iowa
2013

Copyright © Bing Yu, 2013. All rights reserved.

TABLE OF CONTENTS

LIST OF TABLES	iv
LIST OF FIGURES	v
ACKNOWLEDGMENTS	x
ABSTRACT	xi
CHAPTER 1. INTRODUCTION.....	1
1.1 History.....	1
1.2 Motivation of This Study	3
CHAPTER 2. EXPERIMENTAL SETUP AND CALIBRATION	6
2.1 Free-Free Resonant Column Apparatus	6
2.1.1 Modifications to the apparatus.....	8
2.1.2 Pressure, pore water and vacuum control system	10
2.1.3 Instrumentation and data acquisition system	12
2.2 Calibration.....	20
2.2.1 Rotational calibration factors.....	21
2.2.2 Apparatus resonant frequency.....	22
2.2.3 Passive-end platen rotational inertia	26
2.2.4 Active-end platen rotational inertia	28
2.2.5 Apparatus damping coefficient.....	30
2.2.6 Torque/current calibration factor	32
CHAPTER 3. THEORY FOR INTERPRETATION OF EXPERIMENTAL DATA	35
3.1 Analytical Solution for Harmonic Torsional Excitation of Soil Specimen.....	35
3.2 Transfer Functions.....	45
3.2.1 Rotational transfer function	45
3.2.2 Passive rotation/torque transfer function	53
3.3 Measurement Approach	65
3.3.1 Fourier transform	65
3.3.2 Frequency response function	66
3.4 Strain Calculation Using Transfer Function.....	69
CHAPTER 4. SPECIMEN PREPARATION AND TEST PROCEDURES	74

4.1	Material	74
4.2	Specimen Preparation.....	75
4.3	Test Procedures	78
CHAPTER 5. EXPERIMENTAL RESULTS		80
5.1	Modified RC Tests at the University of Colorado at Denver.....	80
5.2	Calibration Rod Using Transfer Function Approach and ASTM Method.....	95
5.3	RC Tests at Iowa State University	101
5.3.1	Tests on 6.0 inch diameter specimen using transfer function approach	101
5.3.2	Tests on 2.8 inch diameter and 6 inch height specimen using transfer function approach	107
5.3.3	Tests on 2.8 inch diameter and 11.2 inch height specimen using transfer function approach and ASTM method.....	109
CHAPTER 6. CONCLUSIONS AND RECOMMENDATIONS.....		143
BIBLIOGRAPHY		147
APPENDIX A. RESONANT COLUMN EQUATION DERIVATION		149
APPENDIX B. RESONANT COLUMN SPECIMEN PREPARATION		164
APPENDIX C. RESONANT COLUMN DATA REDUCTION MATLAB CODE		172
APPENDIX D. MODIFIED RCDARE SPREADSHEET FOR ASTM RESONANT COLUMN TESTING DATA REDUCTION.....		183

LIST OF TABLES

Table 2.1: RC apparatus calibration summary.....	20
Table 2.2: Summary of the calculation of RCF.	22
Table 2.3: Calculated passive end rotational inertias.....	28
Table 2.4: Calibrated active end platen rotational inertia and apparatus spring constant.....	30
Table 2.5: Results of apparatus logarithmic decrement.....	32
Table 2.6: Torque/current calibration factor results.	34
Table 3.1: Assumed properties of specimen and apparatus for demonstrating theoretical rotational transfer functions.	47
Table 3.2: Properties of specimen and apparatus for plotting the rotation/torque transfer function.	55
Table 4.1: Consistency of coarse-grained soil and relative density (adapted from Lambe and Whitman, 1969).....	76
Table 5.1: Specimen and apparatus properties of previous RC tests at University of Colorado at Denver	80
Table 5.2: Results of shear modulus and damping ratio at each peak using “peak only” fitting method and “squared-error” fitting method (confining pressure 69.8 kPa).	82
Table 5.3: Measured properties of calibration rod by transfer function approach.....	96
Table 5.4: Shear modulus of calibration rod using ASTM test method.	98
Table 5.5: The damping ratio of calibration rod using ASTM method.	98
Table 5.6: Results of shear modulus and damping ratio at each peak using “peak only” fitting method and “squared-error” fitting method (ISU 6” specimen at 69.8 kPa confining pressure).	102
Table 5.7: Specimen properties of 2.8”×11.2” specimen.	111
Table 5.8: Details and results of transfer function approach at different excitation levels and confining pressures (ISU 2.8”×11.2” specimen).	114
Table 5.9: Results of ASTM method using RCDARE.	139
Table D.1: Errors in the VB of RCDARE spread sheet.....	185

LIST OF FIGURES

Figure 1.1: Longitudinal resonant column models with different boundary conditions (a) fixed-free, (b) fixed-base spring-top, (c) free-free, (d) spring-base spring-top, (e) fixed-base spring-reaction mass-spring-top, (f) spring-base spring-reaction mass-spring-top (Ashmawy and Drnevich, 1994). M_a , M_p , and M_r denote masses of the active (driven), passive (non-driven) and reaction platens.	2
Figure 2.1: Free-free resonant column test setup (modified from Drnevich, 1987).	8
Figure 2.2: Schematic of the modified resonant column apparatus with accelerometers measuring tangential acceleration of end platens.	10
Figure 2.3: Humboldt HM-4150 pressure and vacuum control panel (source: Humboldt Manufacturing).	11
Figure 2.4: Control and data acquisition system wiring diagram	16
Figure 2.5: LabVIEW network analyzer front panel.	17
Figure 2.6: Sine waveform excitation.	18
Figure 2.7: a). swept-sine with oscillate ON, $F_{start}=1$ Hz and $F_{end}=2000$ Hz; b). swept-sine with oscillate ON, $F_{start}=2000$ Hz and $F_{end}=1$ Hz; c). swept-sine with oscillate OFF, $F_{start}=2000$ Hz and $F_{end}=1$ Hz; d). swept-sine with oscillate OFF, $F_{start}=1$ Hz and $F_{end}=2000$ Hz;	18
Figure 2.8: LabVIEW oscilloscope front panel.	19
Figure 2.9: RC device auxiliary calibration platen (8"×3.5").	21
Figure 2.10: a) Channel output vs. time and b) Lissajous plot recorded by LabVIEW oscilloscope program for calibration of device undamped natural frequency of vibration.	25
Figure 2.11: Acceleration PSD in frequency-domain for calibration of device undamped natural frequency of vibration with swept-sine excitation.	25
Figure 2.12: Passive end platen and attachments.	27
Figure 2.13: Decay curve using a 1 Amp fuse to cut off the power.	31
Figure 2.14: Plot of $\ln(A_1/A_{n+1})$ vs. n to determine the logarithmic decrement δ	31
Figure 3.1: Positive directions of torque, rotation and shear strain.	38
Figure 3.2: Free-body diagrams for E.O.M. at (a) passive and (b) active ends.	42
Figure 3.3: Theoretical rotational transfer function.	48
Figure 3.4: Accelerometers at passive and active ends.	49
Figure 3.5: Effect of hysteretic damping ratio ξ on theoretical rotational transfer function.	50
Figure 3.6: Close-up showing effect of hysteretic damping ratio ξ on theoretical rotational transfer function.	51

Figure 3.7: Effect of shear modulus G on theoretical rotational transfer function.	52
Figure 3.8: Close-up showing effect of shear modulus G on theoretical rotational transfer function.	53
Figure 3.9: Theoretical rotation/torque transfer function	56
Figure 3.10: Theoretical rotational velocity/torque transfer function.....	57
Figure 3.11: Effect of apparatus stiffness k_{st} on theoretical rotational velocity/torque transfer function.	58
Figure 3.12: Close-up showing effect of apparatus stiffness k_{st} on theoretical velocity rotational transfer function.	59
Figure 3.13: Effect of apparatus damping ratio ξ_a on theoretical rotational velocity/torque transfer function.	60
Figure 3.14: Effect of specimen shear modulus G on theoretical rotational velocity/torque transfer function.	61
Figure 3.15: Close-up showing effect of specimen shear modulus G on theoretical velocity rotational transfer function.	62
Figure 3.16: Effect of specimen damping ratio ξ on theoretical rotational velocity/torque transfer function.	63
Figure 3.17: Close-up showing effect of specimen damping ratio ξ on the magnitude of theoretical velocity rotational transfer function.	64
Figure 3.18: Close-up showing effect of specimen damping ratio ξ on the phase of theoretical velocity rotational transfer function.	64
Figure 3.19: An ideal single-input/ single-output system without extraneous noise.....	66
Figure 4.1: Particle size distribution curve of ASTM 20/30 test sand.....	74
Figure 5.1: Representative 0.8 second time-history of end platen tangential accelerations (confining pressure 69.8 kPa). TR: top right, TL: top left, BR: bottom right, BL: bottom left. Modified from Ashlock and Pak (2010).	86
Figure 5.2: Experimental rotational transfer and coherence functions (confining pressure 69.8 kPa). Modified from Ashlock and Pak (2010).	86
Figure 5.3: Experimental rotational transfer functions at different confining pressure. Modified from Ashlock and Pak (2010).	87
Figure 5.4: Theoretical and experimental transfer functions fit to 2 nd peak (confining pressure 69.8 kPa). Modified from Ashlock and Pak (2010).	88
Figure 5.5: Magnitude of theoretical and experimental transfer functions by “peak only” fitting approach (confining pressure 69.8 kPa).	89
Figure 5.6: Surface plots of error function for “squared-error” fitting 1 st peak (confining pressure 69.8 kPa).	90

Figure 5.7: Surface plots of error function for “squared-error” fitting 3 rd peak (confining pressure 69.8 kPa).	90
Figure 5.8: Comparisons between “squared-error” fitting and “peak only” fitting methods (confining pressure 69.8 kPa).	91
Figure 5.9: Accelerometer time histories divided into four-0.2 second windows with applied Hanning windows for taking the FFT.	92
Figure 5.10: Experimental rotational transfer functions of four 0.2 second windows compared to experimental transfer function averaged from thirty 0.8 second windows.	92
Figure 5.11: Strain spectrum (0-2000 Hz) of averaged 4 Hanning windows (confining pressure 69.8 kPa).	93
Figure 5.12: Strain spectrum (0-250 Hz) of averaged 4 Hanning windows vs. 1 Hanning window (confining pressure 69.8 kPa).	93
Figure 5.13: Nonlinear strain-dependent modulus and damping curves obtained by fitting five peaks from a single test (confining pressure 69.8 kPa).	94
Figure 5.14: Rotational transfer function and coherence of the calibration rod (bandwidth 0-250 Hz; swept-sine waveform; oscillate OFF; F_{start} =250 Hz; F_{end} =5 Hz).	99
Figure 5.15: Theoretical rotational velocity/torque transfer function of the calibration rod.	100
Figure 5.16: Complete time-histories under swept-sine vibration with oscillate ON; F_{start} =2000 Hz and F_{end} =0 Hz (ISU 6” specimen at 69.8 kPa confining pressure).	103
Figure 5.17: Experimental transfer functions vs. number of averages (ISU 6” specimen at 69.8 kPa confining pressure).	103
Figure 5.18: Magnitude of theoretical and experimental transfer functions for “peak only” fitting of 5 peaks (ISU 6” specimen at 69.8 kPa confining pressure).	104
Figure 5.19: Magnitude of theoretical and experimental transfer functions for “squared-error” fitting of 5 peaks (ISU 6” specimen at 69.8 kPa confining pressure).	105
Figure 5.20: Averaged strain spectrum magnitude and phase (ISU 6” specimen at 69.8 kPa confining pressure).	106
Figure 5.21: Nonlinear strain-dependent modulus and damping using “peak only” and “squared-error” fitting of first 5 peaks (ISU 6” specimen at 69.8 kPa confining pressure).	106
Figure 5.22: Magnitude of theoretical and experimental transfer functions for “peak only” fitting of 3 peaks (ISU 2.8”×6.0” specimen at 69.8 kPa confining pressure).	108
Figure 5.23: Nonlinear strain-dependent modulus and damping (ISU 2.8”×6.0” specimen at 69.8 kPa confining pressure).	108
Figure 5.24: 2.8 inch diameter and 11.2 inch height ASTM 20/30 sand specimen.	110

Figure 5.25: Theoretical and experimental transfer functions at high excitation level (ISU 2.8"×11.2" specimen at 69.8 kPa confining pressure).	113
Figure 5.26: Arithmetic average and RMS strain spectrum (ISU 2.8"×11.2" specimen at 69.8 kPa confining pressure).	115
Figure 5.27: Magnitudes of theoretical and experimental transfer function from low excitation (top plot) to high excitation (bottom plot). ISU 2.8"×11.2" specimen at 69.8 kPa confining pressure.	116
Figure 5.28: Magnitudes of arithmetic average and RMS strain spectrum from low excitation (top plot) to high excitation (bottom plot). ISU 2.8"×11.2" specimen at 69.8 kPa confining pressure.	117
Figure 5.29: Magnitudes of theoretical and experimental transfer function from low excitation (top plot) to high excitation (bottom plot). ISU 2.8"×11.2" specimen at 344.7 kPa confining pressure.	118
Figure 5.30: Magnitudes of arithmetic average and RMS strain spectrum from low excitation (top plot) to high excitation (bottom plot). ISU 2.8"×11.2" specimen at 344.7 kPa confining pressure.	119
Figure 5.31: Nonlinear strain-dependent modulus and damping curves (ISU 2.8"×11.2" specimen at 69.8 kPa confining pressure).	120
Figure 5.32: Nonlinear strain-dependent modulus and damping curves (ISU 2.8"×11.2" specimen at 137.9 kPa confining pressure).	120
Figure 5.33: Nonlinear strain-dependent modulus and damping curves (ISU 2.8"×11.2" specimen at 206.8 kPa confining pressure).	121
Figure 5.34: Nonlinear strain-dependent modulus and damping curves (ISU 2.8"×11.2" specimen at 275.8 kPa confining pressure).	121
Figure 5.35: Nonlinear strain-dependent modulus and damping curves (ISU 2.8"×11.2" specimen at 344.7 kPa confining pressure).	122
Figure 5.36: G/G_{max} curves using transfer function approach at different confining pressures (ISU 2.8"×11.2" specimen).	122
Figure 5.37: Damping ratio versus strain magnitudes at different confining pressures (ISU 2.8"×11.2" specimen).	123
Figure 5.38: Best-fit maximum shear modulus vs. confining pressure using transfer function method (ISU 2.8"×11.2" specimen).	123
Figure 5.39: Theoretical rotational velocity/torque transfer function for soil specimen with $G=200$ MPa and $\zeta=1\%$	130
Figure 5.40: Shear modulus versus shear strain curves using ASTM from high to low confining pressure (RCDARE data reduction).	131
Figure 5.41: Shear modulus versus shear strain curves using ASTM from high to low confining pressure (simplified data reduction).	131

Figure 5.42: Damping ratio versus shear strain curves using ASTM from high to low confining pressure (RCDARE data reduction).	132
Figure 5.43: Damping ratio versus shear strain curves using ASTM from high to low confining pressure (simplified data reduction).	132
Figure 5.44: G/G_{max} curve comparisons at confining pressure 69.8 kPa (10 psi).....	133
Figure 5.45: ξ curve comparisons at confining pressure 69.8 kPa (10 psi).	133
Figure 5.46: G/G_{max} curve comparisons at confining pressure 137.9 kPa (20 psi).....	134
Figure 5.47: ξ curve comparisons at confining pressure 137.9 kPa (20 psi).	134
Figure 5.48: G/G_{max} curve comparisons at confining pressure 206.8 kPa (30 psi).....	135
Figure 5.49: ξ curve comparisons at confining pressure 206.8 kPa (30 psi).	135
Figure 5.50: G/G_{max} curve comparisons at confining pressure 275.8 kPa (40 psi).....	136
Figure 5.51: ξ curve comparisons at confining pressure 275.8 kPa (40 psi).	136
Figure 5.52: G/G_{max} curve comparisons at confining pressure 344.7 kPa (50 psi).....	137
Figure 5.53: ξ curve comparisons at confining pressure 344.7 kPa (50 psi).	137
Figure 5.54: Best-fit maximum shear modulus vs. confining pressure curve comparisons.	138
Figure 5.55: Comparison of ASTM G/G_{max} vs. γ to previous studies (ISU 2.8"×11.2" specimen). Modified from Seed and Idriss (1970).....	141
Figure 5.56: Comparison of ASTM ξ vs. γ to previous studies (ISU 2.8"×11.2" specimen) Modified from Seed and Idriss (1970).....	142
Figure A.1: Differential slice of specimen.....	150

ACKNOWLEDGMENTS

I would like first to thank my advisor, Dr. Jeramy Ashlock, for his guidance and tremendous help throughout my undergraduate and graduate studies.

I would also like to thank Dr. Vernon Schaefer and Dr. Mervyn Marasinghe for severing on my committee.

I would like to thank Ji Lu for his help in the lab. Thanks to Ted Bechtum for the LabVIEW DAQ program that he wrote.

A special thanks to my parents, Ruilin Yu and Jun Meng, for their support and understanding.

Most of all, I would like to thank my wife, Wanjun, for her encouragement and support throughout this study.

ABSTRACT

This study focuses on advancements in resonant column testing of soil and rock using random vibration techniques. A large free-free resonant column device was built and modified to enable the direct measurement of rotational transfer functions of soil specimens in the frequency domain. Theoretical rotational transfer functions and strain measures were derived and programmed for the new approach. Random (white noise) and swept-sine excitation types were used to vibrate soil specimens over a range of strain levels, confining pressures, and frequencies, while rotational accelerations of the end platens were measured. Shear modulus and damping were then determined by fitting the measured peak frequencies and amplitudes by theoretical rotational transfer functions. Nonlinear strain-dependent modulus and damping curves were generated by measurement of the multi-modal vibration response over a range of excitation intensities. To provide a preliminary validation, results for the new technique are evaluated against those from the current ASTM Standard D4015 for the same soil specimens. Results were found to compare well in terms of maximum shear modulus as a function of confining pressure. The nonlinear strain-dependent modulus reduction and damping curves were found to be similar in shape, but have different values of shear strain, possibly due to the need to account for strain energy at all frequencies in the broadband transfer function tests.

CHAPTER 1. INTRODUCTION

1.1 History

In various civil engineering projects, analysis of wave propagation associated with dynamic loading (for example, traffic loadings, foundations supporting vibratory machinery, earthquakes, or explosions) is often of critical importance. To adequately characterize the dynamic or seismic response of soils for analysis and design, it is often necessary to accurately measure dynamic properties of soil specimens in the laboratory over a range of confining stresses and dynamic strain levels. The resonant column (RC) test is a relatively nondestructive laboratory test employing wave propagation in cylindrical specimens for measurement of shear modulus and damping of soils at small strains (Drnevich, 1978). This test has been used over the past half-century in research and practice problems of soil dynamics and earthquake engineering. The RC technique was first applied to testing soils in Japan by Ishimoto and Iida (1937) and Iida (1938, 1940), and many significant developments of RC testing procedures were made in the 1960's. One of the earlier types of RC devices in the United States was used by Wilson and Dietrich (1960) for testing clay specimens.

There are a number of different types of RC devices, which vary in their boundary conditions and mode of vibration (Wilson and Dietrich, 1960; Hardin and Music, 1965; Drnevich, 1978; Isenhower, 1980; Lewis, 1990; Cascante et al., 1998). The apparatus shown in Figure 1.1a is known as a fixed-free longitudinal apparatus, as it does not have any stiffness or damping elements connected to the top platen. The apparatus with boundary conditions shown in Figure 1.1b is known as Hardin-type apparatus (Hardin and Music, 1965). These RC devices have one end of the specimen fixed and are commonly used due to the relative simplicity of the equipment and data reduction procedures. The apparatus in

Figure 1.1c is termed the free-free apparatus (Drnevich, 1978) as neither end of the specimen is fixed. This type of apparatus is advantageous for testing large or stiff specimens, including rock. Theoretical models for the apparatus shown in Figure 1.1d (Drnevich, 1985) and Figure 1.1e (Min et al., 1990) can be used to account for imperfect fixity conditions. Numerous studies have been performed to compare test results from the different types of RC test devices. Results of these investigations showed that no systematic or consistent differences could be associated with the different apparatus types used (e.g., see Skoglud et al., 1976).

Although the devices shown in Figure 1.1 excite the soil specimen in the longitudinal mode, most devices including the one used in this study use the torsional mode of vibration. For the remainder of this thesis, all discussion of RC testing will refer to the torsional mode of vibration. In practice, the torsional fixed-free RC device is the most commonly used type.

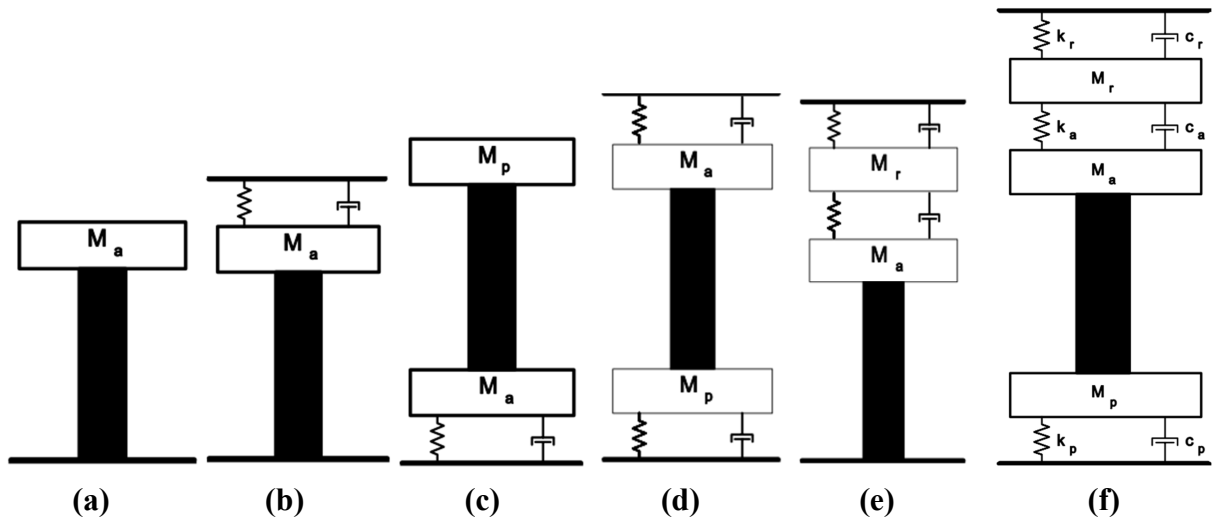


Figure 1.1: Longitudinal resonant column models with different boundary conditions (a) fixed-free, (b) fixed-base spring-top, (c) free-free, (d) spring-base spring-top, (e) fixed-base spring-reaction mass-spring-top, (f) spring-base spring-reaction mass-spring-top (Ashmawy and Drnevich, 1994). M_a , M_p , and M_r denote masses of the active (driven), passive (non-driven) and reaction platens.

1.2 Motivation of This Study

Standard test methods for measuring the modulus and damping of soils are issued by the American Society for Testing and Material (ASTM) through Standard D4015-07 (ASTM 2007). The current standard covers both longitudinal and torsional devices, and specifies the use of harmonic excitation, with determination of a single resonant frequency as the objective.

The current standard procedure also requires many device-dependent calibrations and properties which can introduce additional uncertainties and approximations (such as a linear torque/current relationship), and should be repeated annually. Examples of these quantities for the free-free device are the rotational inertia of the end-platens, stiffness and damping idealized as torsional springs and dashpots connected to the active beam, and the torque/current calibration factor. The calibration processes are usually laborious and restricted. Consider the calibration of active platen rotational inertia for example; the ASTM standard requires that one end of the calibration rod shall be rigidly fixed and the other end shall be rigidly fastened to the active platen. Perfect fixity of the calibration rod is difficult to achieve in a typical laboratory setting, as it would require a stiff reaction frame. An alternative recommendation is to bolt the device upside down to the floor and measure the vibration of the passive beam, which would be very labor intensive and imprecise, as the rotational inertia of the passive beam must be estimated. As an economical and more precise non-standard alternative, a large steel cylindrical plate was fabricated in this study and used as an auxiliary mass for calibrating the rotational inertia of the active platen and all its attached components.

Besides the requirement of a torque/current calibration factor, the standard practice of basing measurements on the current in a magnet-coil driving system in RC devices can also

contribute some bias and error in results. For example, the motion of the magnets results in a magnetic field that induces an electromagnetic force (EMF) in the solenoids (described by Faraday's Law). The induced EMF opposes the motion that produces it, and it is therefore termed back-EMF (described by Lenz's Law). Back-EMF typically leads to negligible errors in measured values of shear modulus, but can appreciably affect the measured material damping ratio (e.g. Cascante et al., 1997; 2003; Wang et al., 2003; Meng and Rix, 2003). Many studies have been conducted on the difference between current and voltage measurement in RC testing. The results of those studies show that commonly used ground-referenced voltage-based measurements can significantly overestimate the damping ratio because of the induced voltage produced by the motion of the magnets along the central axes of elliptical coils (e.g. Li et al., 1998; Cascante et al., 2003; Wang et al., 2003). To avoid the back-EMF problem, it is recommended to directly measure current, or equivalently, to measure the voltage drop across a power resistor, as opposed to the common practice of measuring voltage between a point in the drive circuit and ground.

The motivation of this study was to improve RC testing regarding these disadvantages by further developing a promising transfer-function approach that greatly simplifies testing and analysis procedures. In this study, random vibration techniques (e.g., see Bendat and Piersol, 2010) were applied to RC testing. Random vibration techniques including transfer functions, output-only techniques, and input-output techniques have previously been attempted by many researchers (e.g., Yong et al., 1997; Al-Sanad et al., 1983; Amini et al., 1988; Aggour et al., 1989; Cascante and Santamarina, 1997; Ashlock and Pak, 2010a). In this study, an input-output format transfer function described in Ashlock and Pak (2010a) was used through a direct measurement of the rotational motion at the boundaries of the soil

specimen. As previously mentioned, the existing ASTM approach specifies a sinusoidal excitation to measure the response at only the first resonant peak frequency. In contrast, the transfer function method can apply broadband random excitation types (e.g. swept-sine and white noise) to capture the soil specimen's multi-modal response in the frequency domain. The possibility of simultaneously measuring multiple points on the nonlinear strain-dependent modulus and damping curves in a single test, owing to different strain levels at the different peaks, will also be explored in this thesis.

CHAPTER 2. EXPERIMENTAL SETUP AND CALIBRATION

2.1 Free-Free Resonant Column Apparatus

All tests in this research were performed on a custom free-free Drnevich type RC apparatus which was fabricated at Iowa State University in 2009. This system consists of a cylindrical specimen that has platens attached to each end as shown in Figure 2.1.

The passive-end platen is free, and only the instrumentation wires are attached to it. The active-end platen is connected to a large active beam with electromagnet coils on the ends, which are suspended in the gap of permanent magnets mounted to a stationary passive beam for torsional vibration excitation. When an alternating electric current flows in the coils, the electromagnetic forces push the two ends of the active beam in opposite directions to cause rotation of the active-end platen at the bottom of the soil specimen. An aluminum spool (a rotational spring, actually a hollow tube) with known stiffness is fixed on the ground to support the device. In accordance with the ASTM standard, the stiffness and damping of the spool is modeled as a single-degree-of-freedom (SDOF) spring and dashpot connected in parallel between the active-end platen and the passive reaction beam.

Two geophones located under the base plate monitor the motion of the active platen, and two others are clamped on the passive-end platen. These geophones use a seismic mass magnet suspended by springs, and a coil fixed to the case. Their output signal results from relative movement between the magnet and coil during the vibration. Each pair of geophones is connected in series, so the tangential velocity can be measured by means of their summed output.

The specimen and end platens are enclosed in an acrylic chamber to enable the application of a range of confining pressures via water or air. There are two valves on the

base to control the all-around confining pressure in the chamber, and to enable saturation of soil specimens and monitoring of pore water pressure for controlled conditions representative of in-situ soils (e.g. pore-water pressure and degree of saturation).

The device has three different types of platens with capabilities for testing 2.8, 4 and 6 inch diameter specimens. The bottom platen and top platen have the same geometry. The difference between them is that the bottom platen has a hole in the center to supply water/drainage or vacuum. The 6 inch platen was machined with pyramidal points to increase the friction between the specimen and the top surface of the platen. To ensure sufficient coupling between the soil specimen and the 2.8 and 4 inch platens, matching porous sintered bronze or stainless steel disks are available for attaching to the platens.

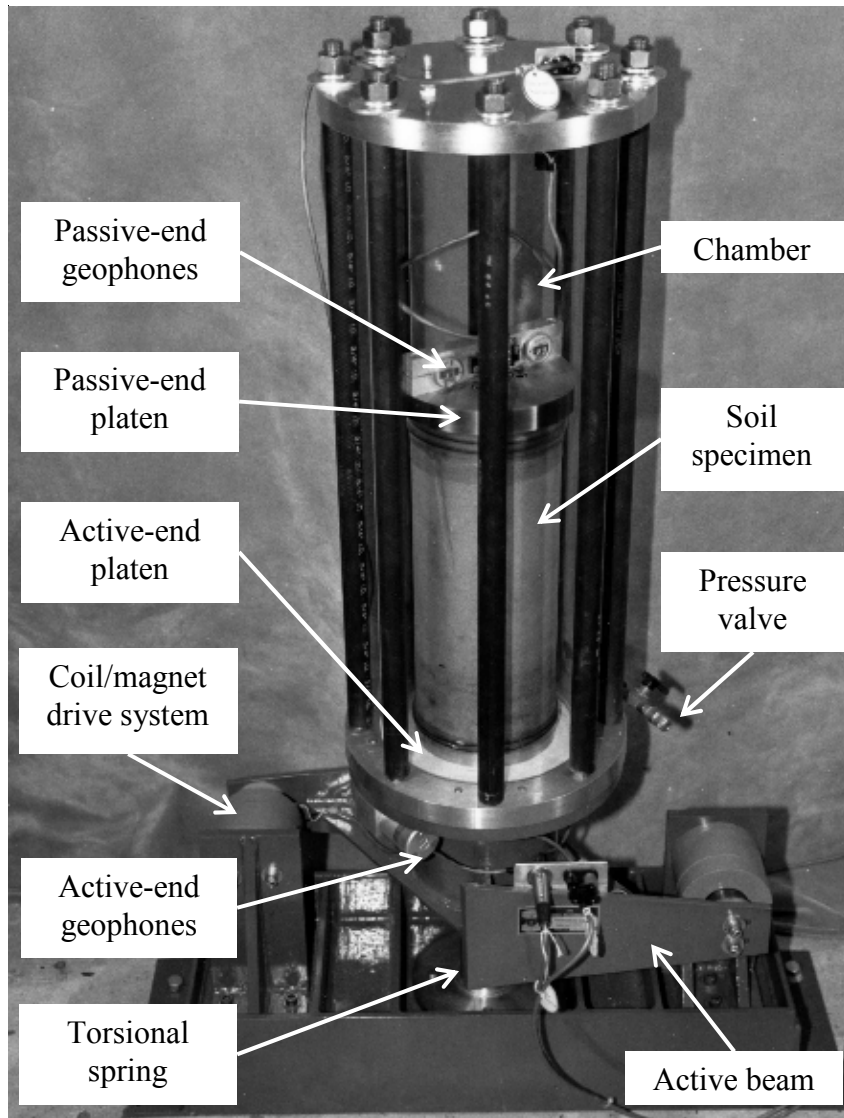


Figure 2.1: Free-free resonant column test setup (modified from Drnevich, 1987).

2.1.1 Modifications to the apparatus

In order to apply the random vibration techniques to RC testing, the device was slightly modified to accommodate two pairs of miniature PCB model 352C66 accelerometers for measuring the tangential accelerations of the top and bottom platen (Figure 2.2). Four instrumentation mounting blocks were fabricated for stud-mounting the accelerometers (Ashlock and Pak, 2010a). Two accelerometers were glued to opposite sides of an aluminum

disc attached to the passive (top) platen. The other two were glued on the base of the active platen assembly at the same diameter as the aluminum disc. The alignments of top and bottom accelerometers were kept in parallel and level. In this way, any unwanted bending modes experienced during torsional vibration can be cancelled out by averaging the two accelerometers outputs.

All accelerometers and cables were enclosed in the chamber during testing. The accelerometer signals were connected to a four channel feedthrough connector block mounted under the top lid. In addition, the traditional RC system's signal generator and oscilloscope were replaced with custom-programmed dynamic signal analyzer and oscilloscope programs written in LabVIEW and using National Instruments (NI) cDAQ-9172 hardware, which are capable of generating periodic and random excitation signals (e.g. sine, swept-sine and white noise). The excitation signals were amplified by an AE Techtron LVC 2016 linear amplifier operating in transconductance (voltage controlled current source, VCCS) mode and sent to the electromagnet drive coils of the RC device. The outputs of the accelerometers were recorded and digitized by the signal analyzer, and processed in the frequency domain when performing transfer function tests. An associated LabVIEW program was used for control, data acquisition, and visualization of the signals.

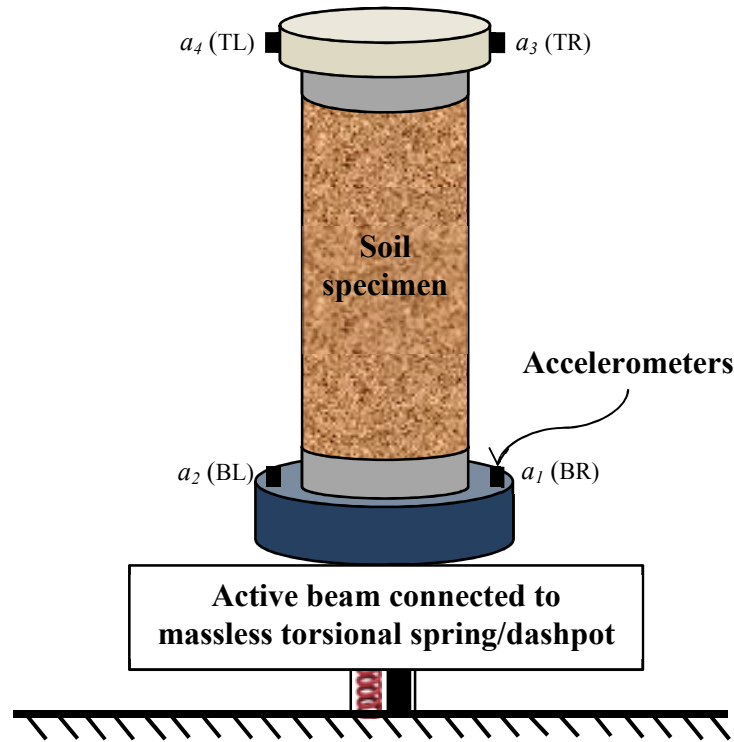


Figure 2.2: Schematic of the modified resonant column apparatus with accelerometers measuring tangential acceleration of end platens.

2.1.2 Pressure, pore water and vacuum control system

A Humboldt HM-4150 FlexPanel was used in this study to control the bottom platen vacuum pressure and cell confining pressure (Figure 2.3). An external vacuum pump and air compressor are connected to the control panel to supply vacuum and pressure. The incoming air pressure can be set from 2 to 150 psi by adjusting the air supply pressure regulator. The FlexPanel consists of three sections (cell, base and top). Only the cell and base pressure control sections were used for the RC tests described herein. The cell pressure control was connected to a hole on the base plate so that a confining pressure could be applied to the specimens during tests. The base pressure control section was connected to the central hole in the bottom platen. A vacuum was applied to the dry sand specimens during their preparation to achieve a net positive effective stress so that the samples could stand on their

own. After assembly of the pressure cell, a positive confining pressure was applied to the specimen and the vacuum was slowly removed. To perform a test on a dry specimen, the selection valve on base section was vented. This was done to allow air to escape rather than inflate the membrane in the event of a small hole in the membrane. Although not used in this study, tests of saturated specimens could also be performed by supplying de-aired water to the panel. The burettes on the panel would then be used to monitor the volume change of a saturated specimen during a drained test, or a sensor would be used to monitor pore pressure in an undrained test.



Figure 2.3: Humboldt HM-4150 pressure and vacuum control panel (source: Humboldt Manufacturing).

2.1.3 Instrumentation and data acquisition system

In traditional RC systems, the instrumentation devices include a sine wave generator, amplifier, multimeter, and an oscilloscope. In the modified RC system, the oscilloscope and sine wave generator were replaced with a NI cDAQ-9172 USB chassis housing two NI 9234 4-channel 24-bit analog input modules and one NI 9263 4-channel 16-bit analog output module. Full-featured network analyzer and oscilloscope programs written in LabVIEW were used for measurement and control of the RC device. The instrumentation and wiring diagrams for both traditional and modified RC systems are shown in Figure 2.4. Detailed descriptions of each of the components are provided below.

Power Amplifier

An AE Techron LVC 2016 linear amplifier was used in this study. This amplifier has two channels which can be operated independently, or combined in bridge-mono mode to double the available voltage, or in parallel-mono mode to double the available output current. The amplifier output was connected to a 1,000 watt, 1 ohm power resistor, then to the electromagnet coils wired in series, each having a DC resistance of 2.7 ohms. Wiring the coils in series rather than parallel ensured that they received the same current and therefore applied equal and opposite forces to the active beam. It also resulted in a greater load of 6.4 ohms (compared to 2.35 ohms for parallel wiring), which increased the amplifier's continuous output power rating. Based on advice from the AE Techron company for this non-standard application, the amplifier was used in parallel-mono mode to power the RC drive circuit. The amplifier's gain level can be adjusted with the level controls on the front panel. A current monitor on the back panel was used to measure a voltage that is proportional

to the output current. When operated in parallel-mono mode, this current monitor signal gives 1 volt for every 6 amps of output current. As a check of the drive circuit current, the voltage drop across the 1 ohm power resistor was also measured as specified in ASTM D4015-07.

Coil/magnet Drive System

A coil/magnet drive system was fabricated for use as the excitation device in RC tests. Two electromagnet coils were wound on a tapered mandrel having a nominal outer diameter of 1.67 in. and length of 2.25 in., which was slowly rotated by a lathe while four passes of 22 AWG magnet wire were placed, with approximately 89 turns per pass. Epoxy was placed over the coil after each of the four passes. After 24 hours of curing of the epoxy, the coils were carefully separated from the temporary portion of the mandrel. The final resistance of each coil was measured at 2.7 ohms, which is close to the theoretical value of 2.65 ohms calculated from the total wire length of 164 ft times the resistance of 16.14 ohms per 1,000 ft for 22 AWG wire. After winding the drive coils, they were mounted on the active beam and aligned so that they could freely move in the gap of their permanent magnets. This condition can be checked by tapping the active beam with a fist or rubber mallet and feeling the vibration of the active beam. If the beam continues to vibrate for several seconds, the coils are not rubbing on the magnets. Another way to check the alignment is to slide a sheet of paper between the coil wires and magnets, although this does not indicate whether rubbing is occurring on the inside of the coils. When an alternating electric current flows in the coils, a magnetic field is created around the wire. The magnetic field interacts with the permanent magnets, resulting in a force applied to the active

beam. The direction of the magnetic field generated around a coil of wire can be found using the right-hand rule (e.g. Ampère's circuital law). This convention is useful for determining how to install the two permanent magnets such that their magnetic (N-S) orientation and the coil wiring polarity correctly create equal and opposite forces applied at the two ends of the active beam as intended.

Multimeter

As described above, a digital multimeter (IDEAL model 61-340) was used to monitor the output AC current of the amplifier by measuring the voltage drop across the power resistor, which has a measured resistance of $1.01\ \Omega$. A second, True RMS multimeter (Tenma model 72-7730A) was also used for some tests. The True-RMS multimeter can display peak, RMS, or True-RMS measurements. For sinusoidal excitation, the RMS voltage can be calculated by

$$V_{rms} = \frac{V_{pk}}{\sqrt{2}} \quad (2.1)$$

If the signal is random, both multimeters will simply report the peak voltage divided by $\sqrt{2}$ when set to RMS mode. The Tenma multimeter in True-RMS mode will integrate the signal over time to calculate the actual RMS value of a non-sinusoidal signal, which results in a time lag between the measurement and its display. To avoid this delay, the True-RMS display mode was not used. Instead, the LabVIEW programs were modified to record the entire time-histories during a test so that True-RMS values could be calculated later if needed.

Data Acquisition Hardware and Software

As described above, the data acquisition (DAQ) system used in this study is a custom built and programmed National Instruments dynamic signal analyzer. For the transfer function testing approach, the DAQ was connected to a computer via USB and was controlled by the LabVIEW control program (Figure 2.5) named “NetworkAnalyzer_UpdatedDAQmx_timebase_externaltask_RC.vi”. Periodic and random excitation waveforms can be generated by the control program, including sine, swept-sine and white noise signals (see e.g., Figure 2.6 and Figure 2.7). The time histories of all input signals were recorded using 4,096 samples in the time-domain. The sampling frequency is fixed at 2.56 times the measurement bandwidth, and software filters are used to remove components above the critical Nyquist frequency (Bendat and Piersol, 2010). An analysis bandwidth of 2,000 Hz was typically selected resulting in a frequency resolution of 1.25 Hz and a sampling rate of 5,120 Hz. Hanning windowing was employed to minimize the effects of aliasing and spectral leakage, and 30 ensemble averages were used to minimize effects of random noise. Several plots are displayed on the front panel of the LabVIEW network analyzer control program, including time domain, FFT, power spectral density, transfer function and coherence. For performing the traditional ASTM standard RC tests, an oscilloscope LabVIEW control program was used as shown in Figure 2.8.

Figure 2.4: Control and data acquisition system wiring diagram

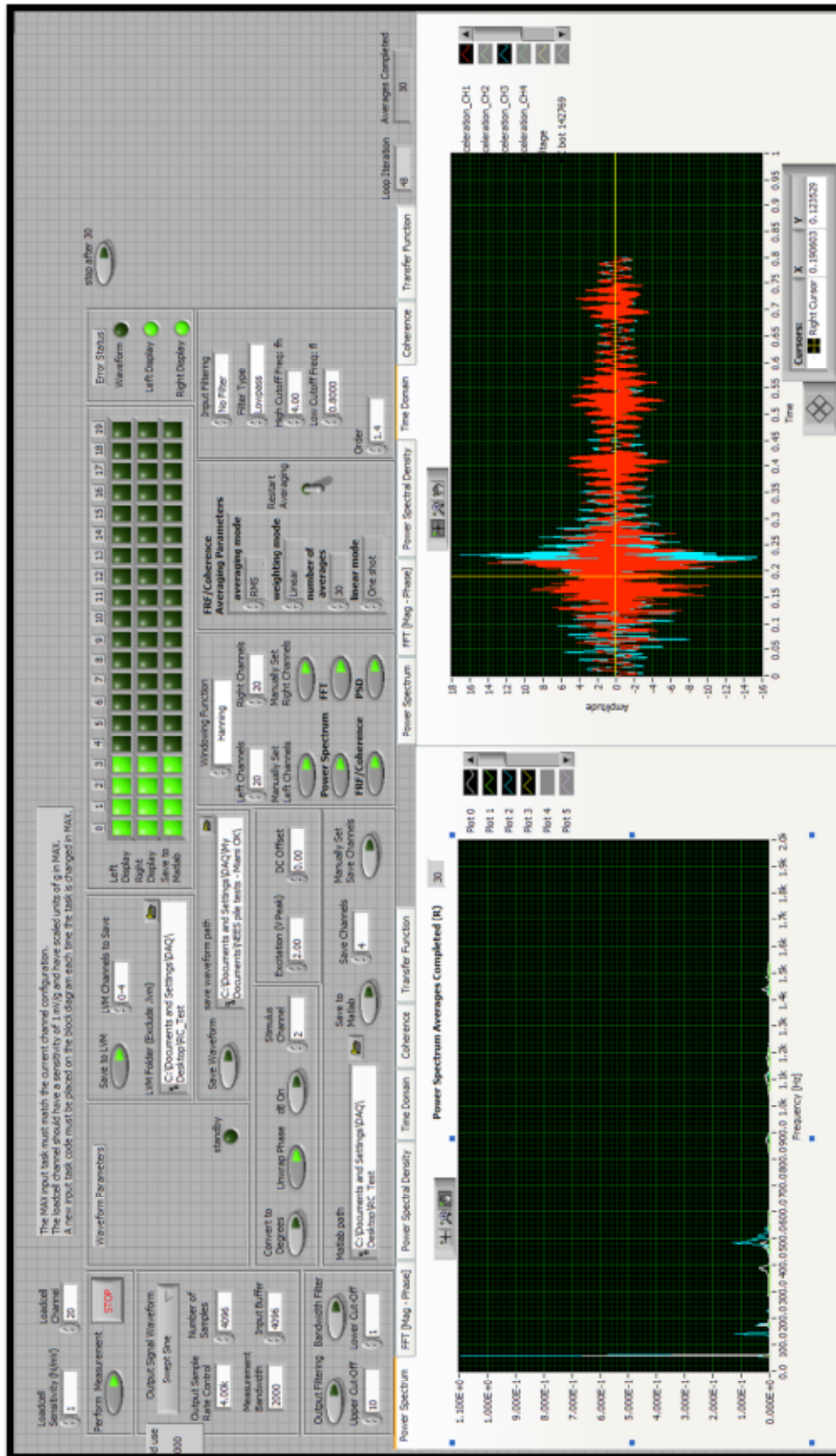


Figure 2.5: LabVIEW network analyzer front panel.

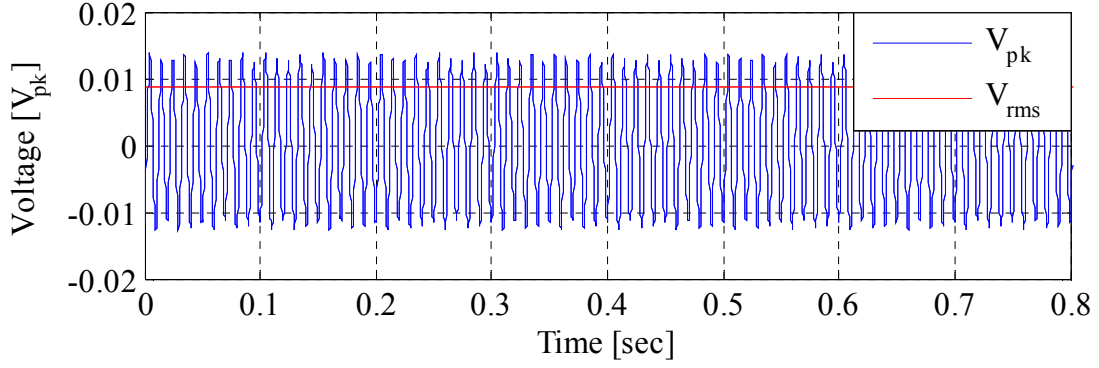


Figure 2.6: Sine waveform excitation

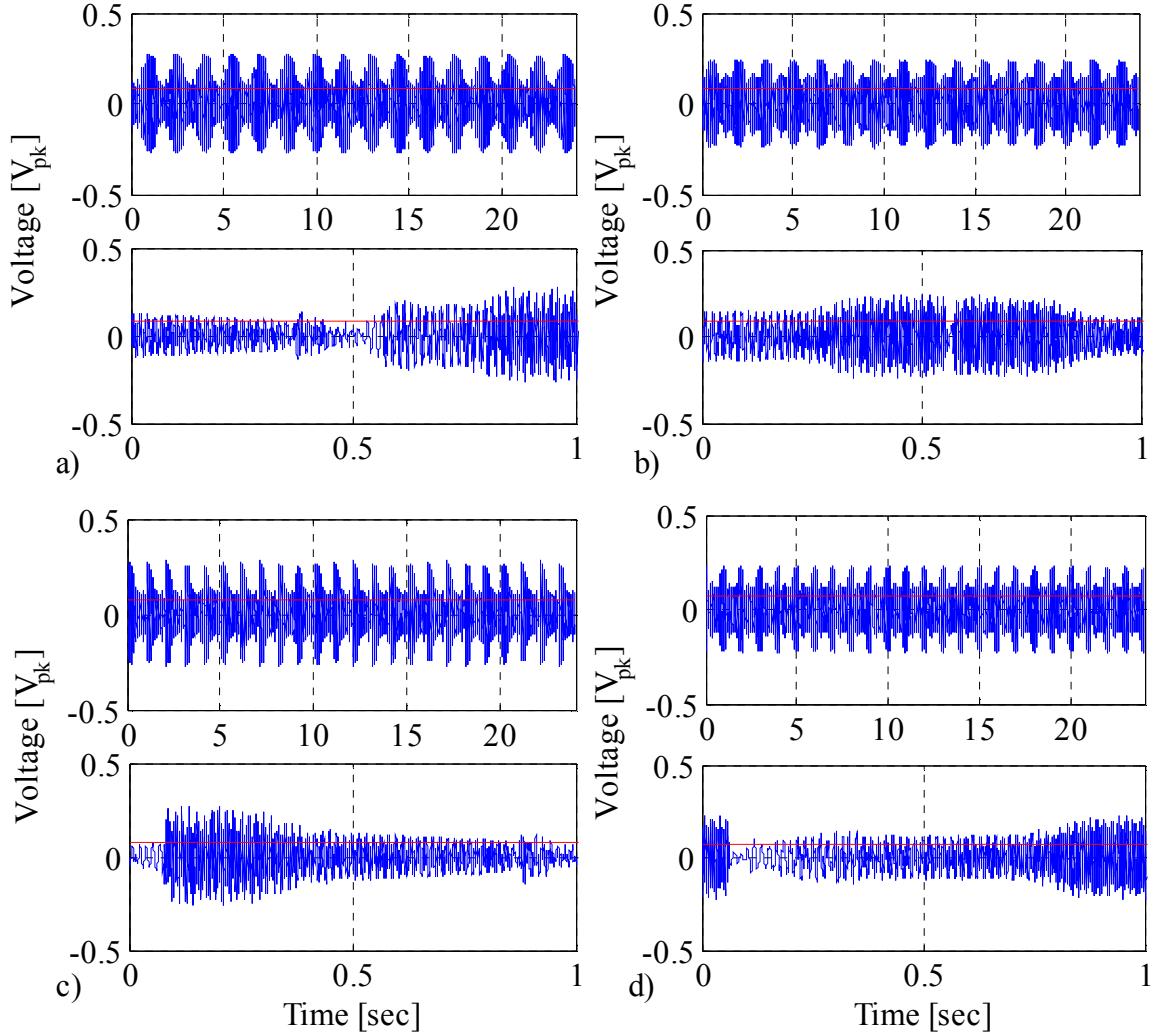


Figure 2.7: a). swept-sine with oscillate ON, $F_{start}=1$ Hz and $F_{end}=2000$ Hz; b). swept-sine with oscillate ON, $F_{start}=2000$ Hz and $F_{end}=1$ Hz; c). swept-sine with oscillate OFF, $F_{start}=2000$ Hz and $F_{end}=1$ Hz; d). swept-sine with oscillate OFF, $F_{start}=1$ Hz and $F_{end}=2000$ Hz;

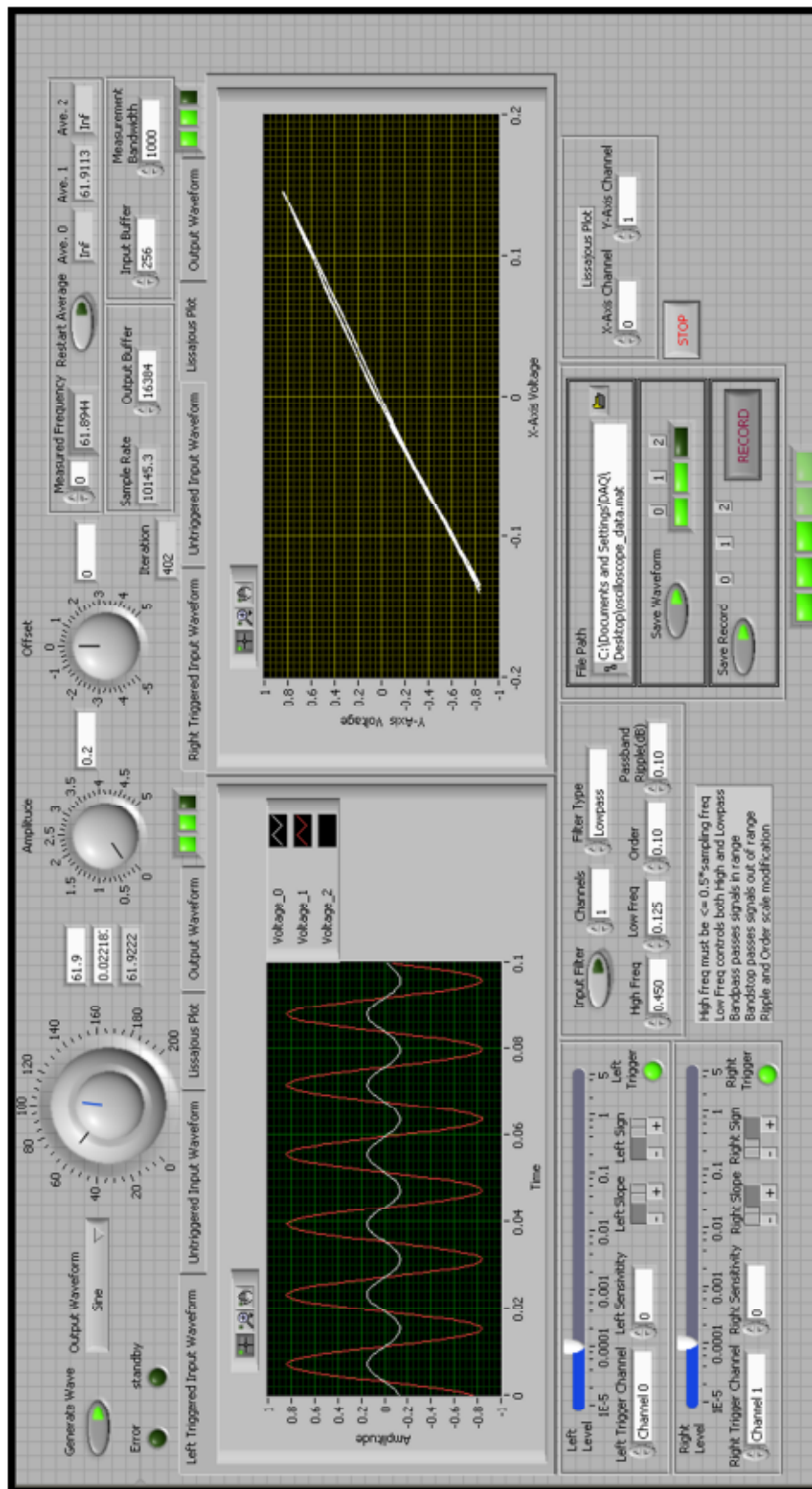


Figure 2.8: LabVIEW oscilloscope front panel.

2.2 Calibration

Calibration of the free-free RC apparatus at Iowa State University was completed in January 2013 following the instructions in Section 8 of ASTM D4015-07. Additionally, a large steel cylindrical plate (Figure 2.9) was fabricated as an auxiliary mass for measurement of the rotational inertia of the active platen and its attachments (J_a). The apparatus calibration summary is presented in Tables 2.1-2.3.

Table 2.1: RC apparatus calibration summary.

Calibration Factor	Units		Specimen Diameter		
			2.8"	4.0"	6.0"
RCF_a	pk-rad/ mV_{rms}		$10.49 \times 10^{-5} / f$		
	pk-rad/pk-volt		$7.42 \times 10^{-2} / f$		
RCF_p	pk-rad/ mV_{rms}		$19.09 \times 10^{-5} / f$		
	pk-rad/pk-volt		$13.50 \times 10^{-2} / f$		
J_p	$kg \cdot m^2$		0.0090	0.0115	0.0236
J_a	$kg \cdot m^2$	1	0.4322	0.4331	0.4452
		2	0.7752	0.7761	0.7882
f_{0T}	Hz	1	76.40	76.37	75.48
		2	61.94	61.90	61.44
k_{st}	N-m/rad		99624		
δ_T			0.0125		
ADC_T	$kg \cdot m^2/sec$	1	0.8255	0.8335	0.8468
		2	1.2004	1.2106	1.2204
TCF	N-m/ A_{rms}		3.85		
	N-m/pk-Amp		2.72		

1: Without chamber, lid, and rods.

2: With chamber, lid, and rods.

f : System resonant frequency for torsional motion [Hz].

Unit conversion: $1[V_{pk}] = 1/\sqrt{2} \times 10^3 [mV_{rms}]$ and $1[A_{pk}] = 1/\sqrt{2} [A_{rms}]$.

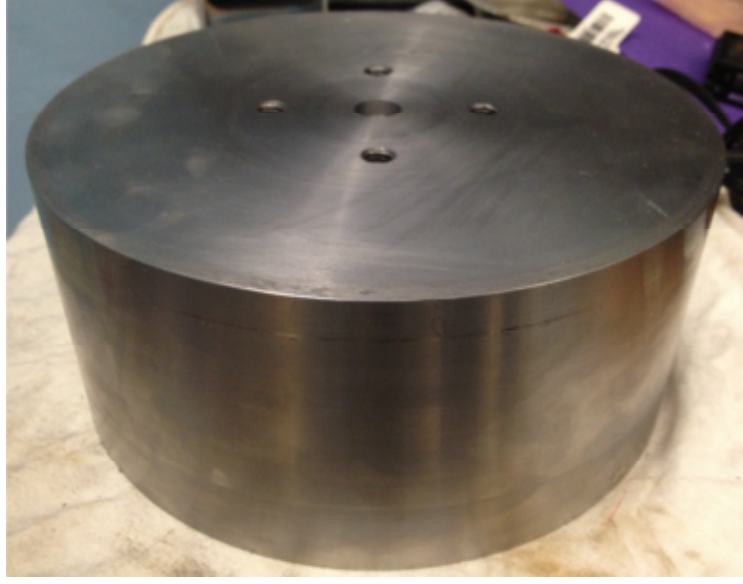


Figure 2.9: RC device auxiliary calibration platen (8"×3.5").

2.2.1 Rotational calibration factors

The rotational calibration factors are used to convert the geophone transducer output (voltage) to the angular rotation in radians. In the traditional free-free RC device, there are a total of four geophones, one pair attached to each end platen, to measure the tangential velocity which will be denoted $\dot{x}_i(t)$, $i = 1, 2, 3, 4$ in the bottom right, bottom left, top right and top left positions, respectively.

The sensitivities of these geophones were calibrated in 2010 by back-to-back comparison against accelerometers mounted to the table of an electromagnetic shaker. The tangential velocity at the geophone location can be expressed as

$$\dot{x} = V_G \times S_G \quad (2.2)$$

where \dot{x} is the tangential velocity [in/s], V_G is the geophone's reading [V_{pk}], and S_G is the sensitivity of the geophone [in/s/ V_{pk}]. The rotational velocity can be expressed as

$$\dot{\theta} = \frac{\dot{x}}{R} = V_G \times \frac{S_G}{R} \quad (2.3)$$

where $\dot{\theta}$ is the rotational velocity [rad/s], R is the radius of the center of the geophone to the center of the end-platens [in], and

$$RVCF \equiv \frac{S_G}{R} \quad (2.4)$$

is defined as the rotational velocity calibration factor [rad/s/V_{pk}].

If the motion of the end platens is harmonic, i.e. $x = A \sin(\omega t + \phi)$, then the amplitude of the angular rotation can be calculated as

$$|\theta| = \frac{1}{\omega} |\dot{\theta}| = V_G \times \frac{RVCF}{2\pi f} \quad (2.5)$$

Therefore, the rotation calibration factor will not be constant but will vary inversely with the measured frequency f . The rotation calibration factor to convert the geophone voltage to rotation in radians can thus be expressed as

$$RCF = \frac{RVCF}{2\pi f} = \frac{S_G}{R \cdot 2\pi f} \quad (2.6)$$

so that

$$|\theta| = V_G \times RCF \quad (2.7)$$

Table 2.2: Summary of the calculation of RCF.

	Geophone S_G [in/s/V _{pk}]		Avg. Sensitivity [in/s/V _{pk}]	Radius [inch]	RVCF [rad/s/V _{pk}]	RCF [pk-rad/V _{pk}]
Active platen	1	2.3723	2.3905	5.125	0.4664	0.0742/ f
	2	2.4086				
Passive platen	3	1.7582	1.7820	2.100	0.8486	0.1350/ f
	4	1.8058				

2.2.2 Apparatus resonant frequency

Due to the stiffness and damping elements attached to the bottom (active) platen as shown in Figure 1.1c, the free-free device itself has a natural frequency of vibration denoted f_{0T} for the torsional mode. The apparatus resonant frequencies can be measured by vibrating the apparatus at low amplitude without a soil specimen or passive platen attached, and

adjusting the excitation frequency until the input torque is in phase ($\phi=0^\circ$) with the rotational velocity of the active end platen system. In other words, a Lissajous plot of the active geophone output versus voltage across the power resistor is proportional to $\dot{\theta}$ vs. torque T and becomes a straight line with a positive slope on the oscilloscope (Figure 2.10). This can be shown by approximating the active platen as a damped single-degree-of-freedom (SDOF) system under forced vibration. The E.O.M at the active end platen without the specimen can be written as

$$\ddot{\theta}(t) \cdot J_a + \dot{\theta}(t) \cdot c_a + \theta(t) \cdot k_{st} = T(t) \quad (2.8)$$

where

J_a is the polar mass moment of inertia of the active platen [$\text{kg}\cdot\text{m}^2$], c_a is the torsional dashpot coefficient [$\text{kg}\cdot\text{m}^2/\text{s}/\text{rad}$], k_{st} is the torsional spring constant [$\text{N}\cdot\text{m}^2/\text{rad}$], and

$$T(t) \equiv T_0 \cdot \sin(\omega t) \quad (2.9)$$

is the applied torque of sinusoidal vibration [$\text{N}\cdot\text{m}$].

The steady-state solution for the rotation can be expressed as

$$\theta(t) = \frac{T_0 / k_{st}}{\sqrt{(1 - \beta^2)^2 + (2\xi\beta)^2}} \sin(\omega t - \phi) \quad (2.10)$$

where

$$\beta \equiv \frac{\omega}{\omega_n} \quad (2.11)$$

is the frequency ratio and

$$\phi = \tan^{-1}\left(\frac{2\xi\beta}{1 - \beta^2}\right) \quad (2.12)$$

is the phase angle between rotation and torque.

If the system is vibrating at the undamped natural frequency ($\beta=1$), the phase angle between angular rotation and torque is

$$\phi = \tan^{-1}(\infty) = \frac{\pi}{2} \quad (2.13)$$

The angular velocity can be calculated by taking the derivative of Eq. (2.10), giving

$$\dot{\theta}(t) = \omega \frac{T_0 / k_{st}}{\sqrt{[1 - \beta^2]^2 + (2\xi\beta)^2}} \sin\left(\omega t - \left(\phi - \frac{\pi}{2}\right)\right) \quad (2.14)$$

The phase angle between rotational velocity and torque at the undamped natural frequency is thus

$$\phi - \frac{\pi}{2} = \tan^{-1}\left(\frac{2\xi\beta}{1 - \beta^2}\right) - \frac{\pi}{2} = 0 \quad (2.15)$$

Therefore a Lissajous plot of the rotation angle of the active platen versus torque forms an ellipse at resonance, while the rotational velocity of the active platen versus torque forms a straight line with a positive slope as shown in Figure 2.10. Another method to measure the apparatus resonant frequency is to attach two accelerometers on the active platen to record its rotational acceleration. The frequency of the first peak of the power spectral density of the acceleration is then recorded as the resonant frequency. For the free-free device in this study with only the active platen attached, the measured resonant frequency is $f_{0T} = 77$ Hz based on the Lissajous plot. Figure 2.11 shows the power spectral density (PSD) of the acceleration. It has an obvious peak at 77.5 Hz, which is very close to the resonant frequency $f_{0T} = 77$ Hz determined by the Lissajous plot.

For the traditional sinusoidal tests of soil specimens in this study, the resonant frequency was measured as the second lowest frequency for which the rotational velocity of the passive platen is 180° out of phase with the applied torque, as specified in ASTM D4015-07. For this condition, the Lissajous plot forms a straight line with a negative slope. The theory behind this situation will be discussed in Chapter 3.

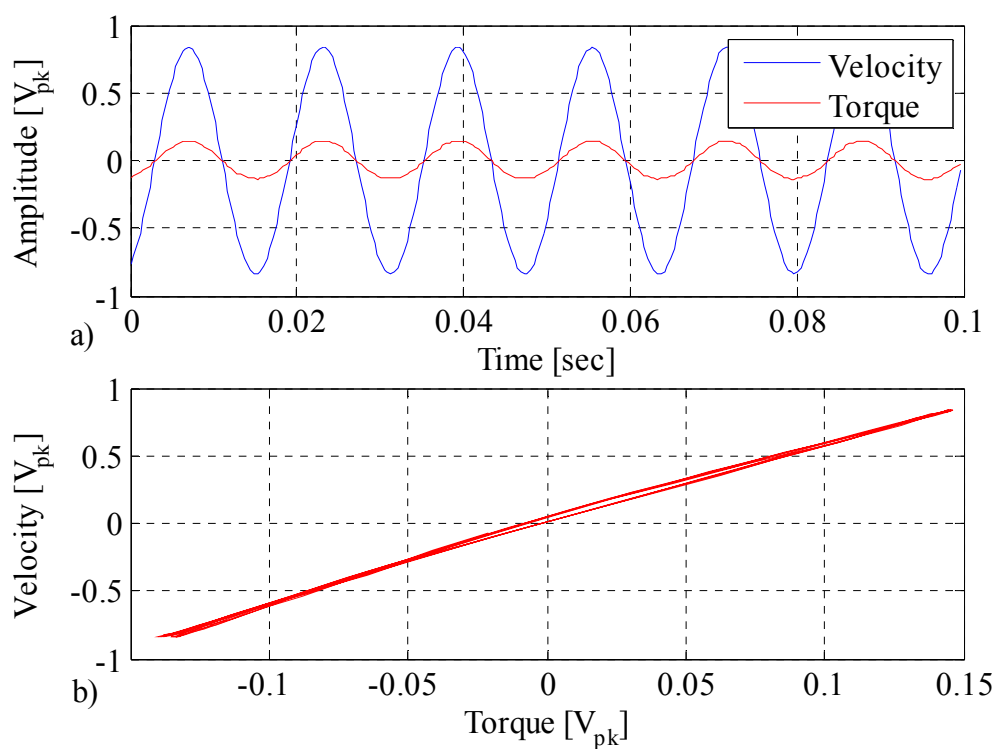


Figure 2.10: a) Channel output vs. time and b) Lissajous plot recorded by LabVIEW oscilloscope program for calibration of device undamped natural frequency of vibration.

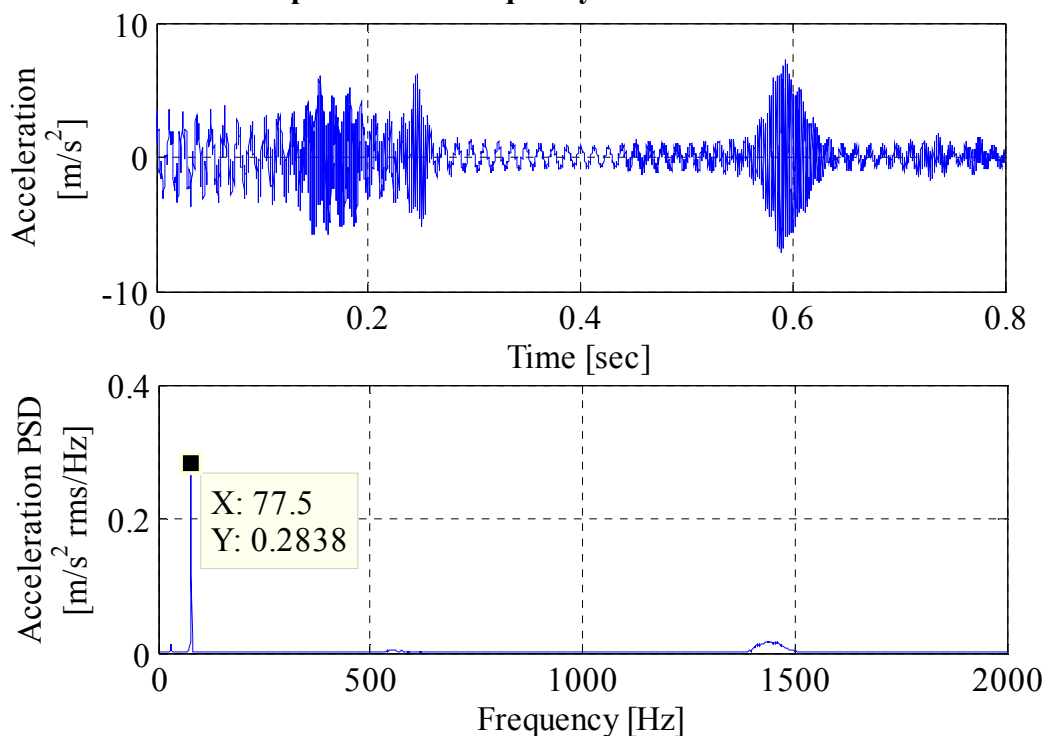


Figure 2.11: Acceleration PSD in frequency-domain for calibration of device undamped natural frequency of vibration with swept-sine excitation.

2.2.3 Passive-end platen rotational inertia

The rotational inertia of the passive end platen (J_p) is calculated with all transducers and other rigid attachments securely in place. Figure 2.12 shows all the components attached to the passive end platen. The mass of each attachment was measured by an electronic scale. The rotational inertia of the concentric solid cylindrical components about the z-axis (i.e., the passive end platen and attached disc) is given by

$$(J_p)_1 = \frac{1}{8} \sum_{i=1}^n M_i d_i^2 \quad (2.16)$$

where

M_i is the mass of the i -th solid cylindrical component [kg];

d_i is the diameter of the i -th solid cylindrical component [m] and;

$n=2$ is the number of solid cylindrical components.

The concentric solid rectangular components (i.e., the geophone clamp bar) attached to this platen can be accounted for using

$$(J_p)_2 = \frac{1}{12} \sum_{i=1}^n M_i l_i^2 \quad (2.17)$$

where

M_i is the mass of i -th solid rectangular component [kg];

l_i is the length of i -th solid rectangular component [m].

The rotational inertia of the solid cylindrical components considering rotations about their own vertical centroidal axes and using the parallel axis theorem (i.e., adding the two geophones and subtracting the two holes of the clamp bar) can be calculated as

$$(J_p)_3 = \frac{1}{12} \sum_{i=1}^n M_i (3r_i^2 + h_i^2) + \sum_{i=1}^n M_i d_i^2 \quad (2.18)$$

where

M_i is the mass of the i -th solid cylindrical component [kg];

r_i is the radius of the i -th solid cylindrical component [m];

h_i is the height of the i -th solid cylindrical component [m];

d_i is the horizontal distance between the specimen's vertical axis and the centroidal axis of the i -th solid cylindrical component [m].

Therefore, the total rotational inertia for the passive end platen assembly can be calculated as

$$J_p = (J_p)_1 + (J_p)_2 + (J_p)_3 \quad (2.19)$$

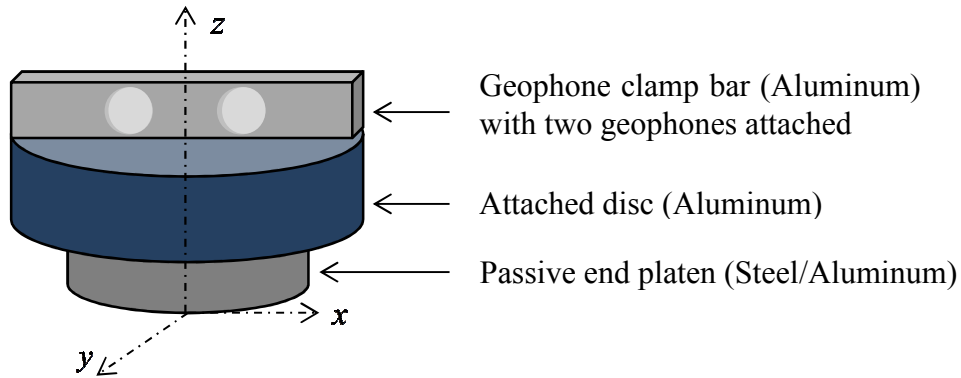


Figure 2.12: Passive end platen and attachments.

For the RC device use in this research, three sizes of passive end platens are available for testing different size soil specimens having diameters of 2.8, 4, and 6 inches. A summary of the rotational inertia of these passive end platens is presented in Table 2.3. The rotational inertia of the passive end platen is required for the sinusoidal test procedure of ASTM D4015, as well as the new free-free transfer function approach described herein.

Table 2.3: Calculated passive end rotational inertias.

Diameter of the passive end platen attached [inch]	Passive end rotational inertia without geophones and clamp bar [kg·m ²]	Total passive end rotational inertia [kg·m ²]
2.8	0.0075	0.0090
4.0	0.0100	0.0115
6.0	0.0221	0.0236

2.2.4 Active-end platen rotational inertia

Calibration of the active end platen rotational inertia must be performed with all transducers and portions of the vibration excitation device including the active beam and electromagnet coils securely in place. Because all the components at the active end do not have simple geometries, the procedure used above for calculation of the passive end platen inertia cannot be used. In ASTM D4015 Section 8.3, it is recommended that a steel calibration rod be used in place of the soil specimen, and the passive end be rigidly fixed. The resulting undamped natural frequency (denoted f_{rod}) is then measured using the procedure of Section 2.2.2. Treating the calibration rod as a spring with known torsional stiffness k_{rod} , and denoting the torsional apparatus spring constant as k_{st} , the undamped natural frequency of vibration for this condition can be written as

$$(2\pi f_{rod})^2 = (k_{rod} + k_{st}) / J_a' \quad (2.20)$$

The test detailed Section 2.2.2 is then performed with only the active platen in place to measure the apparatus resonant frequency ($f = f_{0T}$). For this case, the undamped natural frequency can be written as

$$(2\pi f_{0T})^2 = k_{st} / J_a' \quad (2.21)$$

The rotational inertia of the active end platen system and all attachments may then be calculated by solving Eqs. (2.20) and (2.21) by eliminating k_{st} , to give Eq. (11) of ASTM D4015 Section 8.3, i.e.

$$J_a' = \frac{k_{rod}}{(2\pi)^2(f_{rod}^2 - f_{0T}^2)} \quad (2.22)$$

This method requires that the passive end of the calibration rod shall be rigidly fixed. However, it is very difficult to achieve this requirement in the laboratory. Therefore, an alternative approach was adopted in this study for calibration of the rotational inertia of the active end platen. The approach was to attach to the active beam an auxiliary platen having known rotational inertia J_{aux} . The undamped resonant frequency (f_{aux}) was then measured as described above, for which

$$(2\pi f_{aux})^2 = k_{st} / (J_a' + J_{aux}) \quad (2.23)$$

Solving Eqs. (2.21) and (2.23) for J_a' by eliminating k_{st} , the rotational inertia of active end platen is obtained as

$$J_a' = \frac{J_{aux}(f_{aux})^2}{(f_{0T}^2 - f_{aux}^2)} \quad (2.24)$$

From Eq. (2.21), the torsional apparatus spring constant can then be calculated as

$$k_{st} = J_a' \cdot (2\pi f_{0T})^2 \quad (2.25)$$

The RC device used in this study has three different end-platens of 2.8, 4 and 6 inch diameter for testing a range of soil specimen sizes. The rotational inertia of the active end with the different size platens attached can be calculated as

$$J_a = J_a' + J_{platen} \quad (2.26)$$

The device may be used without the pressure chamber to perform unconfined tests on soil or rock. However, testing of soils is usually performed with the pressure chamber, lid and rods

in place. Attaching these components will increase the rotational inertia of the active end assembly. Calibration results of the rotational inertia of active end platens and torsional apparatus spring constant are presented in Table 2.4.

Table 2.4: Calibrated active end platen rotational inertia and apparatus spring constant.

Condition	f_{0T} [Hz]	f_{aux} [Hz]	J_a' [kg·m ²]	k_{st} [N·m/rad]	J_a [kg·m ²] with		
					2.8'' platen	4.0'' platen	6.0'' platen
Without chamber, lid and rods	76.63	68.00	0.4297	99624	0.4322	0.4331	0.4452
With chamber, lid and rods	62.03	57.84	0.7727	117369	0.7752	0.7761	0.7882

2.2.5 Apparatus damping coefficient

The logarithmic decrement of damping method was adopted to determine the apparatus damping constant from the measured free-vibration response. The apparatus was vibrated at the resonant frequency with only the active platen assembly attached, then power to the excitation device was cut off using fuses or unplugging by hand. The free vibration decay curve was then recorded, an example of which is shown in Figure 2.13. The logarithmic decrement δ can be calculated as

$$\delta = (1/n) \ln(A_1/A_{n+1}) \quad (2.27)$$

where

A_1 is the amplitude of vibration for the first cycle after power is cut off and;

A_{n+1} is the amplitude for the (n+1)-th cycle.

The logarithmic decrement δ for the free-free device was previously calibrated in 2010. At that time, only five peak points on the decay curve were selected for the analysis. In order to estimate a more exact δ , the procedure was repeated and data was analyzed using

all available peak points by plotting $\ln(A_1/A_{n+1})$ versus n . The slope of the resulting best-fit line is the logarithmic decrement δ (Figure 2.14).

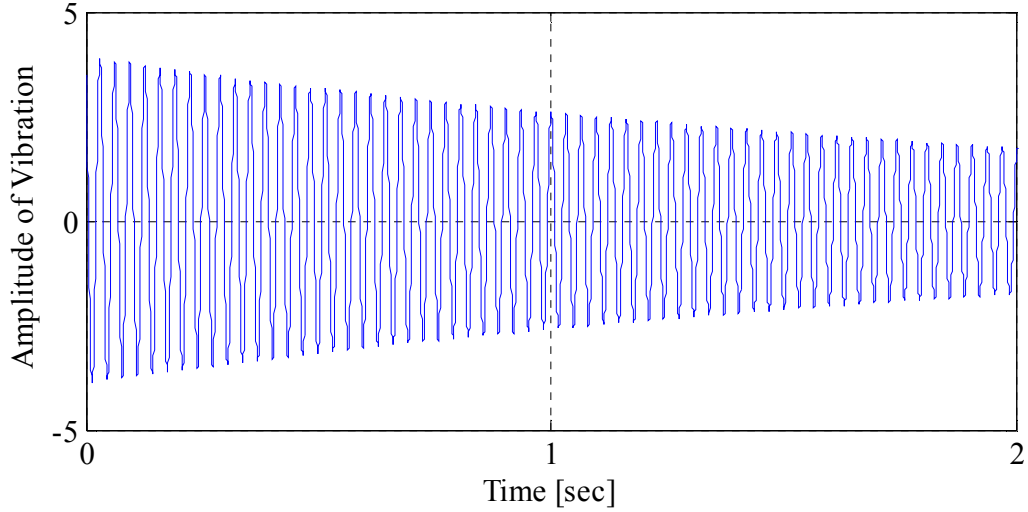


Figure 2.13: Decay curve using a 1 Amp fuse to cut off the power.

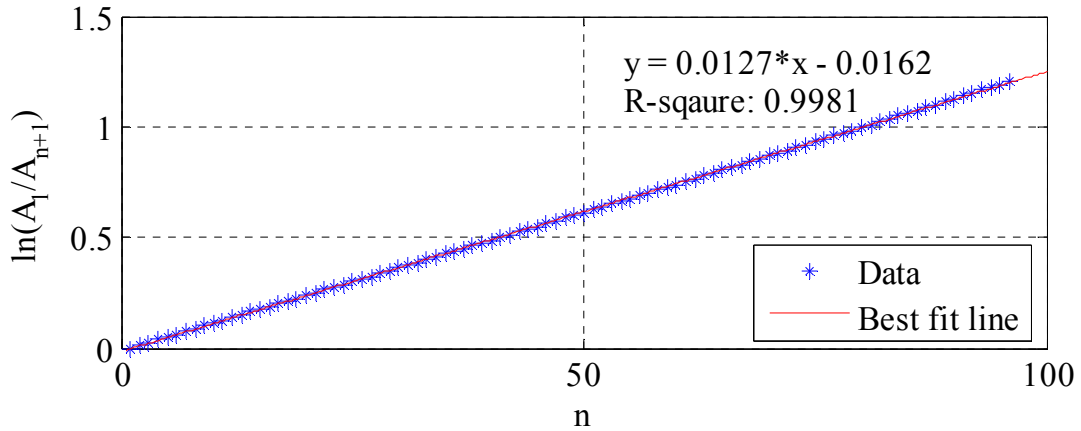


Figure 2.14: Plot of $\ln(A_1/A_{n+1})$ vs. n to determine the logarithmic decrement δ .

The logarithmic decrement was measured for a range of excitation currents using 0.75, 0.5 and 1 Amp fuses to cut off the power, and the resulting logarithmic decrements were used to calculate an average decrement δ_{avg} . A comparison between the results of the analyses is presented in Table 2.5.

If the motion is considered as the free vibration of a mass-spring-dashpot described by Eq. (2.8), the logarithmic decrement can be written as

$$\delta = \frac{2\pi\xi}{\sqrt{1-\xi^2}} \quad (2.28)$$

where ξ is defined as the damping ratio, or fraction of critical damping, i.e.

$$\xi \equiv c_a / c_{cr} \quad (2.29)$$

in which the critical damping is

$$c_{cr} = 2J_a \omega_n \quad (2.30)$$

and $\omega_n = 2\pi f_n = 2\pi f_{0T}$ is the natural circular frequency [rad/s].

If the damping ratio is small, Eq. (2.28) can be approximated as

$$\delta = 2\pi\xi \quad (2.31)$$

Substituting Eq. (2.29) and (2.30) into (2.31), the apparatus damping coefficient (denoted *ADC* in the ASTM standard) can be express as

$$ADC = 2f_{0T} J_a \delta \quad (2.32)$$

Table 2.5: Results of apparatus logarithmic decrement.

Peak current [A]	Trial #	Using five data points		Using all data points	
		δ	δ_{avg}	δ	δ_{avg}
0.5	1	0.0120	0.0120	0.0123	0.0122
0.5	2	0.0120		0.0120	
0.75	1	0.0128	0.0128	0.0125	0.0125
0.75	2	0.0128		0.0125	
1.0	1	0.0134	0.0136	0.0127	0.0128
1.0	2	0.0139		0.0128	
Average			0.0128	Average	0.0125

2.2.6 Torque/current calibration factor

The torque/current calibration factor is used to convert the measured current in Amps to the torque in N-m. For the apparatus with the active end platen only, the SDOF system's E.O.M. for sinusoidal excitation at the frequency ω may be solved for the amplitude of angular rotation to give

$$|\theta(t)| = \frac{T_0 / k_{st}}{\sqrt{[1 - \beta^2]^2 + (2\xi\beta)^2}} \quad (2.33)$$

where $\beta \equiv \frac{\omega}{\omega_n}$ is the frequency ratio. Defining the amplification factor as

$$A.F. \equiv \frac{1}{\sqrt{[1 - \beta^2]^2 + (2\xi\beta)^2}} \quad (2.34)$$

and substituting Eq. (2.34) into (2.33), the torque amplitude can be expressed as

$$T_0 = \frac{|\theta(t)|}{A.F.} k_{st} \quad (2.35)$$

The torque/current calibration factor can be expressed as the torque divided by the current reading, which gives

$$TCF = \frac{T_0}{i} = \frac{|\theta(t)|}{i} \frac{k_{st}}{A.F.} \quad (2.36)$$

where i is the current reading [A_{pk} or A_{rms}], or the voltage [V_{pk} or V_{rms}] across a fixed 1.0Ω resistance which is proportional to the current. When vibrating the system at 0.707 times resonant frequency ($\beta_1 = 1/\sqrt{2}$) and 1.414 times the resonant frequency ($\beta_2 = \sqrt{2}$), the relation between the two amplification factors at these frequencies is

$$A.F.(\beta_1) = 2 A.F.(\beta_2) \quad (2.37)$$

where

$$A.F.(\beta_1) = \frac{2}{\sqrt{1+8\xi^2}} \approx 2 \text{ and } A.F.(\beta_2) = \frac{1}{\sqrt{1+8\xi^2}} \approx 1, \text{ assuming that the damping ratio is very}$$

small.

The torque/current calibration factor for both cases can be written as

$$\begin{aligned} TCF(\beta_1) &= \left(\frac{\theta}{i} \right)_{\beta_1} \frac{k_{st}}{A.F.(\beta_1)}; \\ TCF(\beta_2) &= \left(\frac{\theta}{i} \right)_{\beta_2} \frac{k_{st}}{A.F.(\beta_2)}. \end{aligned} \quad (2.38)$$

Substituting Eq. (2.37) into Eq. (2.38) and assuming a small damping ratio ($A.F.(\beta_2)=1$) gives

$$\begin{aligned} TCF(\beta_1) &= C_1 \cdot k_{st} ; \\ TCF(\beta_2) &= C_2 \cdot k_{st} . \end{aligned} \quad (2.39)$$

where

$$C_1 \equiv \frac{1}{2} \left(\frac{\theta}{i} \right)_{\beta_1} = 0.5(RCF)(TO1) / CR1 \quad (2.40)$$

RCF is the active-end rotation calibration factor (discussed in 2.3.1) [pk-rad/ V_{pk}];

$TO1$ is the transducer output at 0.707 times resonant frequency [V_{pk}];

$CR1$ is the current reading at 0.707 times resonant frequency [A_{pk}];

$$C_2 \equiv \left(\frac{\theta}{i} \right)_{\beta_1} = (RCF)(TO2) / CR2 \quad (2.41)$$

$TO2$ is the transducer output at 1.414 times resonant frequency [V_{pk}];

$CR2$ is the current reading at 1.414 times resonant frequency [A_{pk}];

In the ASTM standard, the torque/current calibration factor is obtained using the average of C_1 and C_2 , i.e.

$$TCF = \frac{1}{2} (C_1 + C_2) k_{st} \quad (2.42)$$

Results of the TCF calibration are presented in Table 2.6.

Table 2.6: Torque/current calibration factor results.

Frequency [Hz]	Current Reading [A_{rms}]	Active-end Geophone Output [V_{pk}]	C1 or C2	Avg. TCF [N-m/ A_{rms}]
$\frac{1}{\sqrt{2}} f_{0T} = 43.86$	0.090	0.0042	2.79×10^{-5}	3.85
	0.880	0.0381	2.59×10^{-5}	
	1.902	0.0837	2.63×10^{-5}	
$\sqrt{2} f_{0T} = 87.71$	0.106	0.0048	2.71×10^{-5}	
	1.027	0.0495	2.88×10^{-5}	
	2.222	0.1022	2.75×10^{-5}	

CHAPTER 3. THEORY FOR INTERPRETATION OF EXPERIMENTAL DATA

The determination of dynamic soil properties from resonant column test data is described in this chapter. In the analytical solutions, the Kelvin-Voigt model (with viscous damping and stiffness in parallel) is assumed to represent the soil specimen. Although soil is a complex material and no simple model can completely describe its behavior under all loading conditions, the Kelvin-Voigt model can be a useful tool for describing the behavior of soil subjected to small amplitude vibration, over a large frequency range (Hardin, 1965).

3.1 Analytical Solution for Harmonic Torsional Excitation of Soil Specimen

Representing the soil specimen as a homogeneous Kelvin-Voigt solid, the wave propagation equation can be expressed as (see Hardin, 1965)

$$G \frac{\partial^2 \varphi}{\partial z^2} + \eta \frac{\partial^3 \varphi}{\partial t \partial z^2} = \rho \frac{\partial^2 \varphi}{\partial t^2}, \quad (3.1)$$

where

G is the shear modulus [Pa];

ρ is the mass density [kg/m³];

η is the Kelvin-Voigt viscous damping coefficient [N·s/m²] and;

$\varphi = \varphi(z, t)$ is the angular rotation along the specimen z -axis [rad].

For harmonic motion, $\varphi(z, t)$ may be written in complex form as

$$\varphi(z, t) = \theta(z) \cdot e^{i\omega t}, \quad 0 \leq z \leq h, \quad (3.2)$$

Where $i = \sqrt{-1}$ is the imaginary complex unit, ω is the circular frequency of vibration [rad/s],

and h is the height of specimen [m]. The coordinate $z = 0$ is the interface of the specimen with the active (bottom) platen and $z = h$ is the interface of specimen with the passive (top) platen.

Substituting Eqs. (3.2) into (3.1) and rearranging gives

$$\frac{d^2\theta}{dz^2} + \frac{\rho\omega^2}{G^*}\theta(z) = 0, \quad (3.3)$$

where

$$G^* \equiv G(1 + i\omega\eta), \quad (3.4)$$

is defined as the complex shear modulus. The viscous damping constant η may be equivalently expressed in the form of a generalized frequency-dependent damping ratio as

$$\xi(\omega) = \frac{\omega\eta}{2G}, \quad (3.5)$$

for which the complex shear modulus becomes

$$G^* = G(1 + i2\xi(\omega)). \quad (3.6)$$

The damping ratio $\xi(\omega)$ may be defined as in Eq. (3.5) for viscous damping, or may be set equal to a constant value ξ_0 for hysteretic damping. The solution for Eq. (3.3) has the form

$$\theta(z) = C_1 e^{iaz} + C_2 e^{-iaz}, \quad (3.7)$$

where

$$a \equiv \omega \sqrt{\frac{\rho}{G^*}}, \quad (3.8)$$

and C_1 and C_2 are complex-valued constants which depend on the specimen boundary conditions.

From Eq. (3.7), the angular rotation at the active (bottom) and passive (top) ends of specimen may be expressed as

$$\begin{aligned} \theta_a &= \theta(0) = C_1 + C_2; \\ \theta_p &= \theta(h) = C_1 e^{i\bar{\omega}^*} + C_2 e^{-i\bar{\omega}^*}, \end{aligned} \quad (3.9)$$

where

$$\bar{\omega}^* \equiv ah, \quad (3.10)$$

is the complex dimensionless frequency.

The complex constants C_1 and C_2 in Eq. (3.9) may be solved in terms of θ_a and θ_p to give

$$C_1 = \frac{\theta_p - \theta_a e^{-i\bar{\omega}^*}}{e^{i\bar{\omega}^*} - e^{-i\bar{\omega}^*}}; \quad C_2 = \frac{\theta_p - \theta_a e^{i\bar{\omega}^*}}{e^{-i\bar{\omega}^*} - e^{i\bar{\omega}^*}}. \quad (3.11)$$

The stress-strain relationship for a Kelvin-Voigt viscoelastic solid is given by

$$\tau(r, z, t) = G\gamma + \eta\dot{\gamma} = G \cdot r \frac{\partial \varphi}{\partial z} + \eta \cdot r \frac{\partial}{\partial t} \left(\frac{\partial \varphi}{\partial z} \right), \quad (3.12)$$

where the shear strain is

$$\gamma(r, z, t) = r \frac{\partial \varphi(z, t)}{\partial z}. \quad (3.13)$$

For harmonic motion, the torsional stress in the specimen may be expressed in complex form as

$$\tau(r, z, t) = \tau'(r, z) \cdot e^{i\alpha t}. \quad (3.14)$$

Substituting Eq. (3.2), (3.7) and (3.14) into (3.12) gives the torsional stress along the specimen that varies with the radius r

$$\tau'(r, z) = iraG^* (C_1 e^{iaz} - C_2 e^{-iaz}), \quad (3.15)$$

Replacing C_1 and C_2 in Eq. (3.15) and using Euler's formula¹, the torsional stress at both ends of specimen may be calculated as

$$\begin{aligned} \tau'_a = \tau'(r, 0) &= raG^* \left[\frac{\theta_p - \theta_a \cos(\bar{\omega}^*)}{\sin(\bar{\omega}^*)} \right]; \\ \tau'_p = \tau'(r, h) &= raG^* \left[\frac{\theta_p \cos(\bar{\omega}^*) - \theta_a}{\sin(\bar{\omega}^*)} \right]. \end{aligned} \quad (3.16)$$

An infinitesimal slice of the soil specimen is shown in Figure 3.1 with definitions of positive directions of torque, rotation, and shear strain. Positive shear stresses act in the same sense as the torques shown in this figure.

¹ Leonhard Euler (1707-1783), Euler's formula: $e^{i\bar{\omega}^*} = \cos(\bar{\omega}^*) + i\sin(\bar{\omega}^*)$; $e^{-i\bar{\omega}^*} = \cos(\bar{\omega}^*) - i\sin(\bar{\omega}^*)$.

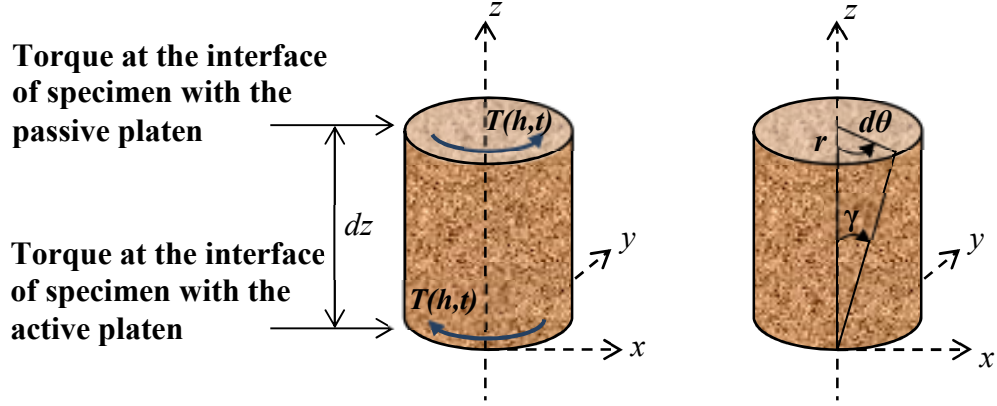


Figure 3.1: Positive directions of torque, rotation and shear strain.

The torque at the top and bottom of the specimen may be obtained by integrating the shear stresses given by Eqs. (3.14) and (3.16) over the area of the interface, i.e.

$$\begin{aligned} T(0,t) &= \int_A r \cdot \tau(r,0,t) dA = I_s a G^* \left[\frac{\theta_p - \theta_a \cos(\bar{\omega}^*)}{\sin(\bar{\omega}^*)} \right] \cdot e^{i\omega t}; \\ T(h,t) &= \int_A r \cdot \tau(r,h,t) dA = I_s a G^* \left[\frac{\theta_p \cos(\bar{\omega}^*) - \theta_a}{\sin(\bar{\omega}^*)} \right] \cdot e^{i\omega t}, \end{aligned} \quad (3.17)$$

where $I_s \equiv \int_A r^2 dA$ is the polar second moment of area of the specimen [m⁴].

Figure 3.2 shows the free-body diagrams for the passive and active end platens. The equations of motion (E.O.M.) at both ends may be written as

$$\begin{aligned} (a). \text{ passive end : } & -T(h,t) = J_p \ddot{\phi}(h,t) \\ (b). \text{ active end : } & T_a(t) - T(0,t) - c_a \dot{\phi}(0,t) - k_{st} \phi(0,t) = J_a \ddot{\phi}(0,t) \end{aligned} \quad (3.18)$$

where $T_a(t) = T_a' \cdot e^{i\omega t}$ is the applied torque and

$$T(0,t) = - \int_A r \cdot \tau(r,0,t) dA = -I_s a G^* \left[\frac{\theta_p - \theta_a \cos(\bar{\omega}^*)}{\sin(\bar{\omega}^*)} \right] \cdot e^{i\omega t}; \quad (3.19)$$

$$T(h,t) = \int_A r \cdot \tau(r,h,t) dA = I_s a G^* \left[\frac{\theta_p \cos(\bar{\omega}^*) - \theta_a}{\sin(\bar{\omega}^*)} \right] \cdot e^{i\omega t}, \quad (3.20)$$

and it is noted that $T(0,t)$ as defined in the free-body diagram acts in the opposite sense as the positive shear stress over the specimen bottom defined in Figure 3.1.

Substituting Eq. (3.2) into (3.18), dividing through by $J_s \omega^2 e^{i\omega t}$, and replacing $\frac{I_s a G^*}{J_s \omega^2}$ with $\frac{1}{\bar{\omega}^*}$ gives

$$\begin{aligned} (a). \quad & \frac{1}{\bar{\omega}^*} \left[\frac{\theta_p \cos(\bar{\omega}^*) - \theta_a}{\sin(\bar{\omega}^*)} \right] - P \cdot \theta_p = 0 \\ (b). \quad & -\frac{1}{\bar{\omega}^*} \left[\frac{\theta_p - \theta_a \cos(\bar{\omega}^*)}{\sin(\bar{\omega}^*)} \right] - T \cdot \theta_a + iADF \cdot \theta_a = \frac{T'_a}{J_s \omega^2} \end{aligned} \quad (3.21)$$

where

$$P \equiv \frac{J_p}{J_s} \quad (3.22)$$

is the passive end inertia ratio,

$$T \equiv \left(\frac{J_a}{J_s} - \frac{k_{st}}{J_s \omega^2} \right) \quad (3.23)$$

is the active end inertia factor and

$$ADF \equiv \frac{c_a}{J_s \omega} \quad (3.24)$$

is the apparatus damping factor as defined in ASTM D4015. It is important to note that ω in the Eqs. (3.23) and (3.24) should be the fixed value ω_T which is the system resonant frequency that measured during a test.

It is possible to rearrange the left-hand-side of Eq. set (3.21) in terms of the angular rotation θ_p and θ_a . The simplified equation set can be written in matrix form as

$$\begin{bmatrix} A_{11} & A_{12} \\ A_{21} & A_{22} \end{bmatrix} \begin{bmatrix} \theta_p \\ \theta_a \end{bmatrix} = \begin{bmatrix} 0 \\ \frac{T'_a}{J_s \omega^2} \end{bmatrix}. \quad (3.25)$$

In the above matrix, the coefficients (A_{ij}) are complex numbers which can be easily defined and the system of complex-valued equations solved in a MATLAB program. It is also possible to work with complex variables in Fortran 77, Fortran 90 and Microsoft Excel with the Analysis ToolPak add-on. However, the data reduction program provided in ASTM D4015 and the RCDARE analysis described Ashmawy and Drnevich (1994) does not take advantage of this, and works with real and imaginary components separately. For such an approach, the complex coefficients of Eq. (3.25) are separated into real and imaginary components to give

$$\begin{bmatrix} a_{11} + ib_{11} & a_{12} + ib_{12} \\ a_{21} + ib_{21} & a_{22} + ib_{22} \end{bmatrix} \begin{bmatrix} \theta_p \\ \theta_a \end{bmatrix} = \begin{bmatrix} 0 \\ \frac{T'_a}{J_s \omega^2} \end{bmatrix}, \quad (3.26)$$

where it can be shown for the free-free apparatus and boundary conditions described in this chapter that

$$a_{11} = \mu_1 + \mu_3 - P$$

$$a_{12} = \mu_2 + \mu_4$$

$$a_{21} = \mu_2 + \mu_4$$

$$a_{22} = \mu_1 + \mu_3 - T$$

$$b_{11} = \nu_1 + \nu_3$$

$$b_{12} = \nu_2 + \nu_4$$

$$b_{21} = \nu_2 + \nu_4$$

$$b_{22} = \nu_1 + \nu_3 + ADF$$

$$\mu_1 = \frac{1}{F} \frac{(\alpha \cdot co \cdot si + \beta \cdot ch \cdot sh)}{(si \cdot ch)^2 + (co \cdot sh)^2}$$

$$\mu_2 = \frac{1}{F} \frac{-(\alpha \cdot si \cdot ch + \beta \cdot co \cdot sh)}{(si \cdot ch)^2 + (co \cdot sh)^2}$$

$$\mu_3 = -2\xi \cdot \nu_1$$

$$\mu_4 = -2\xi \cdot \nu_2$$

$$\nu_1 = \frac{1}{F} \frac{(-\alpha \cdot ch \cdot sh + \beta \cdot co \cdot si)}{(si \cdot ch)^2 + (co \cdot sh)^2}$$

$$\nu_2 = \frac{1}{F} \frac{(\alpha \cdot co \cdot sh - \beta \cdot si \cdot ch)}{(si \cdot ch)^2 + (co \cdot sh)^2}$$

$$\nu_3 = 2\xi \cdot \mu_1$$

$$\nu_4 = 2\xi \cdot \mu_2$$

$$si = \sin(\alpha F)$$

$$co = \cos(\alpha F)$$

$$sh = \sinh(\beta F)$$

$$ch = \cosh(\beta F)$$

$$F \equiv \omega h \sqrt{\rho / G}; \xi = \omega \eta / 2G$$

$$\alpha = [1 + (2\xi)^2]^{-1/4} \cdot \cos(\phi / 2)$$

$$\beta = -[1 + (2\xi)^2]^{-1/4} \cdot \sin(\phi / 2)$$

$$\phi = \tan^{-1}(2\xi)$$

The matrix of coefficients in Eq. (3.26) can be inverted to obtain the explicit solution of the angle of twist θ_p and θ_a using Cramer's rule,

$$\begin{bmatrix} \theta_p \\ \theta_a \end{bmatrix} = \begin{bmatrix} y_{11} + iz_{11} & y_{12} + iz_{12} \\ y_{21} + iz_{21} & y_{22} + iz_{22} \end{bmatrix} \begin{bmatrix} 0 \\ \frac{T'_a}{J_s \omega^2} \end{bmatrix} \quad (3.27)$$

where

$$y_{ij} = \frac{m_{ij} \cdot g_1 + n_{ij} \cdot g_2}{g_1^2 + g_2^2} \quad z_{ij} = \frac{-m_{ij} \cdot g_2 + n_{ij} \cdot g_1}{g_1^2 + g_2^2}; \quad i=1,2 \text{ and } j=1,2$$

$$m_{11} = a_{22}$$

$$m_{12} = -a_{12}$$

$$m_{21} = -a_{21}$$

$$m_{22} = a_{11}$$

$$n_{11} = b_{22}$$

$$n_{12} = -b_{12}$$

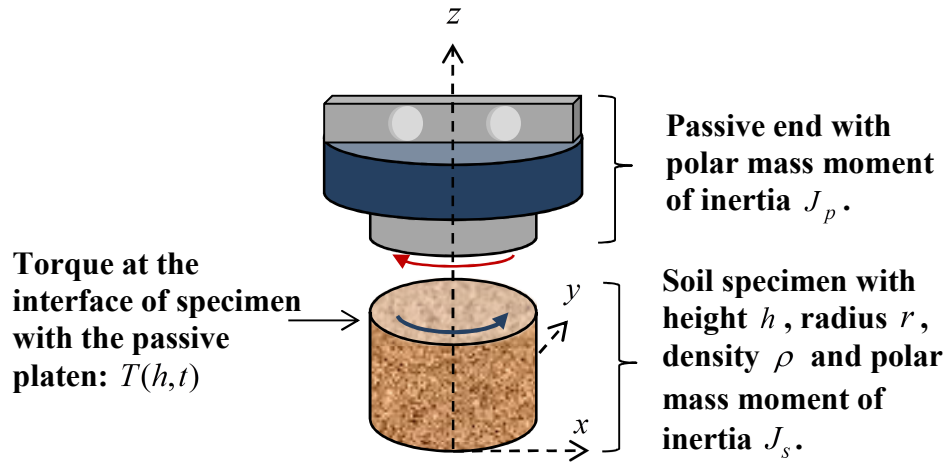
$$n_{21} = -b_{21}$$

$$n_{22} = b_{11}$$

$$g_1 = a_{11}a_{22} - a_{12}a_{21} - b_{11}b_{22} + b_{12}b_{21}$$

$$g_2 = a_{11}b_{22} + a_{22}b_{11} - a_{12}b_{21} - a_{21}b_{12}$$

(a) FBD at passive end:



(b) FBD at active end:

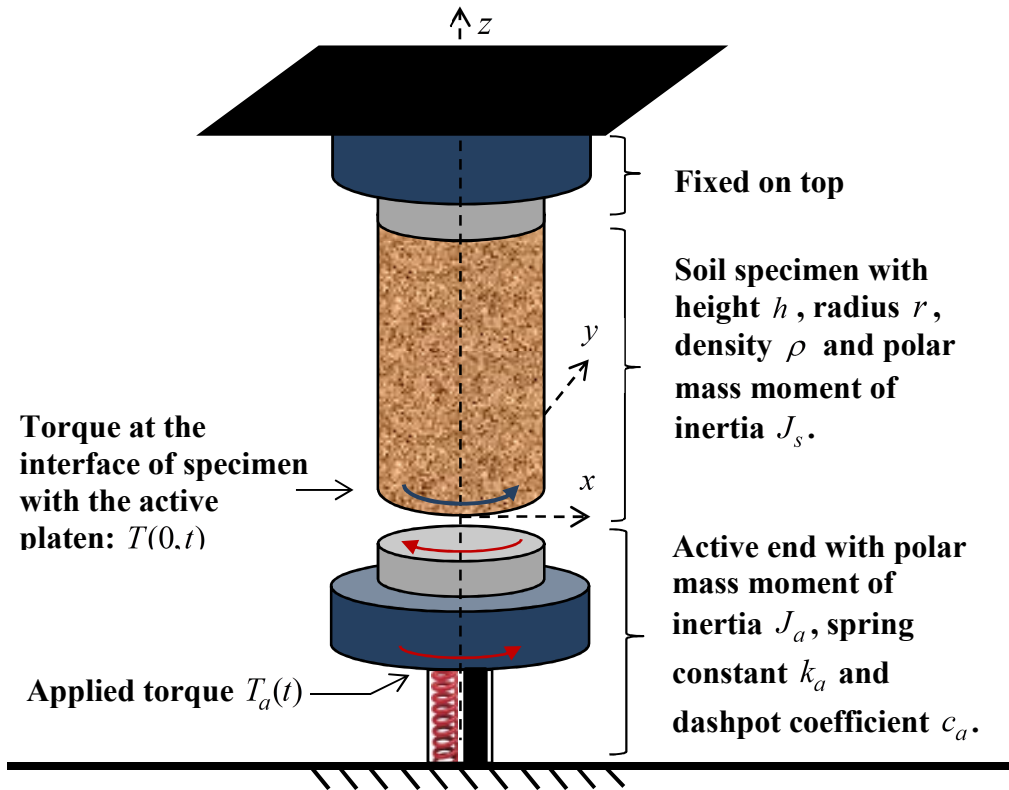


Figure 3.2: Free-body diagrams for E.O.M. at (a) passive and (b) active ends.

The rotation at any location along the specimen axis is given by Eq. (3.7), in which the complex constants C_1 and C_2 are given by Eq. (3.11). The system of equations can be solved rather simply in complex form. Alternatively, if using Euler's formula to separate the real and imaginary components in C_1 and C_2 as in Ashmawy and Drnevich (1994), they can be expressed as

$$C_1 = \frac{-0.5}{(co \cdot sh)^2 + (si \cdot ch)^2} [(\lambda_r co \cdot sh - \lambda_i si \cdot ch) + i(\lambda_r si \cdot ch + \lambda_i co \cdot sh)] \quad (3.28)$$

$$C_2 = (\theta_{ar} - C_{1r}) + i(\theta_{ai} - C_{1i}) \quad (3.29)$$

where

$$\lambda_r = \theta_{pr} - (ch + sh)(\theta_{ar} co + \theta_{ai} si);$$

$$\lambda_i = \theta_{pi} - (ch + sh)(-\theta_{ar} si + \theta_{ai} co);$$

C_{1r} and C_{1i} are the real and imaginary components of C_1 ;

θ_{ar} and θ_{ai} are the real and imaginary components of θ_a .

Substituting Eqs. (3.28) and (3.29) into Eq. (3.7) and using Euler's formula give the rotation along the specimen as

$$\theta(z) = A_1 + iA_2 = \sqrt{A_1^2 + A_2^2} \times e^{i\phi} \quad (3.30)$$

where

$$A_1 = (ch^* - sh^*)[C_{1r} co^* - C_{1i} si^*] + (ch^* + sh^*)[C_{2r} co^* + C_{2i} si^*];$$

$$A_2 = (ch^* - sh^*)[C_{1r} si^* + C_{1i} co^*] + (ch^* + sh^*)[-C_{2r} si^* + C_{2i} co^*];$$

$$\phi = \tan^{-1}(A_2 / A_1);$$

$$si^* = \sin(\alpha F \frac{z}{h}); \quad sh^* = \sinh(\beta F \frac{z}{h});$$

$$co^* = \cos(\alpha F \frac{z}{h}); \quad ch^* = \cosh(\beta F \frac{z}{h}).$$

The strain at any location along the specimen axis can be expressed as

$$\gamma(r, z) = r \cdot \frac{d\theta(z)}{dz} \quad (3.31)$$

For compatibility with commonly assumed stress-strain relationships, a representative shear strain is taken as that corresponding to a radius $r=0.4d$, where d is the diameter of the specimen (e.g. Chen and Stokoe 1979; Isenhowe et al. 1987). Substituting Eq. (3.30) into (3.31) gives a general expression of shear strain

$$\gamma(z) = \frac{0.4d}{h} (A_1' + iA_2') = \frac{0.4d}{h} \sqrt{(A_1')^2 + (A_2')^2} \times e^{i\phi'} \quad (3.32)$$

where

$$\begin{aligned} A_1' = & \alpha F(ch^* - sh^*) [-C_{1r}si^* - C_{1i}co^*] - \beta F(ch^* - sh^*) [C_{1r}co^* - C_{1i}si^*] \\ & + \alpha F(ch^* + sh^*) [-C_{2r}si^* + C_{2i}co^*] + \beta F(ch^* + sh^*) [C_{2r}co^* + C_{2i}si^*] \end{aligned}$$

$$\begin{aligned} A_2' = & \alpha F(ch^* - sh^*) [C_{1r}co^* - C_{1i}si^*] - \beta F(ch^* - sh^*) [C_{1r}si^* + C_{1i}co^*] \\ & + \alpha F(ch^* + sh^*) [-C_{2r}co^* - C_{2i}si^*] + \beta F(ch^* + sh^*) [-C_{2r}si^* + C_{2i}co^*] \end{aligned}$$

$$\phi' = \tan^{-1}(A_2' / A_1')$$

The detailed derivations of the solutions of Eqs. (3.26), (3.27), (3.28), (3.29), (3.30) and (3.32) are provided in Appendix A.

3.2 Transfer Functions

Applying the boundary conditions corresponding to harmonic motion at both passive and active end, a rotational transfer function and a rotation/torque transfer function can also be obtained. The transfer function derivations are discussed in the following sections.

3.2.1 Rotational transfer function

Based on the boundary condition at the passive end, Eq. (3.21a) can be solved to give the complex-valued theoretical transfer function of rotational displacement (or equivalently, rotational acceleration) as (see Ashlock and Pak 2010a)

$$\frac{\theta_p}{\theta_a} = \frac{1}{\cos(\bar{\omega}^*) - P \cdot \bar{\omega}^* \sin(\bar{\omega}^*)} \quad (3.33)$$

where $P = \frac{J_p}{J_s}$ is the passive end inertia ratio and $\bar{\omega}^* = \omega h \sqrt{\frac{\rho}{G^*}}$ is the complex-valued frequency factor as defined above, and

$$\bar{\omega} \equiv \omega h \sqrt{\frac{\rho}{G}} \quad (3.34)$$

is defined as the real-valued dimensionless frequency, which is referred to as the frequency factor F in ASTM D4015 and Ashmawy and Drnevich (1994). It is important to note that this transfer function requires only measurement of the active and passive platen motion and passive end inertia ratio, and does not require calibration of the apparatus stiffness and damping, apparatus frequency, or active end rotational inertia discussed in the previous sections. Use of this transfer function therefore greatly simplifies testing procedures for free-free RC systems, and eliminates a number of potential sources of experimental error.

The relation between the complex frequency factor and dimensionless frequency can be expressed as

$$\bar{\omega}^* = \frac{\bar{\omega}}{\sqrt{1+i \cdot 2\xi}} \quad (3.35)$$

For a specified range of the dimensionless frequency $\bar{\omega}$, damping ratio ξ , and passive end inertia ratio P , the complex-valued theoretical rotational transfer function in Eq. (3.33) can be plotted. Figure 3.3 illustrates typical plots of the magnitude, real part, imaginary part and phase angle of the theoretical rotational transfer function versus dimensionless frequency. From the plot, five peaks can be seen in the given range of $\bar{\omega}$ for a passive end inertia ratio of 0.97 and specimen hysteretic damping ratio of 2%.

In the modified RC tests, accelerometers were mounted to record tangential accelerations on the active and passive platens as shown in Figure 3.4. The acceleration measurements were processed in the frequency-domain by the analyzer to obtain the experimental transfer functions. The effects of the soil modulus and damping ratio on the transfer function are illustrated below.

First, the rotational transfer functions were compared by varying only the hysteretic damping ratio of the specimen. The other properties of soil and apparatus are assumed as shown in Table 3.1. The effect of varying the hysteretic damping ratio on the transfer function is shown in Figure 3.5. As expected, the amplitudes of the peaks decrease with increasing damping ratio, and the effect is more pronounced as frequency increases. At the same time, the peaks move to the right which means the resonant frequency is increasing. However, for realistically small damping ratios below 2%, the resonant frequencies of the peaks change only slightly. This can be illustrated more clearly by zooming in and tracking the peaks as damping is varied, as shown in Figure 3.6. Next, the shear modulus of the specimen was varied using the same properties and assuming a hysteretic damping ratio of

2%, giving the transfer functions shown in Figure 3.7. As expected, the peak frequencies increase with increasing shear modulus, but the amplitudes of the peaks are unchanged due to the use of hysteretic damping (Figure 3.8).

From these figures, it can be concluded that the specimen's hysteretic damping ratio primarily controls the peak amplitudes, and the shear modulus primarily controls peak frequencies. Therefore, to determine the modulus and damping for an experimentally measured transfer function, a value of hysteretic damping ratio was first assumed, and the shear modulus was varied to match the frequency of the first peak of the transfer function's magnitude. The agreement between experimental and theoretical transfer function curves was qualitatively evaluated by adjusting the damping to match the height of the transfer function magnitude. This procedure will henceforth be referred to as the "peak only" fitting approach. A second, "squared-error" fitting approach was also programmed to take into account both the real and imaginary components of the transfer function in the fitting process. Equivalently, one could also propose a "squared-error" fitting procedure that attempts to match the magnitude and phase. However, this would require the use of different weighting factors, since the magnitude and phase have different units. In contrast, the real and imaginary components have the same units. Differences between using the peak only and "squared-error" fitting methods will be discussed in Chapter 5.

Table 3.1: Assumed properties of specimen and apparatus for demonstrating theoretical rotational transfer functions.

Specimen Properties					Apparatus Properties
Diameter [meter]	Height [meter]	Density [kg/m ³]	Shear Modulus [MPa]	Damping Ratio [%]	Passive Platen Rotational Inertia [kg·m ²]
0.1524	0.2731	1683	102	2.0	0.0236

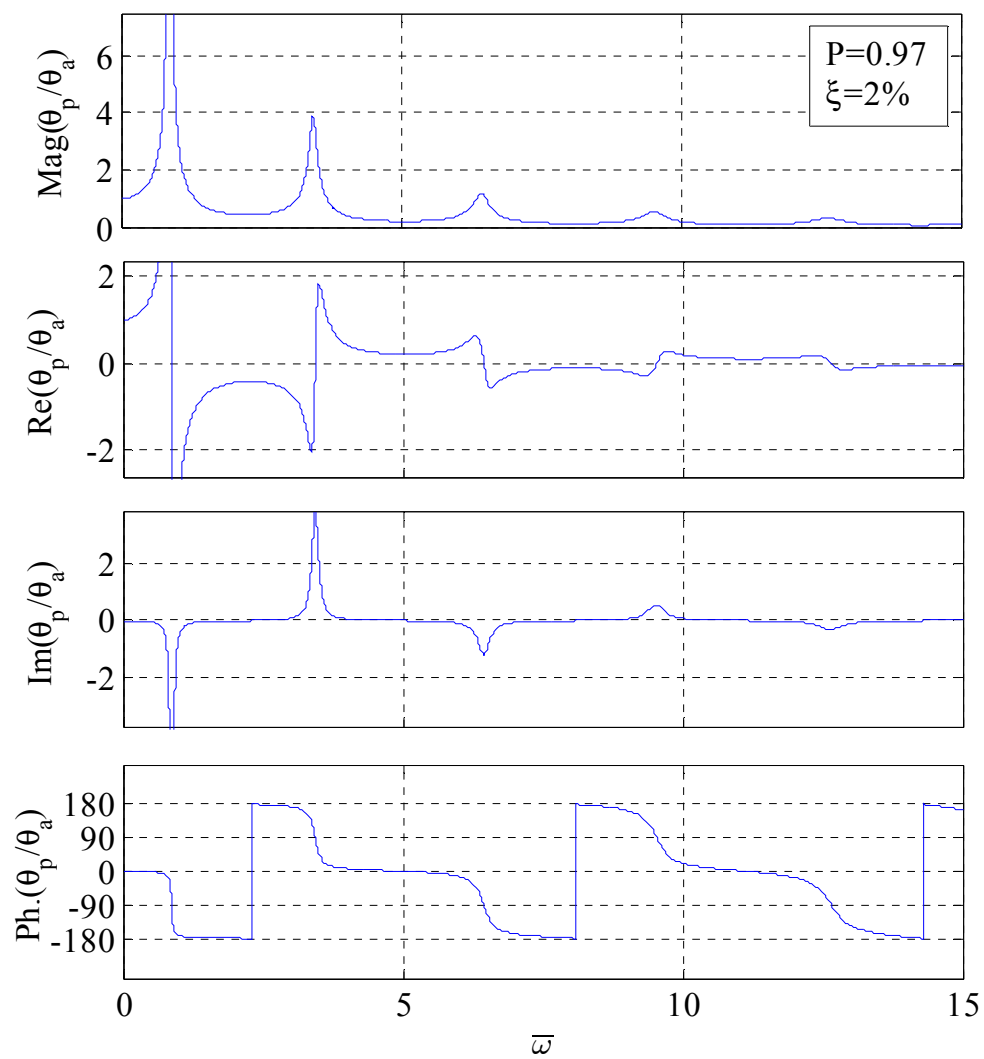
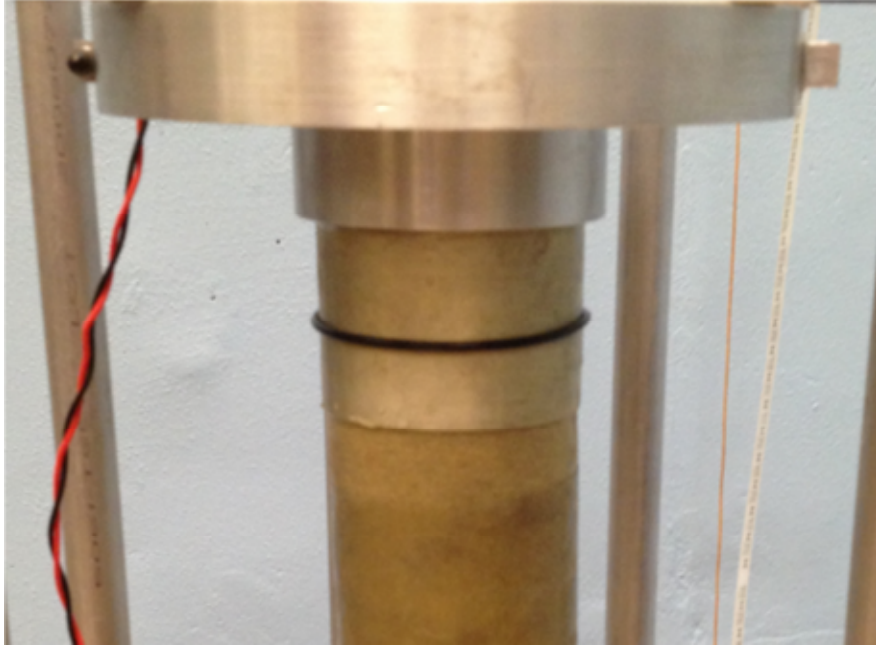


Figure 3.3: Theoretical rotational transfer function.

(a) Accelerometers mounted on top disc:



(b) Accelerometers mounted at bottom base:

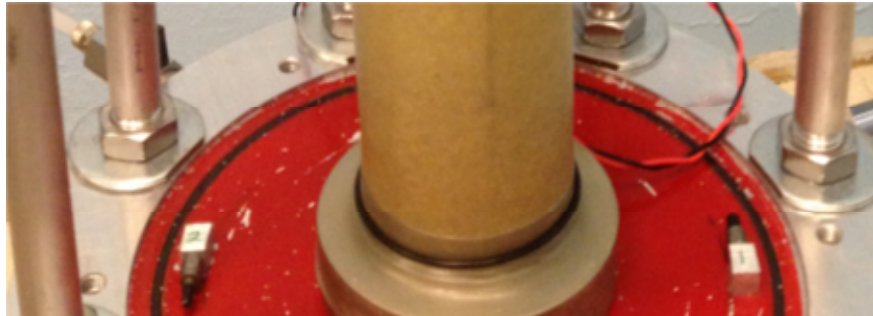


Figure 3.4: Accelerometers at passive and active ends.

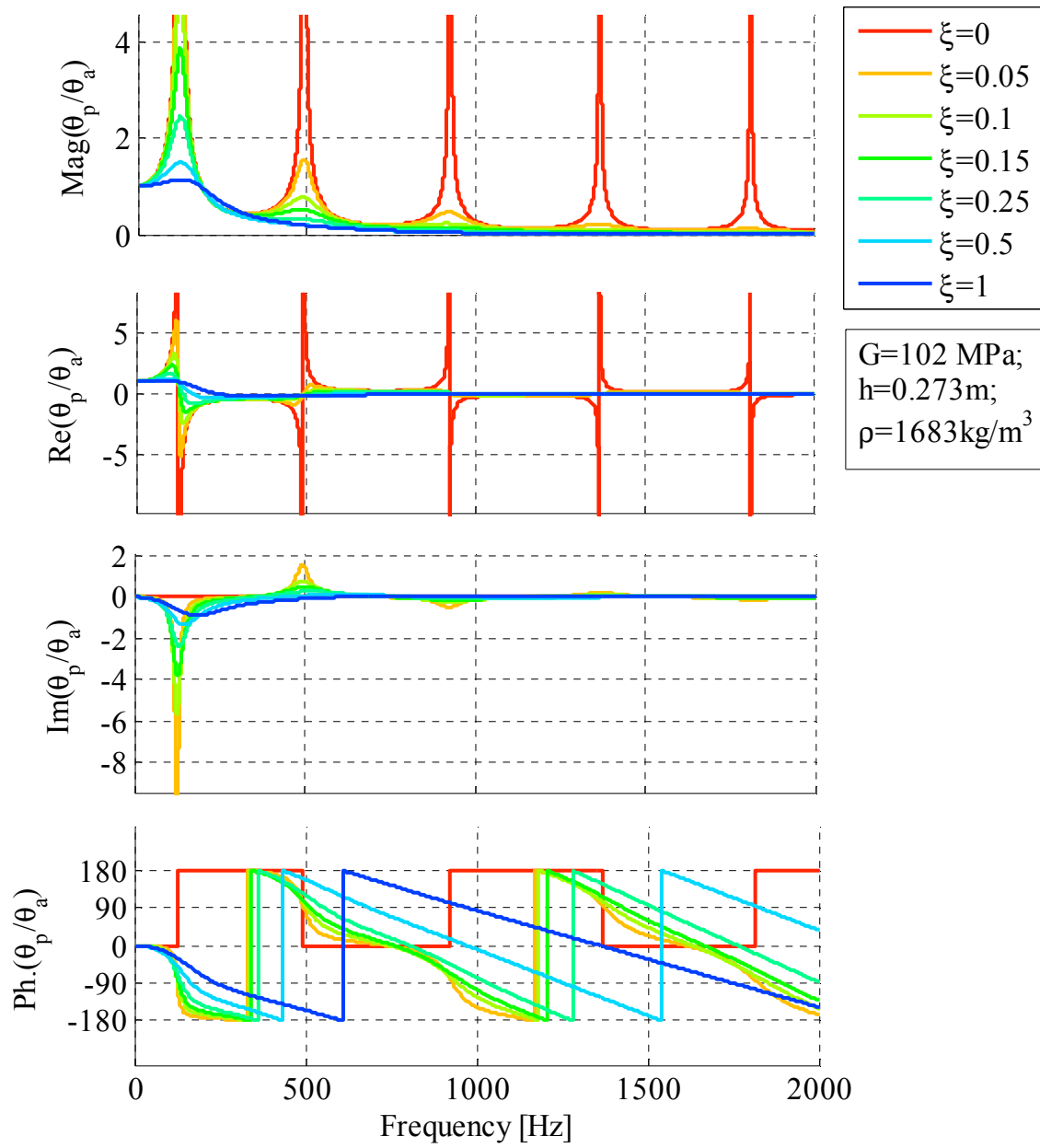


Figure 3.5: Effect of hysteretic damping ratio ξ on theoretical rotational transfer function.

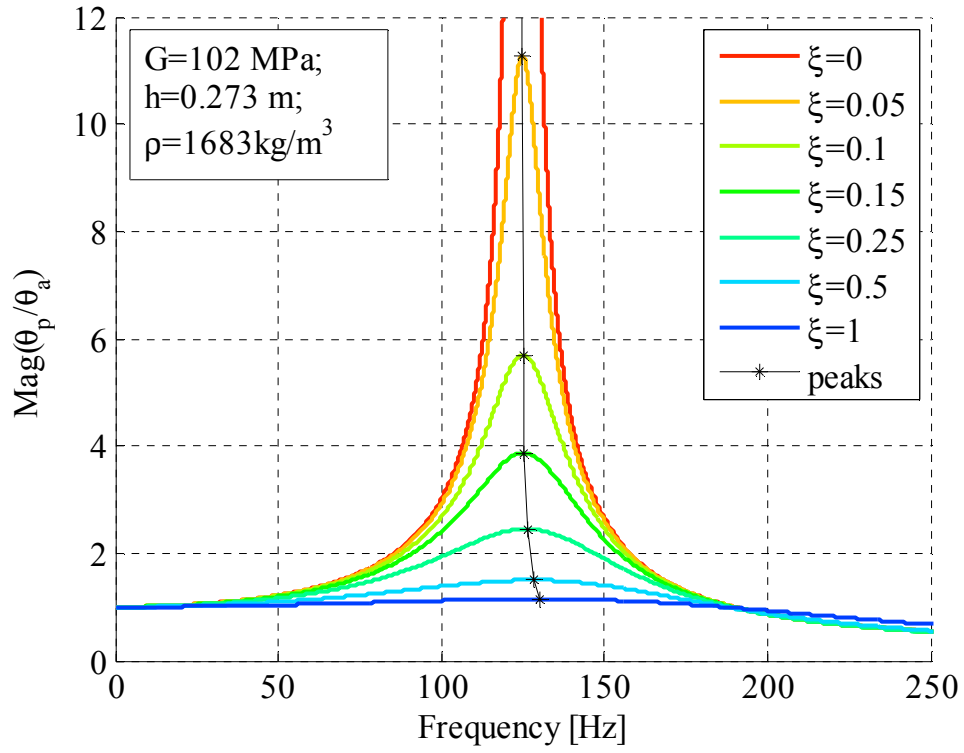


Figure 3.6: Close-up showing effect of hysteretic damping ratio ξ on theoretical rotational transfer function.

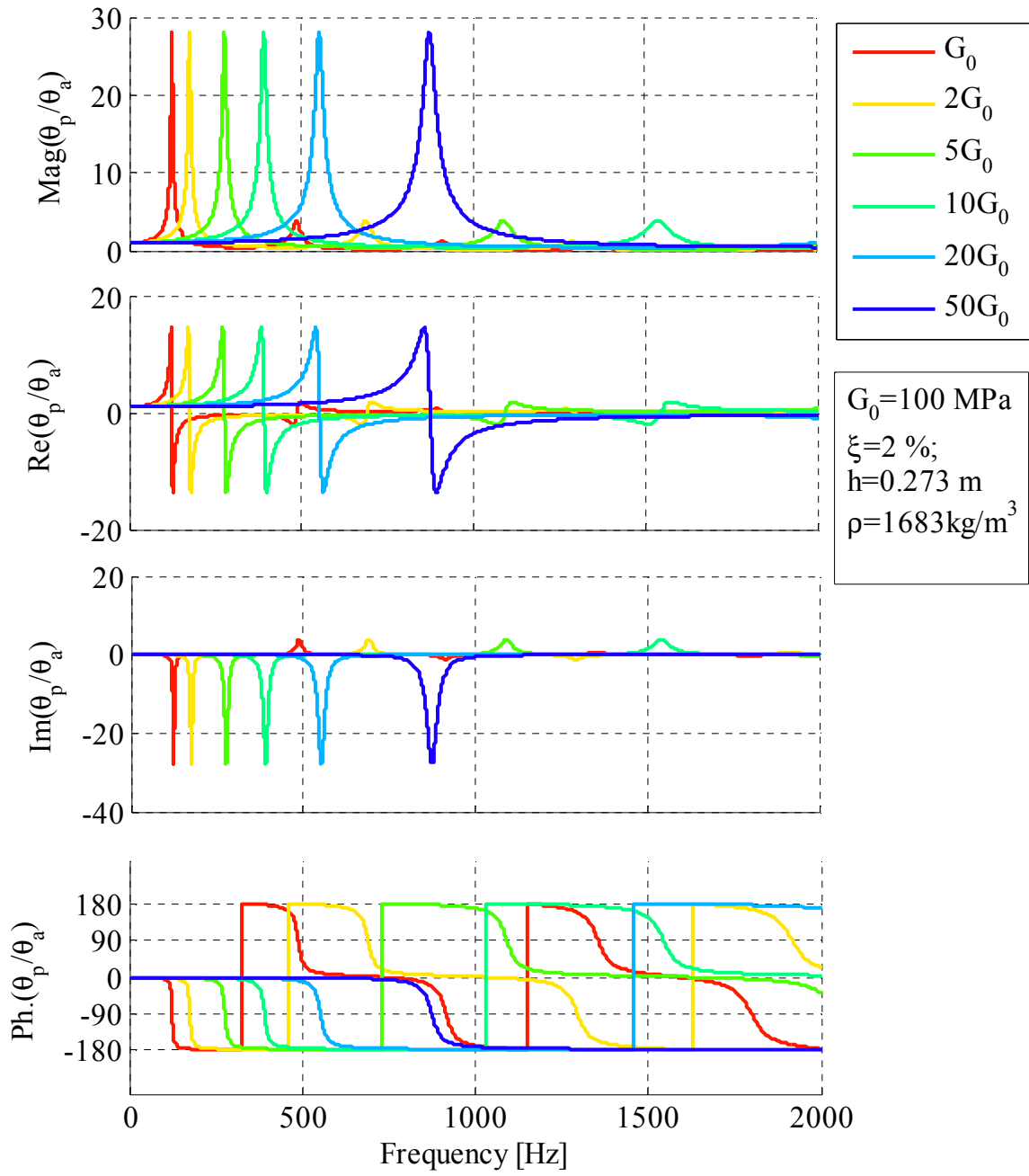


Figure 3.7: Effect of shear modulus G on theoretical rotational transfer function.

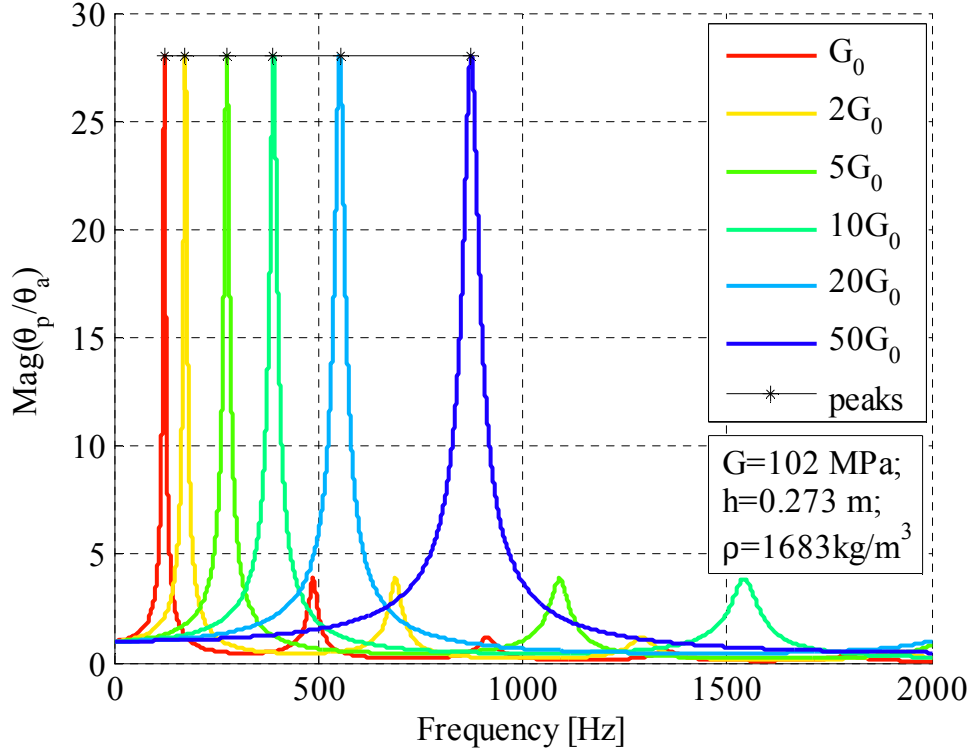


Figure 3.8: Close-up showing effect of shear modulus G on theoretical rotational transfer function.

3.2.2 Passive rotation/torque transfer function

Based on the boundary condition at the passive end in Eq. (3.21b), eliminating the active end rotation using the rotational transfer function in Eq. (3.33) will give the complex-valued theoretical rotation/torque transfer function as

$$\frac{\theta_p}{T_a} = \left[J_s \omega^2 \left(-\frac{1 - \cos(\bar{\omega}^*)}{\bar{\omega}^* \sin(\bar{\omega}^*)} \frac{1}{H} - \frac{T}{H} + i \frac{ADF}{H} \right) \right]^{-1} \quad (3.36)$$

where H is the theoretical rotational transfer function of Eq. (3.33), T is the active end inertia factor of Eq. (3.23) and ADF is the apparatus damping factor of Eq. (3.24).

This function is plotted for the soil properties and apparatus constants of Table 3.2 in Figure 3.9.

The theoretical rotational velocity/torque transfer function can be calculated from the above equation as

$$\frac{\dot{\theta}_p}{T_a} = (i\omega) \left[J_s \omega^2 \left(-\frac{1 - \cos(\bar{\omega}^*)}{\bar{\omega}^* \sin(\bar{\omega}^*)} - \frac{T}{H} + i \frac{ADF}{H} \right) \right]^{-1} \quad (3.37)$$

The plot of this function is shown in Figure 3.10, from which it can be seen that the passive-end geophone outputs (rotational velocity) and applied torque are in phase ($\phi = 0$) at the resonant frequencies, leading to the use of a linear slope of the Lissajous plot of these two quantities in the ASTM method. The shape of this transfer function is similar to the rotational velocity transfer function of Figure 3.9, with five peaks evident in the plot.

In order to investigate the effects of specimen properties and apparatus properties on the rotational velocity/torque transfer function, the parameters were varied similar to the procedure discussed in the previous section. First, a comparison was made by varying the apparatus spring stiffness. As shown in Figure 3.11, the amplitude of rotation/torque transfer function decreases as the stiffness increases. The phase angle is not affected by the device stiffness, and the corresponding frequencies remain constant, as shown in the close-up of Figure 3.12. Second, the apparatus damping was varied as shown in Figure 3.13, for which case the transfer function is not affected by apparatus damping except for the unlikely case that the damping ratio is 100%.

In addition, the effect of varying the specimen's shear modulus and damping were examined. As the shear modulus increases, the transfer function curve moves to the right, and the peak amplitudes increase slightly as shown in Figure 3.14 and Figure 3.15. Increasing the specimen's hysteretic damping ratio (Figure 3.16) causes the amplitudes of the

transfer function peaks to decrease, while the corresponding frequencies and phase angles increase (see Figure 3.17 and Figure 3.18).

Table 3.2: Properties of specimen and apparatus for plotting the rotation/torque transfer function.

Specimen Properties					Apparatus Properties		
Diameter [meter]	Height [meter]	Density [kg/m ³]	Shear Modulus [MPa]	Damping Ratio [%]	Active Platen Inertia [kg·m ²]	Damping Coefficient [kg·m ³ /s]	Spring Constant [N·m/rad]
0.1524	0.2731	1683	102	2.0	0.7882	1.22	99624

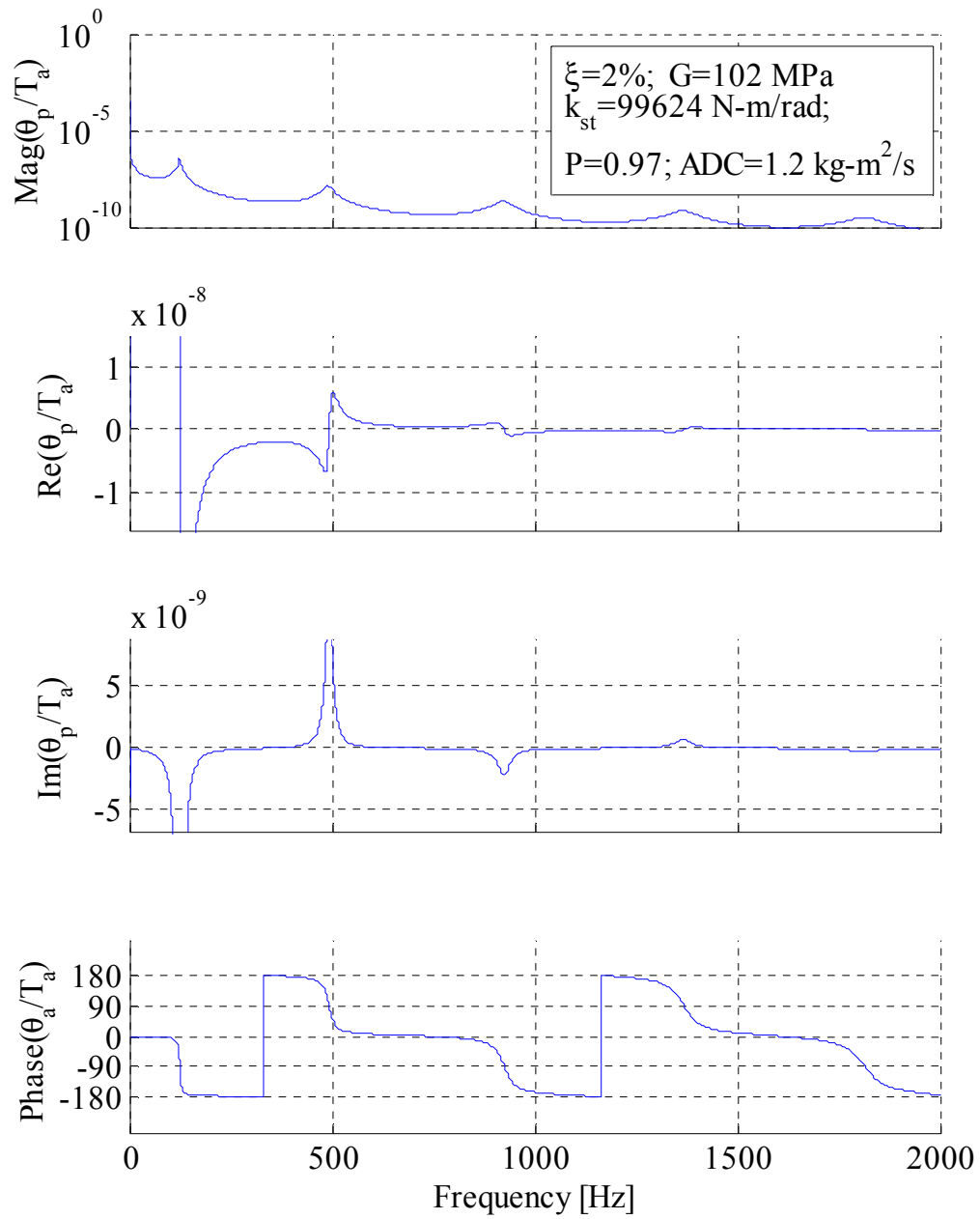


Figure 3.9: Theoretical rotation/torque transfer function

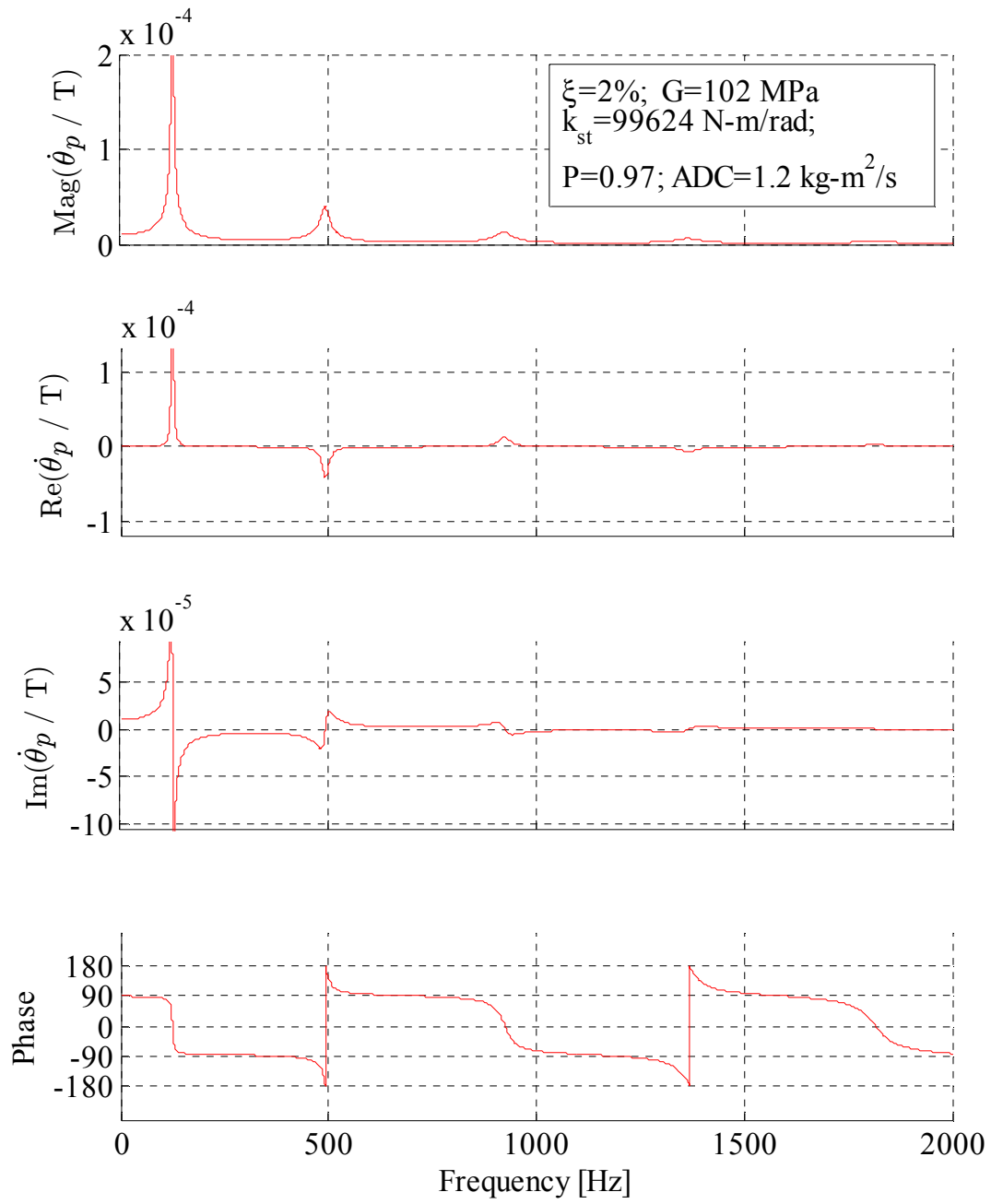


Figure 3.10: Theoretical rotational velocity/torque transfer function

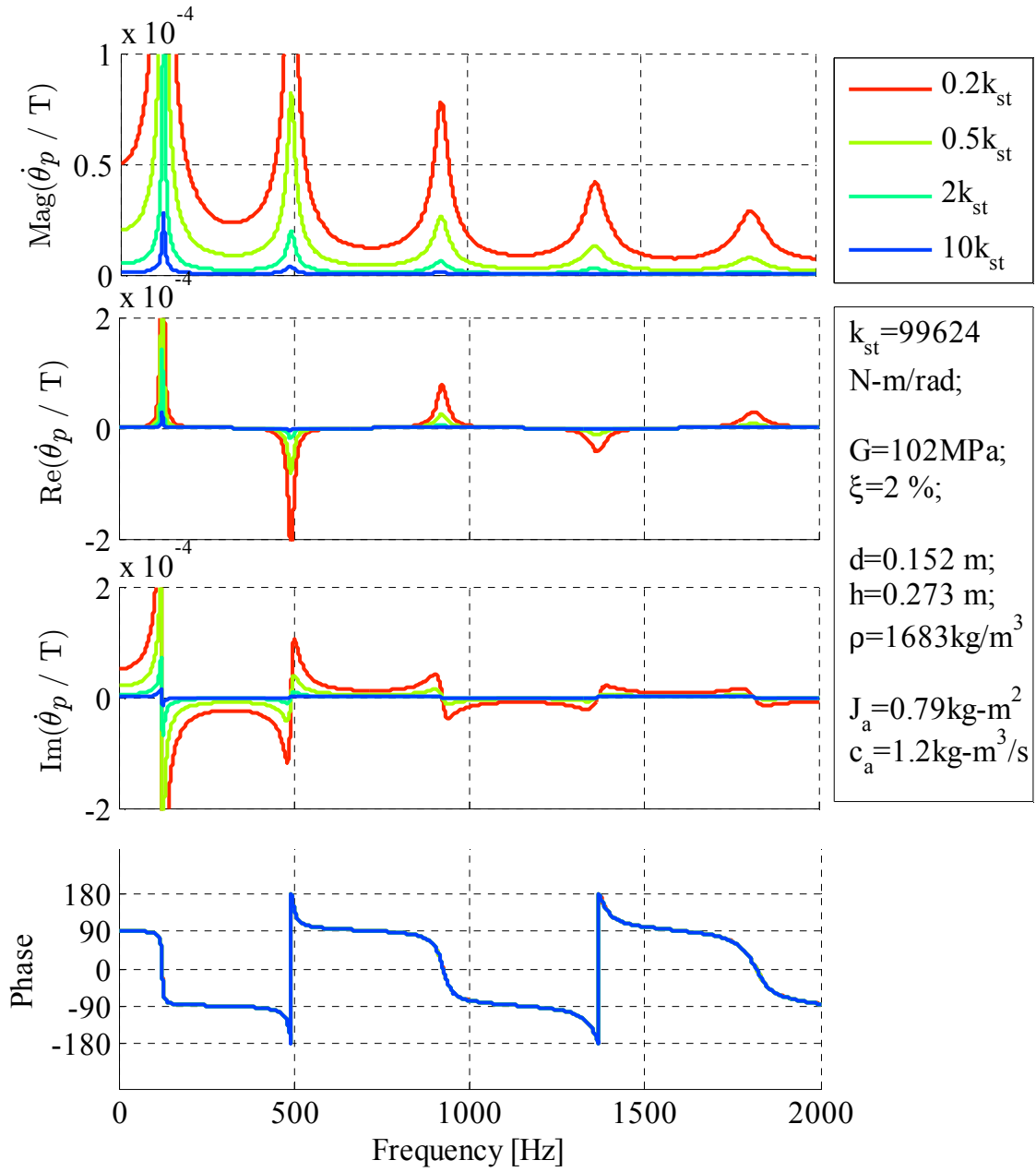


Figure 3.11: Effect of apparatus stiffness k_{st} on theoretical rotational velocity/torque transfer function.

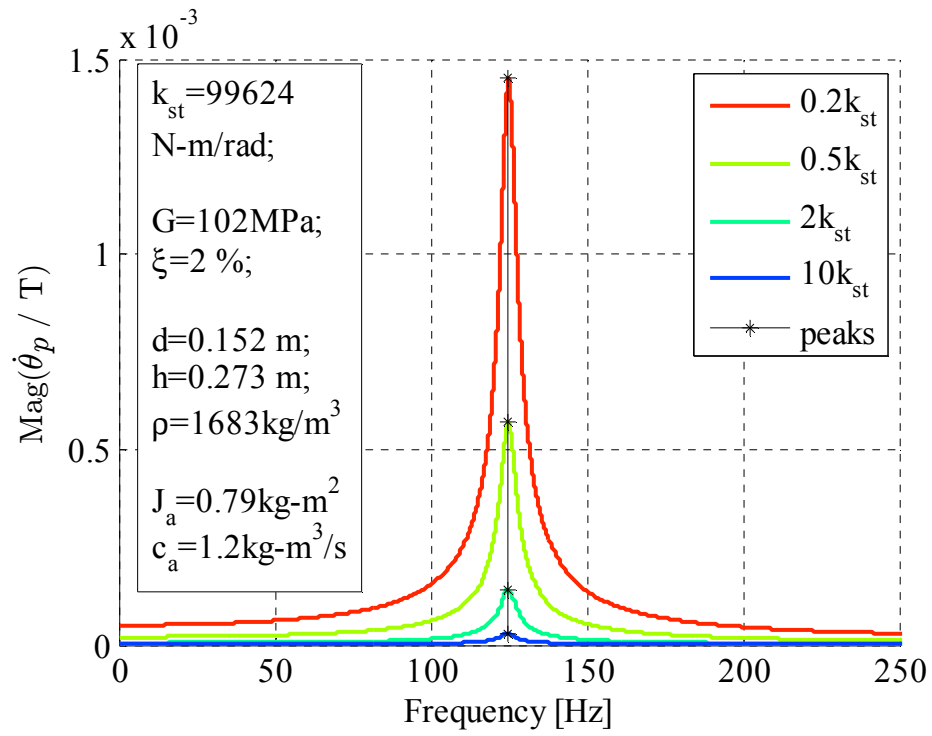


Figure 3.12: Close-up showing effect of apparatus stiffness k_{st} on theoretical velocity rotational transfer function.

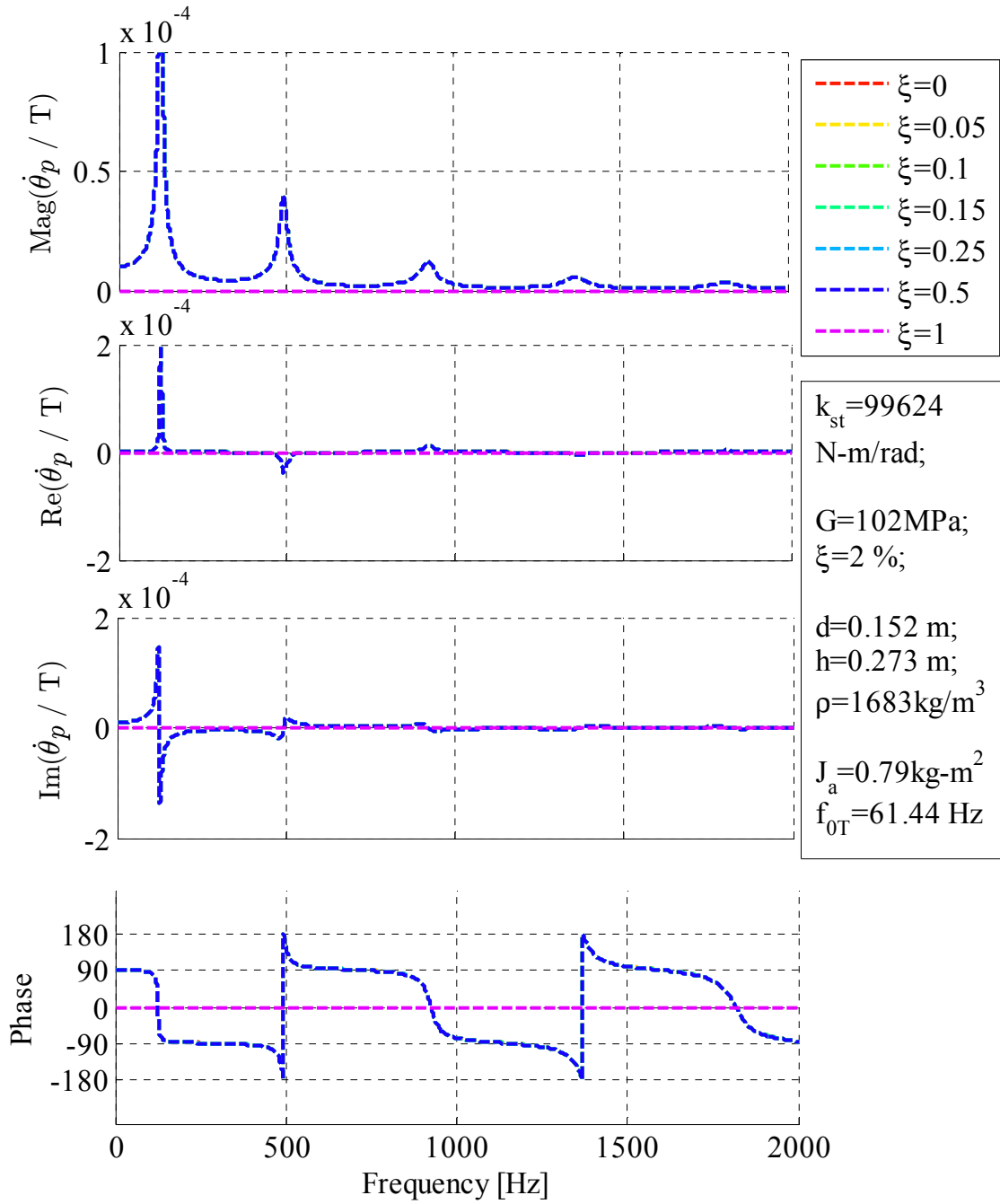


Figure 3.13: Effect of apparatus damping ratio ξ_a on theoretical rotational velocity/torque transfer function.

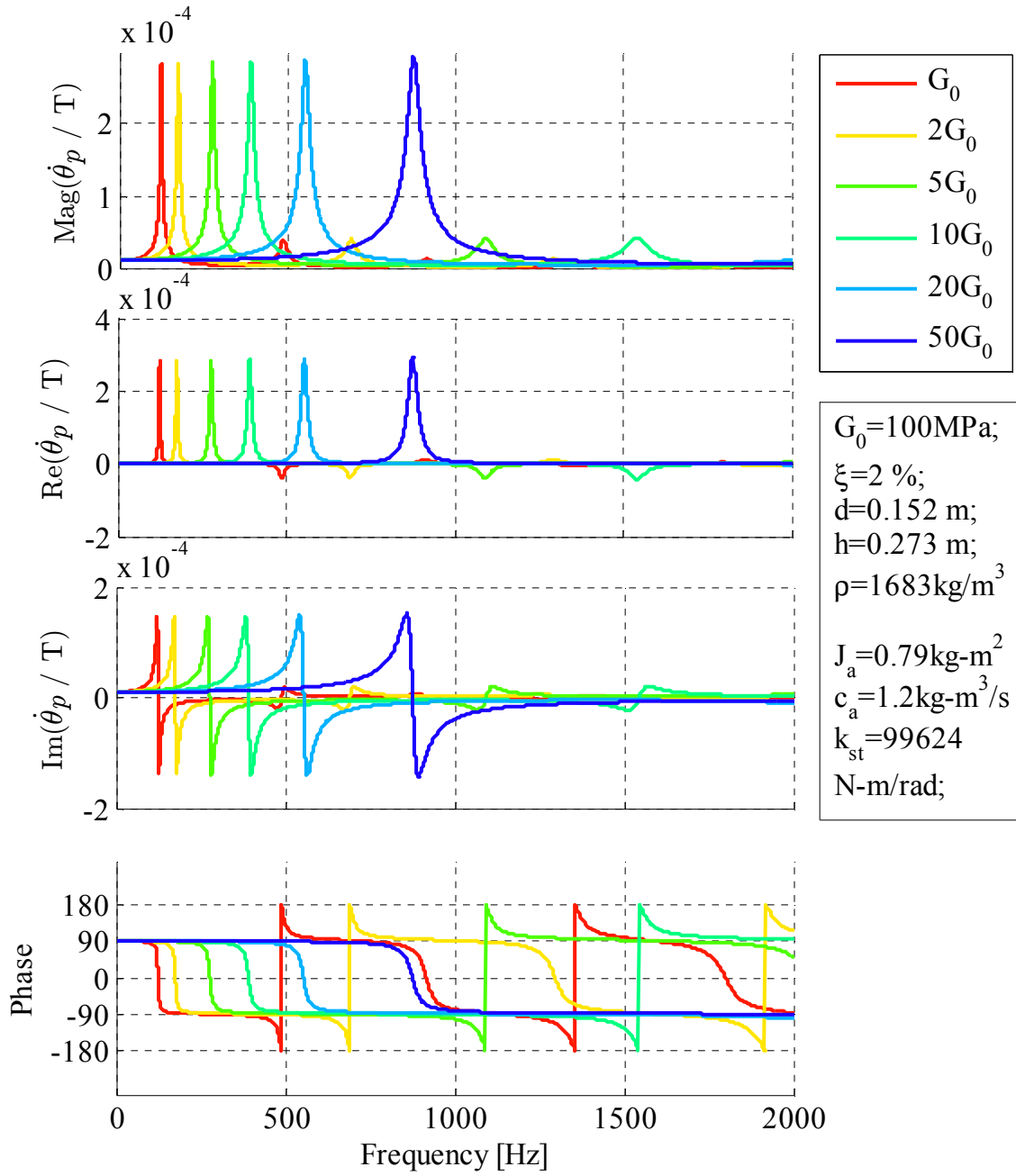


Figure 3.14: Effect of specimen shear modulus G on theoretical rotational velocity/torque transfer function.

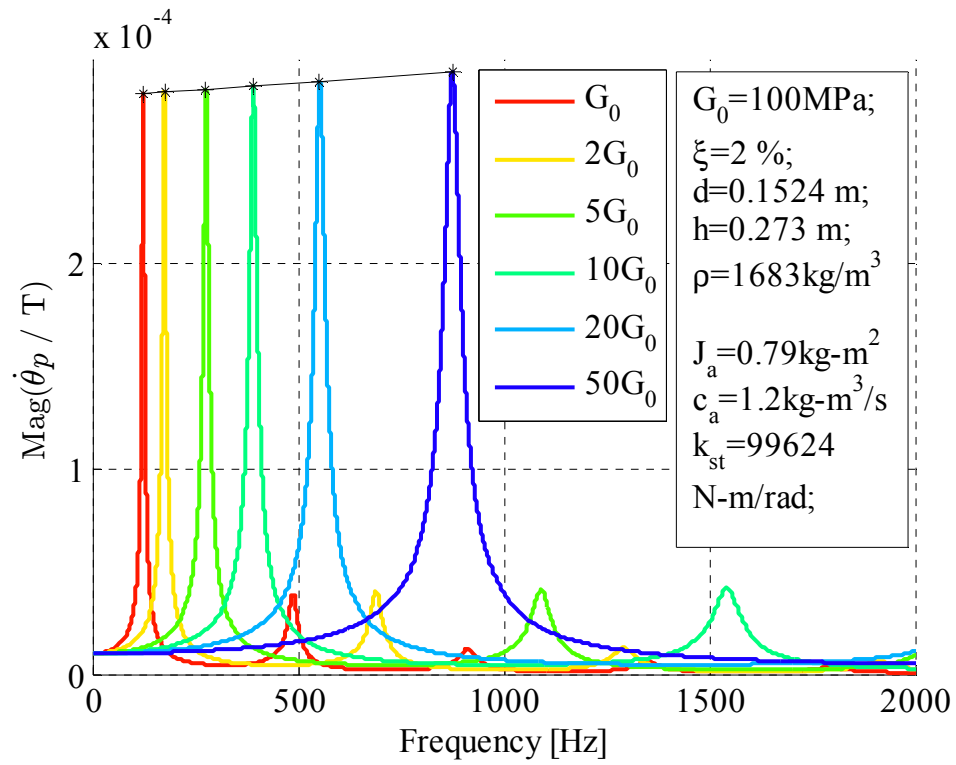


Figure 3.15: Close-up showing effect of specimen shear modulus G on theoretical velocity rotational transfer function.

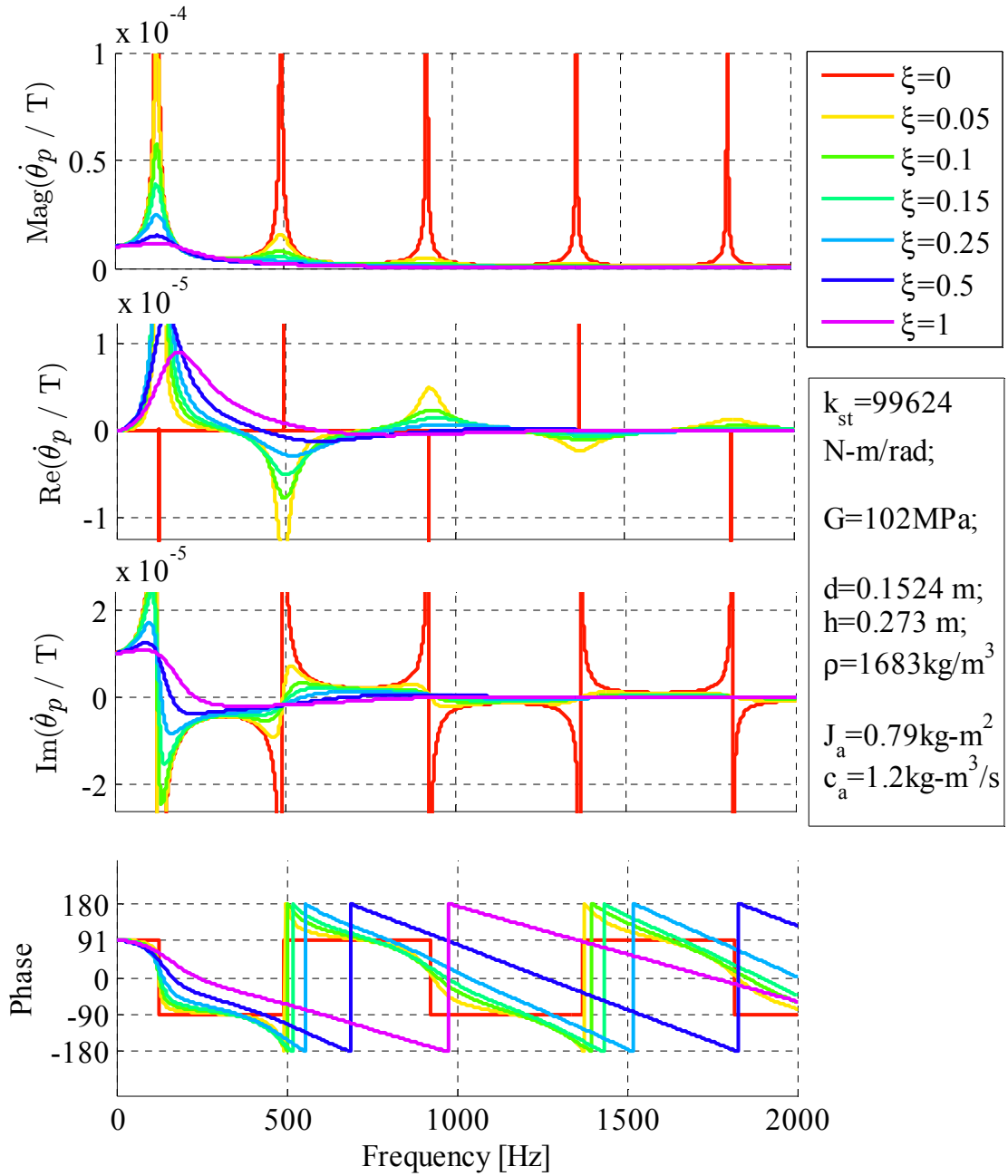


Figure 3.16: Effect of specimen damping ratio ξ on theoretical rotational velocity/torque transfer function.

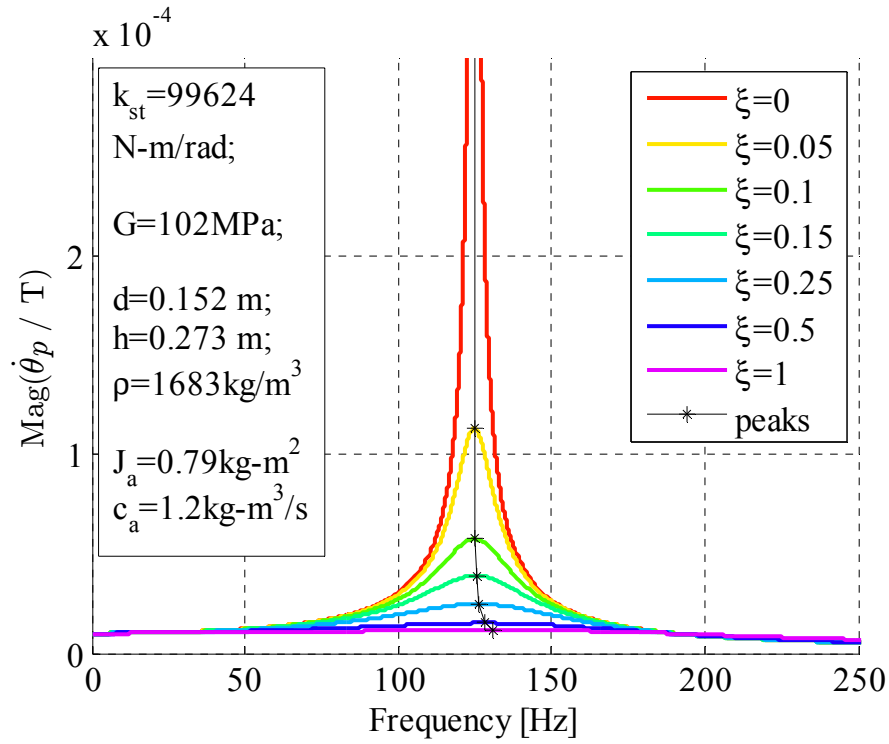


Figure 3.17: Close-up showing effect of specimen damping ratio ξ on the magnitude of theoretical velocity rotational transfer function.

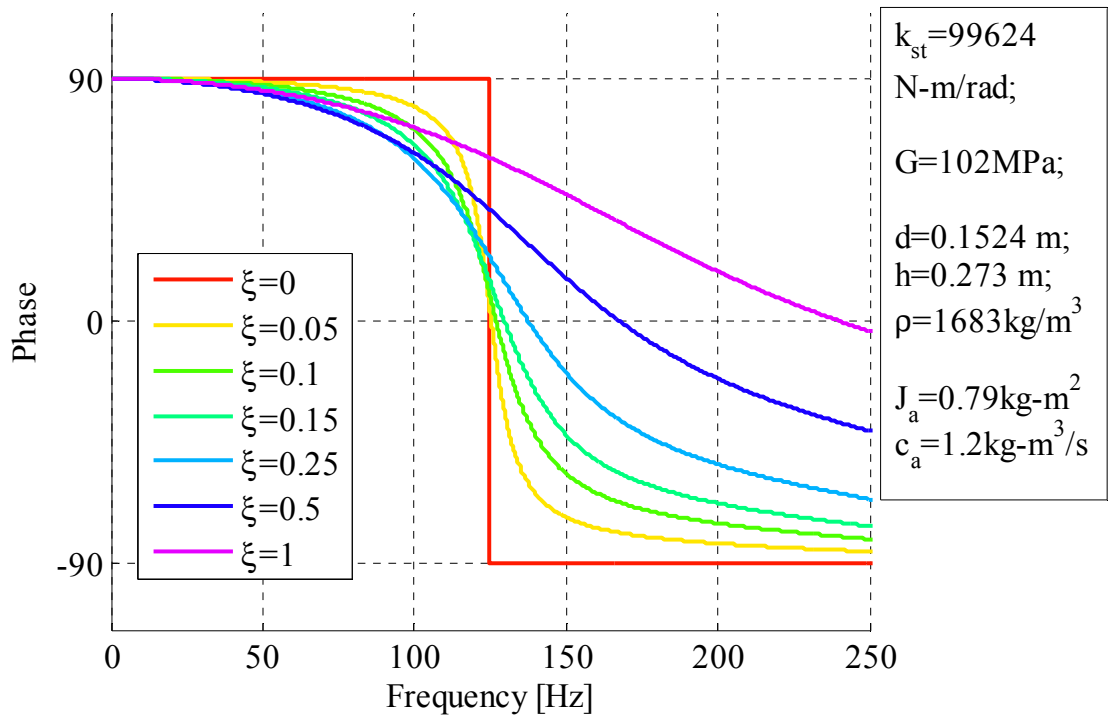


Figure 3.18: Close-up showing effect of specimen damping ratio ξ on the phase of theoretical velocity rotational transfer function.

3.3 Measurement Approach

As discussed in the previous sections, in the modified RC tests, the outputs from the accelerometers were sampled and converted into the frequency-domain using the Fast Fourier Transform (FFT). The corresponding frequency response function (FRF) and coherence functions were calculated using the acceleration signals in the frequency-domain. The detailed calculations will be described in the following sections.

3.3.1 Fourier transform

In the Fourier series, complicated but periodic functions can be written as the sum of simple harmonic components represented mathematically by sine and cosine functions. Due to the properties of sine and cosine and Euler's formula, it is possible to recover the amplitude and phase of each harmonic component in a Fourier series. It can be shown that discrete Fourier series are related to continuous Fourier Transforms of a continuous signal $x(t)$, which can be written as

$$X(f) = \int_{-\infty}^{\infty} x(t)e^{-i2\pi ft} dt \quad (3.38)$$

where

$i = \sqrt{-1}$ is the imaginary unit;

f is the frequency [Hz] and;

t is the time [sec].

The inverse of this transform is given by

$$x(t) = \int_{-\infty}^{\infty} X(f)e^{i2\pi ft} df \quad (3.39)$$

A Hanning window (Hann, 1959) was employed to minimize the effects of aliasing and spectral leakage that arise from discrete sampling over a finite time interval. The Hanning window is defined by

$$u(t) = 1 - \cos^2\left(\frac{\pi t}{T}\right) \quad (3.40)$$

Use of the Hanning window distorts the peak amplitude by a factor of 1/2, requiring that a correction factor of 2 be applied to obtain the correct peak amplitude of a Hanning-windowed Fourier transform.

3.3.2 Frequency response function

An ideal single-input/ single-output system without extraneous noise at input/output points is shown below,

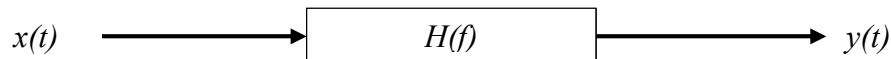


Figure 3.19: An ideal single-input/ single-output system without extraneous noise

where $x(t)$ is the input $y(t)$ is the output for the system, and $H(f)$ is the FRF, often called the transfer function. For a linear system, $H(f)$ can be estimated using deterministic data, transient data, or stationary random data because its properties are independent of the nature of data passing through the system (Bendat and Piersol, 2010). The relation between input and output in terms of the FRF is a simple linear algebraic expression in the frequency-domain,

$$Y(f) = H(f)X(f) \quad (3.41)$$

where $X(f)$ and $Y(f)$ are finite Fourier transforms (actually discrete transforms, or DFT) of $x(t)$ and $y(t)$, respectively. It follows that

$$\begin{aligned}
(a). \quad X^*(f)Y(f) &= H(f)|X(f)|^2 \\
(b). \quad Y^*(f)X(f) &= H^*(f)|X(f)|^2
\end{aligned} \tag{3.42}$$

where $X^*(f)$ is the complex conjugate of $X(f)$

The quantities $G_{xx}(f)$ and $G_{yy}(f)$ may be defined as the one-sided auto-spectral densities (ASD) of X and Y,

$$\begin{aligned}
(a). \quad G_{xx}(f) &= X^*(f)X(f) = |X(f)|^2 \\
(b). \quad G_{yy}(f) &= Y^*(f)Y(f) = |Y(f)|^2
\end{aligned} \tag{3.43}$$

It should be noted that the auto-spectral densities derived from the Fourier transforms are real-valued and retain the DFT magnitude but not the phase. Therefore, they cannot be used to obtain the complex-valued spectrum, and the original complex-valued Fourier transforms must be used. The complex-valued one-sided cross-spectral densities $G_{xy}(f)$ and $G_{yx}(f)$ can be defined as

$$\begin{aligned}
(a). \quad G_{xy}(f) &= X^*(f)Y(f) \\
(b). \quad G_{yx}(f) &= Y^*(f)X(f)
\end{aligned} \tag{3.44}$$

From Eqs. (3.42a) and (3.43) the FRF can be expressed as

$$H(f) = \frac{G_{xy}(f)}{G_{xx}(f)} \tag{3.45}$$

Calculation of the transfer function via auto- and cross-spectral density functions in this form results in a statistical reduction of random error associated with the individual measurements of $x(t)$ and $y(t)$ in Figure 3.19. The transfer function in Eq. (3.45) is complex-valued and can be expressed in polar notation as

$$H(f) = |H(f)|e^{-i\phi(f)} \tag{3.46}$$

where

$|H(f)|$ is gain factor and;

$\phi(f)$ is phase factor of the system.

From Eq. (3.45) the complex conjugate of the FRF is

$$H^*(f) = \frac{G_{yx}(f)}{G_{xx}(f)} \quad (3.47)$$

where $H^*(f) = |H(f)|e^{i\phi(f)}$

Thus, the phase factor of the system may be determined by dividing Eq. (3.45) by (3.47),

$$\frac{H(f)}{H^*(f)} = \frac{G_{xy}(f)}{G_{yx}(f)} = e^{-2i\phi(f)} \quad (3.48)$$

In addition to the FRF, the coherence function can be also calculated from the measured signal as

$$\gamma_{xy}^2(f) = \frac{|G_{xy}(f)|^2}{G_{xx}(f)G_{yy}(f)} \quad (3.49)$$

The coherence function will be a value of one for a perfectly linear and time-invariant system with zero noise. Once the system has deviation from any of these three conditions, the coherence will decrease. Hence the value of coherence function is an indicator of the measurement quality. For the transfer functions measured in this study, it is common that the coherence decreases between the resonant peaks and increases near the resonant peaks. Because the magnitude of acceleration is very small between resonant peaks, the low signal-to noise (SN) ratio leads to a decrease in coherence. Near the peak frequencies, SN ratio increases as the acceleration magnitude increases, while the coherence increases.

3.4 Strain Calculation Using Transfer Function

Tangential acceleration of the end platens are measured using the signal analyzer, and denoted $a_i(t)$, $i=1,2,3,4$ in the bottom right, bottom left, top right and top left positions, respectively. The angular accelerations of the platens are related to the tangential accelerations through

$$a(t) = R \cdot \ddot{\phi}(t) \quad (3.50)$$

where

R is the radius to the accelerometer's central axis and;

$\ddot{\phi}(t)$ is the angular acceleration of the corresponding end platens.

The accelerometers are oriented in opposite directions so that their average value may be used in Eq. (3.50) to cancel out accelerations due to lateral motion and bending modes. For harmonic motion of a platen, $\phi(t) = \phi_0 e^{i\omega t}$ and the relation between the angular acceleration and the angle of twist at any excitation frequency $\omega = 2\pi f$ is

$$\ddot{\phi}(t) = (i\omega)^2 \phi(t). \quad (3.51)$$

Therefore the angles of twist at end platens in the time-domain can be obtained from the measured tangential acceleration as

$$\phi(t) = -\frac{a(t)}{R \cdot \omega^2}. \quad (3.52)$$

While the above is useful for harmonic excitation, Fourier transforms may be used to obtain a more general formulation applicable to harmonic as well as arbitrary forcing functions such as random, swept-sine or impulse. Through the use of the Fourier transform, the angle of twist in the frequency-domain can be obtained as,

$$\tilde{\phi}(f) = \int_{-\infty}^{\infty} \phi(t) \cdot e^{-i2\pi ft} dt. \quad (3.53)$$

By the properties of Fourier transforms, the angular rotation can be related to the angular acceleration through

$$\tilde{\varphi}(f) = \frac{\tilde{\ddot{\varphi}}(f)}{-(2\pi f)^2}, \quad (3.54)$$

where from Eq. (3.50),

$$\tilde{\ddot{\varphi}}(f) = \frac{\tilde{a}(f)}{R}. \quad (3.55)$$

Therefore, the angle of twist in the frequency-domain can be obtained from the measured average platen acceleration as

$$\tilde{\varphi}(f) = -\frac{1}{R \cdot (2\pi f)^2} \int_{-\infty}^{\infty} a(t) \cdot e^{-i2\pi f t} dt = -\frac{\tilde{a}(f)}{R \cdot (2\pi f)^2} \quad (3.56)$$

where $\tilde{\varphi}(f)$ is complex-valued. The angle of twist of the passive-end (top) platen $\tilde{\varphi}_p(f)$ may be obtained by Eq. (3.56) using the average tangential acceleration $a_p(t) = (a_3(t) + a_4(t)) / 2$, and $\tilde{\varphi}_a(f)$ for the active-end (bottom) platen may be obtained using $a_a(t) = (a_1(t) + a_2(t)) / 2$.

The shear strain may be calculated as,

$$\gamma(r, z, t) = r \cdot \frac{\partial \varphi(z, t)}{\partial z}. \quad (3.57)$$

Although the strain and therefore stress vary linearly with radius for an elastic material, a representative shear strain is often taken as that corresponding to a radius $r = 0.4d$, where d is the specimen diameter. This is done so that the equivalent visco-elastic shear strain more closely corresponds to the best estimate of the true strain for the calculated stress according to various nonlinear stress-strain curves (e.g., Isenhowe et al. 1987).

Recalling that $\varphi(z, t) = \theta(z)e^{i\omega t}$ and where $\theta(z) = C_1 e^{iaz} + C_2 e^{-iaz}$, the representative shear strain at any cross-section of the sample is

$$\gamma_r(z, t) = 0.4d \cdot \frac{d\theta(z)}{dz} \cdot e^{i\omega t}. \quad (3.58)$$

Among other possible definitions, the average representative strain along the specimen may be obtained by integrating over the sample length;

$$\begin{aligned} \gamma_{r(avg)}(t) &= \frac{1}{h} \int_0^h \gamma_r(z, t) dz \\ &= 0.4d \cdot e^{i\omega t} \frac{1}{h} \int_0^h \frac{d\theta(z)}{dz} dz \\ &= 0.4d \frac{(\theta(h) - \theta(0))}{h} e^{i\omega t} \end{aligned} \quad (3.59)$$

where

$\theta(h) \cdot e^{i\omega t} = \varphi(h, t) = \varphi_p(t)$ is the measured motion of the passive-end platen and;

$\theta(0) \cdot e^{i\omega t} = \varphi(0, t) = \varphi_a(t)$ is the measured motion of the passive-end platen.

Therefore the shear strain in the time-domain can be expressed as

$$\gamma_{r(avg)}(t) = 0.4d \cdot \frac{\varphi_p(t) - \varphi_a(t)}{h} \quad (3.60)$$

Taking the Fourier transform of Eq. (3.60) gives the frequency spectrum of the average representative shear strain,

$$\tilde{\gamma}_{r(avg)}(f) = 0.4d \cdot \frac{\tilde{\varphi}_p(f) - \tilde{\varphi}_a(f)}{h} \quad (3.61)$$

In the modified RC tests, the soil specimen can be thought of as a single-input single-output system with $x(t)$ taken to be the active platen rotation $\varphi(0, t) = \varphi_a(t)$ and the output $y(t)$ taken to be the passive platen rotation $\varphi(h, t) = \varphi_p(t)$, for which transfer function is

$H(f) = \tilde{\varphi}_p(f) / \tilde{\varphi}_a(f)$. Measurement of such a transfer function by the dynamic signal analyzer would require first averaging the outputs of the two accelerometers on a given platen. However, the sensors have slightly different calibration factors, and an average calibration factor or summing circuit would need to be used for this approach. Alternatively, the soil sample may be thought of as a two-input/two-output system, with accelerometers 1 and 2 on the bottom platen giving two independent measurements of the input platen rotation, and likewise for accelerometers 3 and 4 on the top platen for output. Through the Fourier transforms,

$$\begin{aligned} X_1(f) &= \tilde{a}_1(f) = \int_{-\infty}^{\infty} a_1(t) \cdot e^{-i2\pi ft} dt \\ X_2(f) &= \tilde{a}_2(f) = \int_{-\infty}^{\infty} a_2(t) \cdot e^{-i2\pi ft} dt \\ Y_3(f) &= \tilde{a}_3(f) = \int_{-\infty}^{\infty} a_3(t) \cdot e^{-i2\pi ft} dt \\ Y_4(f) &= \tilde{a}_4(f) = \int_{-\infty}^{\infty} a_4(t) \cdot e^{-i2\pi ft} dt \end{aligned} \quad (3.62)$$

The auto-spectral and cross-spectral densities can be calculated as

$$\begin{aligned} G_{11}(f) &= X_1^*(f)X_1(f) = |X_1(f)|^2, & G_{13}(f) &= X_1^*(f)Y_3(f) \\ G_{22}(f) &= X_2^*(f)X_2(f) = |X_2(f)|^2, & G_{14}(f) &= X_1^*(f)Y_4(f) \\ & & G_{23}(f) &= X_2^*(f)Y_3(f) \\ & & G_{24}(f) &= X_2^*(f)Y_4(f) \end{aligned} \quad (3.63)$$

from which four independent transfer functions can be calculated, i.e.

$$H_{13}(f) = \frac{G_{13}(f)}{G_{11}(f)}; H_{14}(f) = \frac{G_{14}(f)}{G_{11}(f)}; H_{23}(f) = \frac{G_{23}(f)}{G_{22}(f)}; H_{24}(f) = \frac{G_{24}(f)}{G_{22}(f)} \quad (3.64)$$

The average transfer function is then calculated as

$$\bar{H}(f) = \frac{1}{4}(H_{13}(f) + H_{14}(f) + H_{23}(f) + H_{24}(f)) \quad (3.65)$$

giving a measure of the desired transfer function $H(f) = \tilde{\varphi}_p(f) / \tilde{\varphi}_a(f)$. This approach was shown in Ashlock and Pak (2010) to average out spurious peaks associated with bending modes, as would be expected were the two accelerations of each platen first averaged in the single-input/single-output approach. Here,

$$\bar{H}(f) = \frac{\tilde{a}_{top}(f)}{\tilde{a}_{bottom}(f)} = \frac{\tilde{a}_p(f)}{\tilde{a}_a(f)}. \quad (3.66)$$

Substituting Eqs. (3.54) and (3.55) into (3.66) gives

$$\bar{H}(f) = \frac{-\tilde{\varphi}_p(f) \cdot R_p \cdot (2\pi f)^2}{-\tilde{\varphi}_a(f) \cdot R_a \cdot (2\pi f)^2} = \frac{R_p}{R_a} \cdot \frac{\tilde{\varphi}_p(f)}{\tilde{\varphi}_a(f)} = \frac{R_p}{R_a} \cdot \frac{\tilde{\tilde{\varphi}}_p(f)}{\tilde{\tilde{\varphi}}_a(f)}. \quad (3.67)$$

If the accelerometers are mounted at the same distance $R_a = R_p$, then Eq. (3.67) reduces to

$$\bar{H}(f) = \frac{\tilde{\varphi}_p(f)}{\tilde{\varphi}_a(f)}. \quad (3.68)$$

Combining Eqs. (3.61) and (3.68) gives the ensemble average of the representative shear strain spectrum in terms of the input platen rotation and the transfer function as

$$\tilde{\gamma}_{r(avg)}(f) = 0.4d \frac{(\bar{H}(f) - 1)\tilde{\varphi}_a(f)}{h}. \quad (3.69)$$

The inverse Fourier transform of Eq. (3.69) will then give a representative time history of shear strain similar to Eq. (3.60), but representing an average among all time windows in the test. Equation (3.69) is useful for analyzing previous data for which the ensemble average transfer function was measured, as it requires only the Fourier transform of the bottom platen's tangential acceleration time history. For future tests in which the complete time histories of platen accelerations may be recorded, it may be more convenient to employ Eqs. (3.60) and (3.61) directly.

CHAPTER 4. SPECIMEN PREPARATION AND TEST PROCEDURES

4.1 Material

ASTM 20/30 test sand was primarily used in this research which is also known as “Ottawa Sand” originally from Ottawa, Illinois. It is a well-known material that has previously been studied by many researchers (e.g., Hardin and Richart, 1963; Drnevich and Richart, 1970). The particle size distribution curve of this material is shown in Figure 4.1. The Unified Soil Classification System (USCS) group symbol is SP, and the group name is poorly graded sand. The mineral is quartz, grain shape is round, specific gravity is $G_s=2.65$, maximum and minimum void ratios are $e_{max}=0.742$ and $e_{min}=0.502$, and air-dry moisture content of the material tested was $\omega=0.02\%$.

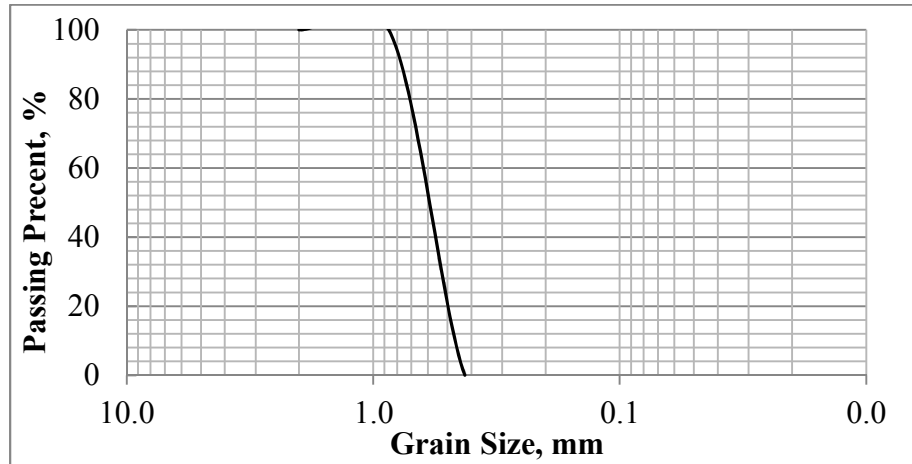


Figure 4.1: Particle size distribution curve of ASTM 20/30 test sand

From the grain size analysis, the coefficients of uniformity and gradation are obtained as

$$\begin{aligned}
 D_{60} &= 0.62\text{mm}, \quad D_{30} = 0.62\text{mm}, \quad D_{10} = 0.48\text{mm} \\
 C_u &= \frac{D_{60}}{D_{10}} = 1.29, \quad C_u = \frac{(D_{30})^2}{D_{10} \cdot D_{60}} = 0.91
 \end{aligned} \tag{4.1}$$

4.2 Specimen Preparation

The specimen preparation is a critical part of this research. To achieve a desired specimen with uniform density throughout requires extremely careful preparation. Based on the author's experience and the recommended specimen preparation procedures described in Makarechi (1981), the detailed procedures below were followed for specimen preparation (photos are attached in Appendix B):

1. Apply vacuum grease to the three O-rings on the base of the apparatus. Screw the bottom platen on the base plate.
2. Prepare the specimen mold and apply vacuum grease to seal the gaps between the two parts of the split mold.
3. Measure the inside diameter of the mold and the thickness of the membrane. The difference between the diameter of the mold and two times the thickness of the membrane is termed the “effective diameter- d_e ” of the specimen.
4. Put the mold on the bottom platen. Measure the inside height of the mold from the bottom platen to the potential position of the top platen. The height is termed “effective height- h_e ”.
5. The “effective volume- V_e ” of the mold can be calculated as

$$V_e = \pi \left(\frac{d_e}{2} \right)^2 \cdot h_e \quad (4.2)$$

6. Choose a certain relative density D_r to achieve the target consistency of the specimen (loose or dense). The corresponding void ratio e can be calculated by

$$e = e_{\max} - D_r (e_{\max} - e_{\min}) \quad (4.3)$$

and the corresponding moist density can be obtained as

$$\rho = \frac{(1 + \omega) G_s \rho_w}{1 + e} \quad (4.4)$$

A relationship between consistency of typical coarse-grained soil and relative density is shown in Table 4.1.

Table 4.1: Consistency of coarse-grained soil and relative density (adapted from Lambe and Whitman, 1969)

Relative Density, D_r (%)	Description
0 - 20	Very loose
20 - 40	Loose
40 - 70	Medium dense
70 - 85	Dense
85 - 100	Very dense

7. The required mass of soil to achieve the target consistency can be calculated as

$$M_{req} = \rho \cdot V_e \quad (4.5)$$

8. Thinly grease the side of the bottom platen. Place the membrane over the bottom platen. Put on the O-ring to seal the membrane on the bottom platen.
9. Place the mold on the bottom platen. Pull the membrane through the mold. Put a piece of filter paper between the membrane and mold at the position of the vacuum hole. Wrap the membrane around the top of the mold.
10. Apply vacuum to the mold so that the membrane sticks to the inner wall of the mold without any wrinkles (Note: If there is always a gap between the membrane and the inner wall, the membrane might have holes or the gaps between the two parts of the mold may not be sealed).
11. Put a piece of filter paper over the top of the bottom platen.
12. Weigh the required mass of soil. Pour the soil in the mold. In order to achieve the target relative density, deposit the soil uniformly in the mold. It is

recommended that a rubber mallet be used to gently tap the mold during pouring to densify the soil.

13. There might be some soil remaining or additional soil needed. Measure the actual mass M_{act} of soil used to make the specimen.
14. Level the specimen by rotating a blade at the top of the specimen.
15. Place the O-ring on the top platen. Apply a thin layer of vacuum grease to the side of the top platen.
16. Carefully place the top platen on the top of specimen. Place a leveling tool on the top platen to ensure that it is level.
17. Place the membrane on the top platen and seal it with the O-ring.
18. Apply a vacuum of 15 psi through the bottom hole to the specimen.
19. Carefully take apart the mold by removing the screws on the mold.
20. Measure the actual diameter d_{act} at three points along the specimen and the actual height h_{act} of the specimen to calculate the actual volume V_{act} .
21. The actual density of the specimen can be calculated by

$$\rho_{act} = \frac{M_{act}}{V_{act}} \quad (4.6)$$

22. Tighten the eight rods on the base of the apparatus.
23. Place the chamber over the specimen and the wires of the transducers and accelerometers.
24. Connect the transducers and accelerometers to the channels on the lid. Apply the vacuum grease to the O-ring on the lid. Place the lid on the apparatus. Carefully hand tighten the eight nuts until they just come in contact with the washers.

25. Use the torque wrench to tighten the nuts to a torque of 30 ft-lbs. Start with one nut and tighten it to 10 ft-lbs. Then move to the nut diametrically opposed and do the same. Next, come back to the first nut and move clockwise to the next nut and tighten it to 10 ft-lbs. Continue the process until the wrench has been placed on all the nuts twice. Use the same procedure to bring the torque in all of the nuts up to 30 ft-lbs. It may be necessary to place the wrench on each nut 3 or 4 times to achieve the desired 30 ft-lbs in each nut. (Drnevich, 1987)

4.3 Test Procedures

For the traditional RC tests, the test procedures are as follows:

1. Connect the electrical devices according to the traditional wiring connection diagram in Figure 2.4.
2. Apply the desired confining stress.
3. Turn on the multimeter to monitor the AC current. Be careful about whether it is displaying the units in peak or RMS or True RMS.
4. Turn on the function generator and select the sine wave form. Decrease the output amplitude to the minimum.
5. Turn on the power amplifier. Slowly increase the output level of Channel 1 on the amplifier. Meanwhile, slowly increase the output amplitude on the function generator. Monitor the multimeter to make sure the current does not exceed 5 Amps, and always ensure that a 5 Amp slow-blow fuse is placed between the amplifier and coils.

6. Adjust the frequency from low to high to find the second lowest frequency for which the velocity of the passive-end platen is 180° out of phase with the applied torque. At this type of resonant frequency, the Lissajous plot on the oscilloscope becomes to a straight line with negative slope.
7. At the resonant frequency, record the following items: a) multimeter reading, b) active geophone reading, c) passive geophone reading, d) the resonant frequency.

In the modified RC tests, the function generator and oscilloscope are replaced with a NI spectrum analyzer. A LabVIEW controlled program in the computer is used to record the data. The testing can begin according to the following procedures:

1. Connect electrical devices according to the modified RC testing wiring diagram in Figure 2.4.
2. Repeat steps 2 and 3 of the traditional RC test procedures.
3. Turn on the amplifier. Increase the output level of Channel 1 to a desired level. Monitor the multimeter to make sure the current is less than 5 Amps.
4. Select a desired waveform in the LabVIEW controlled program. Start the program and record the data.

CHAPTER 5. EXPERIMENTAL RESULTS

The experimental results are presented in this chapter. First, past test data will be analyzed to give an illustration of the transfer function peak fitting approach and strain calculations. These tests were done using the Drenvich free-free type resonant column apparatus at the University of Colorado at Denver (Ashlock and Pak, 2010). Furthermore, a calibration rod was tested using the transfer function approach with the new RC device at ISU to verify the device feasibility by determination of the shear modulus and damping ratio of the steel rod. Finally, several tests were performed at Iowa State University using the material described in Chapter 4. Both the transfer function approach and ASTM method were used to evaluate the same specimen at various confining pressures. Comparisons of experimental results between two methods will be presented in the ensuing sections.

5.1 Modified RC Tests at the University of Colorado at Denver

In the tests from Ashlock and Pak (2010), a large sample of dry F-75 silica sand was tested under small-strain vibration at different confining pressures. The properties of the specimen and apparatus are summarized in Table 5.1.

Table 5.1: Specimen and apparatus properties of previous RC tests at University of Colorado at Denver

Specimen Properties						Apparatus Properties
Specific Gravity	Void Ratio	Relative Density	Diameter [m]	Height [m]	Density [kg/m ³]	Passive Platen Rotational Inertia [kg·m ²]
2.65	0.552	79.60%	0.1532	0.3152	1707.13	0.00356

An ensemble average transfer function was calculated using 30 transfer function measurements with a 0.8 second time window each (see Figure 5.1). This procedure minimizes effects of random error and improves the quality of the transfer and coherence

functions (see Figure 5.2). The magnitudes of experimental rotational transfer functions at different confining pressures are shown in Figure 5.3. Four peaks can clearly be seen in the experimental transfer function curves at confining pressure of 68.9, 137.9, 206.8, 275.8 and 344.7 kPa (10, 20, 30, 40 and 50 psi). The peaks are moving to the left as the confining pressure decreases, and an additional peak appears at the lowest confining pressure of 69.8 kPa (10 psi).

In order to calculate the shear modulus and damping ratio of the specimen, the theoretical rotational transfer function Eq. (3.33) was fit to the experimental curves. As described in Chapter 3, the damping ratio primarily controls the peak amplitude, while modulus primarily controls peak frequencies. Therefore, a hysteretic damping ratio was first assumed as $\xi(\omega) = \xi_0 = 2.0\%$ to determine the shear modulus that matched the frequency of each peak. The agreement between experimental and theoretical transfer function curves was then qualitatively evaluated by adjusting the damping and shear modulus. For example, at a confining pressure of 69.8 kPa (10 psi), the theoretical transfer function that fit the second peak of the experimental curve is presented in Figure 5.4. The remaining of peaks were also fit individually following the same procedure. The magnitudes of theoretical and experimental transfer functions for fitting the five peaks independently are shown in Figure 5.5.

If the accelerometers signals are noisy, there can be many unexpected peaks on the experimental transfer function curve. The results would thus be inaccurate if the theoretical transfer functions were calculated by only fitting the apparent peaks. Due to this shortcoming of the "peak only" fitting method, a "squared-error" fitting method was used in this study to find the best-fitting curve. This method was used to fit the ± 50 frequency points

around peak, which tends to fit the overall shape of the peak rather than fitting only a noise spike in the data. Because the transfer functions are complex valued, the least-squares method was programmed to fit both the imaginary and real parts. An error measure that depends on the shear modulus and damping was formulated as

$$Error = \sum_{i=1}^n \sqrt{\left[\text{Re}(H_{\text{exp}}) - \text{Re}(H_{\text{the}}) \right]^2 + \left[\text{Im}(H_{\text{exp}}) - \text{Im}(H_{\text{the}}) \right]^2} \quad (5.1)$$

where

H_{exp} is the experimental rotational transfer function;

H_{the} is the theoretical rotational transfer function.

A surface of this error function can be plotted against shear modulus and damping for each peak, as shown in Figure 5.6 and Figure 5.7. The lowest point on the surface having the minimum error was selected as the optimum shear modulus and damping ratio for each peak. The theoretical transfer functions using the “squared-error” fitting method were plotted to compare with the “peak only” fitting method as shown in Figure 5.8. From the plots, it can be seen that the “squared-error” curves more accurately match the experimental curves. The results of two methods are presented in Table 5.2.

Table 5.2: Results of shear modulus and damping ratio at each peak using “peak only” fitting method and “squared-error” fitting method (confining pressure 69.8 kPa).

		1 st Peak	2 nd Peak	3 rd Peak	4 th Peak	5 th Peak
“Peak only” fitting method	G [MPa]	110.0	108.1	107.7	109.4	110.0
	D [%]	3.0	0.4	0.8	0.4	0.5
“Squared-error” fitting method	G [MPa]	112.9	108.0	108.3	109.2	109.7
	D [%]	1.8	0.4	0.9	0.4	0.5

For dynamic signal analyzers used in the past tests, the averaged spectral quantities (transfer function, coherence, cross- and auto-spectral densities) are saved along with only the final time history. If one calculates the strain using past test data for which only 1 of 30 time histories was stored, then the resulting strain spectrum will be relatively noisy as it will correspond to a single ensemble average. If the inverse Fourier transform is then taken, the resulting strain time history will correspond to a single time window and will also be noisy. Alternatively, one can re-sample the single time-history by dividing it up into smaller time windows, with the tradeoff of a loss of resolution. For example, the original 0.8 second window with 4,096 data points gives one spectral average with 1,600 data points between 0 and 2 kHz. However, this time window may be considered as four-0.2 second windows each having 1,024 samples in the time domain (see Figure 5.9) and giving four spectral measurements with 400 data points between 0 and 2 kHz in the frequency domain. The experimental rotational transfer functions of each window can be calculated and shown in Figure 5.10. In this case with four-0.2 second windows, one could calculate an ensemble average of the strain spectrum Eq. (3.61), which could be inverted to obtain a single representative 0.2 second time-history. The strain spectrum of averaged 4 Hanning windows can be plotted in the frequency-domain as shown in Figure 5.11. The averaged 4 strain spectrum is less noisy as compared with only 1 Hanning window (see Figure 5.12). Alternatively, Eq. (3.60) could be used to obtain the strain history for the entire 24 second test duration, i.e. for all 30 time windows. If all 30 of the individual windowed Fourier transforms were saved for each accelerometer, Eq. (3.61) could similarly be used to obtain the ensemble average strain spectrum. For processing past test data in which only the ensemble average transfer function $H(f)$ was saved, it will be useful to relate the shear strain

spectrum of Eq. (3.61) to the transfer function and the other saved quantities. To enable additional uses of the test data such as given in Eqs. (3.60) and (3.61), it is recommended that the complete time histories and ensemble-averaged Fourier transforms of all four accelerometer channels be saved in future tests.

At each peak frequency of the experimental transfer function, the associated strain magnitude can be found from the strain spectrum plot. By allowing each peak to be fit individually using different values of modulus and damping, while recognizing that each peak may have a different strain magnitude, it may be possible to obtain multiple points on the modulus and damping curves from a single transfer function test. To examine this hypothesis, the shear modulus and damping ratio each strain magnitude are shown for a representative test in Figure 5.13. The theoretical nonlinear strain-dependent modulus and damping curves from previous studies (e.g., Hardin and Drnevich, 1972) typically exhibit the behavior

$$G = \frac{G_{\max}}{1 + \gamma_h} \quad (5.2)$$

and

$$\xi = \frac{\gamma_h}{1 + \gamma_h} \cdot \xi_{\max} \quad (5.3)$$

where

G_{\max} is the maximum shear modulus [MPa];

ξ_{\max} is the maximum damping ratio [%];

$\gamma_h = \gamma / \gamma_r$ is the hyperbolic shear strain and;

γ_r is the referenced shear strain.

These shear modulus and damping ratio versus strain relationships exhibit the following well-known behavior:

1. The shear modulus G decreases with increasing shear strain. At a very low strain level, the magnitude of the shear modulus reaches a maximum (G_{max}).
2. The damping ratio ζ increases with increasing level of shear strain.

To examine whether the data points obtained by individually fitting each of the five resonant peaks with follow such behavior, best-fit curves for Eqs. (5.2) and (5.3) were determined and plotted with the data in Figure 5.13. At this point, the smooth curves are not intended to be interpreted as measured modulus and damping curves, but are used as benchmarks of expected behavior against which to compare results of the transfer function approach.

Because the strain level was very small for the past tests of Ashlock and Pak (2010), the shear modulus and damping versus strain relationship shows only has a slight variation, and the tests primarily focus on G_{max} . To explore the transfer function RC testing approach for obtaining nonlinear strain dependent modulus and damping curves, new tests were performed in this study with higher excitation levels using random and swept-sine waveforms, as the latter can produce higher strains.

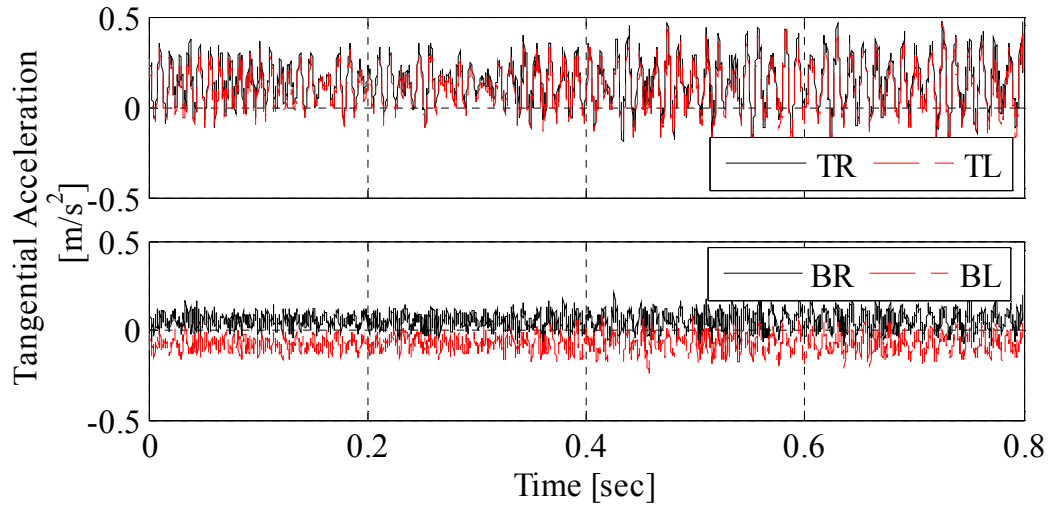


Figure 5.1: Representative 0.8 second time-history of end platen tangential accelerations (confining pressure 69.8 kPa). TR: top right, TL: top left, BR: bottom right, BL: bottom left. Modified from Ashlock and Pak (2010).

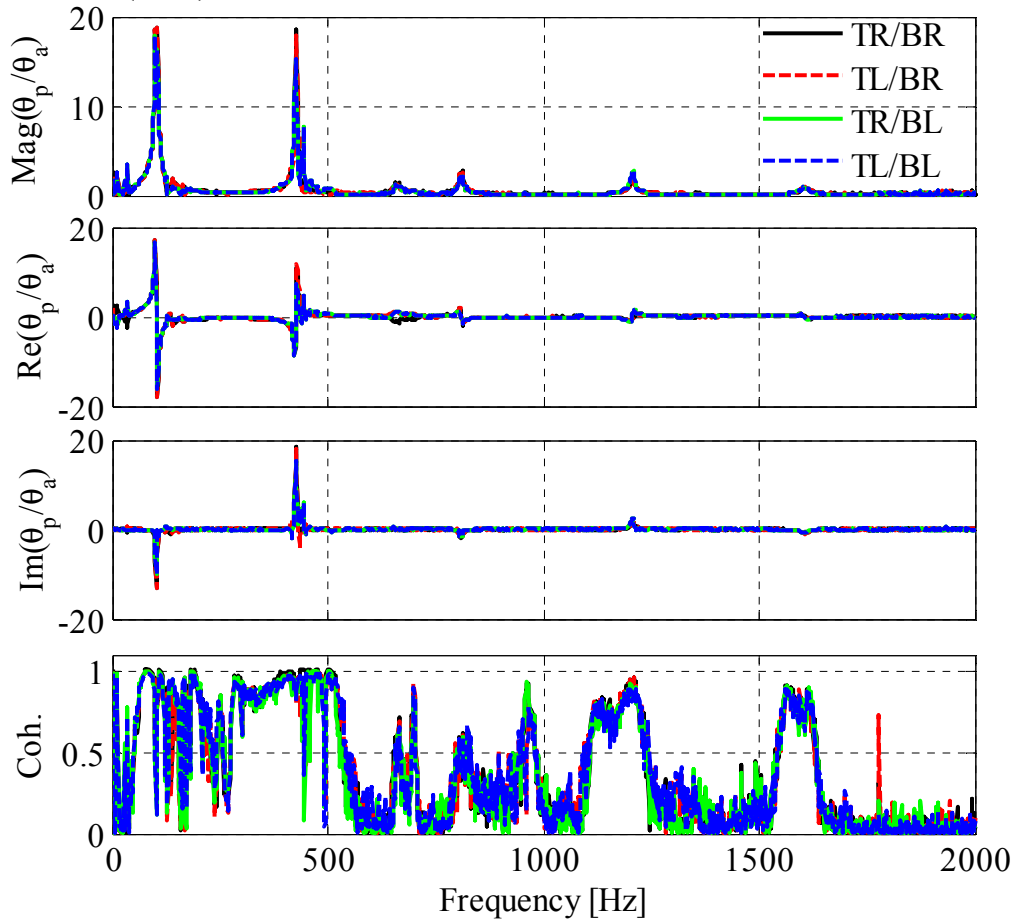


Figure 5.2: Experimental rotational transfer and coherence functions (confining pressure 69.8 kPa). Modified from Ashlock and Pak (2010).

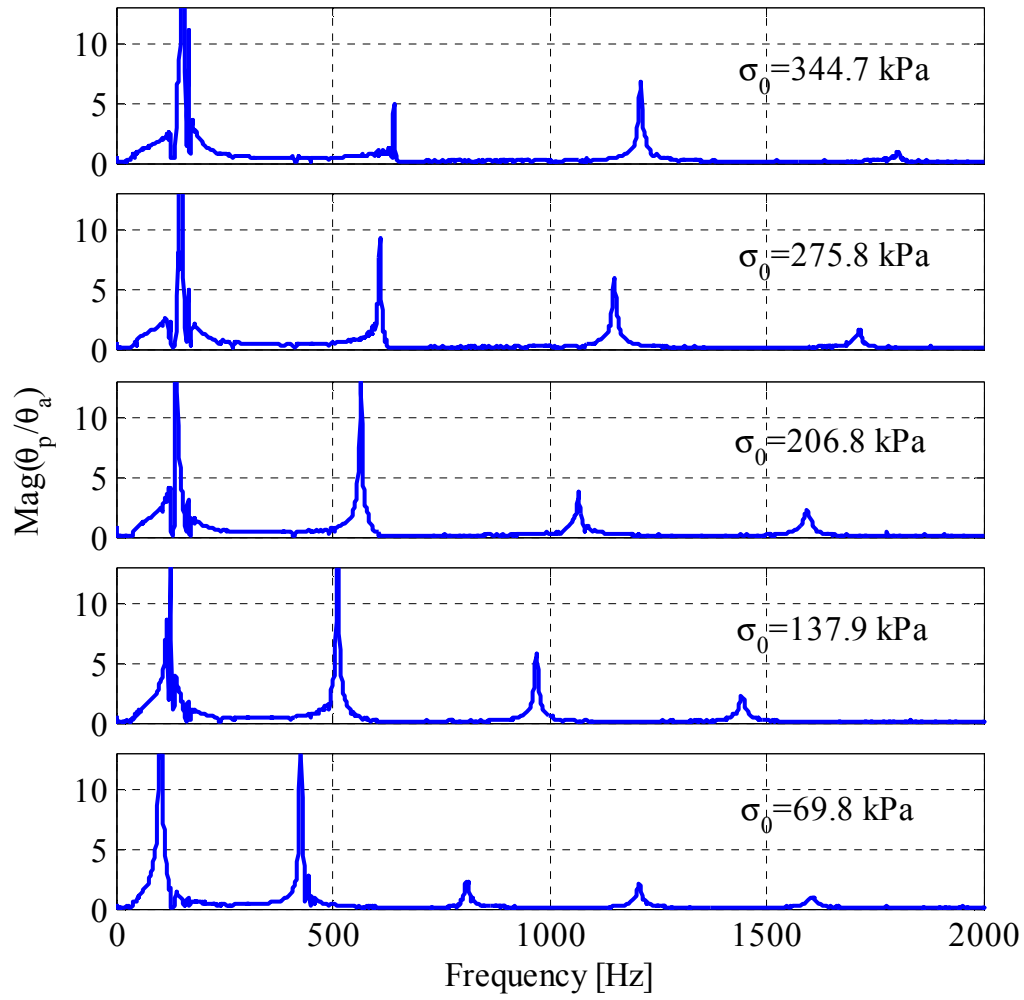


Figure 5.3: Experimental rotational transfer functions at different confining pressure. Modified from Ashlock and Pak (2010).

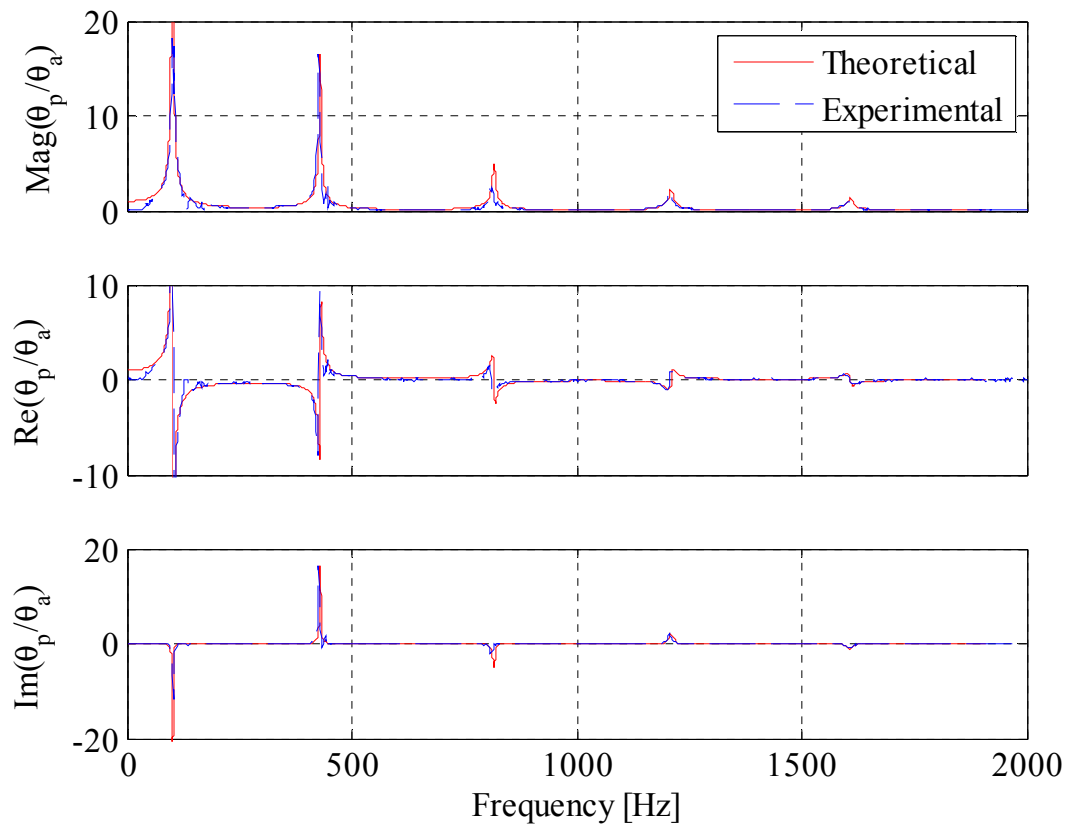


Figure 5.4: Theoretical and experimental transfer functions fit to 2nd peak (confining pressure 69.8 kPa). Modified from Ashlock and Pak (2010).

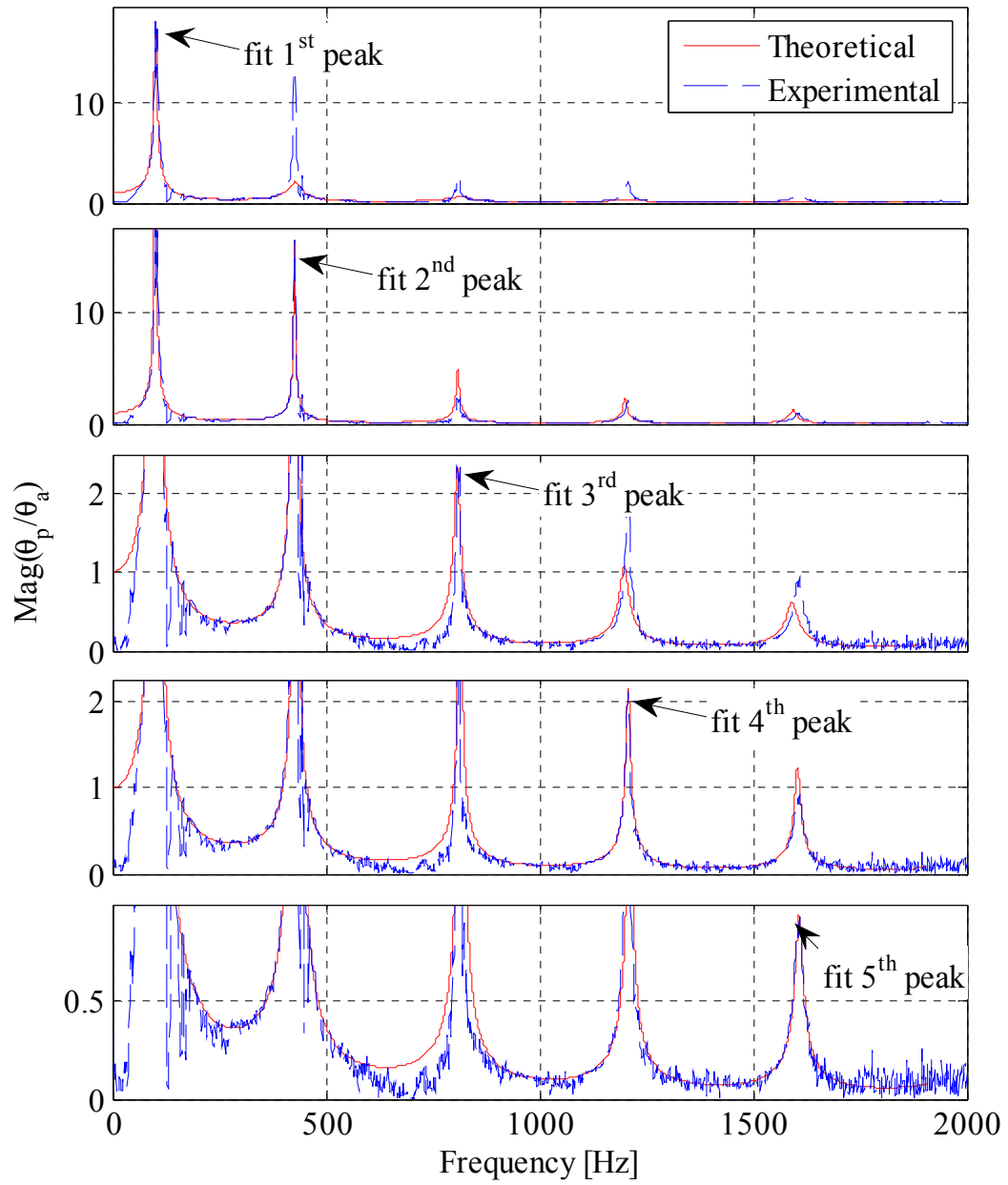


Figure 5.5: Magnitude of theoretical and experimental transfer functions by “peak only” fitting approach (confining pressure 69.8 kPa).

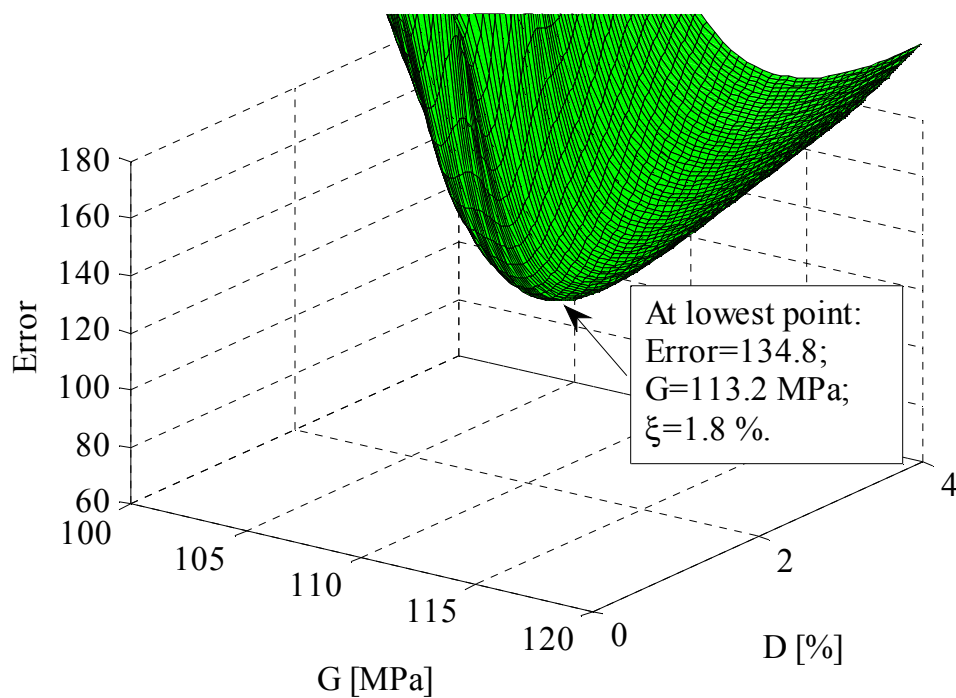


Figure 5.6: Surface plots of error function for “squared-error” fitting 1st peak (confining pressure 69.8 kPa).

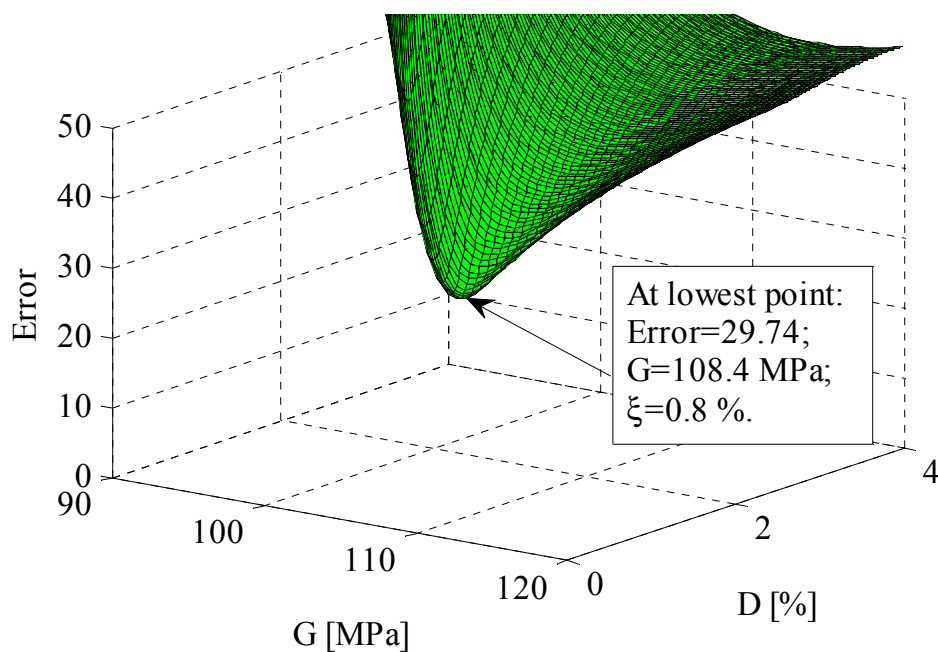


Figure 5.7: Surface plots of error function for “squared-error” fitting 3rd peak (confining pressure 69.8 kPa).

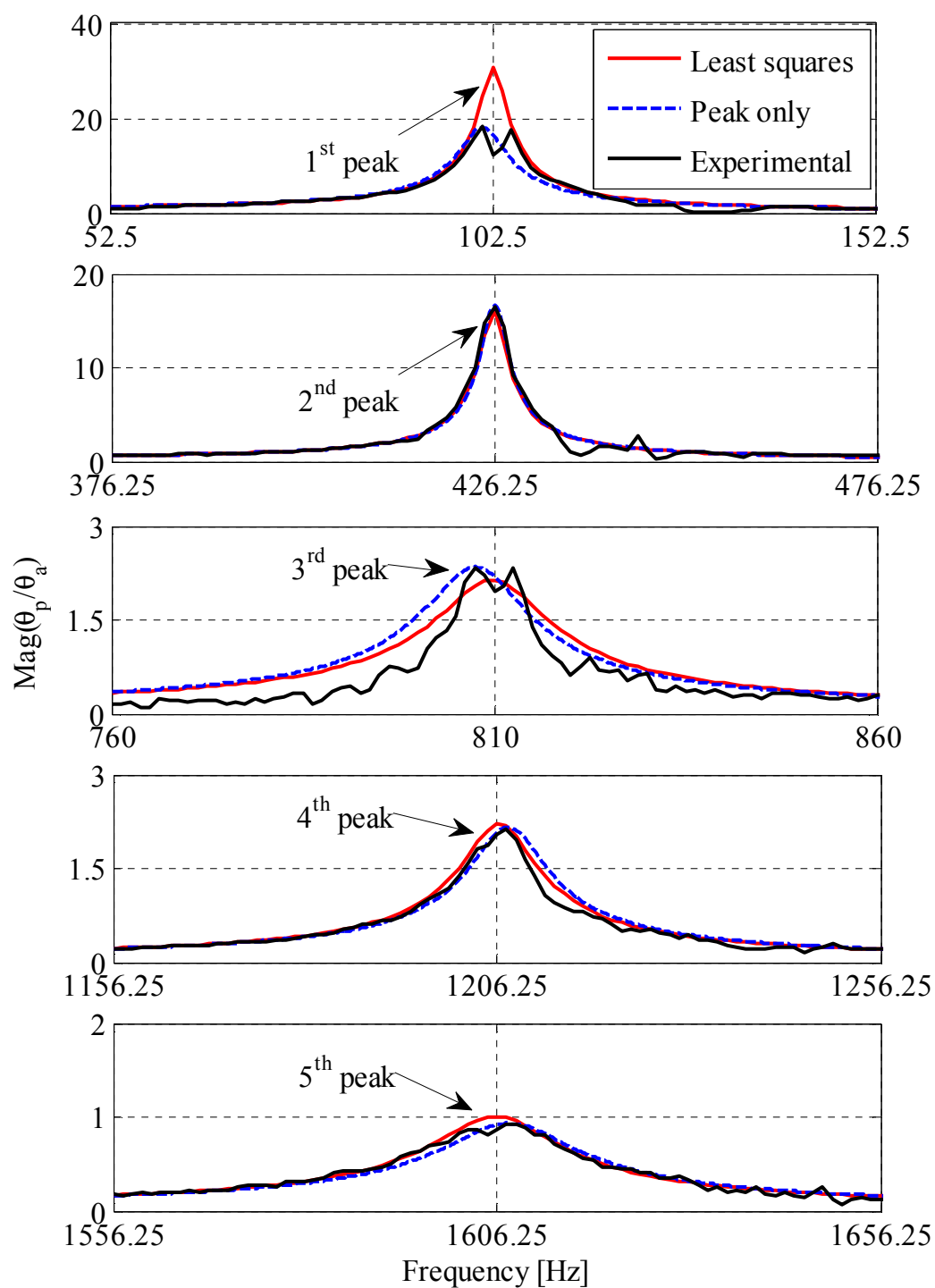


Figure 5.8: Comparisons between “squared-error” fitting and “peak only” fitting methods (confining pressure 69.8 kPa).

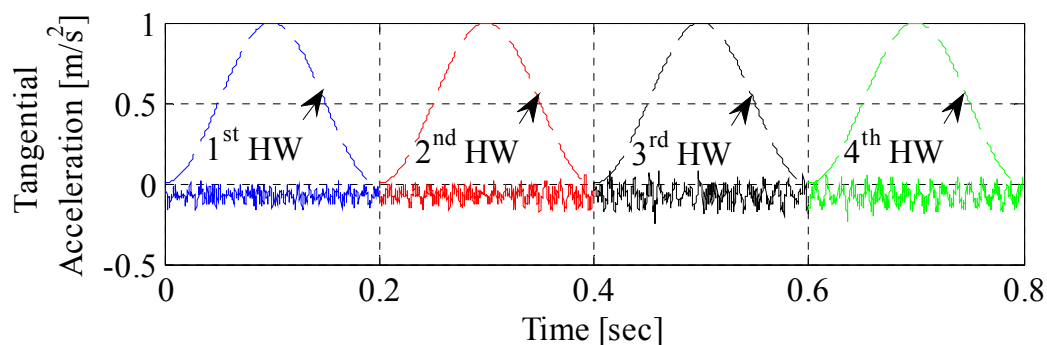


Figure 5.9: Accelerometer time histories divided into four 0.2 second windows with applied Hanning windows for taking the FFT.

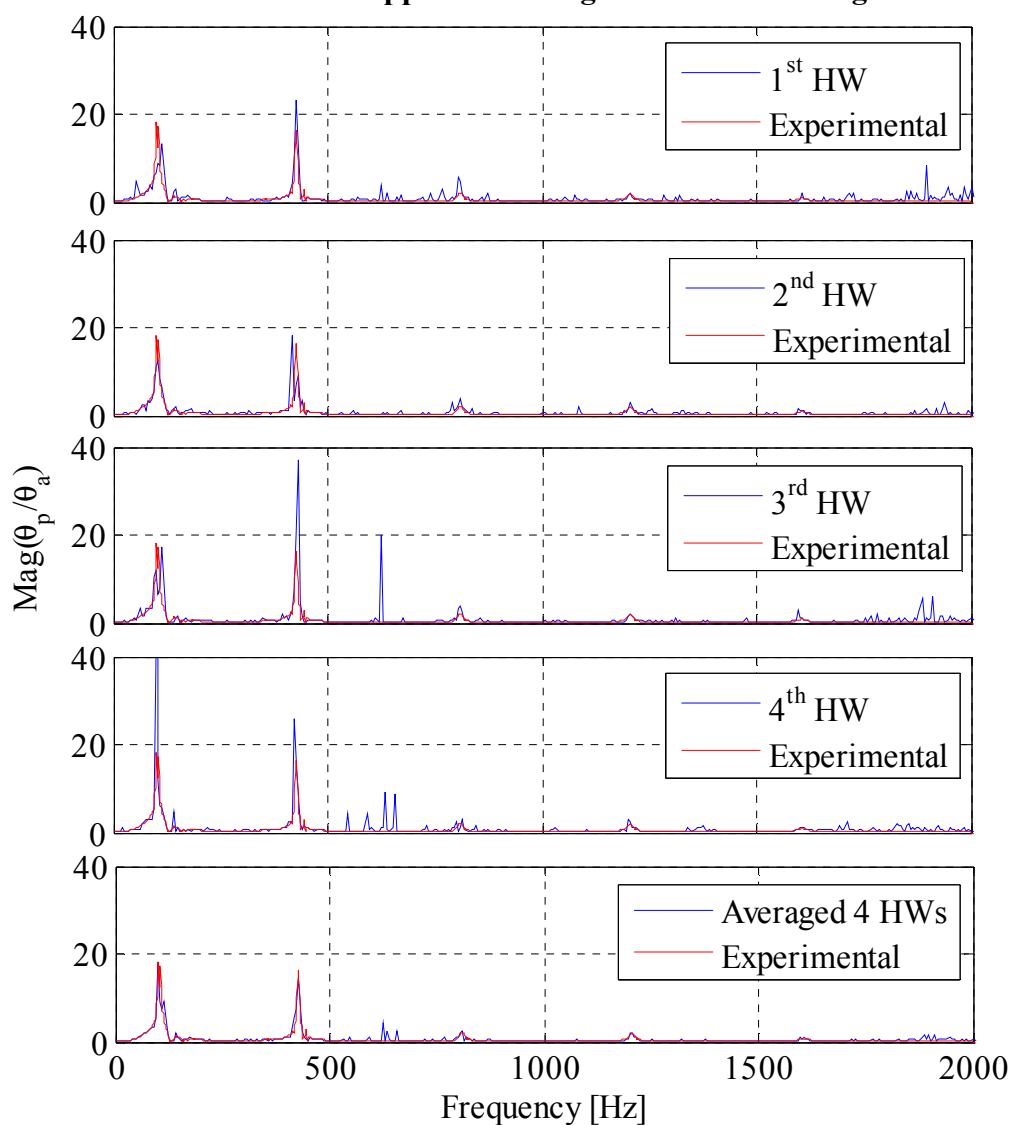


Figure 5.10: Experimental rotational transfer functions of four 0.2 second windows compared to experimental transfer function averaged from thirty 0.8 second windows.

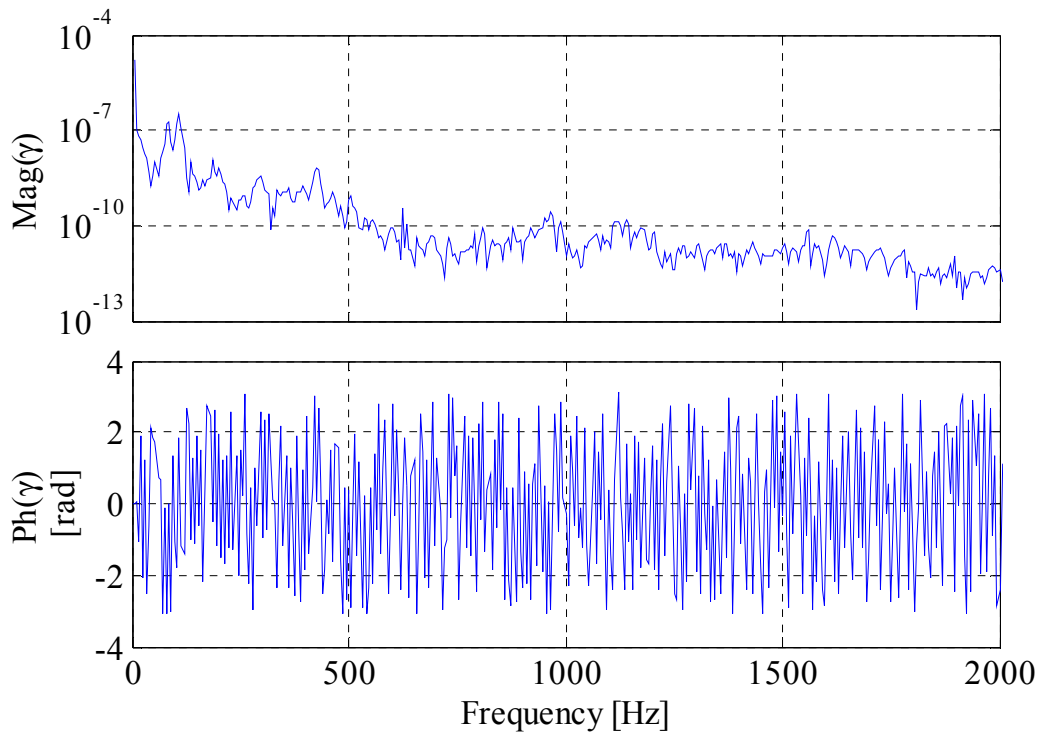


Figure 5.11: Strain spectrum (0-2000 Hz) of averaged 4 Hanning windows (confining pressure 69.8 kPa).

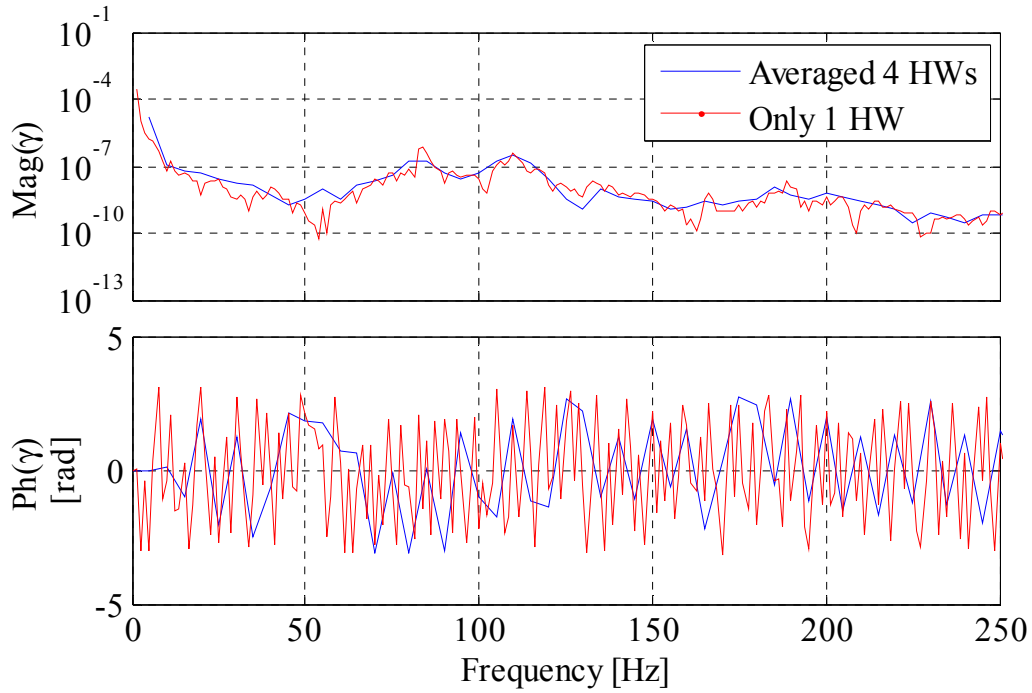


Figure 5.12: Strain spectrum (0-250 Hz) of averaged 4 Hanning windows vs. 1 Hanning window (confining pressure 69.8 kPa).

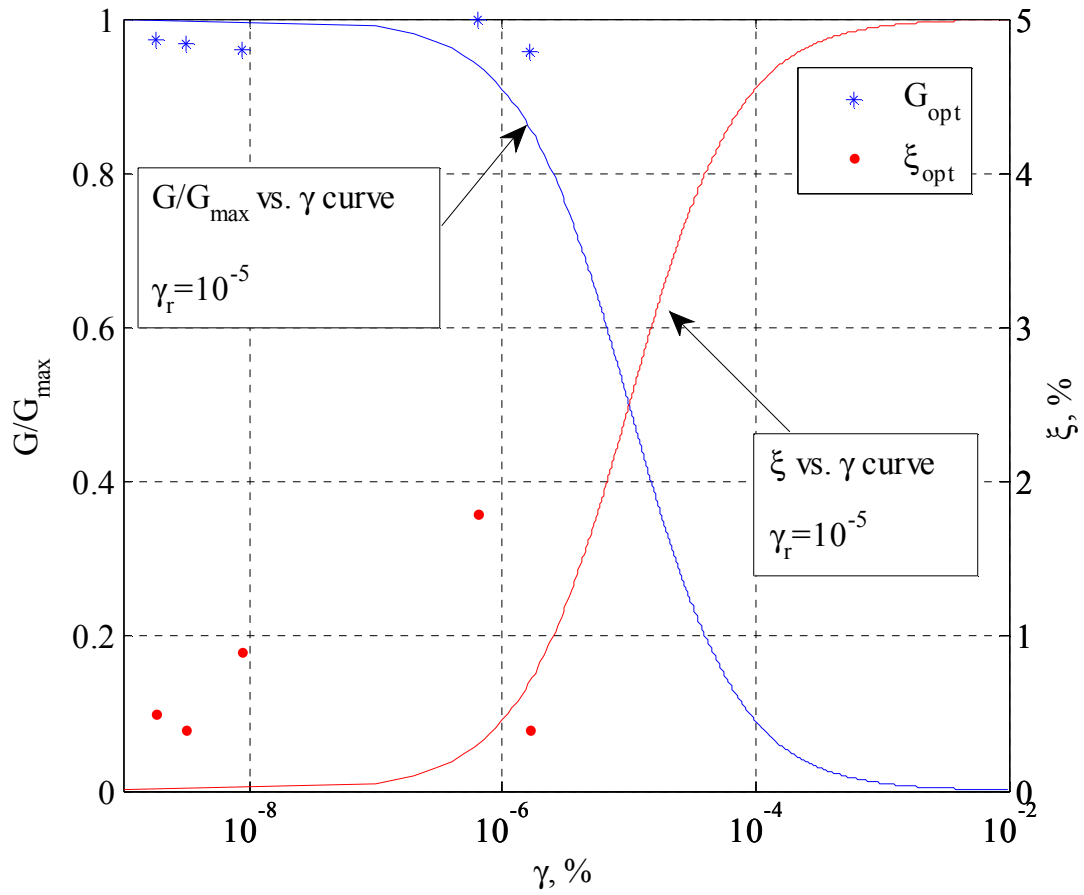


Figure 5.13: Nonlinear strain-dependent modulus and damping curves obtained by fitting five peaks from a single test (confining pressure 69.8 kPa).

5.2 Calibration Rod Using Transfer Function Approach and ASTM Method

A calibration rod with known shear modulus and damping ratio was tested using the transfer function approach and ASTM method. The purposes of this test are to verify the device calibrations and check the feasibility of the transfer function approach.

The calibration rod was permanently fastened by welding into two 4 inches platens. The actual height was measured as the distance between weld fillets on the rod. The properties of the calibration rod are presented in Table 5.3. As the rotational transfer function of the calibration rod only has a single peak in a frequency range of 20-60 Hz, the measurement quality was improved by only testing over a frequency range of 0-250 Hz. Both random excitation and swept-sine waveforms were employed to measure the rod's transfer function using the accelerometers. Different excitation levels were varied to obtain the transfer function with the best coherence (see Figure 5.14). The "peak only" fitting approach was used to determine the experimental value of shear modulus and damping ratio. The measured shear modulus and damping ratio were 83.0 GPa and 0.5 %. Compared to the assumed values of $G \approx 79.3$ GPa and $D \approx 2.0\%$, the shear modulus is within 4.7 % and the damping ratio is within a reasonable range given the difficulty of measuring small values of damping. The differences may be caused by the weld fillets at the rod ends, which affects the free length and fixity of the rod. These findings indicate that the transfer function approach can produce acceptable results for experimental determination of modulus and damping for soil specimens.

Table 5.3: Measured properties of calibration rod by transfer function approach.

Material	Diameter [m]	Height [m]	Density [kg/m ³]	Rotational Inertia [kg·m ²]	Shear Modulus [GPa]	Damping Ratio [%]
C.R. steel	0.0127	0.2972	7300	5.9×10 ⁻⁶	83.0	0.5

For the ASTM approach, a sine wave was produced by the wave function generator as the excitation waveform. The 1st resonant frequency of the calibration rod was measured as 39.5 Hz using the Lissajous plot of passive geophone velocity versus torque. In ASTM D4015-07 for the free-free device, it is recommended to use the second lowest frequency for which the passive rotational velocity is 180° out of phase with the applied torque, because it produces significant strains in the testing specimen. However, in the actual test of calibration rod, this resonant frequency could not be found. In order to verify the resonant frequency of the calibration rod, a theoretical rotational velocity/torque transfer function was instead plotted as shown in Figure 5.15. The shear modulus and damping ratio of the rod was assumed using the results of the transfer function approach (i.e. $G=83.0$ GPa and $D=0.5\%$). From the plot, there is only one peak at 39.68 Hz which is very close to the measured resonant frequency of 39.5 Hz. Therefore, in contrast to the recommendation in ASTM D4015-07, it was determined that the measured 1st resonant frequency should be reasonable to use. The shear modulus of the rod can be calculated using the ASTM method with this 1st resonant frequency as follows.

The active end inertia factor (T) introduced in Eq. (3.23) can be calculated for the rod with rotational mass moment of inertia J as

$$T = \frac{J_a}{J_s} \left[1 - (f_{0T} / f_T)^2 \right] \quad (5.4)$$

where

$f_{0T} = \sqrt{k_{st} / J_a} / (2\pi)$ is the apparatus calibration resonant frequency [Hz] (for this case,

$f_{0T} = 61.9 \text{ Hz}$ see Table 2.1);

f_T is the measured system resonant frequency [Hz] with the specimen in place (for this case,

$f_T = 39.5 \text{ Hz}$).

The passive inertia ratio P (sometimes referred to \bar{J} in the transfer function derivations) is given by

$$P = \frac{J_p}{J} \quad (5.5)$$

The dimensionless frequency F (also known as $\bar{\omega}$) can be calculated from the ASTM FORTRAN program or approximated by (see Drnevich, 1978)

$$F = \sqrt{12(-BD2A^2 - CC / AA)} \quad (5.6)$$

where

$$AA = -48 \times T \times P - 7 \times (T + P) - 1;$$

$$BB = 48 \times T \times P + 20 \times (T + P) + 5;$$

$$CC = -4 \times (T + P) - 4;$$

$$BD2A = BB / (2 \times AA).$$

and the shear modulus (G) can then be calculated as

$$G = \rho(2\pi h)^2 (f_T / F) \quad (5.7)$$

The results of the calculation using the ASTM method are summarized in Table 5.4.

Comparing the results of the ASTM method with the transfer function approach, the shear modulus of the steel calibration rod has only a 0.12% difference. The shear moduli of two approaches are very close to the theoretical steel shear modulus.

Table 5.4: Shear modulus of calibration rod using ASTM test method.

Passive Inertia Ratio	Active Inertia Factor	Frequency Factor	Shear Modulus [GPa]
2.07×10^3	-2.04×10^5	0.0219	83.10

Another more accurate calculation for F , G and D was performed using a modified version of the spreadsheet RCDARE written by Dr. Drenvich for the RC/quasi-static torsional shear apparatus at Purdue University. The original spreadsheet was revised to adapt to the 2DOF free-free RC device at ISU. Detailed information on the modifications to RCDARE are discussed in Appendix D. The results from the RCDARE calculations are presented in Table 5.5. The results using RCDARE are very close to the transfer function approach and theoretical results, although the damping is only 0.26% for the RDCARE approach. These results indicate that two approaches can be used for the data reduction of RC tests and the apparatus calibrations can be considered to be correct.

Table 5.5: The damping ratio of calibration rod using ASTM method.

Current Reading [A_{rms}]	Active Geophone Output [V_{pk}]	Passive Geophone Output [V_{pk}]	Shear Modulus [GPa]	Damping Ratio [%]
0.59	0.0551	3.6743	78.10	0.26

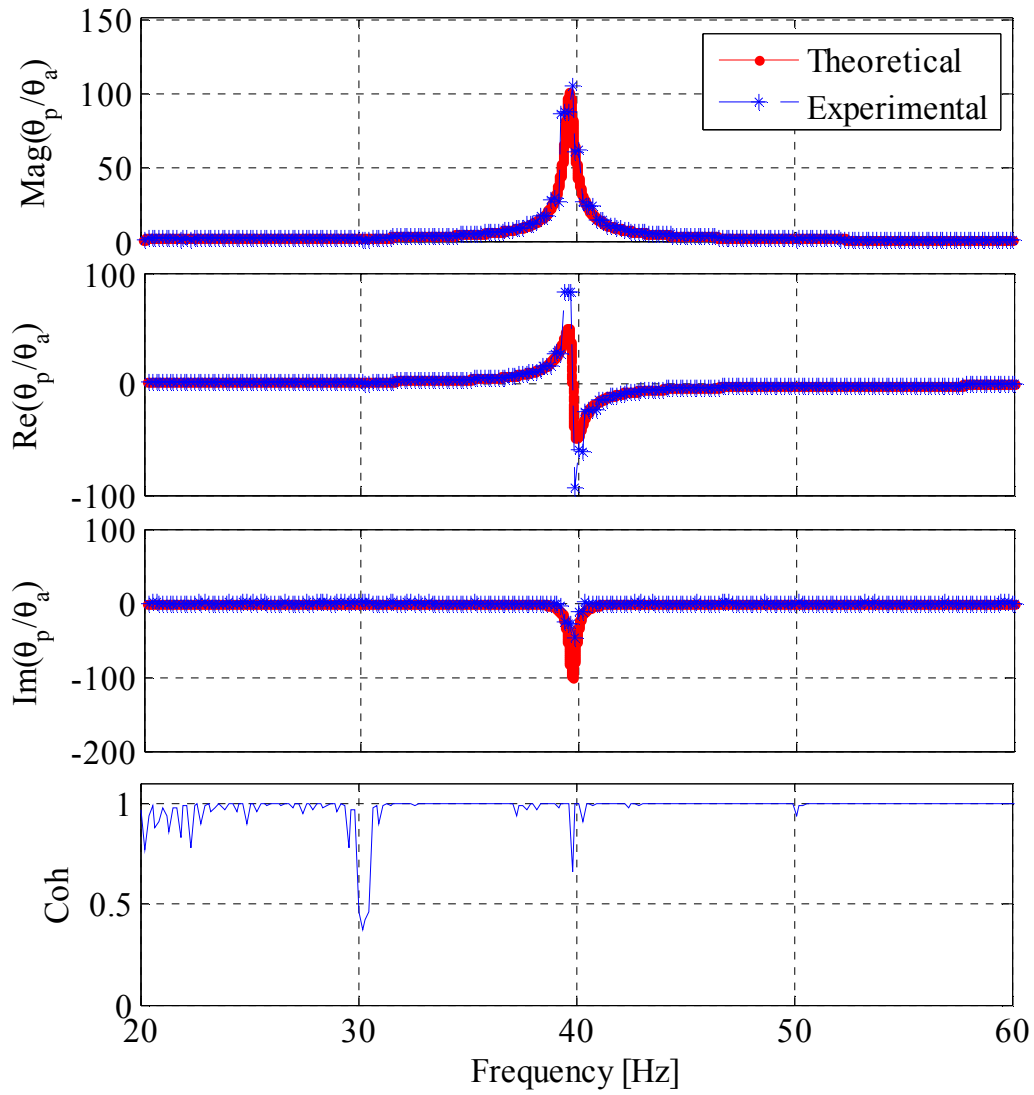


Figure 5.14: Rotational transfer function and coherence of the calibration rod (bandwidth 0-250 Hz; swept-sine waveform; oscillate OFF; F_{start} =250 Hz; F_{end} =5 Hz).

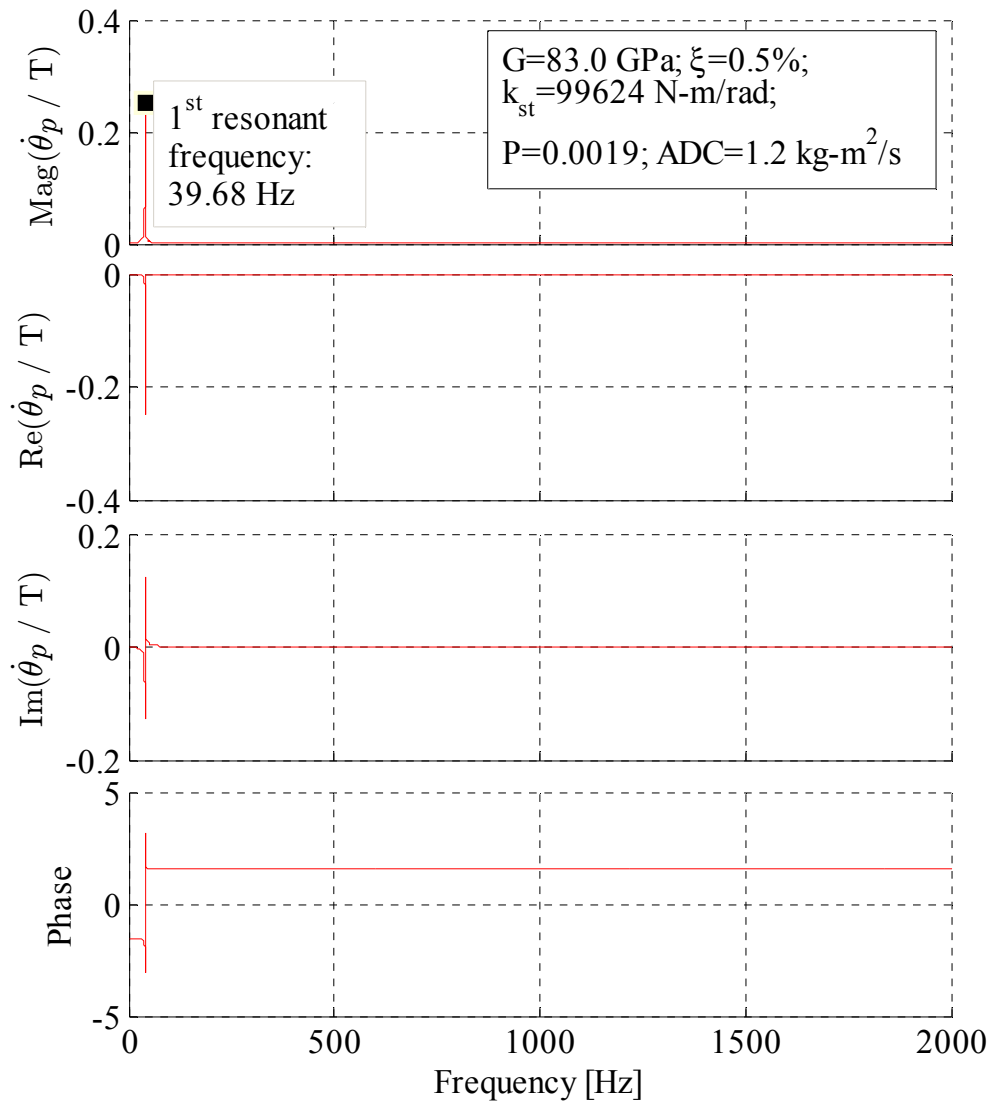


Figure 5.15: Theoretical rotational velocity/torque transfer function of the calibration rod.

5.3 RC Tests at Iowa State University

Several RC tests of Ottawa 20/30 sand were tested using the transfer function approach and ASTM method with the new device at Iowa State University. The properties of the specimen were previously described in Chapter 4. A large sample with 152.4 mm (6.0 inch) diameter and 355.6 mm (14.0 inch) height was first tested to verify the functionality of the new RC device and DAQ system. To achieve higher shear strains, a 71.1 mm (2.8 inch) diameter and 152.4 mm (6.0 inch) height sample was tested using the swept-sine excitation. Finally, a 71.1 mm (2.8 inch) diameter and 283.6 mm (11.2 inch) specimen was tested using both the transfer function approach and ASTM method to determine the feasibility of measuring shear-strain dependent modulus and damping curves of soil specimens by the transfer function approach. Results of the two approaches are compared and discussed in the following sections.

5.3.1 Tests on 6.0 inch diameter specimen using transfer function approach

First, a large specimen of concrete sand with 152.4 mm (6.0 inch) diameter and 355.6 mm (14 inch) height was tested using swept-sine excitation. The time-histories of input signals were recorded and digitized using 4,096 samples in the time-domain. A sampling bandwidth of 2,000 Hz was selected resulting in a sampling rate of 5,120 Hz and frequency resolution of 1.25 Hz. Thirty spectral measurements were averaged to minimize the experimental noise. As recommended from the analysis of the previous tests at the University of Colorado at Denver, the complete 30 time histories and ensemble-averaged Fourier transforms of all four accelerometer channels were saved in the new tests. The complete accelerometer time-histories are shown in Figure 5.16. The auto-spectral densities

G_{xx} and G_{yy} and cross-spectral densities G_{xy} were calculated using Eqs. (3.43) and (3.44). The transfer function of each window was calculated using Eq. (3.45). The averaged magnitudes of 30 rotational transfer functions are shown in Figure 5.17. As shown in the plot, the transfer function with 30 spectral averages is less noisy than the individual spectral measurements. The “peak only” and “squared-error” fitting methods were then used to fit the five peaks as shown in Figure 5.18 and Figure 5.19. Results of the two methods are summarized in Table 5.6. The averaged strain spectrum from 30 spectral measurements is shown in terms of magnitude and phase in Figure 5.20. The strain magnitude of the 1st peak is around 10^{-5} %. The shear modulus and damping ratio corresponding to each peak strain magnitude are plotted in Figure 5.21. As can be seen from the figure, the strain level is still very small, and only a small portion of the nonlinear strain-dependent modulus and damping curves were obtained. Therefore, a smaller diameter sample was tested in order to achieve higher strains for measuring nonlinear strain-dependent modulus and damping curves.

Table 5.6: Results of shear modulus and damping ratio at each peak using “peak only” fitting method and “squared-error” fitting method (ISU 6” specimen at 69.8 kPa confining pressure).

		1 st Peak	2 nd Peak	3 rd Peak	4 th Peak	5 th Peak
“Peak only” fitting method	G [MPa]	203.1	204.7	209.6	209.9	213.0
	D [%]	2.3	1.4	1.4	1.0	1.8
“Squared-error” fitting method	G [MPa]	223.0	204.7	203.0	202.3	223.0
	D [%]	3.6	1.8	1.5	1.7	4.0

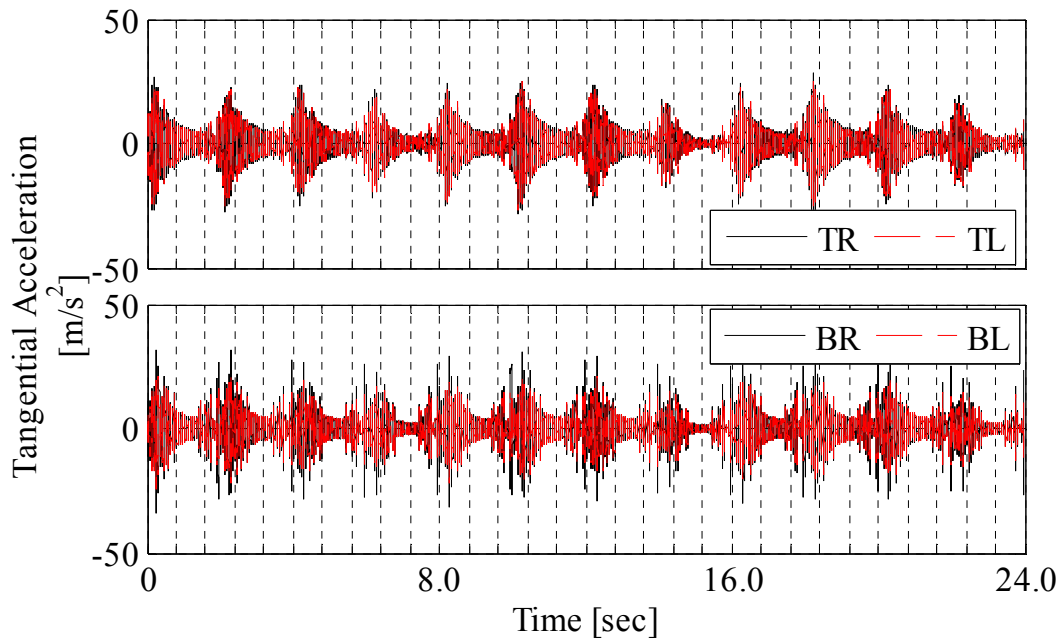


Figure 5.16: Complete time-histories under swept-sine vibration with oscillate ON; $F_{start}=2000$ Hz and $F_{end}=0$ Hz (ISU 6" specimen at 69.8 kPa confining pressure).

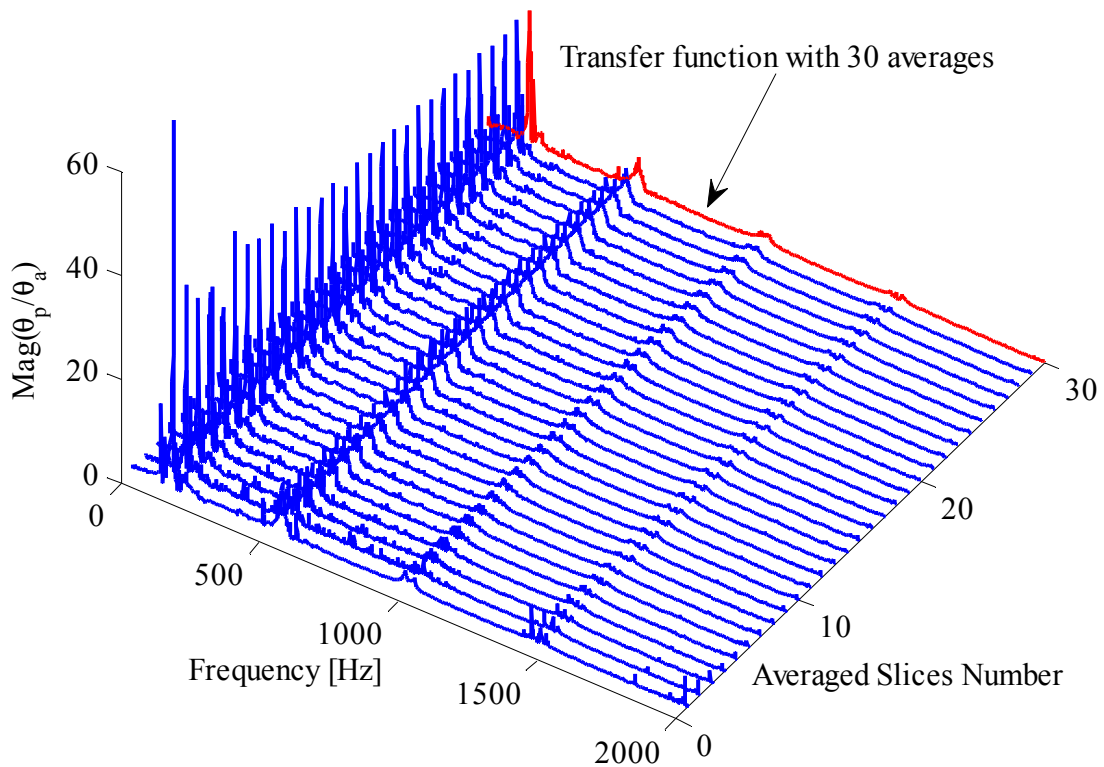


Figure 5.17: Experimental transfer functions vs. number of averages (ISU 6" specimen at 69.8 kPa confining pressure).

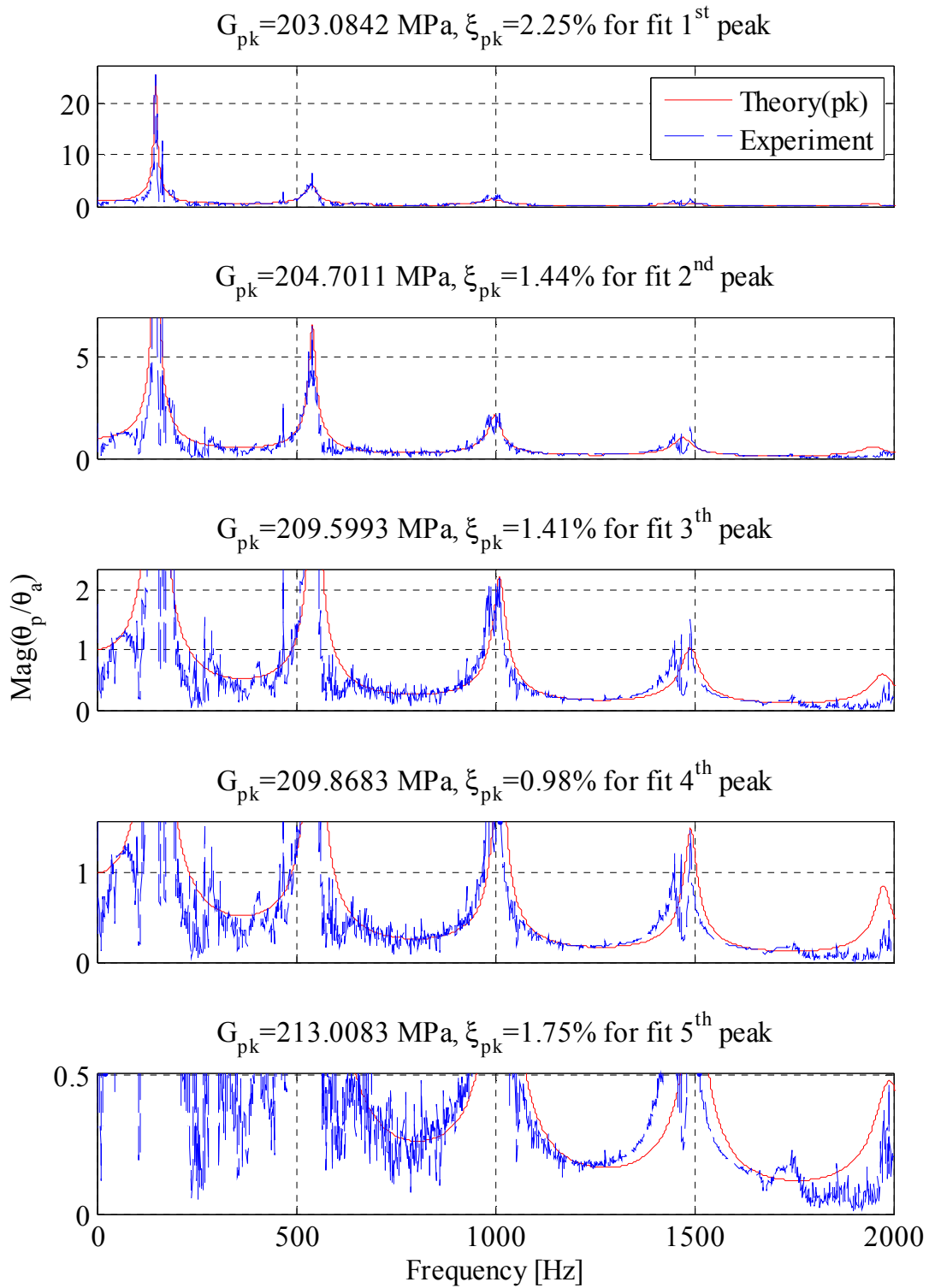


Figure 5.18: Magnitude of theoretical and experimental transfer functions for “peak only” fitting of 5 peaks (ISU 6” specimen at 69.8 kPa confining pressure).

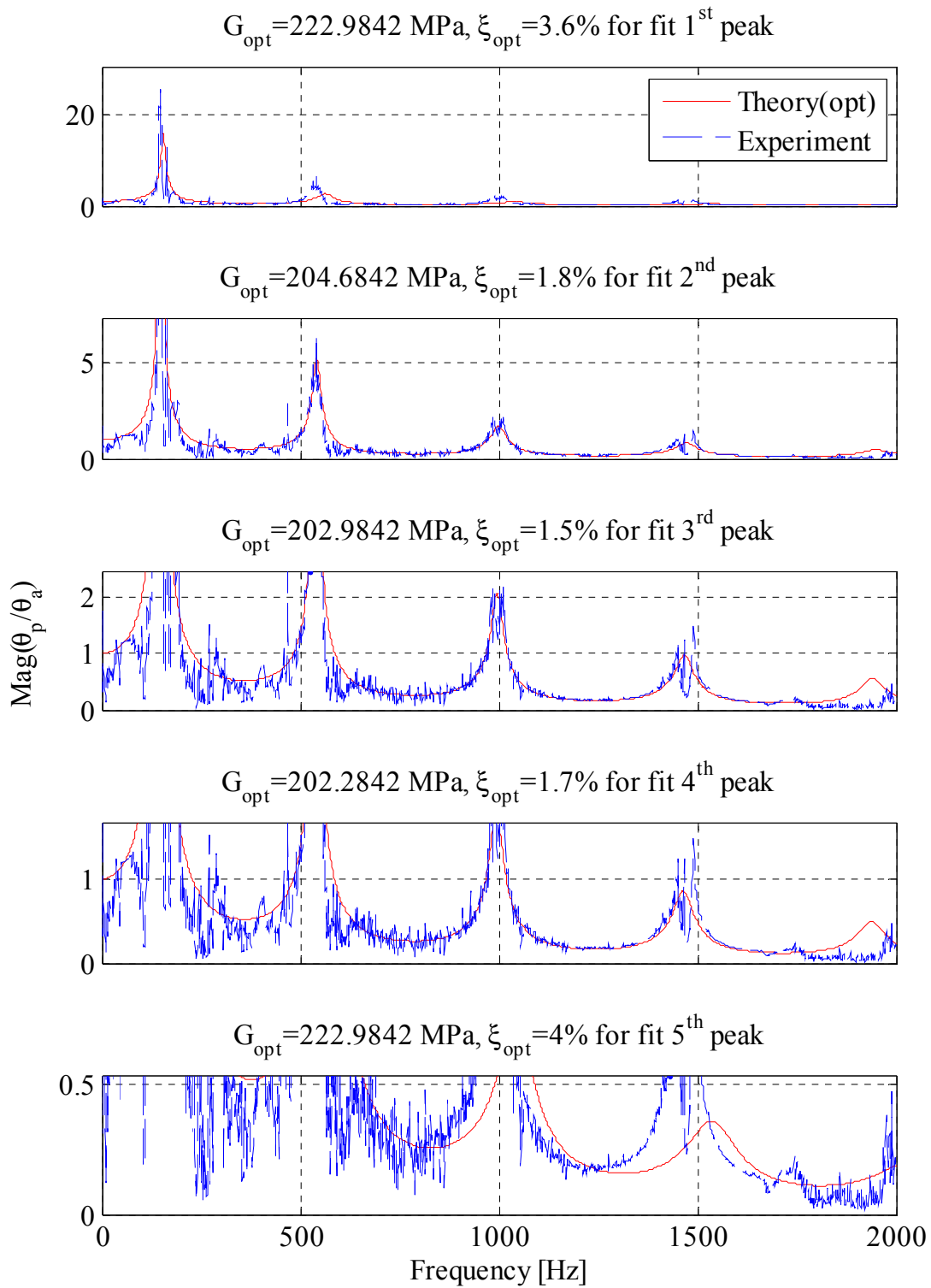


Figure 5.19: Magnitude of theoretical and experimental transfer functions for “squared-error” fitting of 5 peaks (ISU 6” specimen at 69.8 kPa confining pressure).

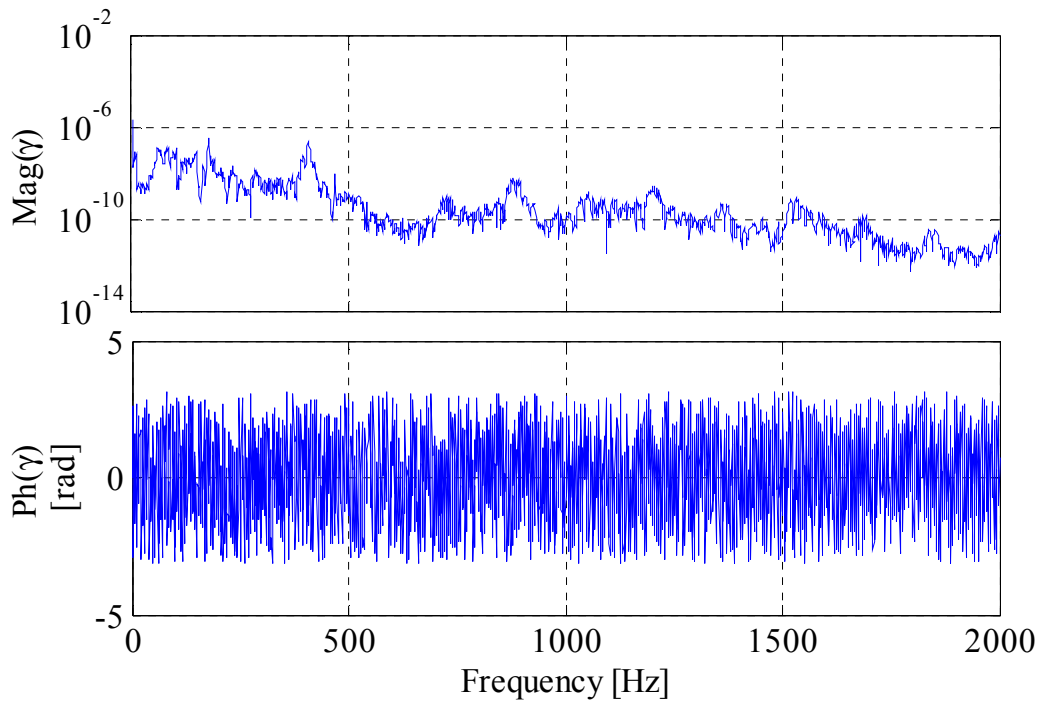


Figure 5.20: Averaged strain spectrum magnitude and phase (ISU 6" specimen at 69.8 kPa confining pressure).

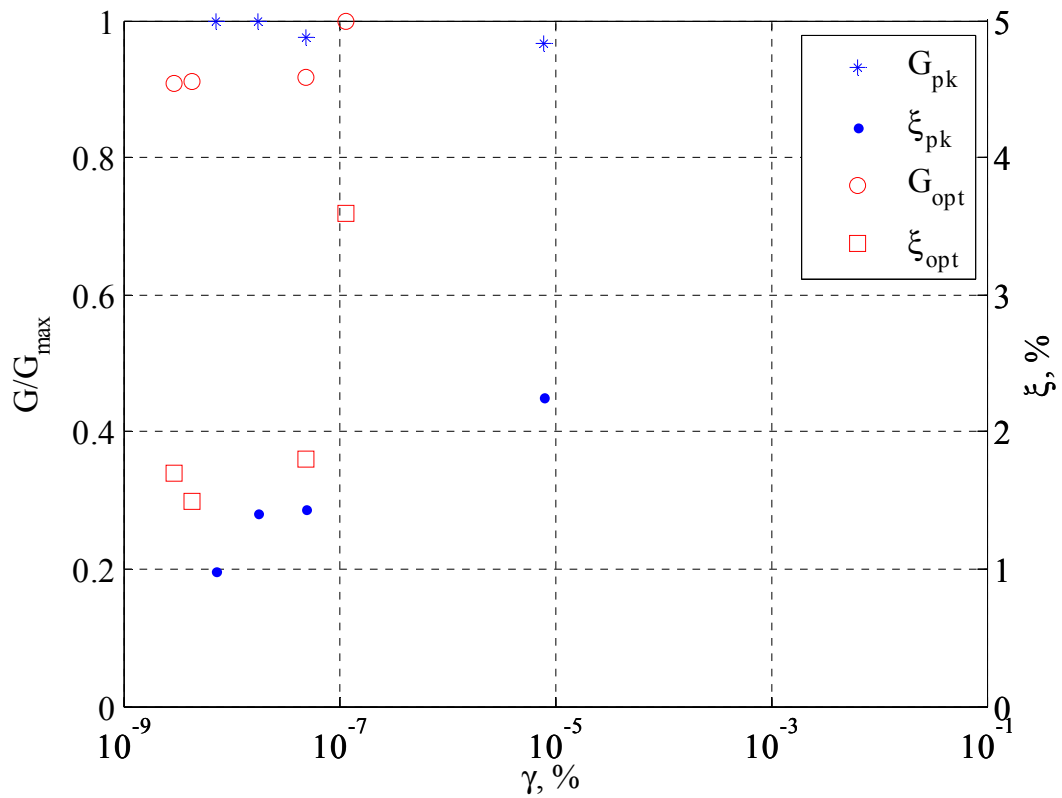


Figure 5.21: Nonlinear strain-dependent modulus and damping using "peak only" and "squared-error" fitting of first 5 peaks (ISU 6" specimen at 69.8 kPa confining pressure).

5.3.2 Tests on 2.8 inch diameter and 6 inch height specimen using transfer function approach

A smaller sample with 71.1 mm (2.8 inch) diameter and 152.4 mm (6.0 inch) height was tested under high level swept-sine excitation to achieve higher strains for measuring nonlinear shear strain-dependent modulus and damping curves. A representative measured transfer function for the lowest confining pressure of this test series is plotted in Figure 5.22. As shown in the figure, the signal is very noisy. Even though a higher excitation level was used, the coherence is still bad. Therefore, it is suggested that a small measurement bandwidth (such 0-250 Hz) be used to examine only the 1st peak in future tests. For this test, the "peak only" fitting method was used to determine the different values of shear modulus and damping ratio at each peak. The corresponding G/G_{max} and ζ versus strain curves obtained by fitting the three peaks in this test are plotted in Figure 5.23. As shown in the plot, the damping ratio curve has a better trend in that damping increase with shear strain, but the shear modulus curve remains almost constant. The maximum strain in this case is around 10^{-4} %, so testing of this smaller diameter specimen had the desired effect of increasing the shear strain level.

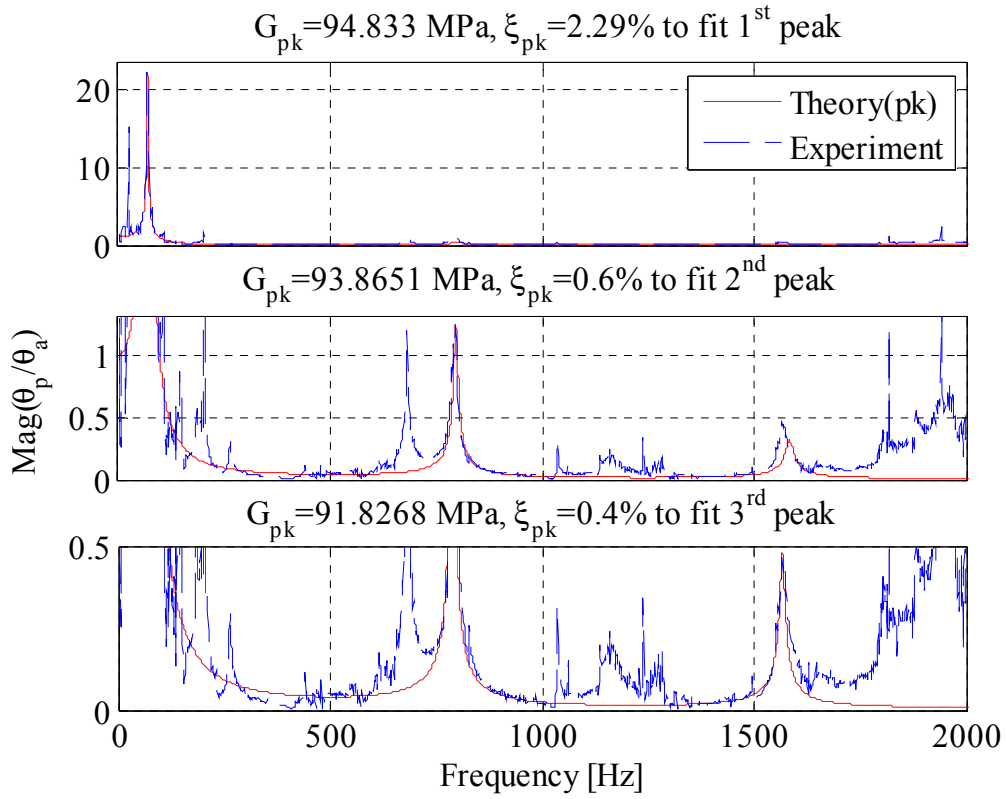


Figure 5.22: Magnitude of theoretical and experimental transfer functions for “peak only” fitting of 3 peaks (ISU 2.8''x6.0'' specimen at 69.8 kPa confining pressure).

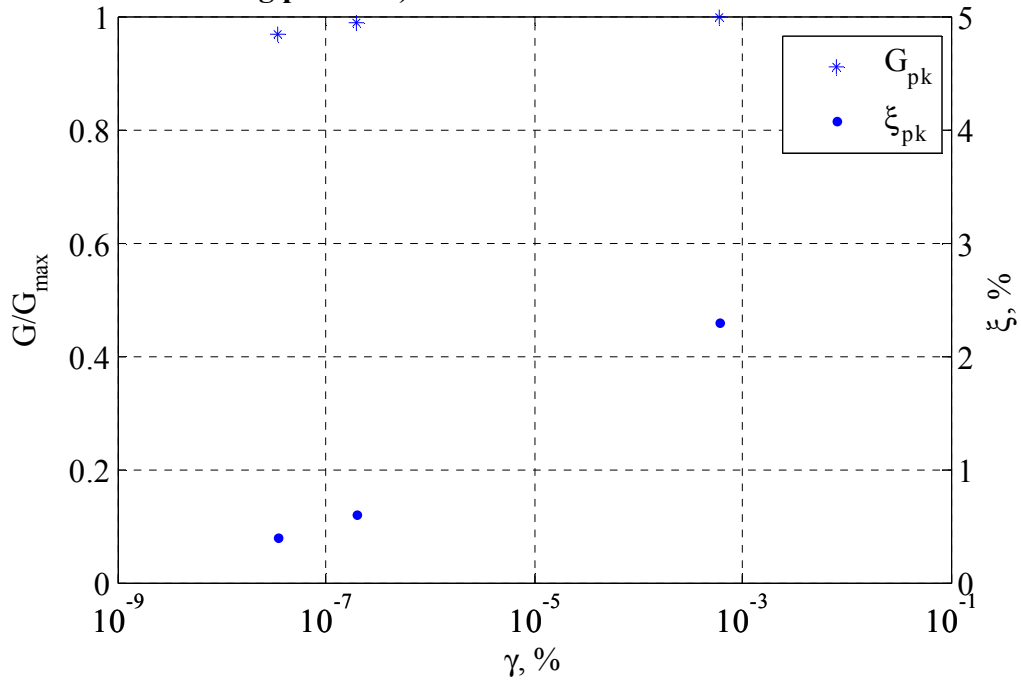


Figure 5.23: Nonlinear strain-dependent modulus and damping (ISU 2.8''x6.0'' specimen at 69.8 kPa confining pressure).

5.3.3 Tests on 2.8 inch diameter and 11.2 inch height specimen using transfer function approach and ASTM method

To achieve even higher strain levels, an ASTM 20/30 sand specimen was prepared with a 70.7 mm (2.78 inch) diameter and 283.6 mm (11.17 inch) height, as shown in Figure 5.24. The detailed physical properties of this specimen are presented in Table 5.7. Both the transfer function approach and ASTM method were used to measure the dynamic properties of the specimen. The purposes of this test were to obtain the shear modulus and damping ratio corresponding to higher strain levels, and to compare the results of the two approaches.

The transfer function approach was first used to analyze the specimen under swept-sine excitation (e.g. see Figure 2.7c with oscillate OFF $F_{\text{start}}=250$ Hz and $F_{\text{end}}=10$ Hz). The specimen was also tested under different confining pressures of 68.9, 137.9, 206.8, 275.8 and 344.7 kPa. Time-histories of the input signals were recorded and digitized using 4,096 samples in the time-domain. As discussed in the previous section, in order to obtain better coherence signals, a lower sampling bandwidth of 250 Hz was used. The reduced bandwidth requires an associated LabVIEW program which uses an external timebase with a master timebase sample rate of $f_s=3.2$ MHz, which results in a sampling rate of $f_s=3.2$ MHz/(19×256)=657.895 Hz, frequency resolution $\Delta f=0.1606$ Hz, $T=6.22592$ sec and $\Delta t=1.52\times 10^{-3}$ sec. Thirty spectral measurements were averaged to minimize the experimental noise. The lower bandwidth and increased sampling period resulted in a test duration of around 3 minutes. If high excitation was used (i.e. RMS current readings above 3 Amps) for this prolonged duration, the current could generate significant heat in the coils, which could potentially damage them. Therefore, a fan was used to circulate air around the coils during the tests. The coils were also allowed to cool for 5 minutes between tests at high excitation.

At each confining pressures, tests were performed from low to high excitation levels to minimize load-history effects. The excitation levels were controlled using the gain knob on the front panel of the amplifier. A swept-sine excitation with 3 second duration and 3 volt amplitude was used. The current reading of each test was monitored by measuring the voltage drop across the 1 Ohm power resistor, or for some tests, using the output current monitor of the amplifier. After a set of tests at each confining pressure, 5 to 10 minutes was allowed for the consolidation of the specimen at next higher different confining pressure. To minimize irreversible load history effects and nonlinearities, it is also recommended that testing be performed from high to low confining pressures.

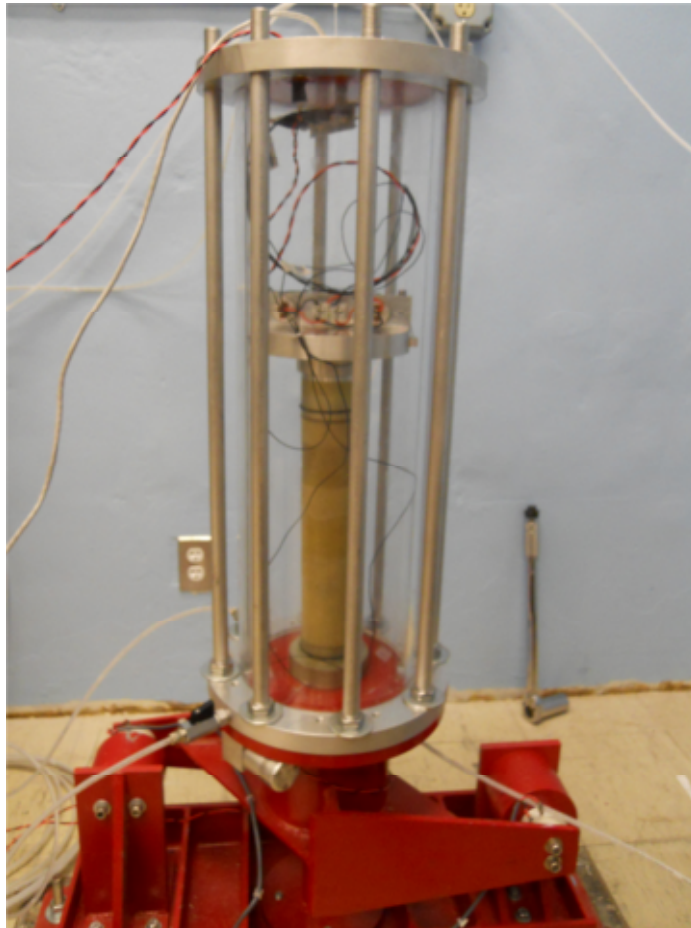


Figure 5.24: 2.8 inch diameter and 11.2 inch height ASTM 20/30 sand specimen.

Table 5.7: Specimen properties of 2.8"×11.2" specimen.

Material	Diameter [m]	Height [m]	Density [kg/m ³]	Void Ratio	Relative Density [%]
ASTM 20/30 Sand	0.0707	0.2836	1851.28	0.593	62.10

A typical 250 Hz bandwidth transfer function from this series of test is shown in Figure 5.25. As can be seen in the figure, the transfer function is relatively clean and coherence is good. There is only one peak in the 250 Hz measurement bandwidth. The “squared-error” fitting approach was used to match the first peak of the theoretical transfer function to the experimental curve using the real imaginary components. The arithmetic average strain spectrum Eq. (3.69) was averaged from 30 transfer functions and 30 FFT’s of platen rotation. The RMS strain spectrum was calculated in terms of the active platen motion as (see Ashlock, Drnevich and Pak, 2013)

$$\tilde{\gamma}_{rms}(r, \omega) = \sqrt{\left(\frac{r\bar{\omega}^* \theta_a(\omega)}{h \sin(\bar{\omega}^*)} \right) \left\{ \left(H^2(\omega) + 1 \right) \left(\frac{2\bar{\omega}^* + \sin(\bar{\omega}^*)}{4\bar{\omega}^*} \right) - H(\omega) \frac{(\bar{\omega}^* \cos(\bar{\omega}^*) + \sin(\bar{\omega}^*))}{\bar{\omega}^*} \right\}} \quad (5.8)$$

Both the arithmetic average spectrum and RMS strain spectrum are plotted in Figure 5.26. The maximum strain is $5.2 \times 10^{-3} \%$ and occurs around 62 Hz, which is the apparatus resonant frequency rather than the peak frequency of the transfer function. If the auto-spectral density of the passive and active platen accelerations are examined, it can be shown that they also contain peaks at the apparatus resonant frequency. Because the transfer function is the ratio of the rotations of two platens, the transfer function is smooth and does not exhibit a peak at the apparatus frequency. However, the strain spectrum is calculated in terms of the difference of the two platen rotations. Hence, there should be a peak in the strain spectrum near the apparatus resonant frequency. The details and results of the tests using the transfer

function approach are shown in Table 5.8. Typical plots of the tests at confining pressures of 68.9 and 344.7 kPa from low excitation to high excitation are shown in Figure 5.27 to Figure 5.30. From the plots, it is found that as the excitation level increases, the peaks of the transfer function move to the left and the amplitudes decreases. As discussed in Section 3.2.1, the frequency of the peak is primarily controlled by shear modulus, while amplitude is primarily controlled by damping. In other words, as the excitation increased, the shear modulus decreased and damping ratio increased. This is reasonable because the higher excitation causes higher strains, for which the well-know-empirical nonlinear strain-dependent modulus and damping curves exhibit a reduction in modulus and increase in damping.

The strain magnitude at each peak was also found using the associated peak frequency of each transfer function. The nonlinear strain-dependent modulus and damping curves plotted using these values are shown in Figure 5.31 through Figure 5.35. A value of G_{max} is then defined as the maximum shear modulus at the lower strain level of each case. As discussed above, the best fit G/G_{max} and ζ curves were found using the curve fitting toolbox in MATLAB for Eqs. (5.2) and (5.3).

From the plots, the data points corresponding to the low excitation usually show large deviations from the theoretical curves. This may be explained by that the low excitation tests possessing lower coherence than the high excitation tests. Hence, the inaccurate modulus and damping were obtained with reduced certainty, causing large differences from theoretical curve shapes.

The best-fit nonlinear strain-dependent modulus and damping curves were also plotted versus the different confining pressures as shown in Figure 5.36 and Figure 5.37. The

68.9 and 137.9 kPa tests show reasonable results that as confining pressure increased, the G/G_{max} curve moves up and ξ curve moves down. However, for the 206.8, 275.8 and 344.7 kPa tests, the curves lay in the region between the curves of 68.9 and 137.9 kPa.

In addition to the results presented above, the maximum shear moduli were plotted against the confining pressures in Figure 5.38. As shown in the figure, the maximum shear moduli loosely follows the expected square-root type dependence on confining pressure (e.g. Hardin and Richart 1963, Hardin and Drnevich 1972, Iwasaki et al. 1978).

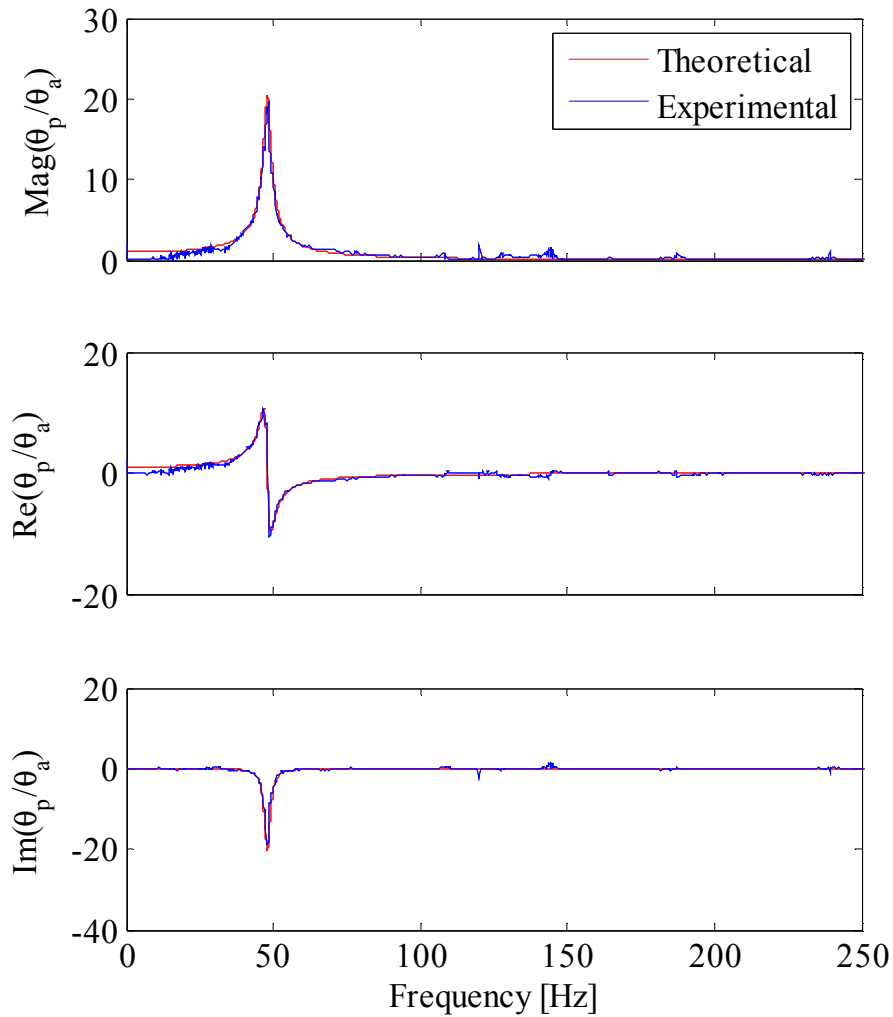


Figure 5.25: Theoretical and experimental transfer functions at high excitation level (ISU 2.8"×11.2" specimen at 69.8 kPa confining pressure).

Table 5.8: Details and results of transfer function approach at different excitation levels and confining pressures (ISU 2.8"×11.2" specimen).

Confining Pressure	Amplitude	Duration	Amplifier Level	Current [A _{rms}]	G [MPa]	ξ [%]	γ [%]
69.8 kPa (10 psi)	3	2	1	0.023	83.3	1.9	8.36E-06
	3	2	2	0.301	73.1	1.2	2.23E-05
	3	2	3	1.459	69.5	1.7	1.59E-04
	3	2	4	2.516	62.0	2.0	1.88E-04
	3	2	5	3.377	62.0	2.4	1.93E-04
	3	2	6	4.034	58.9	3.2	3.15E-04
137.9 kPa (20 psi)	3	2	1	0.025	129.2	1.1	3.45E-05
	3	2	2	0.307	118.7	1.2	1.67E-04
	3	2	3	1.499	117.5	2.0	8.80E-04
	3	2	4	2.514	100.5	2.2	9.14E-04
	3	2	5	3.377	100.0	3.6	1.06E-03
	3	2	6	3.980	98.8	3.7	2.21E-03
206.8 kPa (30 psi)	3	2	1	0.024	188.6	1.0	1.73E-06
	3	2	2	0.320	170.6	1.0	1.05E-04
	3	2	3	1.494	157.2	3.0	5.73E-04
	3	2	4	2.523	136.6	3.1	9.65E-04
	3	2	5	3.394	132.9	3.3	1.20E-03
	3	2	6	4.027	126	4.0	1.45E-03
275.8 kPa (40 psi)	3	2	1	0.026	263.0	0.7	4.80E-06
	3	2	2	0.313	250.7	1.0	2.47E-05
	3	2	3	1.532	231.0	1.4	1.28E-04
	3	2	4	2.547	215.6	1.9	2.34E-04
	3	2	5	3.368	200.6	2.7	7.83E-04
344.7 kPa (50 psi)	3	2	1	0.021	307.0	0.6	2.76E-06
	3	2	2	0.297	297.4	0.7	3.60E-05
	3	2	3	1.530	282.6	1.0	5.47E-05
	3	2	4	2.502	272.4	1.3	2.25E-04
	3	2	5	3.326	263.3	1.6	2.43E-04
	3	2	6	4.038	253.3	1.9	2.81E-04

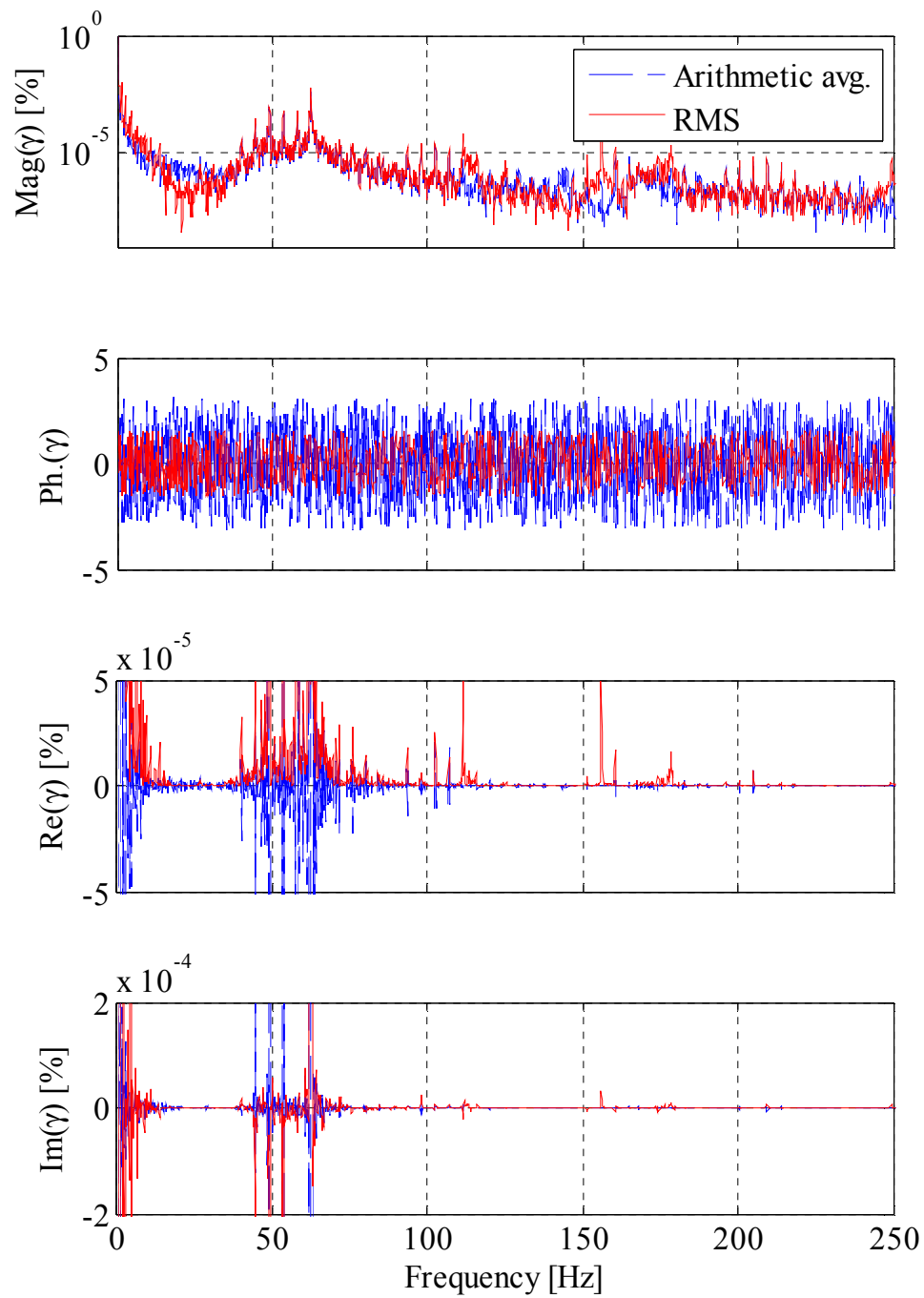


Figure 5.26: Arithmetic average and RMS strain spectrum (ISU 2.8"×11.2" specimen at 69.8 kPa confining pressure).

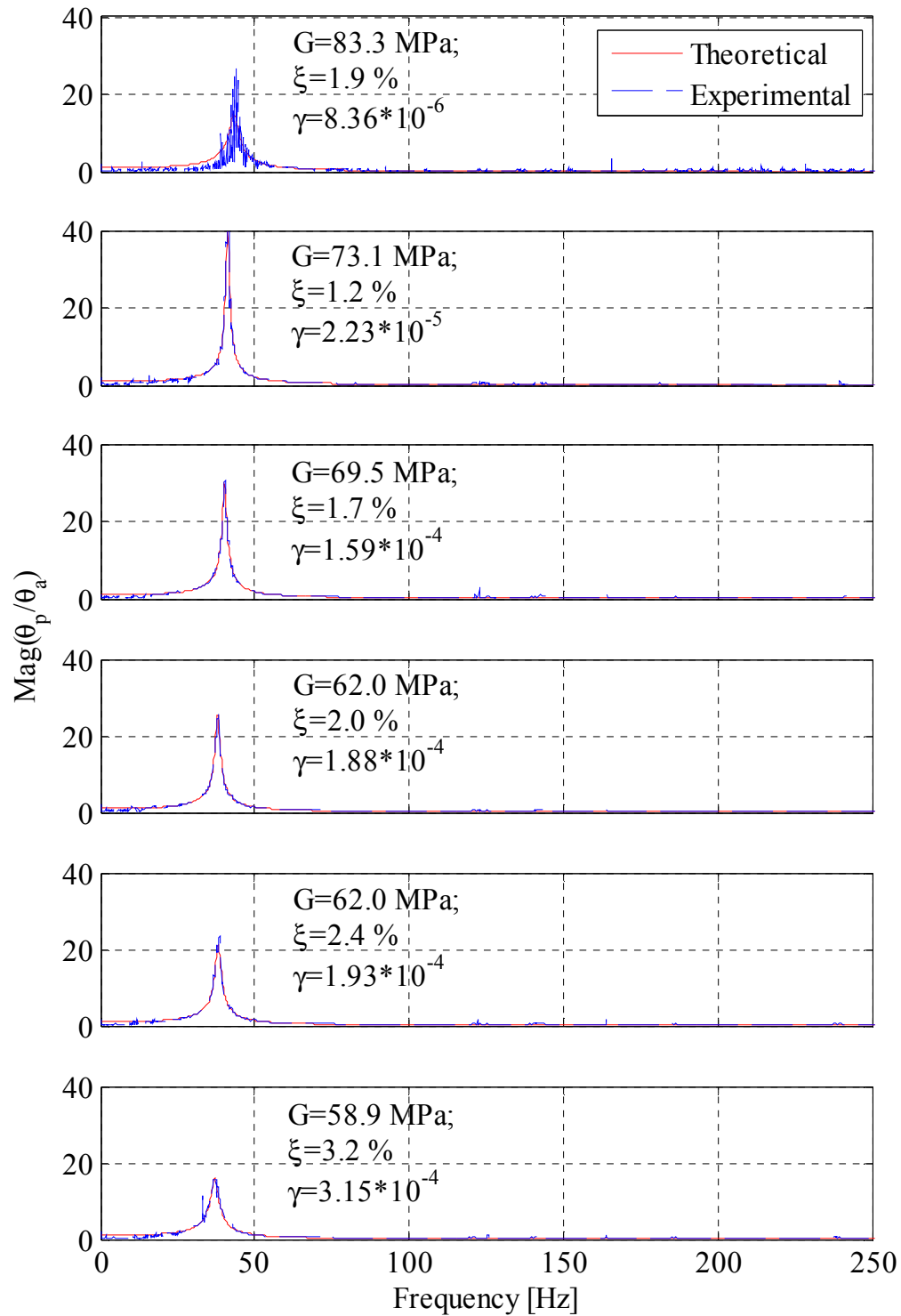


Figure 5.27: Magnitudes of theoretical and experimental transfer function from low excitation (top plot) to high excitation (bottom plot). ISU 2.8''x11.2'' specimen at 69.8 kPa confining pressure.

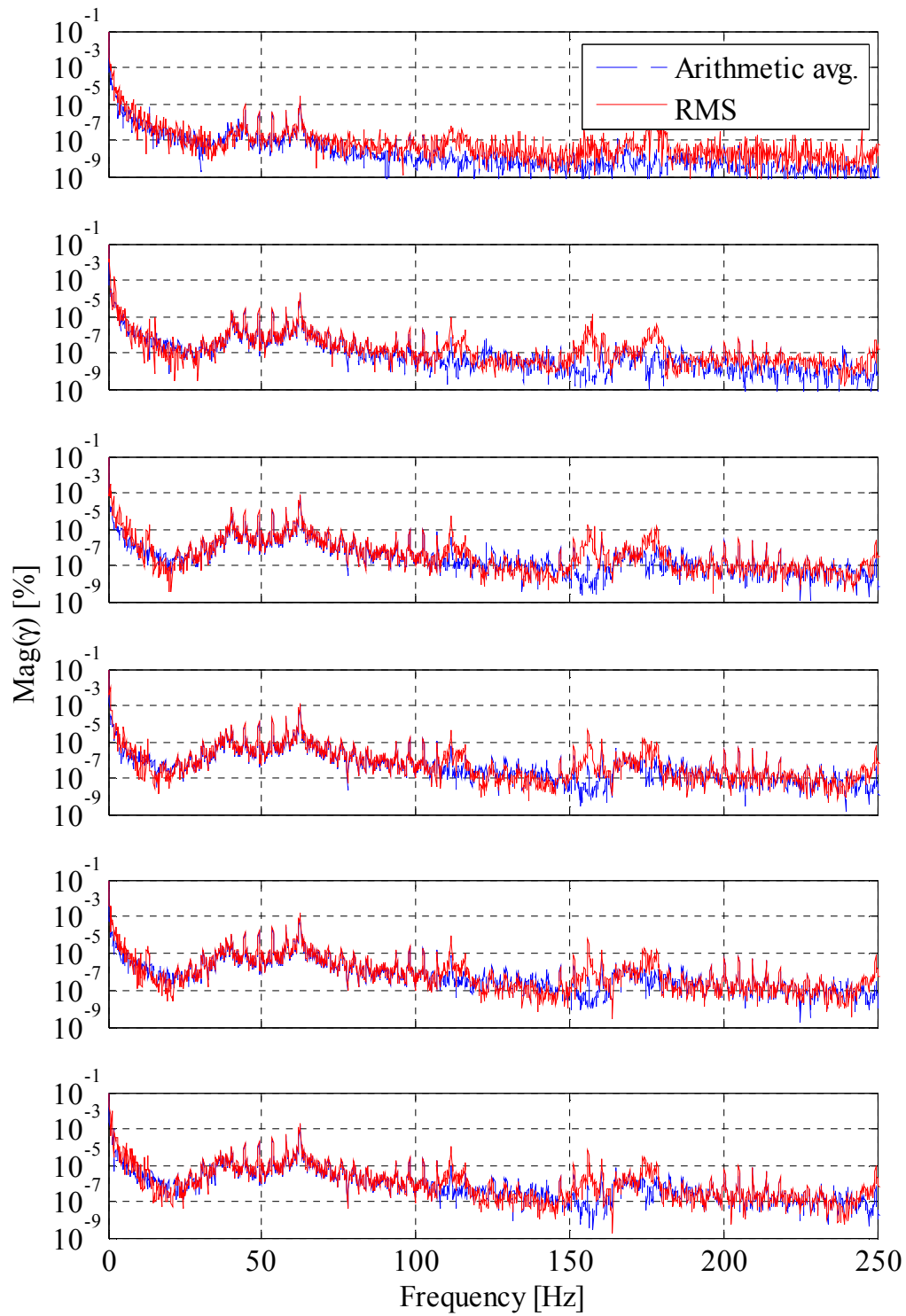


Figure 5.28: Magnitudes of arithmetic average and RMS strain spectrum from low excitation (top plot) to high excitation (bottom plot). ISU 2.8''x11.2'' specimen at 69.8 kPa confining pressure.

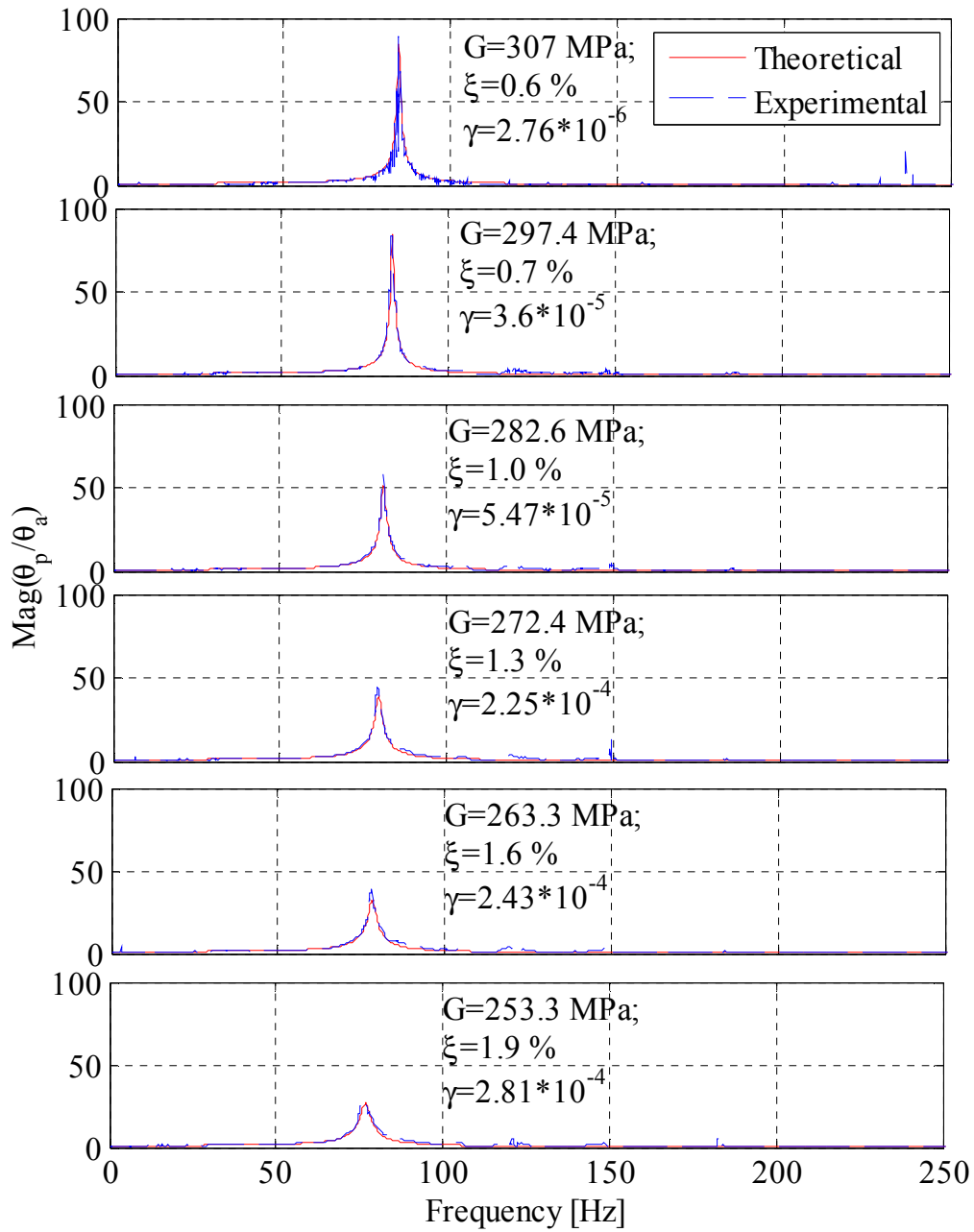


Figure 5.29: Magnitudes of theoretical and experimental transfer function from low excitation (top plot) to high excitation (bottom plot). ISU 2.8''x11.2'' specimen at 344.7 kPa confining pressure.

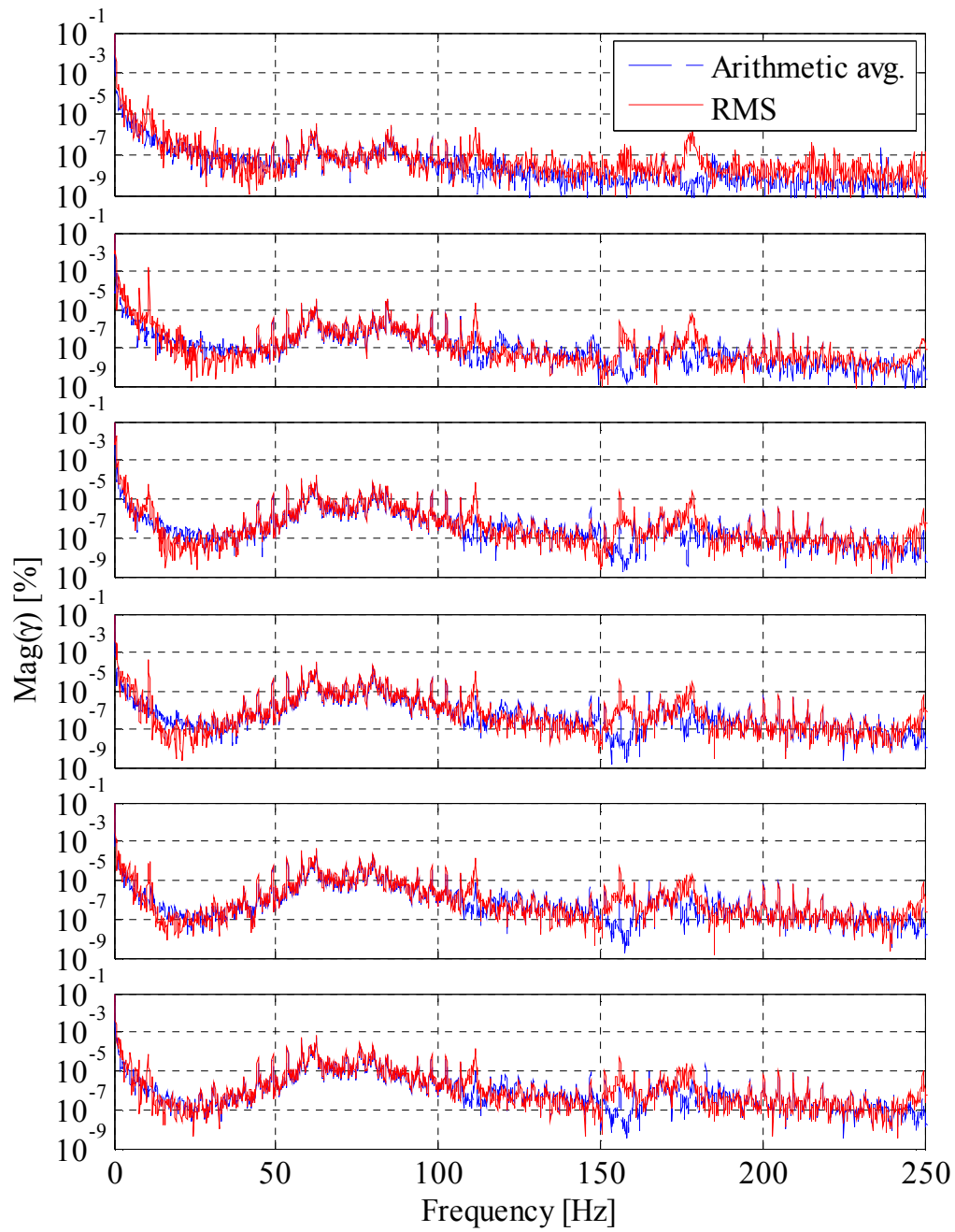


Figure 5.30: Magnitudes of arithmetic average and RMS strain spectrum from low excitation (top plot) to high excitation (bottom plot). ISU 2.8"×11.2" specimen at 344.7 kPa confining pressure.

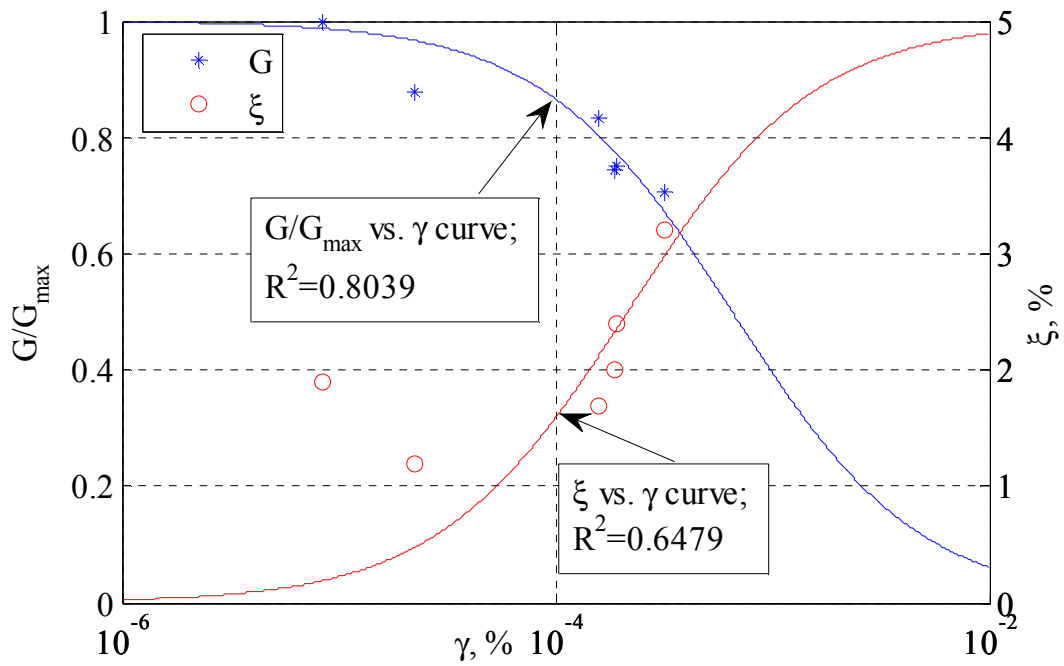


Figure 5.31: Nonlinear strain-dependent modulus and damping curves (ISU 2.8"×11.2" specimen at 69.8 kPa confining pressure).

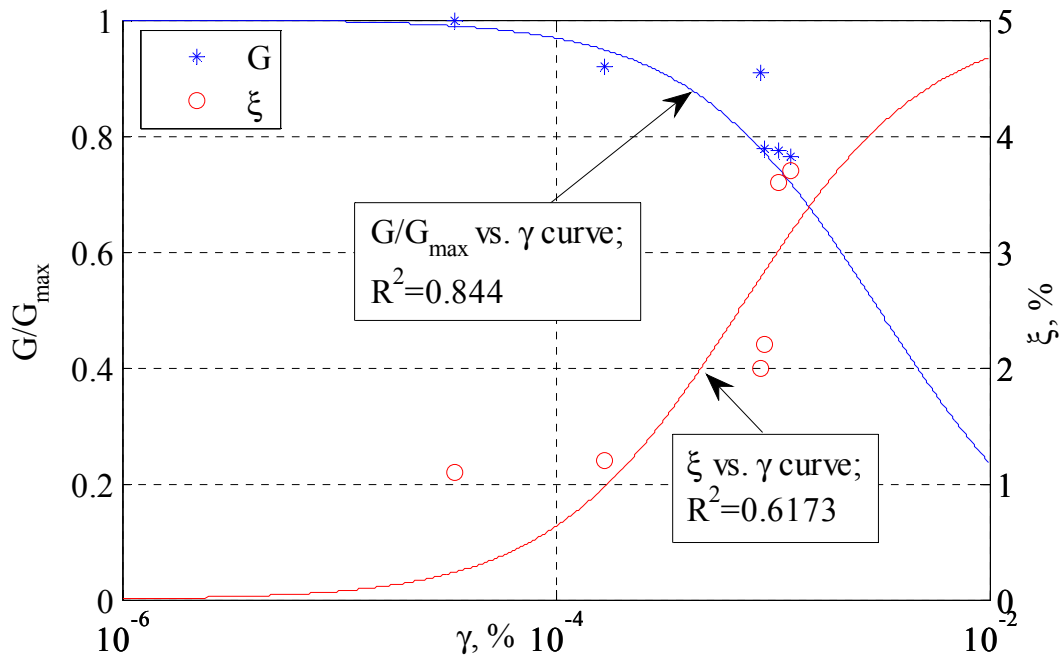


Figure 5.32: Nonlinear strain-dependent modulus and damping curves (ISU 2.8"×11.2" specimen at 137.9 kPa confining pressure).

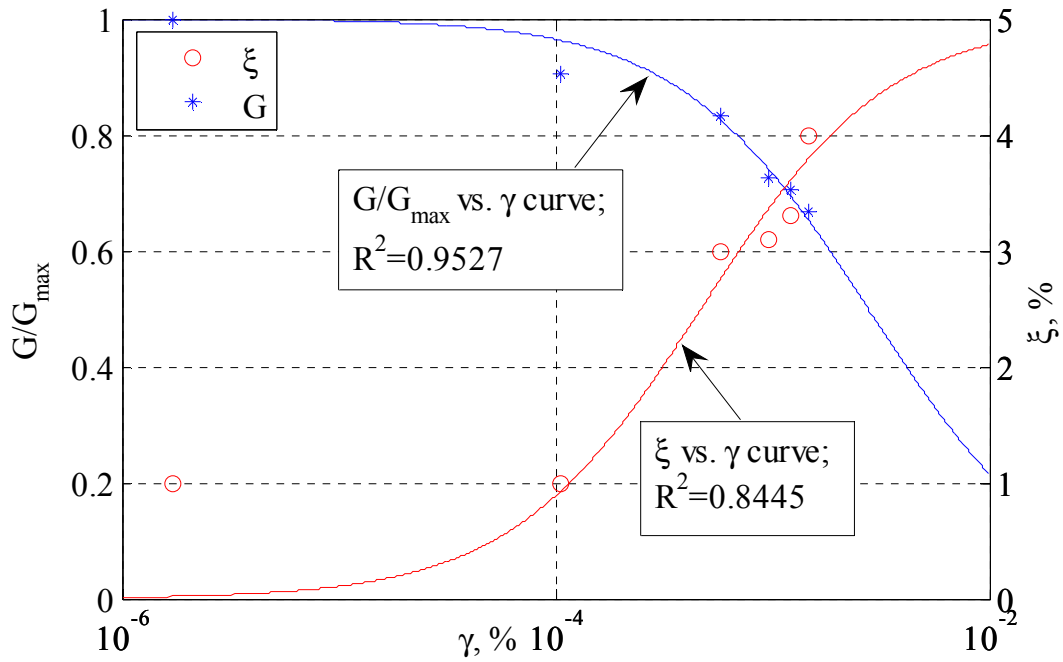


Figure 5.33: Nonlinear strain-dependent modulus and damping curves (ISU 2.8''x11.2'' specimen at 206.8 kPa confining pressure).

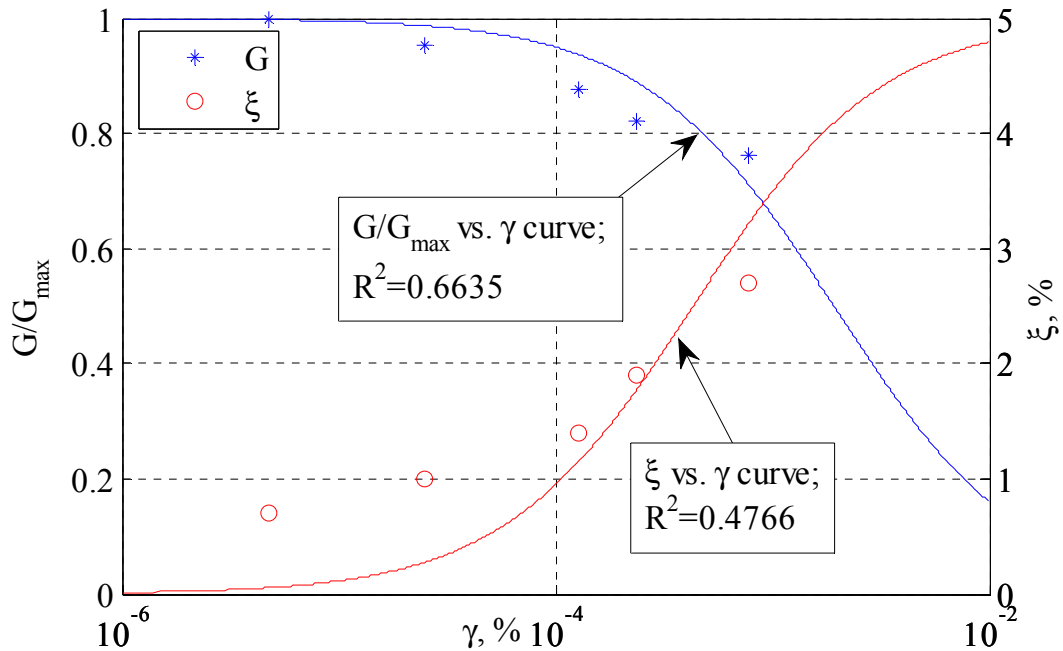


Figure 5.34: Nonlinear strain-dependent modulus and damping curves (ISU 2.8''x11.2'' specimen at 275.8 kPa confining pressure).

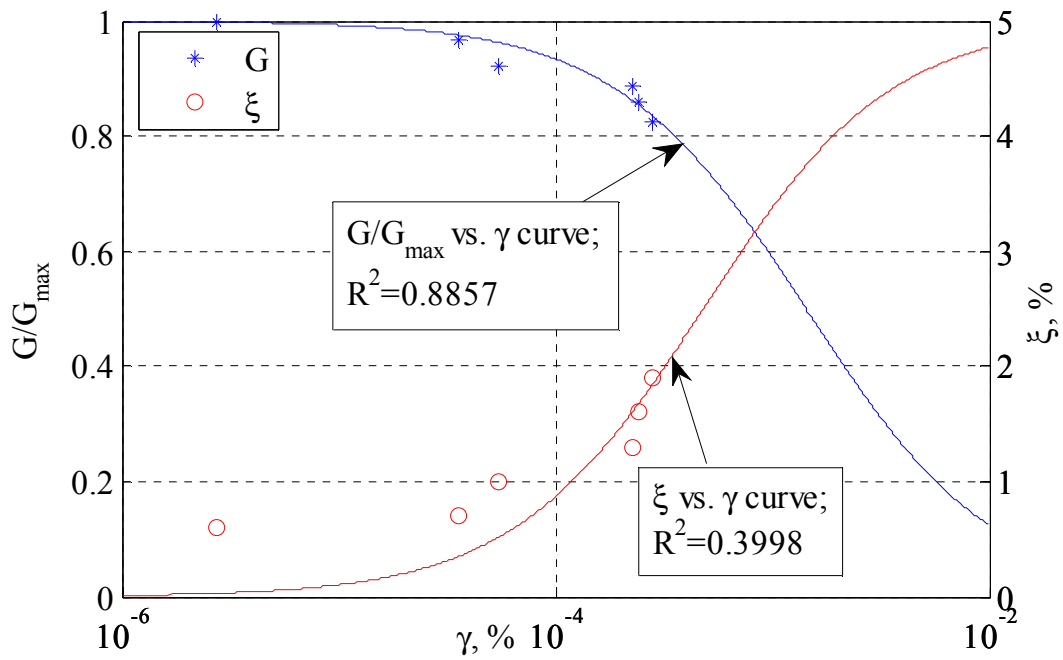


Figure 5.35: Nonlinear strain-dependent modulus and damping curves (ISU 2.8"×11.2" specimen at 344.7 kPa confining pressure).

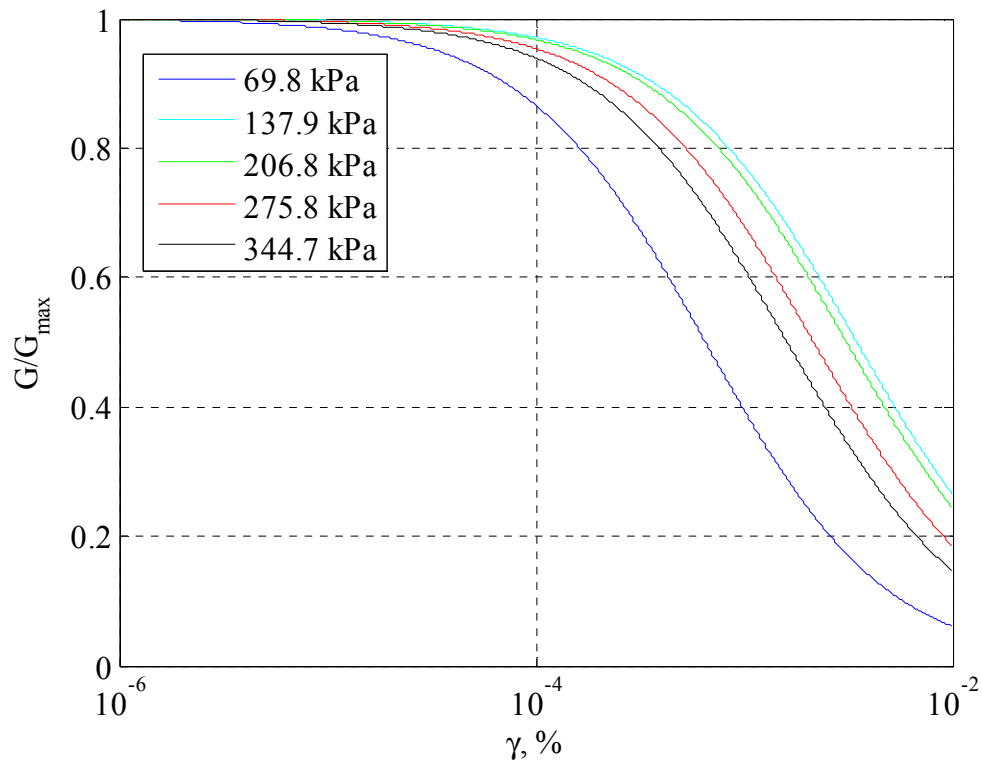


Figure 5.36: G/G_{\max} curves using transfer function approach at different confining pressures (ISU 2.8"×11.2" specimen).

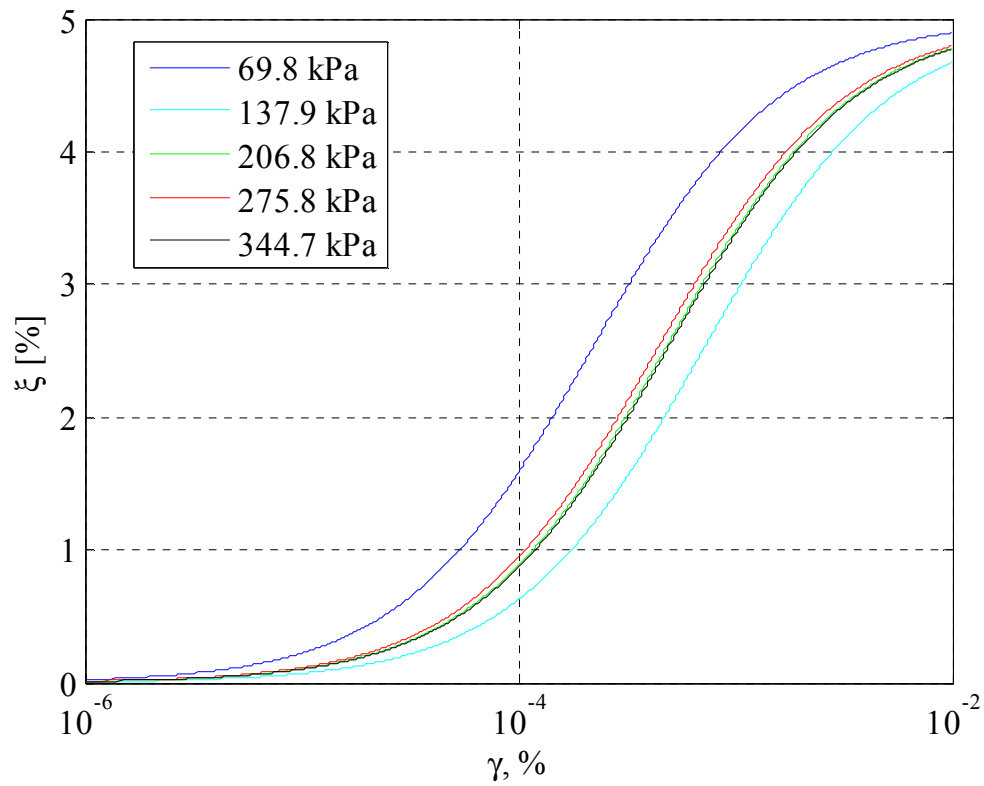


Figure 5.37: Damping ratio versus strain magnitudes at different confining pressures (ISU 2.8"×11.2" specimen).

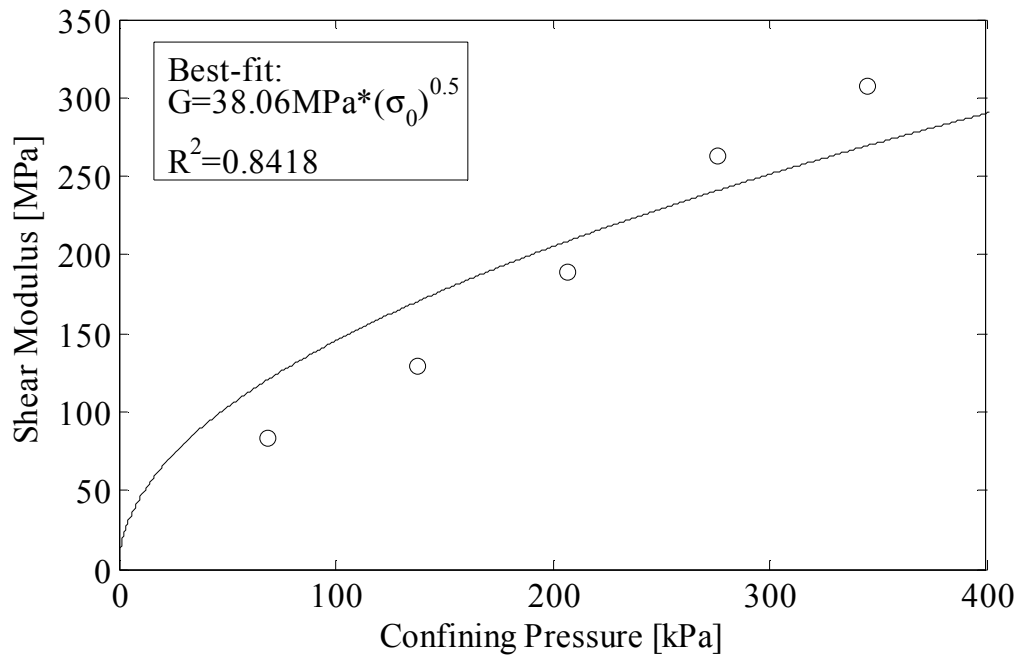


Figure 5.38: Best-fit maximum shear modulus vs. confining pressure using transfer function method (ISU 2.8"×11.2" specimen).

The same specimen discussed above was also tested using the ASTM procedure and an oscilloscope LabVIEW program as the data acquisition system (see Figure 2.8). The system connection for the ASTM method is shown in Figure 2.4. The recommended procedures in section 4.3 of ASTM D4015 (2007) were followed, along with those of the Free-free RC User Manual (Drnevich, 1987). Tests were performed from high to low confining pressures and low to high excitations.

The resonant frequencies were measured as described in ASTM D4015, SDI (1987), and Drnevich (1978). First, the frequency was measured at which the Lissajous plot of torque versus passive velocity on the oscilloscope forms a straight line with positive slope. In Section 3.2.6 of ASTM D4015, it is recommended that the resonant frequency be taken as the second lowest frequency for which torque is in phase with the passive end velocity, because the lowest frequency corresponding to in-phase motion does not produce significant strains in the specimen. However, in the tests presented herein, this second lowest resonant frequency could not be found by judging from the Lissajous plot on the oscilloscope. In order to verify this point, a theoretical rotational velocity/torque transfer function was plotted with the given apparatus properties and a reasonable G and ζ (Figure 5.39). As shown in the figure, the first peak is around 68.25 Hz and the second peak with zero phase angle is around 619.1 Hz, which would be the desired resonant frequency recommended in ASTM D4015. In this high-frequency range, however, the signal is very noisy on the Lissajous plot. In the actual tests herein, the second lowest frequency (straight line with positive slope) therefore could not be measured reliably. According to SDI (1987), it is recommended that the resonant frequency should be the second frequency when the Lissajous plot forms a straight line with a negative slope. Drnevich (1978) recommends for low excitation that the resonant

frequency be taken when the Lissajous plot forms a straight, sloping line. For the case where passive motion is used to establish resonance, the resonant frequency is the second lowest frequency for which the Lissajous plot is a straight, sloping line. When a velocity transducer is used, the slope of the line for the second lowest frequency has the opposite sign as it does for the lowest frequency. For the device used in this study, the lowest frequency occurs when the Lissajous plot of passive velocity versus torque is a straight line with positive slope. In other words, Drnevich (1978) and SDI (1987) recommend that the resonant frequency should be the frequency for which the Lissajous plot is a straight line with negative slope, which corresponds to the second lowest frequency. In this study, it was found that if use the second lowest frequency is taken as the resonant frequency, the results for confining pressures of 275.8 kPa (40 psi) and 344.7 kPa (50 psi) are reasonable. However, at confining pressures of 69.8 kPa (10 psi), 137.9 kPa (20 psi) and 206.8 kPa (30 psi), the second lowest frequency would be near the apparatus resonant frequency, causing errors and unreasonable results for these tests. Therefore, the lowest frequency with positive slope was used for tests at these confining pressures.

After determining the resonant frequency, the electrical current in the coils was recorded from the multimeter. The voltage outputs of passive and active geophones were also measured using the oscilloscope. The data reduction procedures of Section 10 of ASTM D4015 were then followed. The apparatus damping factor is given as

$$ADF = ADC / (2\pi f_T J) \quad (5.9)$$

where

ADC is the apparatus damping coefficient (see Section 2.2.5);

f_T is the measured resonant frequency with the soil specimen in place [Hz].

The magnification factor is defined as the ratio of the rotation to the excitation torque, multiplied by the quantity $J\omega^2$ and can be calculated for the passive end as

$$MMF = \left[\frac{RCF_p \cdot RTO}{TCF \cdot CR} \right] J(2\pi f_T)^2 \quad (5.10)$$

where

RCF_p is the passive rotation calibration factor (see Section 2.2.1);

TCF is the torque/current calibration factor (see Section 2.2.6);

RTO is the passive geophone output [V_{pk} or V_{rms}]. (usually the geophones are connected in series, so the output voltage needs to be divided by 2);

CR is the electrical current reading for the coils [A_{pk} or A_{rms}].

The strain calculation of the ASTM method employs Simpson's rule to numerically integrate the strain along the specimen height to obtain a single average shear strain for the specimen. The equivalent strain profile at a radius of $0.4d$ is also computed for any given cross section of the specimen. The so-called "apparent strain" is defined as the maximum rotation at the passive end divided by the length of the specimen. The strain factor (SF) is defined as the ratio of the "equivalent strain" (the same as average strain) to apparent strain. Hence, the average strain amplitude for the specimen is calculated in ASTM D4015 and RCDARE as

$$\gamma = 0.4d \cdot SF \frac{RCF_p \cdot RTO}{h} \quad (5.11)$$

In this study, the spreadsheet RCDARE was modified for analyzing the results of the ASTM tests using the 2DOF free-free device. The input variables of RCDARE include the properties of the specimen, apparatus calibration factors, and electronic device measurements. More detailed information about the RCDARE spreadsheet is provided in Appendix D. A

simplified data reduction procedure from SDI (1987) was also used to compare the results with RCDARE. The empirical formulas of the parameters to calculate the shear modulus, damping ratios and strain amplitude for the simplified procedure are as follows:

Damping ratio:

$$\xi [\%] = \left(56.54979 \times P^{-0.07417} \right) / \left(\theta_p / \theta_a \right) \quad (5.12)$$

Shear modulus:

$$G = \rho (2\pi h)^2 (f_T / F) \quad (5.13)$$

$$F = [0.84926 + (2.25379 \times \xi + 1.28315 \times \xi^2 \times 10^{-4})] \times P^{-0.357983} \quad (5.14)$$

Strain amplitude:

$$\gamma = 0.4d \times SF \times \theta_p / h \quad (5.15)$$

$$SF = 1.0012 + 0.00083 \times \xi [\%] \quad (5.16)$$

The results of using RCDARE are presented in Table 5.9. The shear modulus vs. strain curves at different confining pressures from RCDARE are shown in Figure 5.40. As shown in the figures, the behavior of shear modulus generally follows the expect trends, decreasing with shear strain and increasing with confining pressure. The corresponding plot from the simplified data reduction procedure is given in Figure 5.41. The shear modulus decreases with increasing strain amplitude, however, the curves for the simplified procedure are below those from RCDARE. The G_{max} can be found as the asymptotic value at small strain levels. The G_{max} results from the ASTM procedure are compared with those of the transfer function approach at different confining pressures in Figure 5.54, along with the best-fit of the expected square-root relationship for two approaches. An excellent agreement between the best-fit G_{max} vs. confining pressure square-root relationships is shown for the two approaches in Figure 5.54. However, the data for each approach shows some scatter from the expected square-root trends.

Comparisons of G/G_{\max} vs. strain data between the transfer function approach and ASTM method at different confining pressures are plotted in Figure 5.44, Figure 5.46, Figure 5.48, Figure 5.50 and Figure 5.52. The best-fit curves having the form of Eqs. (5.2) and (5.3) are also shown for reference against the expected behavior. From the comparison, the curves are clearly different between two methods. Specifically, the strain level of ASTM method is much larger than the transfer function approach. This may be because the sinusoidal excitation of ASTM method brings more energy to the specimen at a single resonant frequency. In contrast, the random vibration excitation of the transfer function approach distributes the energy to the specimen over a large range of frequency. Therefore, rather than selecting only the strain magnitude at the peak frequency in the transfer function approach, a strain formulation that accounts for the total strain energy at all frequencies might be more appropriate, such as a root-mean-square strain integrated with respect to frequency. For the discrete strain spectra presented herein, this would simply correspond to a summation of the spectral strain values. A broadband total strain energy measure of this kind would result in higher strains for the modulus and damping plots, shifting the transfer function curves towards the ASTM ones. Exploring this possibility is beyond the scope of the present study, but is recommended for future research. While these plots illustrate the feasibility of the transfer function approach, the data exhibit some scatter from the expected behavior. This may be a result of imperfect sample preparation or alignment of the RC device components. It is recommended that methods be studied to reduce the experimental scatter using the new device.

The damping ratio versus strain relationships are shown in Figure 5.42 and Figure 5.43 for the range of confining pressures tested by the ASTM approach. As shown in the

plots, the damping ratio generally increases with shear strain as expected. However, the 206.8 kPa (30 psi) damping curve using the simplified data reduction method has an unusual trend. This might be explained by measuring the wrong resonant frequency in the test due to the complications of the device frequency in the ASTM procedure, as discussed above. The comparisons of the damping vs. strain relationships between transfer function and ASTM approaches are shown in Figure 5.45, Figure 5.47, Figure 5.49, Figure 5.51 and Figure 5.53. The damping ratios from the ASTM method are larger than those of the transfer function approach. This may also be a result to the difference in strain energy distribution across the frequency range, as discussed above for the shear modulus curves. The ASTM results were also compared to the results of previous studies. The variation of shear modulus and damping ratio with shear strain for sands has been reported over an approximate range in previous studies (e.g., see Seed and Idriss, 1970). The upper and lower bound curves for shear modulus are reproduced in Figure 5.55 for RC tests on ASTM 20/30 sand. The ASTM method results for G/G_{max} at different confining pressures in this study are shown by the dots in this figure, which almost fit between the bounds. The damping ratio versus shear strain relationship for sands from the same study of Seed and Idriss (1970) are shown in Figure 5.56. The damping ratios from this study compare well with this range as shown in this figure.

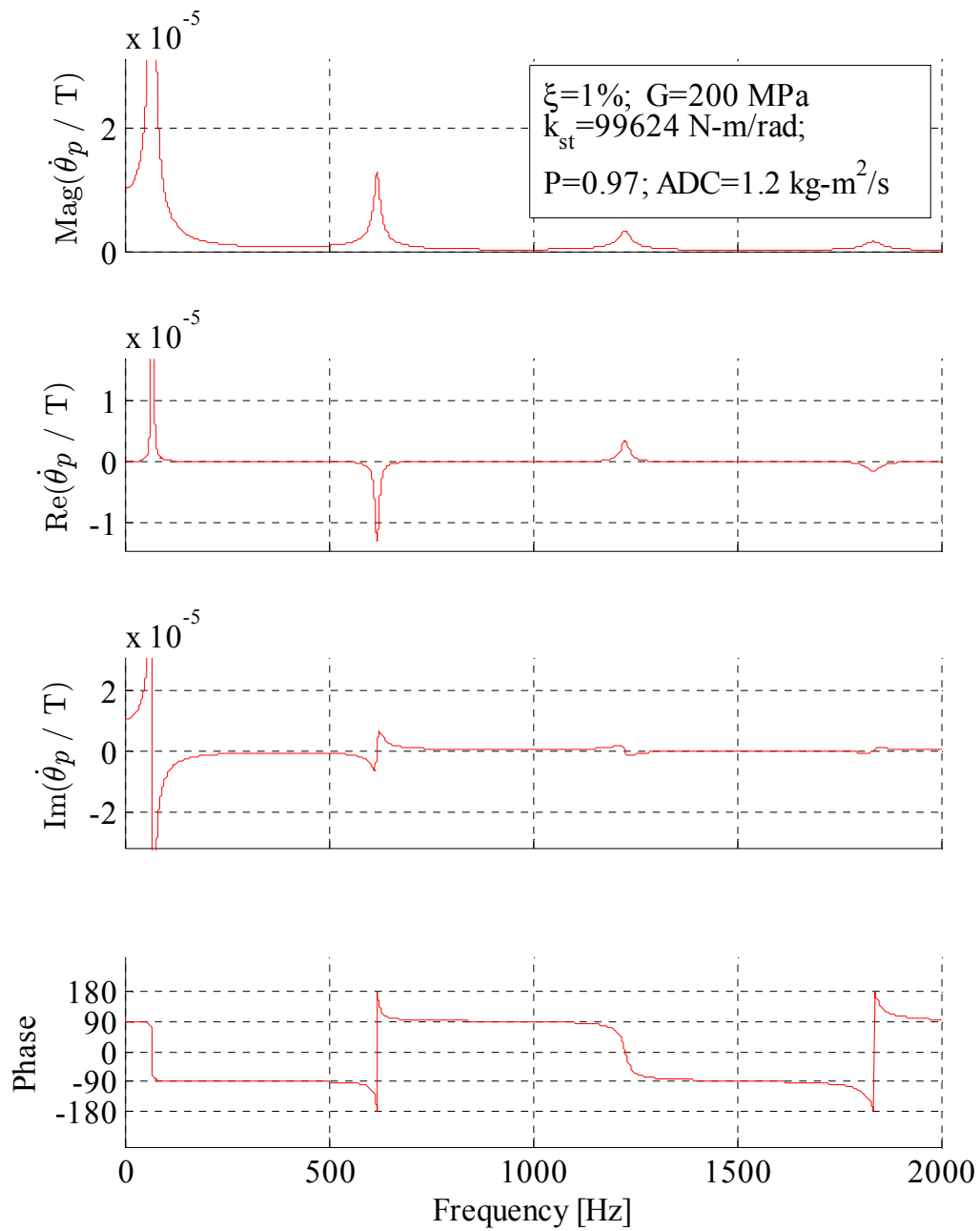


Figure 5.39: Theoretical rotational velocity/torque transfer function for soil specimen with $G=200$ MPa and $\xi=1\%$

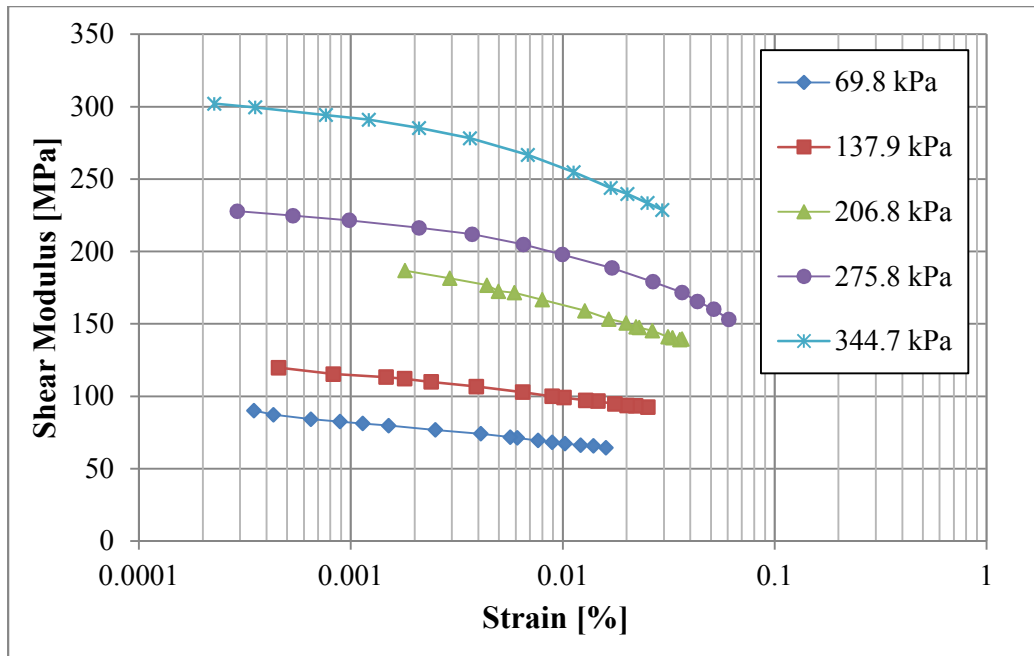


Figure 5.40: Shear modulus versus shear strain curves using ASTM from high to low confining pressure (RCDARE data reduction).

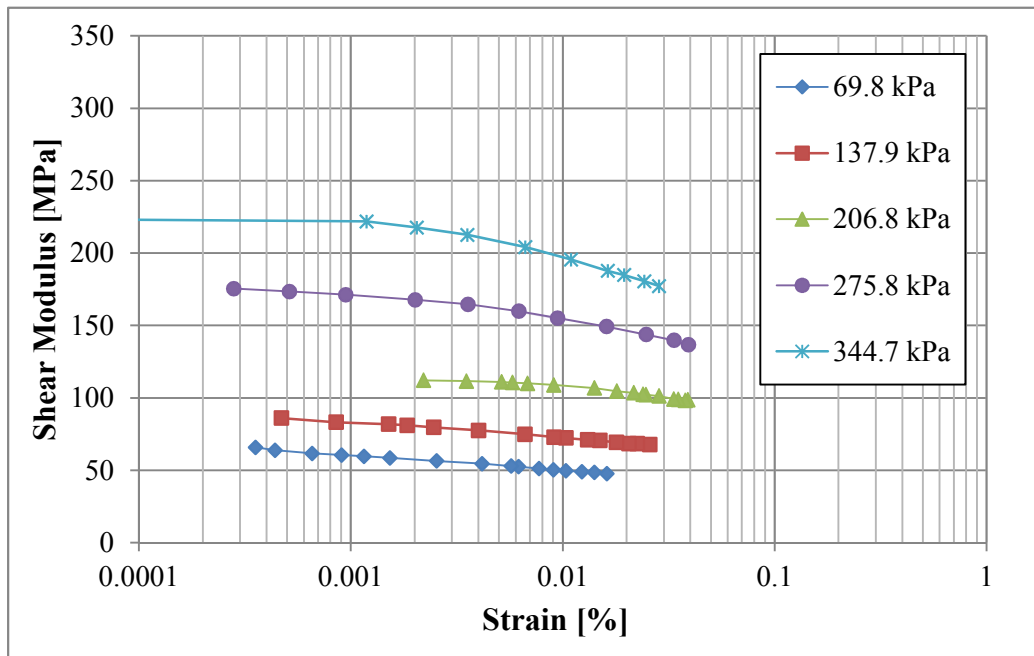


Figure 5.41: Shear modulus versus shear strain curves using ASTM from high to low confining pressure (simplified data reduction).

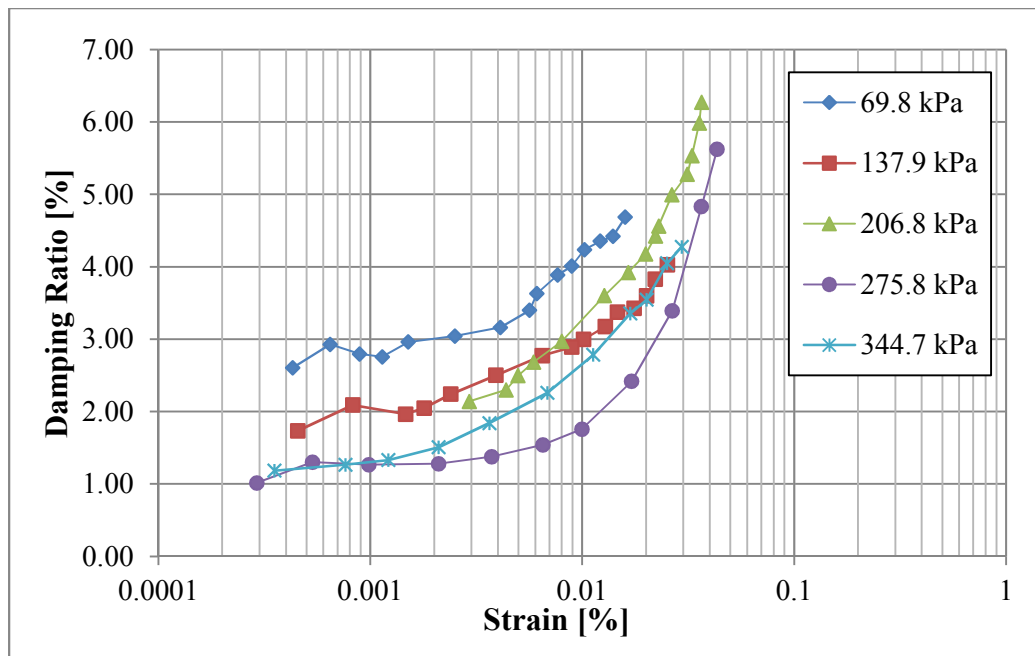


Figure 5.42: Damping ratio versus shear strain curves using ASTM from high to low confining pressure (RCDARE data reduction).

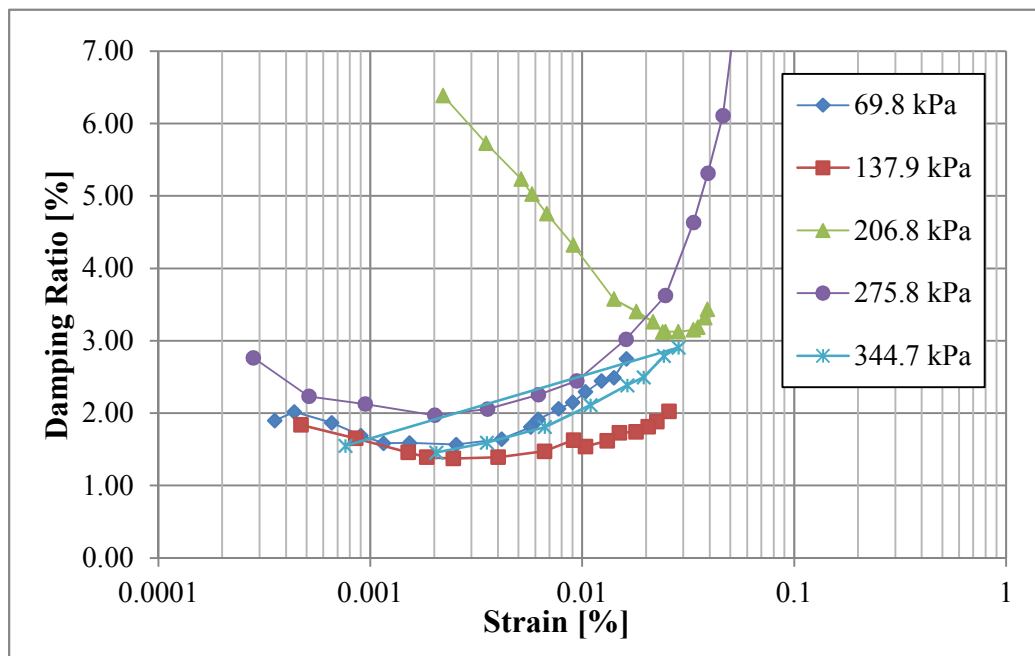


Figure 5.43: Damping ratio versus shear strain curves using ASTM from high to low confining pressure (simplified data reduction).

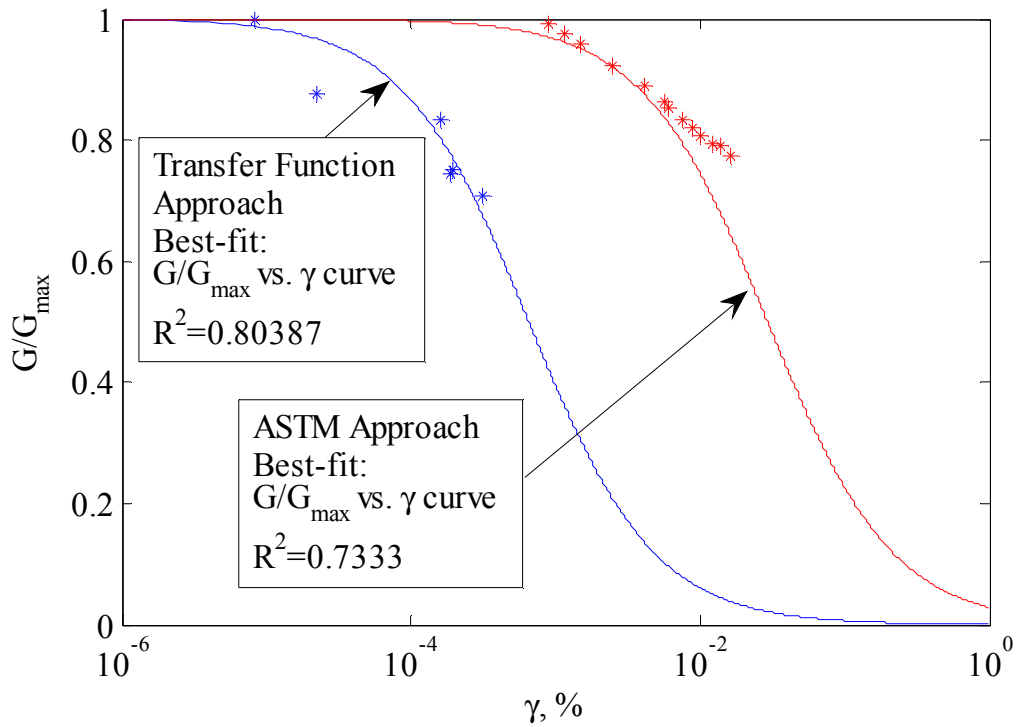


Figure 5.44: G/G_{\max} curve comparisons at confining pressure 69.8 kPa (10 psi).

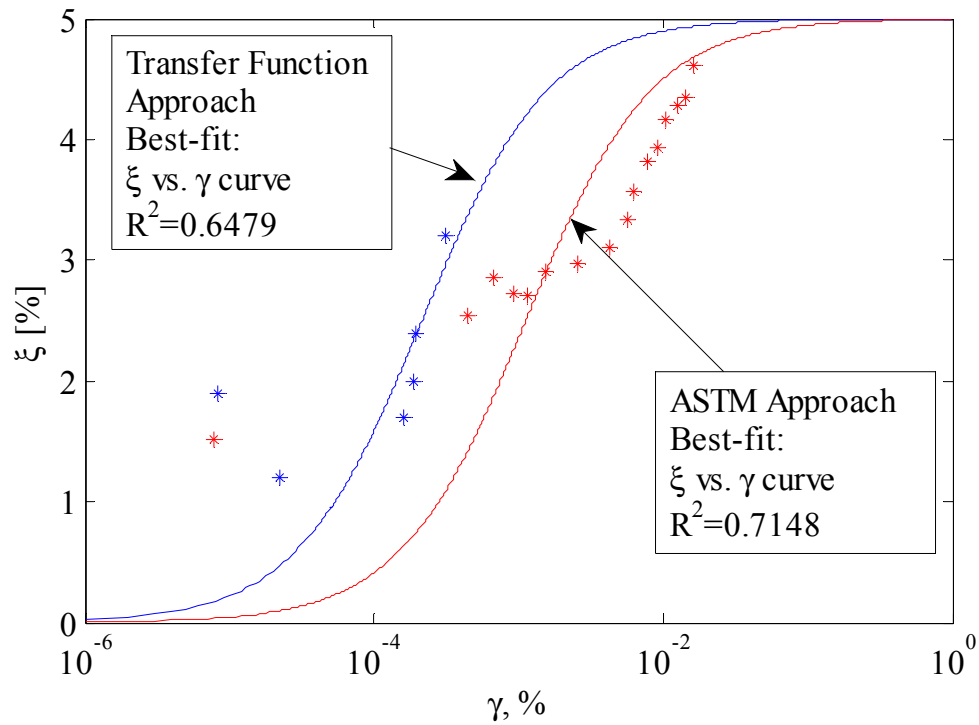


Figure 5.45: ξ curve comparisons at confining pressure 69.8 kPa (10 psi).

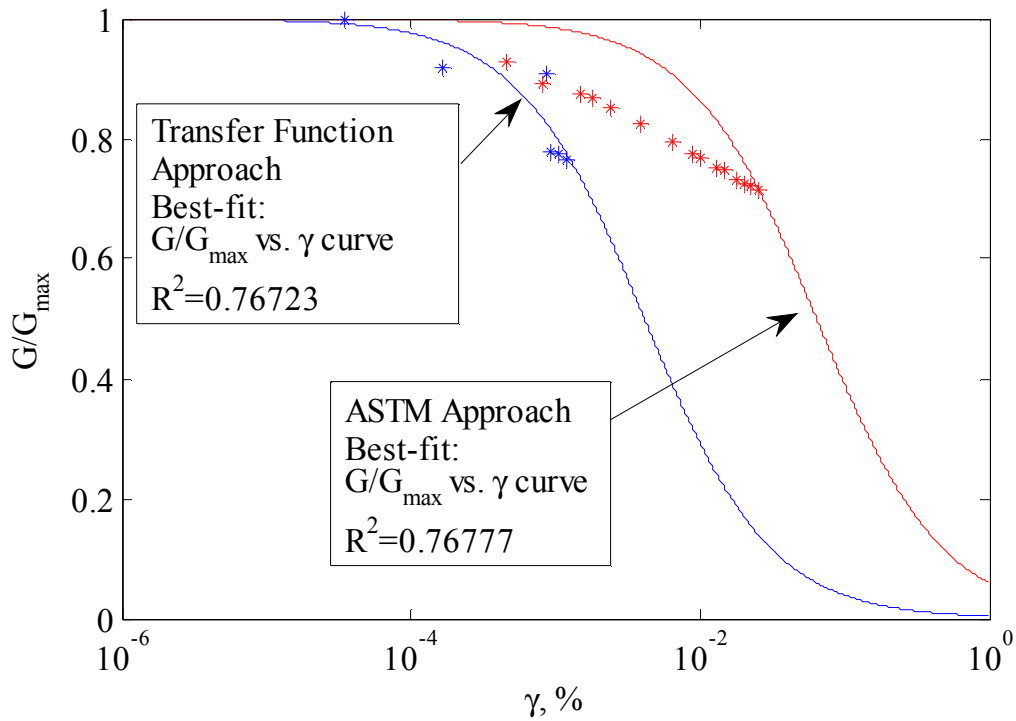


Figure 5.46: G/G_{\max} curve comparisons at confining pressure 137.9 kPa (20 psi).

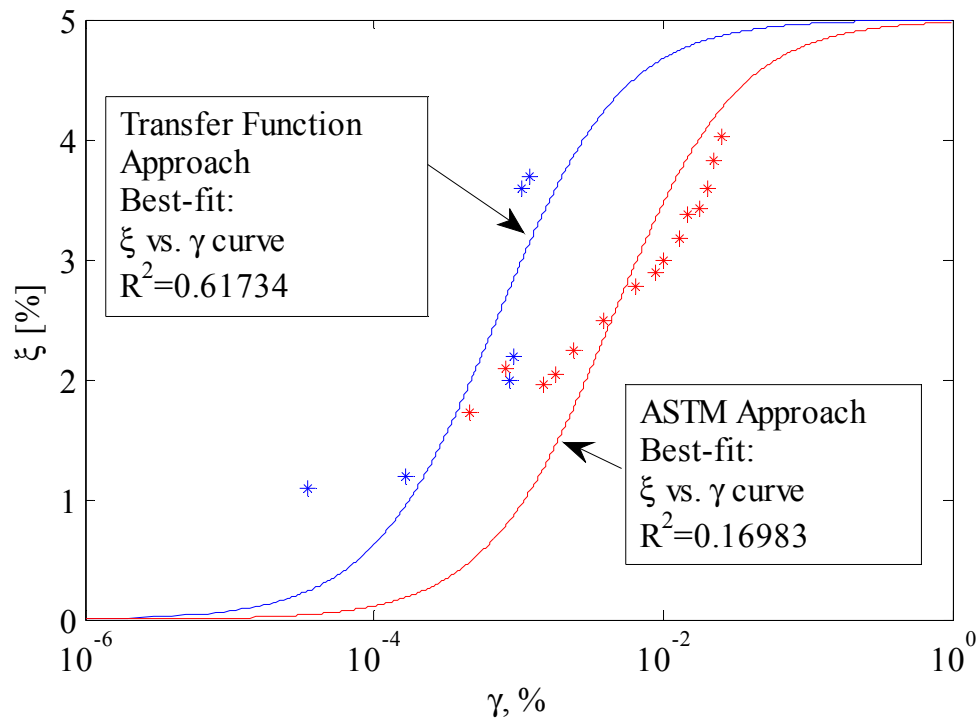


Figure 5.47: ξ curve comparisons at confining pressure 137.9 kPa (20 psi).

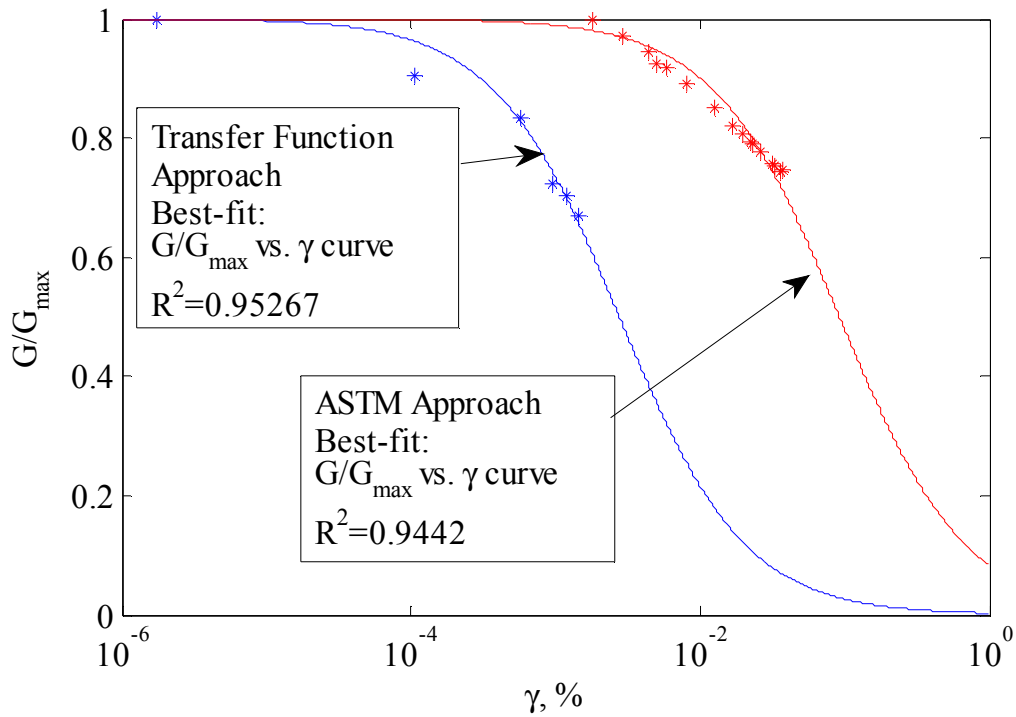


Figure 5.48: G/G_{\max} curve comparisons at confining pressure 206.8 kPa (30 psi).

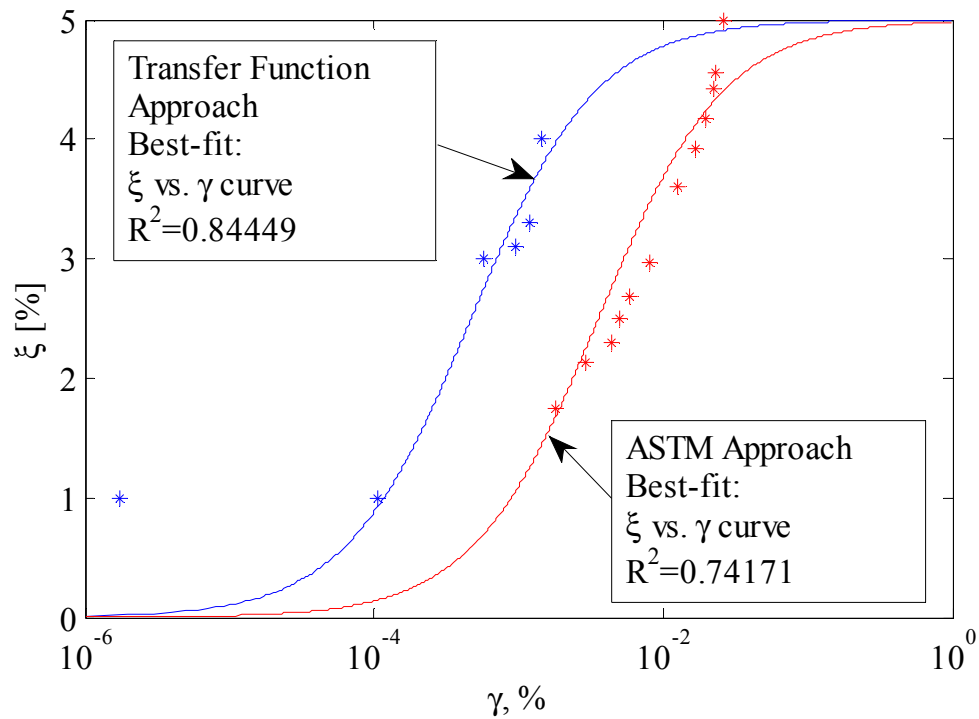


Figure 5.49: ξ curve comparisons at confining pressure 206.8 kPa (30 psi).

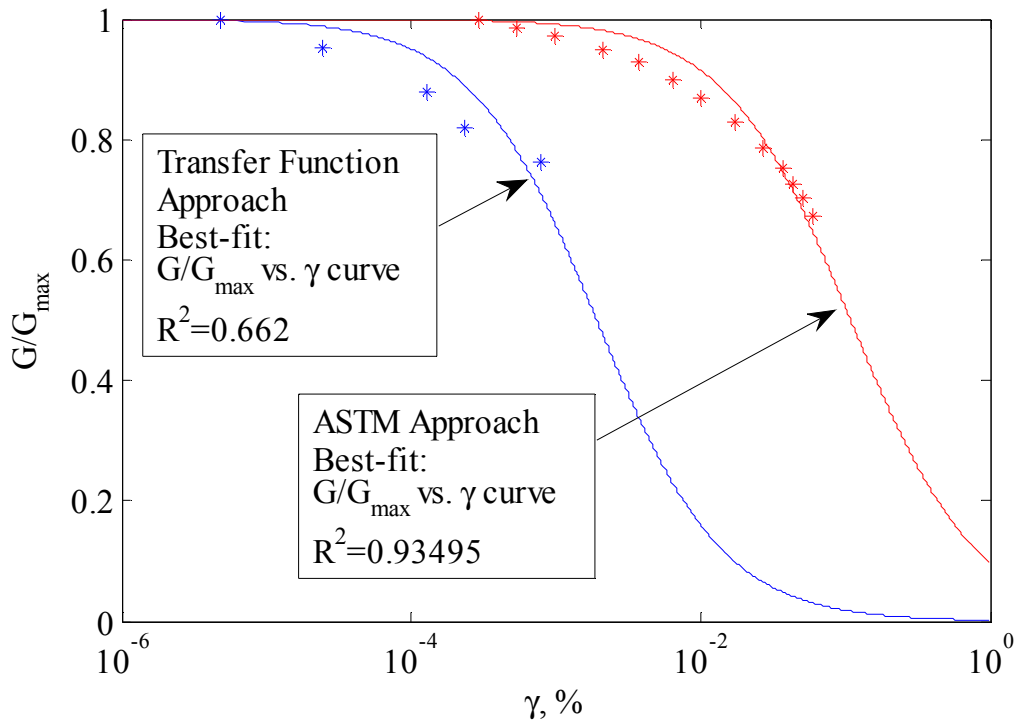


Figure 5.50: G/G_{\max} curve comparisons at confining pressure 275.8 kPa (40 psi).

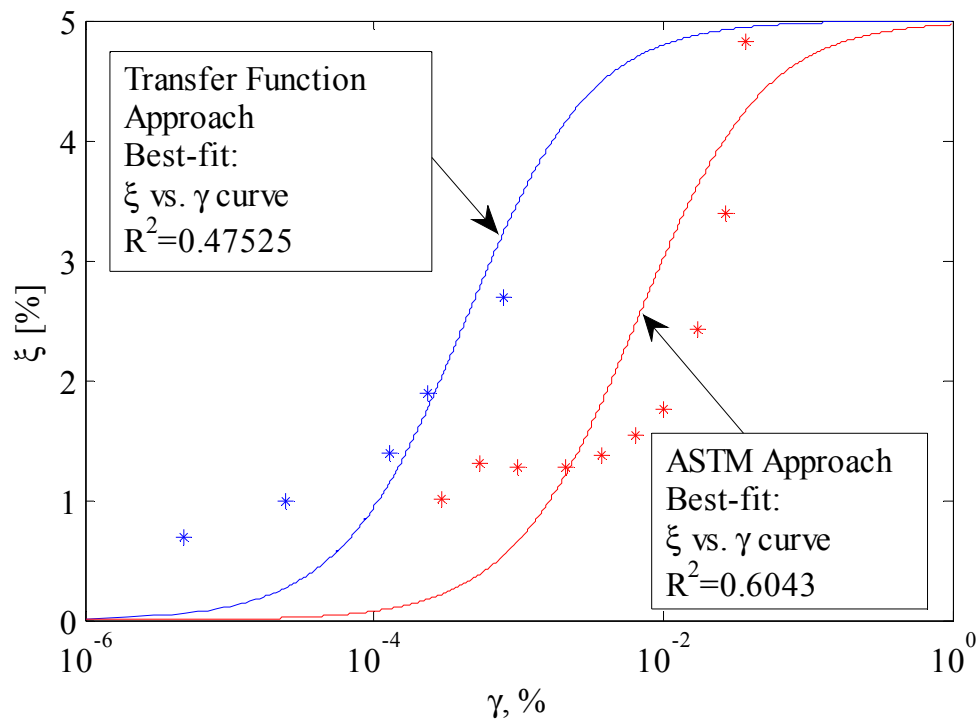


Figure 5.51: ξ curve comparisons at confining pressure 275.8 kPa (40 psi).

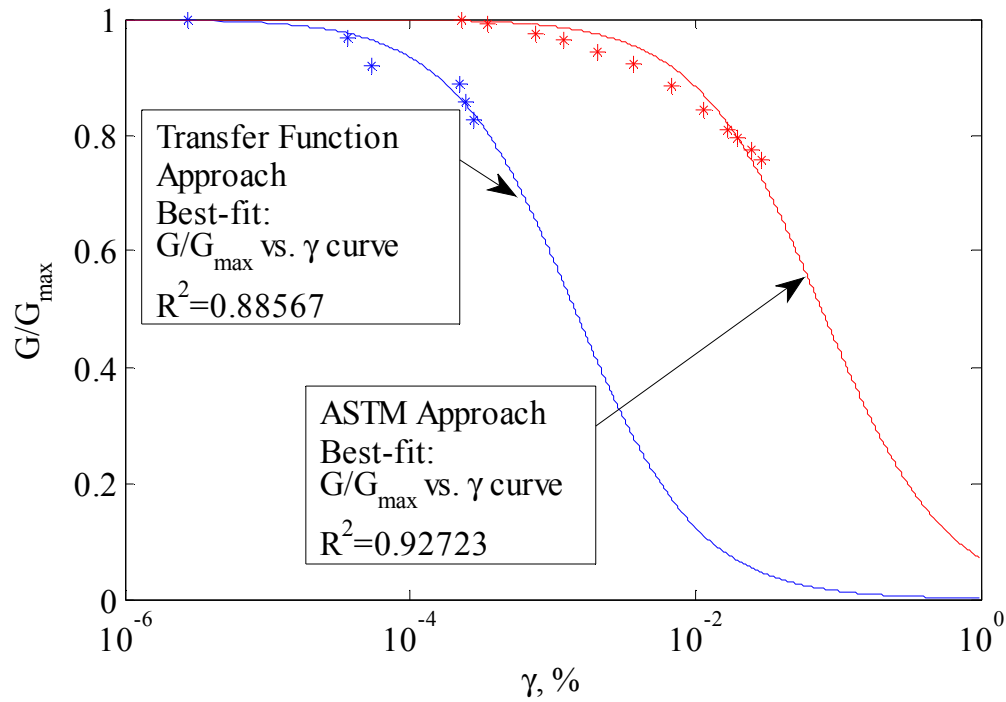


Figure 5.52: G/G_{\max} curve comparisons at confining pressure 344.7 kPa (50 psi).

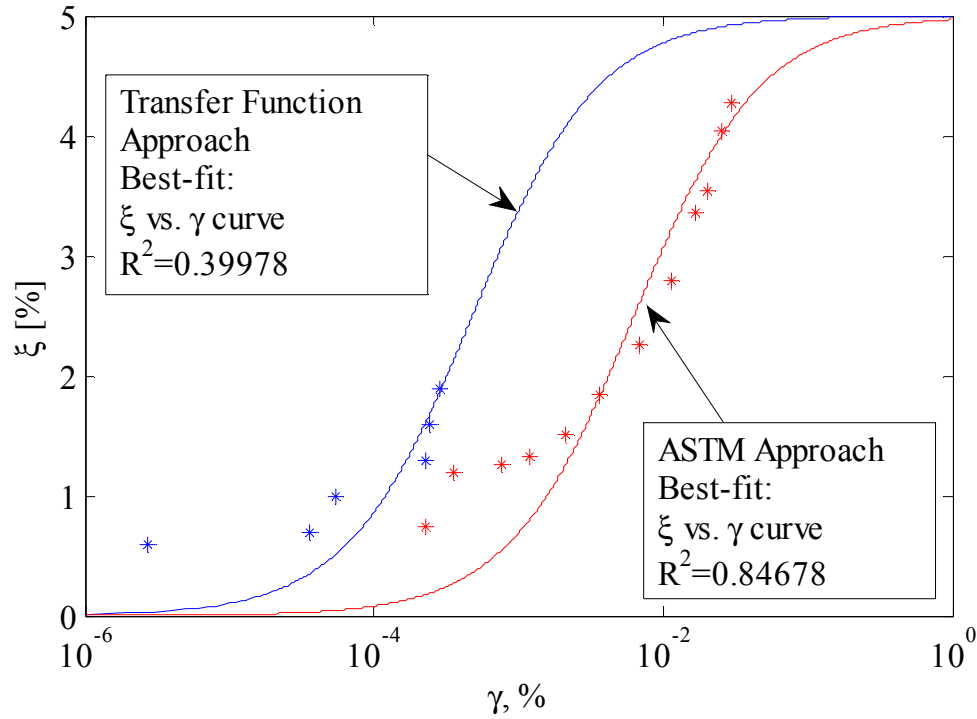


Figure 5.53: ξ curve comparisons at confining pressure 344.7 kPa (50 psi).

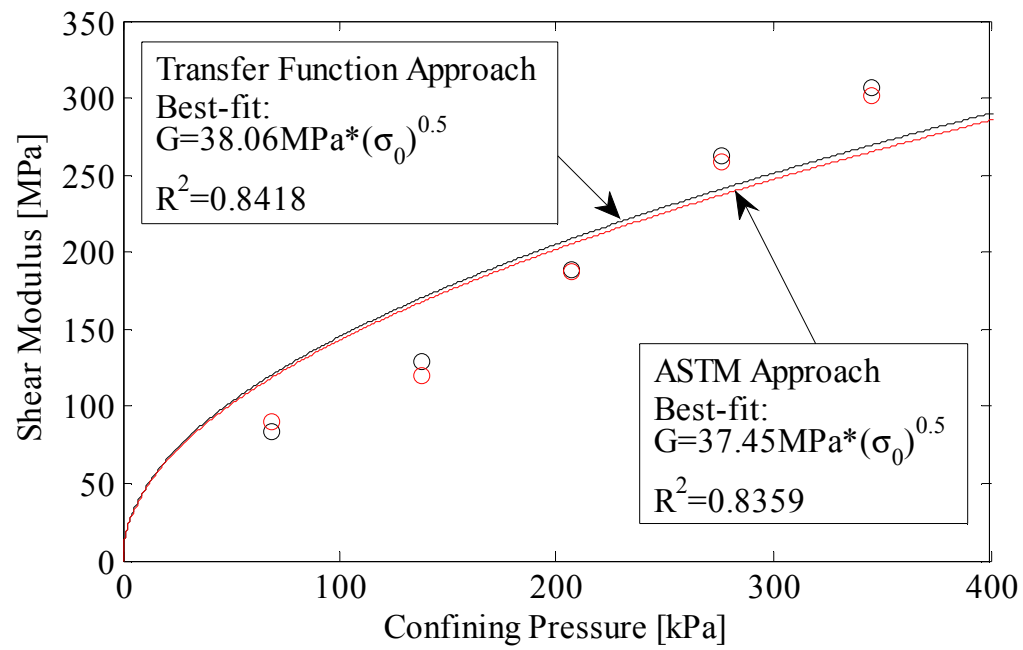


Figure 5.54: Best-fit maximum shear modulus vs. confining pressure curve comparisons.

Table 5.9: Results of ASTM method using RCDARE.

	Undamped Nat. Freq. f_n [Hz]	Modulus G [MPa]	Strain Amplitude [%]	Damping Ratio [%]
344.7 kPa (50 psi)	85.01	302.03	2.27E-04	0.740
	84.68	299.50	3.53E-04	1.184
	83.96	294.24	7.64E-04	1.266
	83.51	290.97	1.21E-03	1.331
	82.73	285.32	2.10E-03	1.507
	81.75	278.22	3.65E-03	1.840
	80.14	266.72	6.84E-03	2.258
	78.45	254.77	1.13E-02	2.785
	76.89	243.79	1.68E-02	3.354
	76.30	239.69	2.01E-02	3.545
	75.43	233.48	2.51E-02	4.049
	74.73	228.64	2.95E-02	4.276
275.8 kPa (40 psi)	74.35	227.80	2.91E-04	1.014
	73.90	224.73	5.33E-04	1.301
	73.41	221.47	9.84E-04	1.267
	72.64	216.34	2.10E-03	1.279
	71.97	211.85	3.74E-03	1.377
	70.93	204.86	6.51E-03	1.541
	69.90	197.83	9.95E-03	1.756
	68.60	188.59	1.71E-02	2.418
	67.36	179.11	2.66E-02	3.392
	66.53	171.72	3.65E-02	4.830
	65.86	165.45	4.33E-02	5.621
	65.38	160.09	5.15E-02	6.668
	64.87	153.06	6.07E-02	8.428
206.8 kPa (30 psi)	59.35	176.78	4.38E-03	2.30
	59.21	172.54	4.97E-03	2.50
	59.05	171.61	5.90E-03	2.68
	58.71	166.71	8.00E-03	2.97
	58.07	159.13	1.27E-02	3.60

Table 5.9: continued

206.8 kPa (30 psi)	57.47	153.35	1.65E-02	3.92
	57.15	150.54	1.99E-02	4.18
	56.85	148.06	2.22E-02	4.42
	56.78	147.46	2.29E-02	4.56
	56.51	145.24	2.65E-02	4.99
	55.94	141.10	3.13E-02	5.28
	55.88	140.57	3.29E-02	5.53
	55.80	139.60	3.66E-02	6.27
	55.71	139.18	3.57E-02	5.99
137.9 kPa (20 psi)	52.03	119.76	4.55E-04	1.73
	51.16	115.35	8.26E-04	2.09
	50.72	113.23	1.47E-03	1.96
	50.49	112.11	1.79E-03	2.05
	50.04	109.94	2.40E-03	2.24
	49.36	106.73	3.91E-03	2.50
	48.51	102.83	6.48E-03	2.77
	47.88	100.01	8.90E-03	2.89
	47.68	99.12	1.01E-02	3.00
	47.25	97.22	1.28E-02	3.17
	47.12	96.61	1.47E-02	3.37
	46.67	94.69	1.76E-02	3.43
	46.43	93.64	2.01E-02	3.60
	46.36	93.29	2.21E-02	3.83
	46.17	92.44	2.52E-02	4.03
69.8 kPa (10 psi)	45.49	90.10	3.48E-04	1.56
	44.82	87.25	4.31E-04	2.60
	44.05	84.14	6.47E-04	2.93
	43.62	82.48	8.89E-04	2.79
	43.29	81.21	1.14E-03	2.76
	42.92	79.76	1.51E-03	2.96
	42.13	76.78	2.50E-03	3.04

Table 5.9: continued

69.8 kPa (10 psi)	41.40	74.07	4.11E-03	3.16
	40.79	71.82	5.64E-03	3.40
	40.63	71.20	6.11E-03	3.63
	40.15	69.45	7.64E-03	3.89
	39.82	68.27	8.92E-03	4.01
	39.56	67.32	1.02E-02	4.24
	39.24	66.20	1.22E-02	4.35
	39.12	65.77	1.39E-02	4.42
	38.77	64.52	1.60E-02	4.68

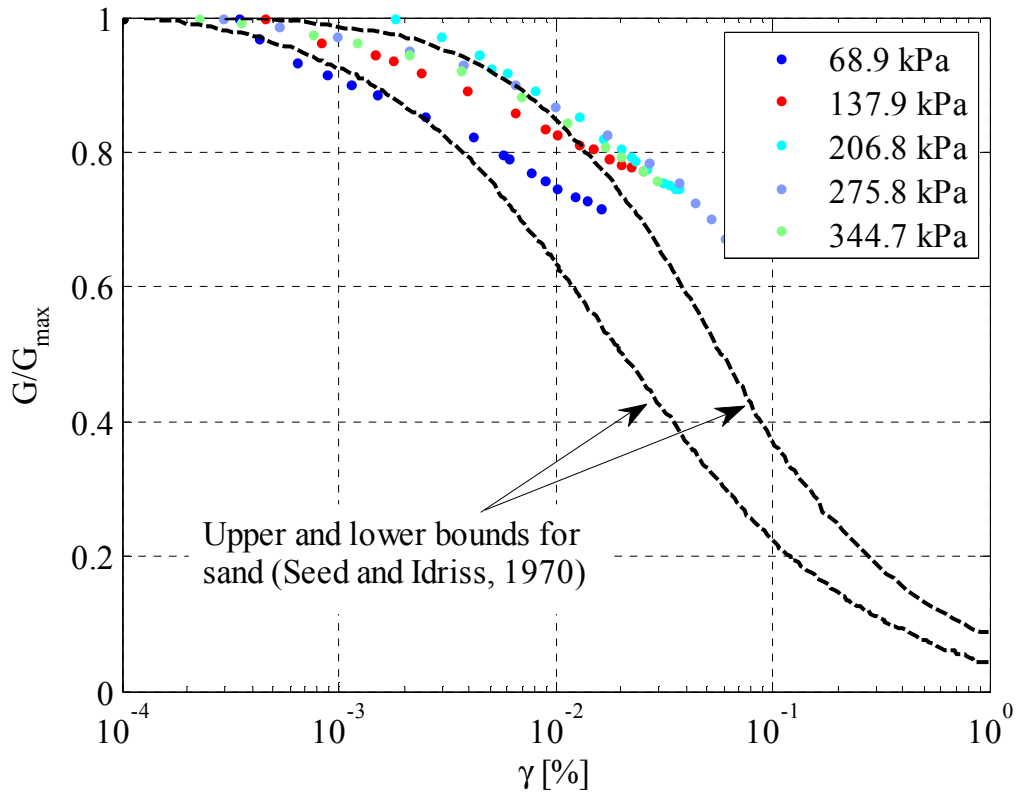


Figure 5.55: Comparison of ASTM G/G_{max} vs. γ to previous studies (ISU 2.8"×11.2" specimen). Modified from Seed and Idriss (1970).

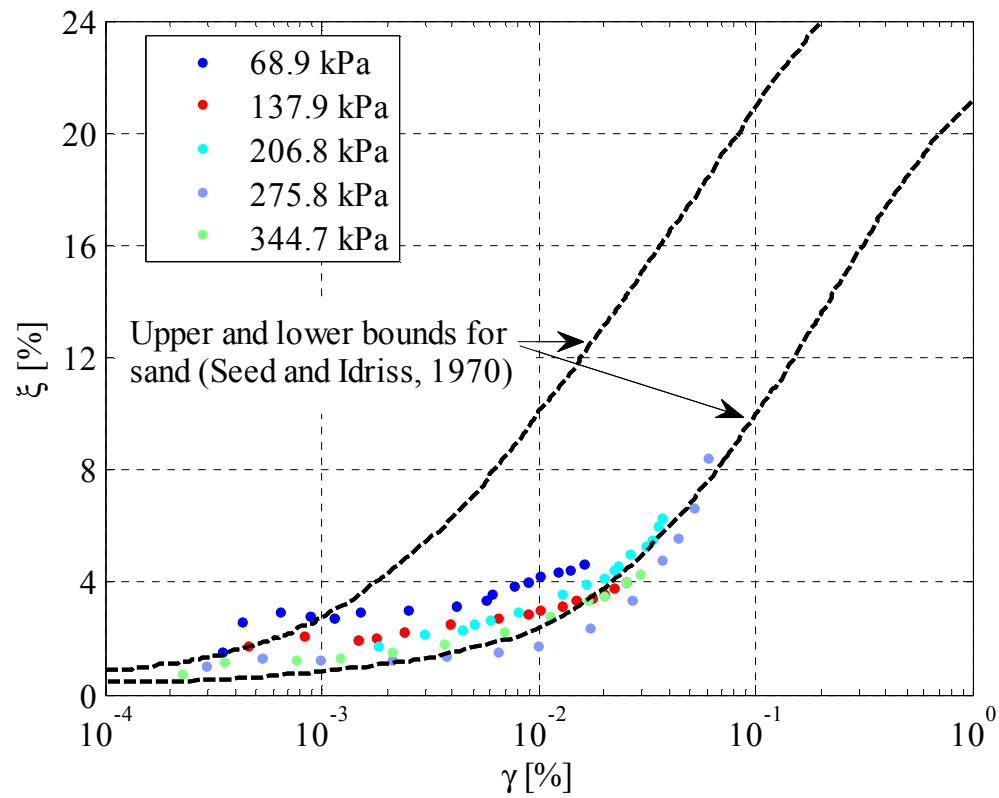


Figure 5.56: Comparison of ASTM ξ vs. γ to previous studies (ISU 2.8"×11.2" specimen) Modified from Seed and Idriss (1970).

CHAPTER 6. CONCLUSIONS AND RECOMMENDATIONS

In this study, the application of random vibration techniques to resonant column testing of soils was investigated. A free-free resonant column device was successfully built and modified to accommodate the new approach. The corresponding theoretical rotational displacement/displacement, displacement/torque, and velocity/torque transfer functions and arithmetic average strains were derived and programmed. White noise and swept-sine excitation were used to test various sizes of specimens at different strain levels. The highest strain level was obtained using swept sine excitation to test a 0.711 meter (2.8 inch) diameter and 0.279 meter (11 inch) high sample. Good agreement between theoretical and experimental transfer functions was obtained using a least squares fitting approach. Multi-modal frequency domain responses were measured for dry sand specimens, and transfer function peaks at multiple frequencies were independently fit by different shear moduli and damping ratios. For the same specimens arithmetic average and RMS strain spectra were obtained in the frequency domain. Reasonable trends of nonlinear strain-dependent modulus and damping curves were found using the transfer function approach. A number of device-dependent calibrations and issues such as back-emf, base fixity and eddy currents are avoided by using the new transfer function approach.

For the ASTM Standard D4015-07 single-frequency resonance approach, the resonant column device was successfully calibrated using a large steel auxiliary plate. The second lowest frequency was used to establish system resonance, for which the Lissajous plot forms a straight line with negative slope. When this frequency was close to the apparatus resonant frequency, the lowest resonant frequency was used instead, for which the Lissajous plot forms a straight line with positive slope. The spreadsheet RCDARE was successfully

modified for the ASTM approach data reduction procedure for the 2DOF free-free device. Reasonable nonlinear strain dependent modulus and damping curves were obtained from RCDARE.

The same soil specimens were evaluated using the two approaches, and excellent agreement was found in the G_{max} versus confining pressure curves. Comparisons of G/G_{max} and ζ curves between the two approaches showed that the ASTM approach imparts larger strains than the transfer function approach, as the sinusoidal excitation of the ASTM approach concentrates the energy at a single frequency, while the random or swept-sine excitations of transfer function approach distributes the energy over a wide frequency band. Comparison of ASTM results to previous studies shows that the shear modulus and damping ratio versus shear strain relationships of this study are similar to those of previous studies on sands.

Based on the results of this study, several recommendations can be made for future studies:

1. In this study, it was found that the spatial RMS strain and arithmetic average strain measures from the transfer function approach both produce a significant difference from the average strain of the ASTM approach. In order to reconcile the results of the two approaches (broadband transfer function vs. single-frequency), the “equivalent” strain measures using the transfer function approach should be investigated in future studies. In particular, it should be determined whether the strain energy over the entire excitation frequency range should be included in the definition of the average shear strain for modulus and damping curves.

2. It is recommended that the active geophones be removed from the device, as only the passive end geophones were used to establish the resonant frequency. The active geophones were only needed for device calibration. However, during high excitation tests, the seismic mass magnets in the active geophones rattled as they impacted their physical stops. The impacts caused significant noise in device measurements over a large range of frequency, and thus limited the excitation amplitude that could be applied. The geophones can be replaced by the active platen accelerometers in the calibration procedure.
3. It is recommended that the bottom accelerometers be mounted on the base outside of the chamber. This will avoid the need to waterproof the accelerometers in tests using a fluid confining medium, and will simplify the device assembly as the accelerometer wires would not need to be passed through the pressure chamber lid. Additionally, the passive geophones could then be connected to the four channel feed-through connector block on the top lid instead of being routed through a separate hole. The amplitude of the new experimental transfer function should then be multiplied by the ratio of the radius of accelerometers on top and bottom according to Eq. (3.56).
4. Porous stones were used with the 2.8 inch platens to increase the friction between the specimen and surface of the platen. Without the porous stones, the specimens may slide against the platen interfaces, causing artificially high damping ratios and low shear moduli. However, the porous stones were attached with only two screws each, which may introduce additional vibration modes at higher

frequencies. It should be determined whether a more rigid platen to porous stone connection is needed.

5. In this study, it was found that the results were very sensitive to the time when using ASTM approach. For example, a delay of 45 minutes could cause a 4% difference in the resonant frequency. Time effects on RC test results have been examined in many previous studies. The effects of time on the measured modulus and damping from the ASTM and transfer function methods are recommended for future studies.
6. In this study, performing tests from low to high confining pressures gave different results from tests performed from high to low confining pressures. It is recommended to study the effects of stress history on RC results via the ASTM and transfer function methods.

BIBLIOGRAPHY

- Aggour, M. S., Taha, M. R., Tawfiq, K. S. and Amini, F. (1989). "Cohesive Soil Behavior Under Random Excitation Conditions." *Geotechnical Testing Journal*, 12(2), pp 135-142.
- Amini, F., Tawfiq, K. S. and Aggour, M. S. (1988). "Cohesionless Soil Behavior Under Random Excitation Conditions." *Journal of Geotechnical Engineering*, 114(8), pp 869-914.
- Ashlock, J. C. and Pak, R.Y.S. (2010a). "Application of Random Vibration Techniques to Resonant Column Testing." *GeoFlorida 2010*, ASCE, Paper No. 750, 11 pgs.
- Ashlock, J. C. and Pak, R.Y.S. (2010b). "Multi-modal Synthesis and Variable Modulus Effects in Resonant Column Tests by Random Excitations." *Fifth International Conference on Recent Advances in Geotechnical Earthquake Engineering and Soil Dynamics*, San Diego, CA, Paper No. 1.31 b, 9 pgs.
- Ashmawy, A. and Drnevich, V.P. (1994). "General Dynamic Model for the Resonant Column/Quasi-Static Torsional Shear Apparatus." *Geotechnical Testing Journal*, ASTM, Vol. 17, No. 3, September, pp 337-348.
- ASTM Standard, D4015-07 2007). "Standard Test Methods for Modulus and Damping of Soils by Resonant-Column Method." ASTM International, West Coshohocken, PA, DOI: 10.1520/D4015-07, www.astm.org.
- Bendat, J. S., and Piersol, A.G. (2010). *Random data: analysis and measurement procedures*. Wiley, New York.
- Cascante, G., Santamarina, C. and Yassir, N. (1998). "Flexural Excitation in a Standard Torsional-Resonant Column Device." *Canadian Geotechnical Journal*, 35(3), pp 478-490.
- Cascante, G., Vanderkooy, J. and Chung, W. (2005). "A New Mathematical Model for Resonant-Column Measurements including Eddy-Current Effects." *Canadian Geotechnical Journal*, 42(1), pp 121-135.
- Chen, A. T. F. and Stokoe, K. H., II (1979), "Interpretation of Strain-Dependent Modulus and Damping From Torsion Soil Tests." United States Geological Survey Report NTIS-PB-298479/AS.
- Drnevich, V. P. (1978). "Resonant Column Test: Final Report", submitted to U. S. Army Engineer Waterways Experiment Station, July 1978
- Soil Dynamics Instruments, Inc. (SDI) (1987), "Free Resonant Column Apparatus User's Manual" for U. S. Dept. of the Interior Bureau of Reclamation, Lexington, Kentucky.

- Hardin, B. O. (1965). "The Nature of Damping in Sands." *Journal of Soil Mechanics and Foundations Division, ASCE*, No. SM 1, pp 63-97.
- Hardin, B. O. and Drnevich, V. P. (1972). "Shear Modulus and Damping in Soils: Design Equation and Curves," *Journal of Soil Mechanics and Foundation Division, ASCE*, Vol. 98, No. SM7, pp. 667-692. With permission from ASCE.
- Isenhower, W. M., Stooe, K. H., II and Allen, J. C. (1987). "Instrumentation for Torsional Shear/Resonant Column Measurements under Anisotropic Stresses." *Geotechnical Testing Journal*. 10(4), 183-191.
- Kumar, J. and Madhusudhan B. N. (2009). "On Determining the Elastic Modulus of a Cylindrical Sample subjected to Flexural Excitation in a Resonant Column Apparatus." *Canadian Geotechnical Journal*, 47, pp 1288-1298.
- Makarechi, H. (1981), "Effects of Grain Size Distribution on Dynamic of Granular Soils at Small Strains." MS thesis. University of California at Los Angeles.
- Meng, J. and Rix, G. J. (2003). "Reduction of Equipment-Generated Damping in Resonant Column Measurements." *Geotechniques* 53, No. 5, pp 503-512.
- Novak, M. and Kim, T. C. (1981). "Resonant Column Technique for Dynamic Testing of Cohesive Soils." *Canadian Geotechnical Journal*, Vol. 18, pp 448-455.
- Seed, H. B., Wong, R. T., Idriss, I. M. and Tokimatsu, k. (1986). "Moduli and Damping Factors for Dynamic Analyses of Cohesionless Soils." *Journal of Geotechnical Engineering*, Vol. 112, No. 11, pp 1016-1032.
- Wang, Y., Cascant, G. and Santamarina, C. (2003). "Resonant Column Testing: The Inherent Counter EMF Effect." *Geotechnical Testing Journal*, Vol. 26, No.3, pp 342-352.

APPENDIX A. RESONANT COLUMN EQUATION DERIVATION

The polar mass moment of inertia of the cylinder specimen and platens can be calculated as

$$J_s = \int_v r^2 dm = \int_A r^2 \rho h dA = \rho h I_s \quad (\text{A.1})$$

$$J_p = \int_v r_t^2 dm \quad (\text{A.2})$$

$$J_a = \int_v r_b^2 dm \quad (\text{A.3})$$

The polar 2nd moment of area of the specimen is given as

$$I_s = \int_A r^2 dA = \int_0^{2\pi} \int_0^{a_0} r^2 r \cdot dr d\theta = 2\pi \int_0^{a_0} r^3 dr = \frac{\pi a_0^4}{2} \quad (\text{A.4})$$

Considering the specimen as the Kelvin-Voigt model with viscous damping, the shear stress is given as

$$\tau = G\gamma + \eta\dot{\gamma} \quad (\text{A.5})$$

The shear strain and strain rate are expressed as

$$\gamma = r \frac{\partial \varphi}{\partial z} \quad (\text{A.6})$$

$$\dot{\gamma} = r \frac{\partial}{\partial t} \left(\frac{\partial \varphi}{\partial z} \right) \quad (\text{A.7})$$

where φ is the angle of twist along the specimen axis. Substituting Eqs. (A.6) and (A.7) into (A.5) gives

$$\tau = G \cdot r \frac{\partial \varphi}{\partial z} + \eta \cdot r \frac{\partial}{\partial t} \left(\frac{\partial \varphi}{\partial z} \right) \quad (\text{A.8})$$

The torque can be calculated by integrating the first moment of shear stress over the specimen area,

$$T = \int_A \tau r dA \quad (\text{A.9})$$

Substituting Eq. (A.8) into (A.9) gives

$$T = \int_A \left(G \frac{\partial \varphi}{\partial z} + \eta \frac{\partial}{\partial t} \left(\frac{\partial \varphi}{\partial z} \right) \right) \cdot r^2 dA \quad (\text{A.10})$$

from which

$$T = \left(G \frac{\partial \varphi}{\partial z} + \eta \frac{\partial}{\partial t} \left(\frac{\partial \varphi}{\partial z} \right) \right) \cdot I_s \quad (\text{A.11})$$

Taking the derivative with respect to height for a homogeneous sample with uniform radius gives

$$\frac{\partial T}{\partial z} = \left(G \frac{\partial^2 \varphi}{\partial z^2} + \eta \frac{\partial}{\partial t} \left(\frac{\partial^2 \varphi}{\partial z^2} \right) \right) \cdot I_s \quad (\text{A.12})$$

The E.O.M. for a differential slice of the specimen (Figure A.1) can be written as

$$\sum T = dT = \int_V r(r\ddot{\varphi})dm = \int_A r^2 \ddot{\varphi} \rho dz dA = \rho \ddot{\varphi} dz \cdot I_s \quad (\text{A.13})$$

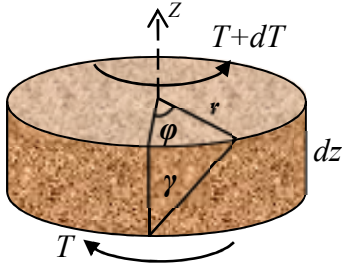


Figure A.1: Differential slice of specimen

Expressing the total differential in Eq. (A.13) in terms of the partial derivative as by

$$dT = \frac{\partial T}{\partial z} dz \text{ and dividing by } dz \text{ gives}$$

$$\frac{\partial T}{\partial z} = \rho \ddot{\varphi} I_s \quad (\text{A.14})$$

Combining Eqs. (A.12) and (A.14) gives

$$\frac{\partial T}{\partial z} = \left(G \frac{\partial^2 \varphi}{\partial z^2} + \eta \frac{\partial}{\partial t} \left(\frac{\partial^2 \varphi}{\partial z^2} \right) \right) \cdot I_s = \rho \ddot{\varphi} I_s \quad (\text{A.15})$$

For harmonic motion, the angle of twist can be expressed as

$$\varphi = \varphi(z, t) \quad (\text{A.16})$$

and assuming the governing differential equation is separable, the angle of twist along the specimen can be written as

$$\varphi(z, t) = \theta(z) \cdot e^{i\omega t} \quad (\text{A.17})$$

Dividing Eq. (A.15) by $G \cdot I_s$ gives the Kelvin-Voigt wave propagation equation as

$$\frac{\partial^2}{\partial z^2} \left(\varphi + \frac{\eta}{G} \frac{\partial \varphi}{\partial t} \right) = \frac{\rho}{G} \left(\frac{\partial^2 \varphi}{\partial t^2} \right) \quad (\text{A.18})$$

Substituting Eq. (A.17) into (A.18) gives

$$\frac{\partial^2}{\partial z^2} \left(G \cdot \theta(z) \cdot e^{i\omega t} + i\omega\eta\theta(z) \cdot e^{i\omega t} \right) = \rho (i\omega)^2 \theta(z) \cdot e^{i\omega t} \quad (\text{A.19})$$

Factoring out and cancelling $e^{i\omega t}$ in the above partial differential equation gives the ordinary differential equation

$$\frac{d^2 \theta}{dz^2} (G + i\omega\eta) = -\rho\omega^2 \cdot \theta(z) \quad (\text{A.20})$$

The complex shear modulus can be defined as

$$G^* \equiv G + i\omega\eta \quad (\text{A.21})$$

Substituting Eq. (A.21) into (A.20) then gives

$$\frac{d^2 \theta}{dz^2} + \frac{\rho\omega^2}{G^*} \theta(z) = 0 \quad (\text{A.22})$$

The angle of twist along the specimen can be written as the solution for Eq. (A.22) as

$$\theta(z) = C_1 e^{iaz} + C_2 e^{-iaz} \quad (\text{A.23})$$

where C_1 and C_2 are complex constants. Defining the complex-valued frequency factor a as

$$a \equiv \omega \sqrt{\frac{\rho}{G^*}} \quad (\text{A.24})$$

and applying the boundary conditions at the active and passive ends, the rotations can be written as

$$\theta_p = \theta(h) = C_1 e^{iah} + C_2 e^{-iah} \quad (\text{A.25})$$

$$\theta_a = \theta(0) = C_1 + C_2 \quad (\text{A.26})$$

Solving for the constants C_1 and C_2 in terms of the rotations gives

$$C_1 = \frac{\theta_p - \theta_a e^{-iah}}{e^{iah} - e^{-iah}} \quad (\text{A.27})$$

$$C_2 = \frac{\theta_p - \theta_a e^{iah}}{e^{-iah} - e^{iah}} \quad (\text{A.28})$$

The torsional stress at any position in the soil specimen can be written as

$$\tau(r, z, t) = G \cdot r \frac{\partial \theta}{\partial z} \cdot e^{i\omega t} + i\omega \eta \cdot r \frac{\partial \theta}{\partial z} \cdot e^{i\omega t} \quad (\text{A.29})$$

Substituting Eq. (A.23) into (A.29) gives

$$\tau(r, z, t) = r(G + i\omega \eta) \left[(ia \cdot C_1 e^{iaz} - ia \cdot C_2 e^{-iaz}) \cdot e^{i\omega t} \right] \quad (\text{A.30})$$

Replacing G^* with Eq. (A.21) in the above Eq. gives

$$\tau(r, z, t) = \tau'(r, z) \cdot e^{i\omega t} \quad (\text{A.31})$$

in which the shear stress at any position in the specimen is defined as

$$\tau'(r, z) \equiv r \cdot G^* \cdot ia(C_1 e^{iaz} - C_2 e^{-iaz}) \quad (\text{A.32})$$

which can also be expressed in terms of the active and passive end platen rotations using Eqs.

(A.27) and (A.28) as

$$\tau'(r, z) = r \cdot G^* \cdot ia \left(\frac{\theta_p - \theta_a e^{-iah}}{e^{iah} - e^{-iah}} \cdot e^{iaz} - \frac{\theta_p - \theta_a e^{iah}}{e^{-iah} - e^{iah}} \cdot e^{-iaz} \right) \quad (\text{A.33})$$

The torsional stress in the soil specimen at the active and passive ends is then given by

$$\tau'(r, h) = r \cdot G^* \cdot ia \left(\frac{\theta_p - \theta_a e^{-iah}}{e^{iah} - e^{-iah}} \cdot e^{iah} - \frac{\theta_p - \theta_a e^{iah}}{e^{-iah} - e^{iah}} \cdot e^{-iah} \right) \quad (\text{A.34})$$

and

$$\tau'(r, 0) = r \cdot G^* \cdot ia \left(\frac{\theta_p - \theta_a e^{-iah}}{e^{iah} - e^{-iah}} - \frac{\theta_p - \theta_a e^{iah}}{e^{-iah} - e^{iah}} \right) \quad (\text{A.35})$$

The two preceding equations can be simplified using Euler's formula to give

$$\tau'(r, h) = r \cdot G^* \cdot a \left[\frac{\theta_p \cos(ah) - \theta_a}{\sin(ah)} \right] \quad (\text{A.36})$$

$$\tau'(r, 0) = r \cdot G^* \cdot a \left[\frac{\theta_p - \theta_a \cos(ah)}{\sin(ah)} \right] \quad (\text{A.37})$$

Based on the free-body diagram of Figure 3.2a, the E.O.M. at the passive end platen can be written as

$$\sum T = J_p \ddot{\phi}(h, t) \quad (\text{A.38})$$

where

$$\sum T = -T(h, t) = -\int_A r \cdot \tau(r, h, t) dA \quad (\text{A.39})$$

i.e.,

$$-\int_A r \cdot \tau'(r, h) \cdot e^{i\omega t} dA = J_p \ddot{\phi}(h, t) \quad (\text{A.40})$$

Substituting Eqs. (A.17) and (A.36) into (A.40) gives

$$-I_s a G^* \cdot \left[\frac{\theta_p \cos(ah) - \theta_a}{\sin(ah)} \right] \cdot e^{i\omega t} = -J_p \omega^2 \cdot \theta_p \cdot e^{i\omega t} \quad (\text{A.41})$$

Dividing Eq. (A.41) by $J_s \omega^2 e^{i\omega t}$ gives

$$\frac{I_s a G^*}{J_s \omega^2} \cdot \left[\frac{\theta_p \cos(ah) - \theta_a}{\sin(ah)} \right] - \frac{J_p}{J_s} \cdot \theta_p = 0 \quad (\text{A.42})$$

Based on Figure 3.2b, the E.O.M. at the active end platen can be written as

$$\sum T = J_a \ddot{\phi}(0, t) \quad (\text{A.43})$$

where

$$\sum T = T_a(t) - \left(-\int_A r \cdot \tau(r, 0, t) dA \right) - c_a \cdot \dot{\phi}(0, t) - k_a \cdot \phi(0, t) \quad (\text{A.44})$$

Combining Eqs. (A.43) and (A.44) gives

$$T_a' \cdot e^{i\omega t} + \int_A r \cdot \tau'(r, 0) \cdot e^{i\omega t} dA - i\omega c_a \cdot \theta_a \cdot e^{i\omega t} - k_a \cdot \theta_a \cdot e^{i\omega t} = J_a \ddot{\phi}(0, t) \quad (\text{A.45})$$

Substituting Eq. (A.17) and (A.37) into (A.45) gives

$$T_a' \cdot e^{i\omega t} + I_s a G^* \cdot \left[\frac{\theta_p - \theta_a \cos(ah)}{\sin(ah)} \right] \cdot e^{i\omega t} - i\omega c_a \cdot \theta_a \cdot e^{i\omega t} - k_a \cdot \theta_a \cdot e^{i\omega t} = -J_a \omega^2 \cdot \theta_a \cdot e^{i\omega t} \quad (\text{A.46})$$

Dividing Eq. (A.46) by $J_a \omega^2 e^{i\omega t}$ gives

$$-\frac{I_s a G^*}{J_s \omega^2} \cdot \left[\frac{\theta_p - \theta_a \cos(ah)}{\sin(ah)} \right] - \frac{J_a}{J_s} \cdot \theta_a + \frac{k_a}{J_s \omega^2} \cdot \theta_a + i \frac{c_a}{J_s \omega} \cdot \theta_a = \frac{T_a'}{J_s \omega^2} \quad (\text{A.47})$$

The following parameters can then be defined and used to simplify Eqs. (A.42) and (A.47) for the passive and active ends; for the case of Kevin-Voigt viscous damping, the damping ratio is defined as

$$\xi(\omega) = \frac{\omega\eta}{2G} \quad (\text{A.48})$$

Substituting Eq. (A.48) into (A.21) gives

$$G^* = G(1 + i \cdot 2\xi) \quad (\text{A.49})$$

where ξ can also be taken as a frequency independent constant for hysteretic damping.

Substituting Eq. (A.49) into (A.24) gives

$$a = \omega \sqrt{\frac{\rho}{G}} (1 + i \cdot 2\xi)^{-\frac{1}{2}} \quad (\text{A.50})$$

The dimensionless frequency is defined as

$$F = \omega h \sqrt{\frac{\rho}{G}} \quad (\text{A.51})$$

and substituting Eq. (A.51) into (A.50) therefore gives

$$a = \frac{F}{h} (1 + i \cdot 2\xi)^{-\frac{1}{2}} \quad (\text{A.52})$$

From Eq. (A.51), the shear modulus can be written as

$$G = \frac{\omega^2 h^2 \rho}{F^2} \quad (\text{A.53})$$

Substituting Eq. (A.53) into (A.49) gives

$$G^* = \frac{\omega^2 h^2 \rho}{F^2} (1 + i \cdot 2\xi) \quad (\text{A.54})$$

Recalling that the polar 2nd moment of area of the specimen is

$$I_s = J_s / \rho h \quad (\text{A.55})$$

and combining Eqs. (A.52), (A.54) and (A.55) gives

$$I_s a G^* = \frac{J_s \omega^2}{F} (1 + i \cdot 2\xi)^{-\frac{1}{2}} (1 + i \cdot 2\xi) \quad (\text{A.56})$$

The complex term $(1+i \cdot 2\xi)^{-\frac{1}{2}}$ can be simplified as

$$(1+i \cdot 2\xi)^{-\frac{1}{2}} = \alpha + i \cdot \beta \quad (\text{A.57})$$

where

$$\alpha = \left(1 + (2\xi)^2\right)^{-\frac{1}{4}} \cdot \cos\left(\frac{\phi}{2}\right) \quad (\text{A.58})$$

$$\beta = -\left(1 + (2\xi)^2\right)^{-\frac{1}{4}} \cdot \sin\left(\frac{\phi}{2}\right) \quad (\text{A.59})$$

$$\phi = \tan^{-1}(2\xi) \quad (\text{A.60})$$

Substituting Eq. (A.57) into (A.56) gives

$$I_s a G^* = \frac{J_s \omega^2}{F} (\alpha + i \cdot \beta)(1 + i \cdot 2\xi) \quad (\text{A.61})$$

Defining the passive end inertia factor as

$$P \equiv \frac{J_p}{J_s} \quad (\text{A.62})$$

the apparatus damping factor as

$$ADF \equiv \frac{c_a}{J_s \omega} \quad (\text{A.63})$$

and the active end inertia factor as

$$T \equiv \frac{J_a}{J_s} - \frac{k_a}{J_s \omega^2} \quad (\text{A.64})$$

It is noted that ω in the Eqs. (A.63) and (A.64) is the fixed value ω_r , which is the system resonant frequency that measured during a test.

Eqs. (A.61) and (A.62) can then be substituted into (A.42) to give

$$\frac{1}{F} (\alpha + i \cdot \beta)(1 + i \cdot 2\xi) \cdot \left[\frac{\theta_p \cos(\alpha F + i \cdot \beta F) - \theta_a}{\sin(\alpha F + i \cdot \beta F)} \right] - P \cdot \theta_p = 0 \quad (\text{A.65})$$

while substituting Eqs. (A.61), (A.63) and (A.64) into (A.47) gives

$$-\frac{1}{F} (\alpha + i \cdot \beta)(1 + i \cdot 2\xi) \cdot \left[\frac{\theta_p - \theta_a \cos(\alpha F + i \cdot \beta F)}{\sin(\alpha F + i \cdot \beta F)} \right] - T \cdot \theta_a + i ADF \cdot \theta_a = \frac{T'_a}{J_s \omega^2} \quad (\text{A.66})$$

The E.O.M. Eqs. (A.65) and (A.66) can be written in matrix form as

$$\begin{bmatrix} a_{11} + ib_{11} & a_{12} + ib_{12} \\ a_{21} + ib_{21} & a_{22} + ib_{22} \end{bmatrix} \begin{bmatrix} \theta_p \\ \theta_a \end{bmatrix} = \begin{bmatrix} 0 \\ \frac{T_a'}{J_s \omega^2} \end{bmatrix} \quad (\text{A.67})$$

The following expressions and applications of Euler's formula can be used to simplify Eqs.

(A.65) and (A.66);

$$(\alpha + i \cdot \beta)(1 + i \cdot 2\xi) = [(\alpha - 2\xi \cdot \beta) + i(2\xi \cdot \alpha + \beta)] \quad (\text{A.68})$$

$$\sin(\alpha F + i \cdot \beta F) = \sin(\alpha F) \cos(i \cdot \beta F) + \cos(\alpha F) \sin(i \cdot \beta F) \quad (\text{A.69})$$

$$\cos(\alpha F + i \cdot \beta F) = \cos(\alpha F) \cos(i \cdot \beta F) - \sin(\alpha F) \sin(i \cdot \beta F) \quad (\text{A.70})$$

$$\cos(i \cdot \beta F) = \cosh(\beta F) \quad (\text{A.71})$$

$$\sin(i \cdot \beta F) = i \cdot \sinh(\beta F)$$

To further simplify the expressions, allow the notation

$$\begin{aligned} \sin(\alpha F) &= si \\ \cos(\alpha F) &= co \\ \sinh(\beta F) &= sh \\ \cosh(\beta F) &= ch \end{aligned} \quad (\text{A.72})$$

as in Ashmawy and Drnevich (1994). Substituting Eqs. (A.71) and (A.72) into (A.69) and

(A.70) gives

$$\sin(\alpha F + i \cdot \beta F) = si \cdot ch + i \cdot co \cdot sh \quad (\text{A.73})$$

$$\cos(\alpha F + i \cdot \beta F) = co \cdot ch - i \cdot si \cdot sh \quad (\text{A.74})$$

$$\frac{1}{\sin(\alpha F + i \cdot \beta F)} = \frac{si \cdot ch - i \cdot co \cdot sh}{(si \cdot ch)^2 + (co \cdot sh)^2} \quad (\text{A.75})$$

$$\frac{\cos(\alpha F + i \cdot \beta F)}{\sin(\alpha F + i \cdot \beta F)} = \frac{co \cdot si - i \cdot ch \cdot sh}{(si \cdot ch)^2 + (co \cdot sh)^2} \quad (\text{A.76})$$

Substituting Eqs. (A.68), (A.75) and (A.76) into (A.65) gives

$$\frac{1}{F} [(\alpha - 2\xi \cdot \beta) + i(2\xi \cdot \alpha + \beta)] \cdot \left[\frac{co \cdot si - i \cdot ch \cdot sh}{(si \cdot ch)^2 + (co \cdot sh)^2} \cdot \theta_p - \frac{si \cdot ch - i \cdot co \cdot sh}{(si \cdot ch)^2 + (co \cdot sh)^2} \cdot \theta_a \right] - P \cdot \theta_p = 0$$

Therefore, the coefficients $a_{11} + ib_{11}$ and $a_{12} + ib_{12}$ in Eq. (A.67) are

$$a_{11} + ib_{11} = \left[\frac{1}{F} \frac{((\alpha - 2\xi \cdot \beta) + i(2\xi \cdot \alpha + \beta)) \times (co \cdot si - i \cdot ch \cdot sh)}{(si \cdot ch)^2 + (co \cdot sh)^2} - P \right] \quad (A.77)$$

$$a_{12} + ib_{12} = \left[-\frac{1}{F} \frac{((\alpha - 2\xi \cdot \beta) + i(2\xi \cdot \alpha + \beta)) \times (si \cdot ch - i \cdot co \cdot sh)}{(si \cdot ch)^2 + (co \cdot sh)^2} \right] \quad (A.78)$$

where

$$a_{11} = \frac{1}{F} \frac{((\alpha \cdot co \cdot si + \beta \cdot ch \cdot sh) + 2\xi \cdot (\alpha \cdot ch \cdot sh - \beta \cdot co \cdot si))}{(si \cdot ch)^2 + (co \cdot sh)^2} - P \quad (A.79)$$

$$b_{11} = \frac{1}{F} \frac{((- \alpha \cdot ch \cdot sh + \beta \cdot co \cdot si) + 2\xi \cdot (\alpha \cdot co \cdot si + \beta \cdot ch \cdot sh))}{(si \cdot ch)^2 + (co \cdot sh)^2} \quad (A.80)$$

$$a_{12} = \frac{1}{F} \frac{(-(\alpha \cdot si \cdot ch + \beta \cdot co \cdot sh) + 2\xi \cdot (-\alpha \cdot co \cdot sh + \beta \cdot si \cdot ch))}{(si \cdot ch)^2 + (co \cdot sh)^2} \quad (A.81)$$

$$b_{12} = \frac{1}{F} \frac{((\alpha \cdot co \cdot sh - \beta \cdot si \cdot ch) + 2\xi \cdot (-\alpha \cdot si \cdot ch - \beta \cdot co \cdot sh))}{(si \cdot ch)^2 + (co \cdot sh)^2} \quad (A.82)$$

Substituting Eqs. (A.68), (A.75) and (A.76) into (A.66) gives

$$-\frac{1}{F} [(\alpha - 2\xi \cdot \beta) + i(2\xi \cdot \alpha + \beta)] \cdot \left[\frac{si \cdot ch - i \cdot co \cdot sh}{(si \cdot ch)^2 + (co \cdot sh)^2} \cdot \theta_p - \frac{co \cdot si - i \cdot ch \cdot sh}{(si \cdot ch)^2 + (co \cdot sh)^2} \cdot \theta_a \right] - T \cdot \theta_a + iADF \cdot \theta_a = \frac{T'_a}{J_s \omega^2}$$

Therefore, the coefficients $a_{21} + ib_{21}$ and $a_{22} + ib_{22}$ in Eq. (A.67) are

$$a_{21} + ib_{21} = \left[-\frac{1}{F} \frac{((\alpha - 2\xi \cdot \beta) + i(2\xi \cdot \alpha + \beta)) \times (si \cdot ch - i \cdot co \cdot sh)}{(si \cdot ch)^2 + (co \cdot sh)^2} \right] \quad (A.83)$$

$$a_{22} + ib_{22} = \left[\frac{1}{F} \frac{((\alpha - 2\xi \cdot \beta) + i(2\xi \cdot \alpha + \beta)) \times (co \cdot si - i \cdot ch \cdot sh)}{(si \cdot ch)^2 + (co \cdot sh)^2} - T + iADF \right] \quad (A.84)$$

from which

$$a_{21} = a_{12} \quad (A.85)$$

$$b_{21} = b_{21} \quad (A.86)$$

$$a_{22} = \frac{1}{F} \frac{((\alpha \cdot co \cdot si + \beta \cdot ch \cdot sh) + 2\xi \cdot (\alpha \cdot ch \cdot sh - \beta \cdot co \cdot si))}{(si \cdot ch)^2 + (co \cdot sh)^2} - T \quad (A.87)$$

$$b_{22} = \frac{1}{F} \frac{((- \alpha \cdot ch \cdot sh + \beta \cdot co \cdot si) + 2\xi \cdot (\alpha \cdot co \cdot si + \beta \cdot ch \cdot sh))}{(si \cdot ch)^2 + (co \cdot sh)^2} + ADF \quad (A.88)$$

The following parameters may then be defined to simplify the coefficients in the matrix;

$$\mu_1 = \frac{1}{F} \frac{(\alpha \cdot co \cdot si + \beta \cdot ch \cdot sh)}{(si \cdot ch)^2 + (co \cdot sh)^2} \quad (\text{A.89})$$

$$\mu_2 = \frac{1}{F} \frac{-(\alpha \cdot si \cdot ch + \beta \cdot co \cdot sh)}{(si \cdot ch)^2 + (co \cdot sh)^2} \quad (\text{A.90})$$

$$\nu_1 = \frac{1}{F} \frac{(-\alpha \cdot ch \cdot sh + \beta \cdot co \cdot si)}{(si \cdot ch)^2 + (co \cdot sh)^2} \quad (\text{A.91})$$

$$\nu_2 = \frac{1}{F} \frac{(\alpha \cdot co \cdot sh - \beta \cdot si \cdot ch)}{(si \cdot ch)^2 + (co \cdot sh)^2} \quad (\text{A.92})$$

$$\mu_3 = -2\xi \cdot \nu_1 \quad (\text{A.93})$$

$$\mu_4 = -2\xi \cdot \nu_2 \quad (\text{A.94})$$

$$\nu_3 = 2\xi \cdot \mu_1 \quad (\text{A.95})$$

$$\nu_4 = 2\xi \cdot \mu_2 \quad (\text{A.96})$$

The matrix coefficients can be then simplified as

$$a_{11} = \mu_1 + \mu_3 - P \quad (\text{A.97})$$

$$b_{11} = \nu_1 + \nu_3$$

$$a_{12} = \mu_2 + \mu_4 \quad (\text{A.98})$$

$$b_{12} = \nu_2 + \nu_4$$

$$a_{21} = \mu_2 + \mu_4 \quad (\text{A.99})$$

$$b_{12} = \nu_2 + \nu_4$$

$$a_{22} = \mu_1 + \mu_3 - T \quad (\text{A.100})$$

$$b_{22} = \nu_1 + \nu_3 + ADF$$

Using Cramer's rule, the matrix (A.67) can be inverted to obtain the explicit solution for the angles of twist θ_p and θ_a as,

$$\begin{bmatrix} \theta_p \\ \theta_a \end{bmatrix} = \begin{bmatrix} y_{11} + iz_{11} & y_{12} + iz_{12} \\ y_{21} + iz_{21} & y_{22} + iz_{22} \end{bmatrix} \begin{bmatrix} 0 \\ \frac{T'_a}{J_s \omega^2} \end{bmatrix} \quad (\text{A.101})$$

where

$$\begin{bmatrix} y_{11} + iz_{11} & y_{12} + iz_{12} \\ y_{21} + iz_{21} & y_{22} + iz_{22} \end{bmatrix} = \begin{bmatrix} a_{11} + ib_{11} & a_{12} + ib_{12} \\ a_{21} + ib_{21} & a_{22} + ib_{22} \end{bmatrix}^{-1} \quad (\text{A.102})$$

Defining parameters g_1 and g_2 as

$$g_1 = (a_{11}a_{22} - a_{12}a_{21} - b_{11}b_{22} + b_{12}b_{21}) \quad (\text{A.103})$$

$$g_2 = (a_{11}b_{22} + a_{22}b_{11} - a_{12}b_{21} - a_{21}b_{12}) \quad (\text{A.104})$$

The inverted matrix can be written as

$$\begin{bmatrix} a_{11} + ib_{11} & a_{12} + ib_{12} \\ a_{21} + ib_{21} & a_{22} + ib_{22} \end{bmatrix}^{-1} = \frac{g_1 - ig_2}{g_1^2 + g_2^2} \begin{bmatrix} a_{22} + ib_{22} & -(a_{12} + ib_{12}) \\ -(a_{21} + ib_{21}) & a_{11} + ib_{11} \end{bmatrix} \quad (\text{A.105})$$

where the coefficients in matrix (A.101) can be simplified

$$y_{ij} = \frac{m_{ij} \cdot g_1 + n_{ij} \cdot g_2}{g_1^2 + g_2^2} \quad (\text{A.106})$$

$$z_{ij} = \frac{-m_{ij} \cdot g_2 + n_{ij} \cdot g_1}{g_1^2 + g_2^2} \quad (\text{A.107})$$

where

$$\begin{aligned} m_{11} &= a_{22} \\ m_{12} &= -a_{12} \\ m_{21} &= -a_{21} \\ m_{22} &= a_{11} \end{aligned} \quad (\text{A.108})$$

$$\begin{aligned} n_{11} &= b_{22} \\ n_{12} &= -b_{12} \\ n_{21} &= -b_{21} \\ n_{22} &= b_{11} \end{aligned} \quad (\text{A.109})$$

The above solution of the matrix equation then gives the platen rotations.

To obtain the specimen rotation at any location along the specimen axis, Eq. (A.27)

can be expressed using Euler's formula as

$$C_1 = \frac{\theta_p - \theta_a (\cos ah - i \sin ah)}{\cos ah + i \sin ah - \cos ah - i \sin ah} \quad (\text{A.110})$$

Recalling $ah = (\alpha F + i\beta F)$ and substituting into the above Eq. gives

$$C_1 = \frac{\theta_p - \theta_a [\cos(\alpha F + i\beta F) - i \sin(\alpha F + i\beta F)]}{\cos(\alpha F + i\beta F) + i \sin(\alpha F + i\beta F) - \cos(\alpha F + i\beta F) - i \sin(\alpha F + i\beta F)} \quad (\text{A.111})$$

Substituting Eqs. (A.69), (A.70), (A.71) and (A.72) into (A.111) gives

$$C_1 = \frac{\theta_p - \theta_a (co \cdot ch - i \cdot si \cdot sh - i \cdot si \cdot ch + co \cdot sh)}{-2(co \cdot sh - i \cdot si \cdot ch)} \quad (\text{A.112})$$

$$C_1 = \frac{[\theta_p - \theta_a (co \cdot ch - i \cdot si \cdot sh - i \cdot si \cdot ch + co \cdot sh)] \times (co \cdot sh + i \cdot si \cdot ch)}{-2(co \cdot sh - i \cdot si \cdot ch) \times (co \cdot sh + i \cdot si \cdot ch)} \quad (\text{A.113})$$

$$C_1 = \frac{-0.5}{(co \cdot sh)^2 + (si \cdot ch)^2} [\theta_p (co \cdot sh + i \cdot si \cdot ch) - \theta_a (co(ch + sh) - i \cdot si(ch + sh)) \times (co \cdot sh + i \cdot si \cdot ch)] \quad (A.114)$$

Denoting the rotations in terms of their real and imaginary components, i.e.

$$\theta_p = \theta_{pr} + i\theta_{pi} \quad (A.115)$$

$$\theta_a = \theta_{ar} + i\theta_{ai} \quad (A.116)$$

and substituting Eqs. (A.115) and (A.116) into (A.114) gives

$$C_1 = \frac{-0.5}{(co \cdot sh)^2 + (si \cdot ch)^2} [(\theta_{pr} + i\theta_{pi})(co \cdot sh + i \cdot si \cdot ch) - (\theta_{pr} + i\theta_{pi})(co(ch + sh) - i \cdot si(ch + sh)) \times (co \cdot sh + i \cdot si \cdot ch)] \quad (A.117)$$

Separating real and imaginary components in Eq. (A.117) gives

$$C_{1r} = \frac{-0.5}{(co \cdot sh)^2 + (si \cdot ch)^2} \{co \cdot sh[\theta_{pr} - (ch + sh)(\theta_{ar}co + \theta_{ai}si)] - si \cdot ch[\theta_{pi} - (ch + sh)(-\theta_{ar}si + \theta_{ai}co)]\} \quad (A.118)$$

$$C_{1i} = \frac{-0.5}{(co \cdot sh)^2 + (si \cdot ch)^2} \{si \cdot ch[\theta_{pr} - (ch + sh)(\theta_{ar}co + \theta_{ai}si)] + co \cdot sh[\theta_{pi} - (ch + sh)(-\theta_{ar}si + \theta_{ai}co)]\} \quad (A.119)$$

Defining

$$\lambda_r = \theta_{pr} - (ch + sh)(\theta_{ar}co + \theta_{ai}si) \quad (A.120)$$

$$\lambda_i = \theta_{pi} - (ch + sh)(-\theta_{ar}si + \theta_{ai}co) \quad (A.121)$$

Substituting Eqs. (A.120) and (A.121) into (A.118) and (A.119)

$$C_{1r} = \frac{-0.5}{(co \cdot sh)^2 + (si \cdot ch)^2} (\lambda_r co \cdot sh - \lambda_i si \cdot ch) \quad (A.122)$$

$$C_{1i} = \frac{-0.5}{(co \cdot sh)^2 + (si \cdot ch)^2} (\lambda_r si \cdot ch + \lambda_i co \cdot sh) \quad (A.123)$$

Recalling Eq. (A.26), the complex constant C_2 can be calculated as

$$C_2 = \theta_a - C_1 \quad (A.124)$$

Separating real and imaginary components gives

$$C_{2r} = \theta_{ar} - C_{1r} \quad (A.125)$$

$$C_{2i} = \theta_{ai} - C_{1i} \quad (A.126)$$

The rotation along the specimen in Eq. (A.23) can be expressed using Euler's formula as

$$\theta(z) = C_1 (\cos az + i \sin az) + C_2 (\cos az - i \sin az) \quad (\text{A.127})$$

where

$$\cos az = \cos \left(\alpha F \frac{z}{h} + i \beta F \frac{z}{h} \right) \quad (\text{A.128})$$

$$\sin az = \sin \left(\alpha F \frac{z}{h} + i \beta F \frac{z}{h} \right) \quad (\text{A.129})$$

Defining the notation

$$\sin \left(\alpha F \frac{z}{h} \right) \equiv si^* \quad (\text{A.130})$$

$$\cos \left(\alpha F \frac{z}{h} \right) \equiv co^* \quad (\text{A.131})$$

$$\sinh \left(\beta F \frac{z}{h} \right) \equiv sh^* \quad (\text{A.132})$$

$$\cosh \left(\beta F \frac{z}{h} \right) \equiv ch^* \quad (\text{A.133})$$

The rotation can be written as

$$\begin{aligned} \theta(z) = & C_1 (co^* \cdot ch^* - i \cdot si^* \cdot sh^* + i \cdot si^* \cdot ch^* - co^* \cdot sh^*) \\ & + C_2 (co^* \cdot ch^* - i \cdot si^* \cdot sh^* - i \cdot si^* \cdot ch^* + co^* \cdot sh^*) \end{aligned} \quad (\text{A.134})$$

where

$$C_1 = C_{1r} + i \cdot C_{1i} \quad (\text{A.135})$$

$$C_2 = C_{2r} + i \cdot C_{2i} \quad (\text{A.136})$$

Substituting Eqs. (A.135) and (A.136) into (A.134) gives

$$\begin{aligned} \theta(z) = & (C_{1r} + i \cdot C_{1i}) (co^* \cdot ch^* - i \cdot si^* \cdot sh^* + i \cdot si^* \cdot ch^* - co^* \cdot sh^*) \\ & + (C_{2r} + i \cdot C_{2i}) (co^* \cdot ch^* - i \cdot si^* \cdot sh^* - i \cdot si^* \cdot ch^* + co^* \cdot sh^*) \end{aligned} \quad (\text{A.137})$$

$$\begin{aligned} \theta(z) = & (ch^* - sh^*) [C_{1r} co^* - C_{1i} si^*] + (ch^* + sh^*) [C_{2r} co^* + C_{2i} si^*] \\ & + i \cdot \{ (ch^* - sh^*) [C_{1r} si^* + C_{1i} co^*] + (ch^* + sh^*) [-C_{2r} si^* + C_{2i} co^*] \} \end{aligned} \quad (\text{A.138})$$

Therefore the rotation along the specimen can be expressed as

$$\theta(z) = A_1 + i A_2 = \sqrt{A_1^2 + A_2^2} \times e^{i\phi} \quad (\text{A.139})$$

where

$$A_1 = (ch^* - sh^*)[C_{1r}co^* - C_{1i}si^*] + (ch^* + sh^*)[C_{2r}co^* + C_{2i}si^*] \quad (A.140)$$

$$A_2 = (ch^* - sh^*)[C_{1r}si^* + C_{1i}co^*] + (ch^* + sh^*)[-C_{2r}si^* + C_{2i}co^*] \quad (A.141)$$

$$\phi = \tan^{-1}(A_2 / A_1) \quad (A.142)$$

The strain at any location along the specimen axis is

$$\gamma(r, z) = r \cdot \frac{d\theta(z)}{dz} \quad (A.143)$$

A representative shear corresponding to a radius $r=0.4d$ where d is the diameter of the specimen gives the expression for strain along the specimen as

$$\gamma(z) = 0.4d \cdot \frac{d\theta(z)}{dz} \quad (A.144)$$

Substituting Eq. (A.23) into (A.144) gives

$$\gamma(z) = 0.4d \cdot ia \cdot [C_1 e^{iaz} - C_2 e^{-iaz}] \quad (A.145)$$

where the term (ia) can be simplified by substituting Eq. (A.57) into (A.52) as

$$ia = \frac{1}{h}(i\alpha F - \beta F) \quad (A.146)$$

As $\theta(z) = C_1 e^{iaz} + C_2 e^{-iaz} = A_1 + iA_2$, hence the term $C_1 e^{iaz} - C_2 e^{-iaz}$ can be written as

$$C_1 e^{iaz} - C_2 e^{-iaz} = A_1^* + iA_2^* \quad (A.147)$$

where the A_1^* and A_2^* have similar components as A_1 and A_2 , but with different signs of C_{2r} and C_{2i} ;

$$A_1^* = (ch^* - sh^*)[C_{1r}co^* - C_{1i}si^*] + (ch^* + sh^*)[-C_{2r}co^* - C_{2i}si^*] \quad (A.148)$$

$$A_2^* = (ch^* - sh^*)[C_{1r}si^* + C_{1i}co^*] + (ch^* + sh^*)[C_{2r}si^* - C_{2i}co^*] \quad (A.149)$$

Substituting Eq. (A.146) and (A.147) into (A.145) gives

$$\gamma(z) = \frac{0.4d}{h}[i\alpha F - \beta F][A_1^* + iA_2^*] \quad (A.150)$$

$$\gamma(z) = \frac{0.4d}{h}\left[(-\beta F \cdot A_1^* - \alpha F \cdot A_2^*) + i \cdot (\alpha F \cdot A_1^* - \beta F \cdot A_2^*)\right] \quad (A.151)$$

Finally, substituting Eqs. (A.148) and (A.149) into (A.151), the shear strain along the specimen can be expressed as

$$\gamma(z) = \frac{0.4d}{h} (A_1' + iA_2') = \frac{0.4d}{h} \sqrt{(A_1')^2 + (A_2')^2} \times e^{i\phi'} \quad (\text{A.152})$$

where

$$A_1' = \alpha F(ch^* - sh^*) [-C_{1r}si^* - C_{1i}co^*] - \beta F(ch^* - sh^*) [C_{1r}co^* - C_{1i}si^*] \\ + \alpha F(ch^* + sh^*) [-C_{2r}si^* + C_{2i}co^*] + \beta F(ch^* + sh^*) [C_{2r}co^* + C_{2i}si^*] \quad (\text{A.153})$$

$$A_2' = \alpha F(ch^* - sh^*) [C_{1r}co^* - C_{1i}si^*] - \beta F(ch^* - sh^*) [C_{1r}si^* + C_{1i}co^*] \\ + \alpha F(ch^* + sh^*) [-C_{2r}co^* - C_{2i}si^*] + \beta F(ch^* + sh^*) [-C_{2r}si^* + C_{2i}co^*] \quad (\text{A.154})$$

$$\phi' = \tan^{-1}(A_2' / A_1') \quad (\text{A.155})$$

The above equations are programmed into the spreadsheet RCDARE, along with a nonlinear solver to determine the optimum frequency factor F and damping ξ to match the theoretical solution to the measured specimen response.

APPENDIX B. RESONANT COLUMN SPECIMEN PREPARATION

1. Apply vacuum grease to the three O-rings on the base of the apparatus. Screw the bottom platen on the base plate.



2. Prepare the specimen mold and apply vacuum grease to seal the gaps between the two parts of the split mold.



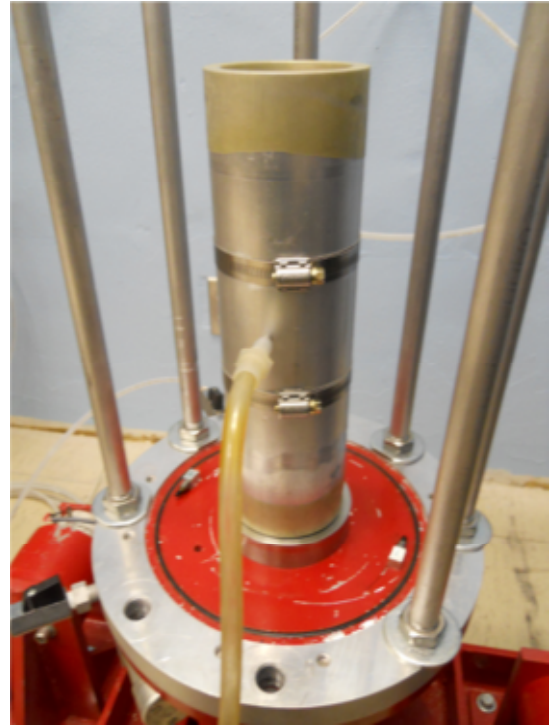
3. Measure the inside diameter of the mold and the thickness of the membrane. The difference between the diameter of the mold and two times the thickness of the membrane is termed the “effective diameter- d_e ” of the specimen.



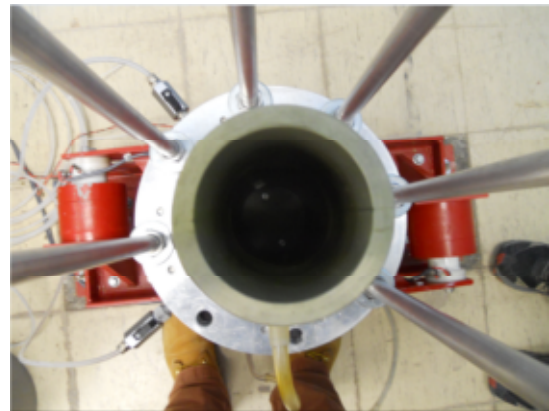
8. Thinly grease the side of the bottom platen. Place the membrane over the bottom platen. Put on the O-ring to seal the membrane on the bottom platen.



9. Place the mold on the bottom platen. Pull the membrane through the mold. Put a piece of filter paper between the membrane and mold at the position of the vacuum hole. Wrap the membrane around the top of the mold.



10. Apply vacuum to the mold so that the membrane sticks to the inner wall of the mold without any wrinkles (Note: If there is a gap between the membrane and the inner wall, the membrane might have holes or the gaps between the two parts of the mold might not be sealed).



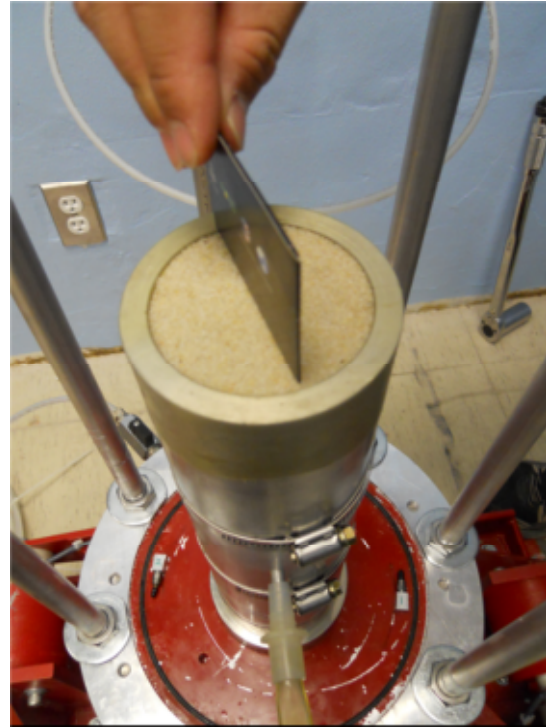
12. Weigh the required mass of soil. Pour the soil in the mold. In order to achieve the target relative density, deposit the soil uniformly in the mold. It is recommended that a rubber mallet be used gently tap the mold during pouring to densify the soil.



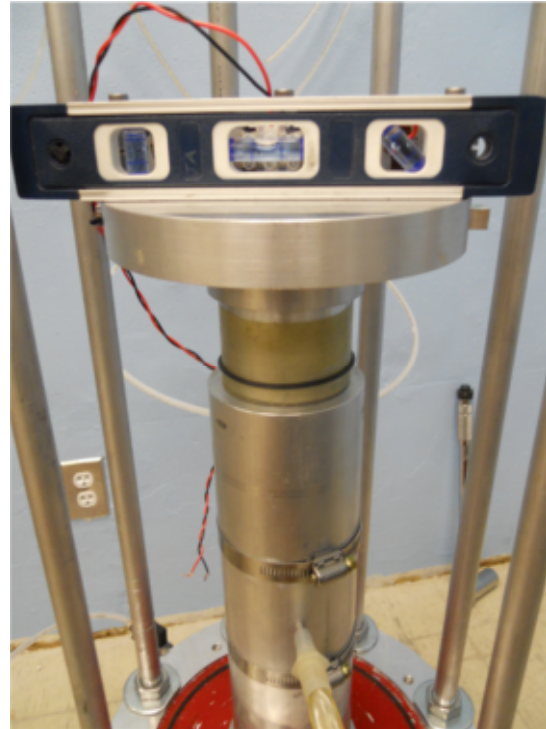
13. There might be some soil remaining or additional soil needed. Measure the actual mass M_{act} of soil used to make the specimen.



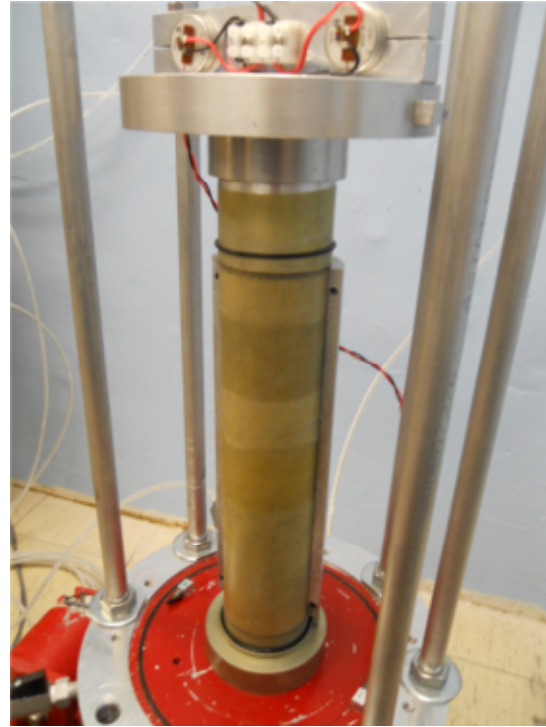
14. Level the specimen by rotating a blade at the top of the specimen.



15-17. Place the O-ring on the top platen. Apply a thin layer of vacuum grease to the side of the top platen. Carefully place the top platen on the top of specimen. Place a leveling tool on the top platen to ensure that it is level. Stretch the membrane up around the top platen and seal it with the O-ring.



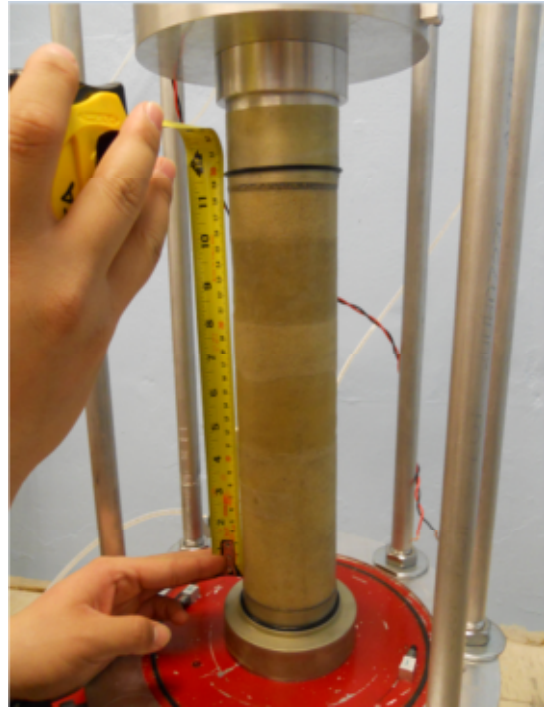
19. Carefully take apart the mold by removing the screws on the mold and remove it from around the specimen.



20. Measure the actual diameter d_{act} at three points along the specimen (bottom, center and top).



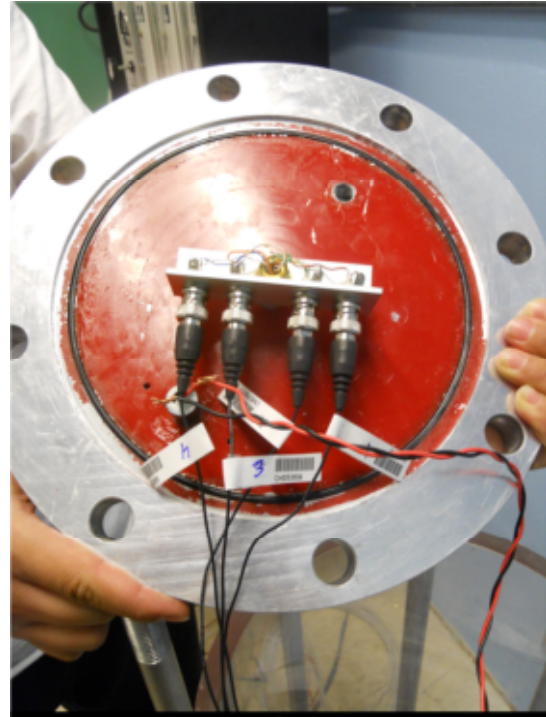
20. Measure the actual height h_{act} of the specimen to calculate the actual volume V_{act} .



22-23. Place the acrylic chamber over the specimen and the wires of the transducers and accelerometers.



24. Connect the transducers and accelerometers to the channels on the lid. Apply vacuum grease to the O-ring on the lid. Place the lid on the acrylic chamber. Carefully hand tighten the eight nuts until they just come in contact with the washers.



25. Use the torque wrench to tighten the nuts to a torque of 30 ft-lbs. Start with one nut and tighten it to 10 ft-lbs. Then move to the nut diametrically opposed and do the same. Come back to the first nut and move clockwise to the next nut and tighten it to 10 ft-lbs. Continue the process until the wrench has been placed on all the nuts twice. Use the same procedure to bring the torque in all of the nuts up to 30 ft-lbs. It may be necessary to place the wrench on each nut 3 or 4 times to achieve the desired 30 ft-lbs.



APPENDIX C. RESONANT COLUMN DATA REDUCTION MATLAB CODE

```

%%%%%%%%%%%%%%%%%%%%%%%%%%%%%%%%%%%%%%%%%%%%%%%%%%%%%%%%%%%%%%%%%%%%%%%%
%%      Data Recorded in SigLab      %%
%%      Channel 3 is bottom right    %%
%%      Channel 4 is bottom left     %%
%%      Channel 5 is top right       %%
%%      Channel 6 is top left        %%
%%%%%%%%%%%%%%%%%%%%%%%%%%%%%%%%%%%%%%%%%%%%%%%%%%%%%%%%%%%%%%%%%%%%%%%%

clear all
close all
clc
%%%%%%%%%%%%%%%%%%%%%%%%%%%%%%%%%%%%%%%%%%%%%%%%%%%%%%%%%%%%%%%%%%%%%%%%
%%
%% Sampling Parameters
load RC10psi_103108_01.vna -mat
t = SLm.tdxvec; % size:4096
f = SLm.fdxvec; % [0:1.25:2000Hz] size:1601
fs = 2.56*2000;
N = length(t);
T = N/fs;
df = 1/T;
dt = T/N;
i=sqrt(-1);
f_fft=[0:N-1]*df;
f_posneg=[f_fft(1:N/2+1) -f_fft(N/2:-1:2)]';
%% Specimen and platen properties
d=(6)*0.0254; % diameter (m)
h=(12.41)*0.0254; % height (m)
rho=1730; % density (kg/m^3)
mass=pi*(d/2)^2*h*rho; % mass (kg)
J_soil=mass*d^2/8; % sample's polar mass moment of inertia (kg*m^2)
J_top=0.0356; % 6" top platen's polar mass moment of inertia (kg*m^2)
Jbar=J_top/J_soil;
disp('-----');
');
disp('-----Specimen Parameters-----');
');
disp(['height=', num2str(h) ' m']);
disp(['diameter=', num2str(d) ' m']);
disp(['density=', num2str(rho) ' kg/m^3']);
disp(['Jbar=', num2str(Jbar)]);
disp('-----');
');
%%%%%%%%%%%%%%%%%%%%%%%%%%%%%%%%%%%%%%%%%%%%%%%%%%%%%%%%%%%%%%%%%%%%%%%%
%%
%% Load SigLab data file
%% Take the FFT of the last time history since ensemble average FFT's
were not saved
a3=SLm.scmeas(3).tdmeas * SLm.scmeas(3).eu_val; % Bottom right accel
a4=SLm.scmeas(4).tdmeas * SLm.scmeas(4).eu_val; % Bottm left accel
a5=SLm.scmeas(5).tdmeas * SLm.scmeas(5).eu_val; % Top right accel

```



```

a6=SLm.scmeas(6).tdmeas * SLm.scmeas(6).eu_val; % Top left accel

a0=(a3+a4)/2; % Average bottom platen tangential acceleration in time
domain
ah=(a5+a6)/2; % Average top platen tangential acceleration in time domain

xfer53 = SLm.xcmeas(3,5).xfer *
SLm.scmeas(5).eu_val/SLm.scmeas(3).eu_val;
xfer63 = SLm.xcmeas(3,6).xfer *
SLm.scmeas(6).eu_val/SLm.scmeas(3).eu_val;
xfer54 = SLm.xcmeas(4,5).xfer *
SLm.scmeas(5).eu_val/SLm.scmeas(4).eu_val;
xfer64 = SLm.xcmeas(4,6).xfer *
SLm.scmeas(6).eu_val/SLm.scmeas(4).eu_val;

% averaged transfer function [ch1/refch1 + ch2/refch1 + ch1/refch2 +
ch2/refch2]/4
xfer_exp = transpose(xfer53+xfer63+xfer54+xfer64)/4;

%%% Accel. FFT Hanning window and strain
H=1-cos(pi*t./T)'.^2; Ca=4; Cp=8/3;
Xk=fft(H.*a0);Xk(1)=Xk(1)/2; a0fft=2*sqrt(Ca)*Xk/N;
for n=1:N
theta0fft(n)=-1/(d/2)*a0fft(n)/(2*pi*f_posneg(n))^2;
end
for n=1:1601
gamma(n)=0.4*d/h*(xfer_exp(n)-1)*theta0fft(n);
gamma(1)=0;
end
figure(120);
subplot(2,1,1);semilogy(f,abs(gamma));ylabel('Mag(\gamma)');grid
on;set(gca,'XTickLabel','|');
subplot(2,1,2);plot(f,angle(gamma));ylabel('Ph(\gamma)');xlabel('Frequency [Hz]');
%%%%%%%%%%%%%%%%%%%%%%%%%%%%%%%%%%%%%%%%%%%%%%%%%%%%%%%%%%%%%%%%%%%%%%%%
%%
%% Only fit peaks
%%% Determine G (with G increased, xfer moves right)
wbar=[15/8000:15/8000:0.75 0.7501:1e-4:.85 .85125:15/8000:15]; % size:
1x8947
xi=2/100; % assume the initial damping in order to fit the amplitude of
peaks
D=1+i*2*xi; % hysteretic damping
wstar=wbar./sqrt(D);
xfer=1./(cos(wstar)-Jbar.*wstar.*sin(wstar)); % theory transfer function

[xferpk,ipk]=findpeaks(abs(xfer),'npeaks',5); % find the 5 peaks of the
theory XFER
wbarpk=wbar(ipk);
wstarpk=wstar(ipk);

[xferpk_exp,fpk]=RCfindpk(abs(xfer_exp),f); % find the
amplitudes(Hpk_exp) and frequencies(fpk) associated with the peaks of
experiment transfer function (xfer_exp)

```

```

for n=1:5
    G0(n)=(2*pi*fpk(n)*h)^2*rho/(wbarpk(n))^2; % calculate G0 using
    wbarpk and fpk by knowing rho and h.
    fscal(:,n)=sqrt(G0(n)/rho)*wbar./(2*pi*h); % convert wbar to f using
    calculated G0
end

%%% Determine D (with D increased, xfer moves down)
for n=1:5 % to fit 5 peaks
    for xiD=xi:sign(xferpk(n)-xferpk_exp(n))*0.01/100:(xi+sign(xferpk(n)-
    xferpk_exp(n))*2/100) % (e.g. xiD=[2%:0.01%(or -0.01%):4%(or 0%)])
        D=1+i*2*xiD;
        wstar=wbar./sqrt(D);
        xferD=1./(cos(wstar)-Jbar.*wstar.*sin(wstar));
        [xferpkD,ipkD]=findpeaks(abs(xferD),'npeaks',5);
        if sign(xferpk(n)-xferpk_exp(n))==1
            if sign(xferpkD(n)-xferpk_exp(n))~=1
                break
            end
        else
            if sign(xferpkD(n)-xferpk_exp(n))~-1
                break
            end
        end
    end
end
xir(n)=xiD;
end
xi=xir;
Dr=1+i*2*xi; % hysteretic damping
for n=1:5
    wstar(n,:)=wbar./sqrt(Dr(n));
    xfer(n,:)=1./(cos(wstar(n,:))-Jbar.*wstar(n,:).sin(wstar(n,:)));
end

% Plot H_theory vs. H_experiment (only fit 5 peaks)
figure(12)

subplot(5,1,1);
plot(fscal(:,1),abs(xfer(1,:)),'r');hold on;plot(f,abs(xfer_exp),'b--
');grid on;xlim([0 2000]);ylim([0
xferpk_exp(1)+xferpk_exp(1)/15]);set(gca,'XTick',[0 500 1000 1500 2000]);
set(gca,'XTickLabel','|');legend('Theory(pk)','Experiment');ylabel('Mag(H
)');%title([strcat('G_{pk}=',num2str(G0(1)/1e6),' MPa',' ',
\xi_{pk}=',num2str(xi(1)*100),'%', ' for fit 1^{st} peak')]);

subplot(5,1,2);
plot(fscal(:,2),abs(xfer(2,:)),'r');hold on;plot(f,abs(xfer_exp),'b--
');grid on;xlim([0 2000]);ylim([0
xferpk_exp(2)+xferpk_exp(2)/15]);set(gca,'XTick',[0 500 1000 1500 2000]);
set(gca,'XTickLabel','|');ylabel('Mag(H)');%title([strcat('G_{pk}=',num2
str(G0(2)/1e6),' MPa',' ', \xi_{pk}=',num2str(xi(2)*100),'%', ' for fit
2^{nd} peak')]);

```

```

subplot(5,1,3);
plot(fscal(:,3),abs(xfer(3,:)), 'r');hold on;plot(f,abs(xfer_exp), 'b--
');grid on;xlim([0 2000]);ylim([0
xferpk_exp(3)+xferpk_exp(3)/15]);set(gca, 'XTick', [0 500 1000 1500 2000]);
set(gca, 'XTickLabel', '|');ylabel('Mag(H)');%title([strcat('G_{pk}=', num2
str(G0(3)/1e6), ' MPa', ', ', \xi_{pk}=', num2str(xi(3)*100), '%', ' for fit
3^{th} peak')]))

subplot(5,1,4);
plot(fscal(:,4),abs(xfer(4,:)), 'r');hold on;plot(f,abs(xfer_exp), 'b--
');grid on;xlim([0 2000]);ylim([0
xferpk_exp(4)+xferpk_exp(4)/15]);set(gca, 'XTick', [0 500 1000 1500 2000]);
set(gca, 'XTickLabel', '|');ylabel('Mag(H)');%title([strcat('G_{pk}=', num2
str(G0(4)/1e6), ' MPa', ', ', \xi_{pk}=', num2str(xi(4)*100), '%', ' for fit
4^{th} peak')]))

subplot(5,1,5);
plot(fscal(:,5),abs(xfer(5,:)), 'r');hold on;plot(f,abs(xfer_exp), 'b--
');grid on;xlim([0 2000]);ylim([0
xferpk_exp(5)+xferpk_exp(5)/15]);set(gca, 'XTick', [0 500 1000 1500 2000]);
set(gca, 'XTickLabel', '0|500|1000|1500|2000');ylabel('Mag(H)');xlabel('Fr
equency [Hz]');%title([strcat('G_{pk}=', num2str(G0(5)/1e6), ' MPa', ', ',
\xi_{pk}=', num2str(xi(5)*100), '%', ' for fit 5^{th} peak')])));

fontstyle('times',12);
%%
figure(109)

subplot(3,1,1);
plot(fscal(:,1),abs(xfer(2,:)), 'r');hold on;plot(f,abs(xfer_exp), 'b--
');grid on;xlim([0 2000]);set(gca, 'XTick', [0 500 1000 1500 2000]);ylim([0
20])
set(gca, 'XTickLabel', '|');legend('Theoretical', 'Experimental');ylabel('Ma
g(\theta_p/\theta_a)');
subplot(3,1,2);
plot(fscal(:,1),real(xfer(2,:)), 'r');hold on;plot(f,real(xfer_exp), 'b--
');grid on;xlim([0 2000]);set(gca, 'XTick', [0 500 1000 1500 2000]);ylim([-
10 10])
set(gca, 'XTickLabel', '|');ylabel('Re(\theta_p/\theta_a)');
subplot(3,1,3);
plot(fscal(:,1),imag(xfer(2,:)), 'r');hold on;plot(f,imag(xfer_exp), 'b--
');grid on;xlim([0 2000]);set(gca, 'XTick', [0 500 1000 1500 2000]);ylim([-
20 20])
xlabel('Frequency [Hz]');ylabel('Im(\theta_p/\theta_a)');

% Output G and D
disp('-----
');
disp('-----Output G and D for fit peaks only-----
');

```

```

disp(['shear modulus(5 peaks)=', num2str(G0/1e6,'%4.1f MPa; ')]);
disp(['damping ratio(5 peaks)=', num2str(xi*100,'%3.1f; ') ' [%]' ]]);
disp('-----')
');
%%%%%%%%%%%%%%%%%%%%%%%%%%%%%%%%%%%%%%%%%%%%%%%%%%%%%%%%%%%%%%%%%%%%%%%%
%%
%% Squares-error fit +-50 points around each peak
%%% Determine Gopt and Dopt
omega=(2*pi*f)*h*sqrt(rho/G0(1)); % using f(1601) and G0(1) to back
calculate wbar
D=1+i*2*xi(1);
omegastar=omega./sqrt(D);
xfer1601=1./(cos(omegastar)-Jbar.*omegastar.*sin(omegastar));
[xfer1601pk,ipk]=findpeaks(abs(xfer1601),'npeaks',5);

n=1;
for Gr=[min(G0)-10e6:0.1e6:max(G0)+10e6]
    m=1;
    for xir=0:0.1/100:4/100
        omega=(2*pi*f)*h*sqrt(rho/Gr);
        D=1+i*2*xir;
        omeagastar=omega./sqrt(D);
        xfer1601=1./(cos(omegastar)-Jbar.*omegastar.*sin(omegastar));
        E1(m,n)=sum(abs(xfer_exp(ipk(1)-50:ipk(1)+50)-xfer1601(ipk(1)-
50:ipk(1)+50)));
        E2(m,n)=sum(abs(xfer_exp(ipk(2)-50:ipk(2)+50)-xfer1601(ipk(2)-
50:ipk(2)+50)));
        E3(m,n)=sum(abs(xfer_exp(ipk(3)-50:ipk(3)+50)-xfer1601(ipk(3)-
50:ipk(3)+50)));
        E4(m,n)=sum(abs(xfer_exp(ipk(4)-50:ipk(4)+50)-xfer1601(ipk(4)-
50:ipk(4)+50)));
        E5(m,n)=sum(abs(xfer_exp(ipk(5)-50:ipk(5)+20)-xfer1601(ipk(5)-
50:ipk(5)+20)));
        m=m+1;
    end
    n=n+1;
end

Gr=[min(G0)-10e6:0.1e6:max(G0)+10e6];
xir=0:0.1/100:4/100;

% Plot the surface of G,D vs. Error
figure(13)

subplot(5,1,1);surf(Gr/1e6,xir*100,E1);zlim([0 180]);xlabel('G
[MPa]');ylabel('D [%]');zlabel('E');
subplot(5,1,2);surf(Gr/1e6,xir*100,E2);zlim([0 100]);xlabel('G
[MPa]');ylabel('D [%]');zlabel('E');
subplot(5,1,3);surf(Gr/1e6,xir*100,E3);zlim([0 50]);xlabel('G
[MPa]');ylabel('D [%]');zlabel('E');
subplot(5,1,4);surf(Gr/1e6,xir*100,E4);zlim([0 50]);xlabel('G
[MPa]');ylabel('D [%]');zlabel('E');
subplot(5,1,5);surf(Gr/1e6,xir*100,E5);zlim([0 50]);xlabel('G
[MPa]');ylabel('D [%]');zlabel('E');

```

```

fontstyle('times',11);

% find the minimum point on the surface (minmum value in the matrix)
[Eimin irow]=min(E1);[Eijmin
jcol]=min(Eimin);imin=irow(jcol);jmin=jcol;Dopt(1)=xir(imin);Gopt(1)=Gr(j
min);
[Eimin irow]=min(E2);[Eijmin
jcol]=min(Eimin);imin=irow(jcol);jmin=jcol;Dopt(2)=xir(imin);Gopt(2)=Gr(j
min);
[Eimin irow]=min(E3);[Eijmin
jcol]=min(Eimin);imin=irow(jcol);jmin=jcol;Dopt(3)=xir(imin);Gopt(3)=Gr(j
min);
[Eimin irow]=min(E4);[Eijmin
jcol]=min(Eimin);imin=irow(jcol);jmin=jcol;Dopt(4)=xir(imin);Gopt(4)=Gr(j
min);
[Eimin irow]=min(E5);[Eijmin
jcol]=min(Eimin);imin=irow(jcol);jmin=jcol;Dopt(5)=xir(imin);Gopt(5)=Gr(j
min);

% Output Gopt and Dopt
disp('-----');
disp('----Output optimum G and D for least squares fit +- 50 points
around peaks only-----');
disp(['optimum shear modulus(5 peaks)=', num2str(Gopt/1e6,'%4.1f MPa;
')]);
disp(['optimum damping ratio(5 peaks)=', num2str(Dopt*100,'%3.1f; ')
'[%]']);
disp('-----');

% calculate xfer_opt using Gopt and Dopt
for n=1:5
    omega=(2*pi*f)*h*sqrt(rho/Gopt(n));
    D=1+i*2*Dopt(n); % hysteretic damping
    omegastar(n,:)=omega./sqrt(D);
    xferopt(n,:)=1./(cos(omegastar(n,:))-
Jbar.*omegastar(n,:).*sin(omegastar(n,:)));
end

% Plot H_theory_optimum(Gopt and Dopt) vs. H_experiment
figure(15)
subplot(5,1,1);
plot(f,abs(xferopt(1,:)), 'r');hold on;plot(f,abs(xfer_exp), 'b--');grid
on;xlim([0 2000]);ylim([0
xferpk_exp(1)+xferpk_exp(1)/5]);set(gca,'XTick',[0 500 1000 1500 2000]);
set(gca,'XTickLabel','|');legend('Theory(opt)','Experiment');ylabel('Mag(
H)');title(['G_{opt}=',num2str(Gopt(1)/1e6),' MPa',' ',
\xi_{opt}=',num2str(Dopt(1)*100),'%', ' for fit 1^{st} peak']));
subplot(5,1,2);
plot(f,abs(xferopt(2,:)), 'r');hold on;plot(f,abs(xfer_exp), 'b--');grid
on;xlim([0 2000]);ylim([0
xferpk_exp(2)+xferpk_exp(2)/8]);set(gca,'XTick',[0 500 1000 1500 2000]);

```

```

set(gca, 'XTickLabel', '|'); ylabel('Mag(H)'); title([strcat('G_{opt}=', num2
str(Gopt(2)/1e6), ' MPa', ', \xi_{opt}=', num2str(Dopt(2)*100), '%', ' for fit
2^{nd} peak')]);
subplot(5,1,3);
plot(f,abs(xferopt(3,:)), 'r'); hold on; plot(f,abs(xfer_exp), 'b--'); grid
on; xlim([0 2000]); ylim([0
xferpk_exp(3)+xferpk_exp(3)/8]); set(gca, 'XTick', [0 500 1000 1500 2000]);
set(gca, 'XTickLabel', '|'); ylabel('Mag(H)'); title([strcat('G_{opt}=', num2
str(Gopt(3)/1e6), ' MPa', ', \xi_{opt}=', num2str(Dopt(3)*100), '%', ' for fit
3^{rd} peak')]);
subplot(5,1,4);
plot(f,abs(xferopt(4,:)), 'r'); hold on; plot(f,abs(xfer_exp), 'b--'); grid
on; xlim([0 2000]); ylim([0
xferpk_exp(4)+xferpk_exp(4)/8]); set(gca, 'XTick', [0 500 1000 1500 2000]);
set(gca, 'XTickLabel', '|'); ylabel('Mag(H)'); title([strcat('G_{opt}=', num2
str(Gopt(4)/1e6), ' MPa', ', \xi_{opt}=', num2str(Dopt(4)*100), '%', ' for fit
4^{th} peak')]);
subplot(5,1,5);
plot(f,abs(xferopt(5,:)), 'r'); hold on; plot(f,abs(xfer_exp), 'b--'); grid
on; xlim([0 2000]); ylim([0
xferpk_exp(5)+xferpk_exp(5)/8]); set(gca, 'XTick', [0 500 1000 1500 2000]);
ylabel('Mag(H)'); xlabel('Frequency
[Hz]'); title([strcat('G_{opt}=', num2str(Gopt(5)/1e6), ' MPa', ',
\xi_{opt}=', num2str(Dopt(5)*100), '%', ' for fit 5^{th} peak')]);
set(gca, 'XTickLabel', '0|500|1000|1500|2000' );
fontstyle('times', 11);

% Plot H_theory_optimum(Gopt and Dopt) and H_theory_fitpeaks vs.
H_experiment
figure(16)
subplot(5,1,1);
plot(f,abs(xferopt(1,:)), 'r'); hold on; plot(f,abs(xfer_exp), 'b--
'); plot(fscal(:,1),abs(xfer(1,:)), 'c');
grid on; xlim([fpk(1)-50 fpk(1)+50]); ylim([0
xferpk_exp(1)+xferpk_exp(1)]); set(gca, 'XTick', [0:20:2000]);
legend('Theory(opt)', 'Experiment', 'Theory(pk)'); ylabel('Mag(H)'); title([
strcat('G_{opt}=', num2str(Gopt(1)/1e6), ' MPa', ',
\xi_{opt}=', num2str(Dopt(1)*100), '%', '
G_{pk}=', num2str(G0(1)/1e6, '%4.1f'), ' MPa', ',
\xi_{pk}=', num2str(xi(1)*100, '%3.1f'), '%', ' for fit 1^{st} peak')]);
subplot(5,1,2);
plot(f,abs(xferopt(2,:)), 'r'); hold on; plot(f,abs(xfer_exp), 'b--
'); plot(fscal(:,2),abs(xfer(2,:)), 'c');
grid on; xlim([fpk(2)-50 fpk(2)+50]); ylim([0
xferpk_exp(2)+xferpk_exp(2)/8]); set(gca, 'XTick', [0:20:2000]);
ylabel('Mag(H)'); title([strcat('G_{opt}=', num2str(Gopt(2)/1e6), ' MPa', ',
\xi_{opt}=', num2str(Dopt(2)*100), '%', '
G_{pk}=', num2str(G0(2)/1e6, '%4.1f'), ' MPa', ',
\xi_{pk}=', num2str(xi(2)*100, '%3.1f'), '%', ' for fit 2^{nd} peak')]);
subplot(5,1,3);
plot(f,abs(xferopt(3,:)), 'r'); hold on; plot(f,abs(xfer_exp), 'b--
'); plot(fscal(:,3),abs(xfer(3,:)), 'c');
grid on; xlim([fpk(3)-50 fpk(3)+50]); ylim([0
xferpk_exp(3)+xferpk_exp(3)/8]); set(gca, 'XTick', [0:20:2000]);
ylabel('Mag(H)'); title([strcat('G_{opt}=', num2str(Gopt(3)/1e6), ' MPa', ',

```

```

\ xi_{opt}=',num2str(Dopt(3)*100),'%',';
G_{pk}=',num2str(G0(3)/1e6,'%4.1f'),' MPa',',',
\ xi_{pk}=',num2str(xi(3)*100,'%3.1f'),'%',', for fit 3^{rd} peak')}]])
subplot(5,1,4);
plot(f,abs(xferopt(4,:)), 'r');hold on;plot(f,abs(xfer_exp), 'b--
');plot(fscal(:,4),abs(xfer(4,:)), 'c');
grid on;xlim([fpk(4)-50 fpk(4)+50]);ylim([0
xferpk_exp(4)+xferpk_exp(4)/8]);set(gca, 'XTick', [0:20:2000]);
ylabel('Mag(H)');title([strcat('G_{opt}=',num2str(Gopt(4)/1e6),' MPa',',',
\ xi_{opt}=',num2str(Dopt(4)*100),'%',';
G_{pk}=',num2str(G0(4)/1e6,'%4.1f'),' MPa',',',
\ xi_{pk}=',num2str(xi(4)*100,'%3.1f'),'%',', for fit 4^{th} peak')}]])
subplot(5,1,5);
plot(f,abs(xferopt(5,:)), 'r');hold on;plot(f,abs(xfer_exp), 'b--
');plot(fscal(:,5),abs(xfer(5,:)), 'c');
grid on;xlim([fpk(5)-50 fpk(5)+50]);ylim([0
xferpk_exp(5)+xferpk_exp(5)/8]);set(gca, 'XTick', [0:20:2000]);
ylabel('Mag(H)');xlabel('Frequency
[Hz]');title([strcat('G_{opt}=',num2str(Gopt(5)/1e6),' MPa',',',
\ xi_{opt}=',num2str(Dopt(5)*100,'%4.1f'),'%',';
G_{pk}=',num2str(G0(5)/1e6,'%4.1f'),' MPa',',',
\ xi_{pk}=',num2str(xi(5)*100,'%3.1f'),'%',', for fit 5^{th} peak')}]]);
fontstyle('times',11);

%%%%%%%%%%%%%%%%%%%%%%%%%%%%%%%%%%%%%%%%%%%%%%%%%%%%%%%%%%%%%%%%%%%%%%%%%%%%%%
%%%
%% find strain associated with the optimum peak frequencies

for n=1:5
    [xferoptpk,ioptpk]=findpeaks(abs(xferopt(n,:)), 'npeaks',n);
    foptpk(n)=f(ioptpk(n));
end
gammapk=gamma(fpk/df+1);
gammaoptpk=gamma(foptpk/df+1);

%%
figure(116)
subplot(5,1,1);
plot(f,abs(xferopt(1,:)), 'r', 'linewidth',1.5);hold
on;plot(fscal(:,1),abs(xfer(1,:)), 'b--
', 'linewidth',1.5);plot(f,abs(xfer_exp), 'k', 'linewidth',1.5);
grid on;xlim([foptpk(1)-50 foptpk(1)+50]);ylim([0
40]);set(gca, 'XTick', [foptpk(1)-50:50:foptpk(1)+50]);
legend('Least squares fitting', 'Peak
fitting', 'Experimental');ylabel('Mag(H)');title([strcat('G_{opt}=',num
2str(Gopt(1)/1e6),' MPa',',', \ xi_{opt}=',num2str(Dopt(1)*100),'%',';
G_{pk}=',num2str(G0(1)/1e6,'%4.1f'),' MPa',',',
\ xi_{pk}=',num2str(xi(1)*100,'%3.1f'),'%',', for fit 1^{st} peak')}]])
subplot(5,1,2);
plot(f,abs(xferopt(2,:)), 'r', 'linewidth',1.5);hold
on;plot(fscal(:,2),abs(xfer(2,:)), 'b--
', 'linewidth',1.5);plot(f,abs(xfer_exp), 'k', 'linewidth',1.5);

```

```

grid on;xlim([foptpk(2)-50 foptpk(2)+50]);ylim([0
20]);set(gca,'XTick',[foptpk(2)-50:50:foptpk(2)+50]);
ylabel('Mag(H)');%title([strcat('G_{opt}=',num2str(Gopt(2)/1e6),'
MPa',' ', \xi_{opt}=',num2str(Dopt(2)*100),'%',',');
G_{pk}=',num2str(G0(2)/1e6,'%4.1f'),' MPa',' ',
\xi_{pk}=',num2str(xi(2)*100,'%3.1f'),'%',', for fit 2^{nd} peak'))])
subplot(5,1,3);
plot(f,abs(xferopt(3,:)), 'r', 'linewidth',1.5);hold
on;plot(fscal(:,3),abs(xfer(3,:)), 'b--
', 'linewidth',1.5);plot(f,abs(xfer_exp), 'k', 'linewidth',1.5);
grid on;xlim([foptpk(3)-50 foptpk(3)+50]);ylim([0
3]);set(gca,'XTick',[foptpk(3)-50:50:foptpk(3)+50]);set(gca,'YTick',[0
1.5 3]);
ylabel('Mag(\theta_p/\theta_a)');%title([strcat('G_{opt}=',num2str(Gopt(
3)/1e6),' MPa',' ', \xi_{opt}=',num2str(Dopt(3)*100),'%',',');
G_{pk}=',num2str(G0(3)/1e6,'%4.1f'),' MPa',' ',
\xi_{pk}=',num2str(xi(3)*100,'%3.1f'),'%',', for fit 3^{rd} peak'))])
subplot(5,1,4);
plot(f,abs(xferopt(4,:)), 'r', 'linewidth',1.5);hold
on;plot(fscal(:,4),abs(xfer(4,:)), 'b--
', 'linewidth',1.5);plot(f,abs(xfer_exp), 'k', 'linewidth',1.5);
grid on;xlim([foptpk(4)-50 foptpk(4)+50]);ylim([0
3]);set(gca,'XTick',[foptpk(4)-50:50:foptpk(4)+50]);set(gca,'YTick',[0
1.5 3]);
ylabel('Mag(H)');%title([strcat('G_{opt}=',num2str(Gopt(4)/1e6),'
MPa',' ', \xi_{opt}=',num2str(Dopt(4)*100),'%',',');
G_{pk}=',num2str(G0(4)/1e6,'%4.1f'),' MPa',' ',
\xi_{pk}=',num2str(xi(4)*100,'%3.1f'),'%',', for fit 4^{th} peak'))])
subplot(5,1,5);
plot(f,abs(xferopt(5,:)), 'r', 'linewidth',1.5);hold
on;plot(fscal(:,5),abs(xfer(5,:)), 'b--
', 'linewidth',1.5);plot(f,abs(xfer_exp), 'k', 'linewidth',1.5);
grid on;xlim([foptpk(5)-50 foptpk(5)+50]);ylim([0
2]);set(gca,'XTick',[foptpk(5)-50:50:foptpk(5)+50]);
ylabel('Mag(H)');%title([strcat('G_{opt}=',num2str(Gopt(5)/1e6),'
MPa',' ', \xi_{opt}=',num2str(Dopt(5)*100,'%4.1f'),'%',',');
G_{pk}=',num2str(G0(5)/1e6,'%4.1f'),' MPa',' ',
\xi_{pk}=',num2str(xi(5)*100,'%3.1f'),'%',', for fit 5^{th} peak'))]);
xlabel('Frequency [Hz]');
fontstyle('times',12);

% Plot Gpk and Dpk vs. strain
%figure(18)
%[AX,Hd1,Hd2]=plotyy(abs(gammapk(1:5))*100,G0/max(G0(1:5)),abs(gammapk(1:
5))*100,xi*100,'plot');xlabel('\gamma, %');
%set(AX(1),'XColor','k','YColor','k','xscale','log');xlim(AX(1),[1e-09
0.1]);ylim(AX(1),[0 1]);set(AX(1),'XTick',[10^-9 10^-7 10^-5 10^-3 10^-
1],'YTick',[0:0.2:1]);
%set(AX(2),'XColor','k','YColor','k','xscale','log');xlim(AX(2),[1e-09
0.1]);ylim(AX(2),[0 5]);set(AX(2),'XTick',[10^-9 10^-7 10^-5 10^-3 10^-
1],'YTick',[0:5]);
%set(Hd1,'LineStyle','none','Marker','*','color','b');
%set(Hd2,'LineStyle','none','Marker','.');
%set(get(AX(1),'Ylabel'),'String','G/G_{HD}');
%set(get(AX(2),'Ylabel'),'String','\xi, %'); grid

```



```

on;fontstyle('times',11);

% Plot Gopt and Dopt vs. strain
figure(19)
%[AX,Hd1,Hd2]=plotyy(abs(gammaoptpk(1:5))*100,Gopt/max(Gopt(1:5)),abs(gam
mapk(1:5))*100,Dopt*100,'plot');xlabel('\gamma, %');
%set(AX(1),'XColor','k','YColor','k','xscale','log');xlim(AX(1),[1e-09
0.1]);ylim(AX(1),[0 1]);set(AX(1),'XTick',[10^-9 10^-7 10^-5 10^-3 10^-
1],'YTick',[0:0.2:1]);
%set(AX(2),'XColor','k','YColor','k','xscale','log');xlim(AX(2),[1e-09
0.1]);ylim(AX(2),[0 5]);set(AX(2),'XTick',[10^-9 10^-7 10^-5 10^-3 10^-
1],'YTick',[0:5]);
%set(Hd1,'LineStyle','none','Marker','*','color','b');
%set(Hd2,'LineStyle','none','Marker','.');
%set(get(AX(1),'Ylabel'),'String','G/G_{HD}');
%set(get(AX(2),'Ylabel'),'String','\xi, %'); grid
on;fontstyle('times',11);

% Plot G and D vs. strain
figure(20)
[AX,Hd1,Hd2]=plotyy(abs(gammapk(1:5))*100,G0/max(G0(1:5)),abs(gammapk(1:5
))*100,xi*100,'plot');xlabel('\gamma, %');
set(AX(1),'XColor','k','YColor','k','xscale','log');xlim(AX(1),[1e-09
0.1]);ylim(AX(1),[0 1]);set(AX(1),'XTick',[10^-9 10^-7 10^-5 10^-3 10^-
1],'YTick',[0:0.2:1]);
set(AX(2),'XColor','k','YColor','k','xscale','log');xlim(AX(2),[1e-09
0.1]);ylim(AX(2),[0 5]);set(AX(2),'XTick',[10^-9 10^-7 10^-5 10^-3 10^-
1],'YTick',[0:5]);
set(Hd1,'LineStyle','none','Marker','*','color','b');
set(Hd2,'LineStyle','none','Marker','.','color','b');
set(get(AX(1),'Ylabel'),'String','G/G_{HD}');
set(get(AX(2),'Ylabel'),'String','\xi, %'); grid on
hold on;
[AX,Hd3,Hd4]=plotyy(abs(gammaoptpk(1:5))*100,Gopt/max(Gopt(1:5)),abs(gamm
aoptpk(1:5))*100,Dopt*100,'plot');xlabel('\gamma, %');
set(AX(1),'XColor','k','YColor','k','xscale','log');xlim(AX(1),[1e-09
0.1]);ylim(AX(1),[0 1]);set(AX(1),'XTick',[10^-9 10^-7 10^-5 10^-3 10^-
1],'YTick',[0:0.2:1]);
set(AX(2),'XColor','k','YColor','k','xscale','log');xlim(AX(2),[1e-09
0.1]);ylim(AX(2),[0 5]);set(AX(2),'XTick',[10^-9 10^-7 10^-5 10^-3 10^-
1],'YTick',[0:5]);
set(Hd3,'LineStyle','none','Marker','o','color','r');
set(Hd4,'LineStyle','none','Marker','s','color','r');
set(get(AX(1),'Ylabel'),'String','G/G_{HD}');
set(get(AX(2),'Ylabel'),'String','\xi, %'); grid on
legend([Hd1 Hd2 Hd3 Hd4],{'G_{pk}','\xi_{pk}','G_{opt}','\xi_{opt}'});
fontstyle('times',11);
%%
figure(21)
[AX,Hd1,Hd2]=plotyy(imag(gammaoptpk(1:5))*100,Gopt/max(Gopt(1:5)),imag(ga
mmaoptpk(1:5))*100,Dopt*100,'plot');xlabel('\gamma, %');
set(AX(1),'XColor','k','YColor','k','xscale','log');xlim(AX(1),[1e-10
0.01]);ylim(AX(1),[0 1]);set(AX(1),'XTick',[10^-10 10^-8 10^-6 10^-4 10^-
2],'YTick',[0:0.2:1]);
set(AX(2),'XColor','k','YColor','k','xscale','log');xlim(AX(2),[1e-10

```

```

0.01]);ylim(Ax(2),[0 5]);set(Ax(2),'XTick',[10^-10 10^-8 10^-6 10^-4 10^-
2],'YTick',[0:5]);
set(Hd1,'LineStyle','none','Marker','*','color','b');
set(Hd2,'LineStyle','none','Marker','.','color','b');
set(get(Ax(1),'Ylabel'),'String','G/G_{HD}');
set(get(Ax(2),'Ylabel'),'String','\xi, %'); grid on
hold on;
[AX,Hd3,Hd4]=plotyy(abs(gammaoptpk(1:5))*100,Gopt/max(Gopt(1:5)),abs(gamm
aoptpk(1:5))*100,Dopt*100,'plot');xlabel('\gamma, %');
set(Ax(1),'XColor','k','YColor','k','xscale','log');xlim(Ax(1),[1e-10
0.01]);ylim(Ax(1),[0 1]);set(Ax(1),'XTick',[10^-10 10^-8 10^-6 10^-4 10^-
2],'YTick',[0:0.2:1]);
set(Ax(2),'XColor','k','YColor','k','xscale','log');xlim(Ax(2),[1e-10
0.01]);ylim(Ax(2),[0 5]);set(Ax(2),'XTick',[10^-10 10^-8 10^-6 10^-4 10^-
2],'YTick',[0:5]);
set(Hd3,'LineStyle','none','Marker','o','color','r');
set(Hd4,'LineStyle','none','Marker','s','color','r');
set(get(Ax(1),'Ylabel'),'String','G/G_{HD}');
set(get(Ax(2),'Ylabel'),'String','\xi, %'); grid on
legend([Hd1 Hd2 Hd3 Hd4],{'G-Im(\gamma)','\xi-Im(\gamma)','G-
Mag(\gamma)','\xi-Mag(\gamma)'});
fontstyle('times',11);
%%
figure(200)
[AX,Hd1,Hd2]=plotyy(abs(gammaoptpk(1:5))*100,Gopt(1:5)/max(Gopt),abs(gamm
aoptpk(1:5))*100,Dopt(1:5)*100,'plot');xlabel('\gamma, %')
set(Ax(1),'XColor','k','YColor','k','xscale','log');xlim(Ax(1),[1e-9
0.01]);ylim(Ax(1),[0 1]);set(Ax(1),'XTick',[10^-10 10^-8 10^-6 10^-4 10^-
2],'YTick',[0:0.2:1]);
set(Ax(2),'XColor','k','YColor','k','xscale','log');xlim(Ax(2),[1e-9
0.01]);ylim(Ax(2),[0 5]);set(Ax(2),'XTick',[10^-10 10^-8 10^-6 10^-4 10^-
2],'YTick',[0:5]);
set(Hd1,'LineStyle','none','Marker','*','color','b');
set(Hd2,'LineStyle','none','Marker','.','color','r');
set(get(Ax(1),'Ylabel'),'String','G/G_{max}');
set(get(Ax(2),'Ylabel'),'String','\xi, %'); grid on
legend([Hd1 Hd2],{'G_{opt}','\xi_{opt}'});

gamma_fit=[1e-9:0.0000001:0.01];
gamma_ref=0.00001;
G_m=1./(1+gamma_fit/gamma_ref);
xi_max=5;
xi_m=(gamma_fit./gamma_ref)./(1+gamma_fit./gamma_ref)*5;
figure(200);hold on
[AX,Hd3,Hd4]=plotyy(gamma_fit,G_m,gamma_fit,xi_m,'plot');
set(Ax(1),'XColor','k','YColor','k','xscale','log');xlim(Ax(1),[1e-9
0.01]);ylim(Ax(1),[0 1]);
set(Ax(2),'XColor','k','YColor','k','xscale','log');xlim(Ax(2),[1e-9
0.01]);ylim(Ax(2),[0 5]);
set(Hd3,'LineStyle','-','color','b');
set(Hd4,'LineStyle','-','color','r');

fontstyle('times',12);

```

APPENDIX D. MODIFIED RCDARE SPREADSHEET FOR ASTM RESONANT COLUMN TESTING DATA REDUCTION

In this study, a modified spreadsheet RCDARE was used for the data reduction. It was written by Dr. Drnevich for a quasi-static torsional shear RC apparatus at Purdue University. That device is a three-degree-of-freedom model with active mass, passive mass and reaction mass. The RC free-free device used in this study is a two-degree-of-freedom system. There are only two equations of motion (EOM), corresponding to the active and passive boundary conditions. Hence, RCDARE was simplified to adapt it for the free-free device at Iowa State University. The detailed changes are discussed as follows

1. In the original RCDARE, accelerometers were used instead of geophones. Therefore, any factor in the spreadsheet related to the rotation shall be multiplied by the measured resonant frequency f_T . For example, the calculation of magnification factor in sheet-“Intermed” and strain calculation in sheet-“Results” were revised to multiply by f_T .
2. The quasi-static RC device has an active mass at the top. The passive mass at the bottom was used to establish resonance. On the contrary, the free-free RC device has the active platen at the bottom, and passive platen at top used to establish resonance. To make the spreadsheet clear, the text “top” and “bottom” were switched and marked in red color. Since the free-free RC device uses the top platen (passive) to establish resonance, the active rotational calibration factor (RCFA) in the sheet-“Appart” was changed to RCFP (see section 2.2).
3. For the strain calculation in RCDARE, only the imaginary parts of the strain along the specimen are numerically integrated to calculate the strain factor. An

explanation for this may be because sinusoidal excitation was used in the ASTM approach, for which the strain in the time-domain can be expressed as $\gamma = \gamma_0 \cdot e^{i\omega t} = \gamma_0 (\cos \omega t + i \sin \omega t)$. Therefore, only the imaginary parts of strain correspond to the sinusoidal forcing, while the real parts correspond to the cosinel excitation. In contrast, the transfer function approach used the complex magnitude of strain.

4. Coefficients for the complex simultaneous equations in the sheet-“HRESCOL” were originally programmed for a three-degree-of-freedom model. They were simplified for the free-free two-degree-of-freedom RC device presented herein. The derivation of this new matrix is presented in Section 3.1 and Appendix A. The equations of the coefficients in RCDARE were changed based on this derivation. The numbers shown in red next to each coefficient in the modified version of RCDARE were used to verify whether the calculations were correct.
5. Three plots can be produced by RCDARE, in which the Microsoft Visual Basic (VB) language is used to copy the parameters from the “Results” sheet to paste on the related columns in the plotting sheets. However, the particular version of the original RCDARE program used in this study did not produce the plots due to an error in the VB (see Table D.1). The column numbers were corrected by the text shown in red to produce the plots.

Table D.1: Errors in the VB of RCDARE spread sheet

```

...
Go to Results Sheet and Check for Numbers in StrnPlot Column

    rBEGIN = 13
    rEND = 53

    For i = rBEGIN To rEND
    Sheets("Results").Select
    Row = i
    Cells(Row, 12).Select
    CurvNo = ActiveCell

    If CurvNo < 1 Then GoTo 4
    If CurvNo > 3 Then GoTo 4

    Cells(Row, 1).Select
    Line = ActiveCell
    Cells(Row, 3).Select
    EffStr = ActiveCell
    Cells(Row, 8).Select
    G = ActiveCell
    Cells(Row, 9).Select
    Gam = ActiveCell
    Cells(Row, 10).Select
    D = ActiveCell

```

After the above modifications, the new RCDARE program worked well for the ASTM procedure data reduction in this study. Instructions for using this modified RCDARE are as follows:

1. Start with the “Apparat.” sheet. Input the calibration factors according to the apparatus calibration table (Table 2.1).
2. Input the specimen properties in “Spec. Init.” sheet.
3. On the “Input” sheet, place the cursor on the “Date Time Reading” cell and press “Ctrl r” to record the time. Then enter the recorded test data in the columns labeled “Torq. Rdg.”, “Accel. Rdg.” and “Resonant Frequency”.
4. Select the “Results” sheet. Follow the instructions to calculate shear modulus, shear strain and damping ratio. The shear modulus and damping ratio versus

strain plots can be obtained by pressing “Ctrl n”. Plots versus confining pressure can be obtained by pressing “Ctrl s”. “Ctrl t” will give the plots versus consolidation time. Plots are shown in the sheets “StrsPlt”, “StrnPlt” and “tPlt”.

5. No inputs are needed for the “HRESCOL” sheet. Do not make changes in this sheet.